



**UNIVERSIDAD NACIONAL AUTÓNOMA DE MÉXICO**  
**PROGRAMA DE MAESTRÍA Y DOCTORADO EN INGENIERÍA**  
**INGENIERÍA EN ENERGÍA – FUENTES RENOVABLES**

**METODOLOGÍA PARA LA OPTIMIZACIÓN DEL USO DEL RECURSO EÓLICO APLICANDO  
ANÁLISIS DE DINÁMICA DE FLUIDOS COMPUTACIONAL PARA LA INSTALACIÓN DE  
AEROGENERADORES DE BAJA POTENCIA EN ZONAS URBANAS Y RURALES**

**TESIS**  
**QUE PARA OPTAR POR EL GRADO DE**  
**DOCTOR EN INGENIERÍA**

**PRESENTA:**  
**ERNESTO ARTEAGA LÓPEZ**

**TUTOR PRINCIPAL**  
**DR. CÉSAR ANGELES CAMACHO, INSTITUTO DE INGENIERÍA, UNAM**

**COMITÉ TUTOR**  
**DR. OSCAR ALFREDO JARAMILLO SALGADO, INSTITUTO DE ENERGÍAS RENOVABLES, UNAM**  
**DR. DAVID MORILLÓN GÁLVEZ, INSTITUTO DE INGENIERÍA, UNAM**  
**DR. ERASMO CADENAS CALDERÓN, FACULTAD DE ING. MECÁNICA, UMSNH**  
**DR. FRANCISCO BAÑUELOS RUEDAS, INGENIERÍA ELÉCTRICA, UAZ**

**CIUDAD DE MÉXICO**  
**ENERO 2020**



Universidad Nacional  
Autónoma de México



**UNAM – Dirección General de Bibliotecas**  
**Tesis Digitales**  
**Restricciones de uso**

**DERECHOS RESERVADOS ©**  
**PROHIBIDA SU REPRODUCCIÓN TOTAL O PARCIAL**

Todo el material contenido en esta tesis esta protegido por la Ley Federal del Derecho de Autor (LFDA) de los Estados Unidos Mexicanos (México).

El uso de imágenes, fragmentos de videos, y demás material que sea objeto de protección de los derechos de autor, será exclusivamente para fines educativos e informativos y deberá citar la fuente donde la obtuvo mencionando el autor o autores. Cualquier uso distinto como el lucro, reproducción, edición o modificación, será perseguido y sancionado por el respectivo titular de los Derechos de Autor.



**UNIVERSIDAD NACIONAL AUTÓNOMA DE MÉXICO**  
MASTER AND DOCTORAL PROGRAM IN ENGINEERING  
ENERGY ENGINEERING – RENEWABLE SOURCES

**METHODOLOGY FOR THE OPTIMIZATION OF THE USE OF THE WIND RESOURCE BY  
APPLYING COMPUTATIONAL FLUID DYNAMICS FOR THE INSTALLATION OF SMALL WIND  
TURBINES IN URBAN AND RURAL ZONES**

DISSERTATION IN FULFILLMENT OF THE REQUIREMENTS  
FOR THE DEGREE OF  
DOCTOR OF PHILOSOPHY IN ENGINEERING

**PRESENTED BY:**  
ERNESTO ARTEAGA LÓPEZ

**THESIS ADVISOR**  
DR. CÉSAR ANGELES CAMACHO, INSTITUTO DE INGENIERÍA, UNAM

**COMMITTEE MEMBERS**  
DR. OSCAR ALFREDO JARAMILLO SALGADO, INSTITUTO DE ENERGÍAS RENOVABLES, UNAM  
DR. DAVID MORILLÓN GÁLVEZ, INSTITUTO DE INGENIERÍA, UNAM  
DR. ERASMO CADENAS CALDERÓN, FACULTAD DE ING. MECÁNICA, UMSNH  
DR. FRANCISCO BAÑUELOS RUEDAS, INGENIERÍA ELÉCTRICA, UAZ

MEXICO CITY, MEXICO  
ENERO 2020

COMMITTEE MEMBERS:

President	DR. OSCAR ALFREDO JARAMILLO SALGADO
Secretary	DR. DAVID MORILLÓN GÁLVEZ
1st vocal	DR. CÉSAR ÁNGELES CAMACHO
2nd vocal	DR. ERASMO CADENAS CALDERÓN
3rd vocal	DR. FRANCISCO BAÑUELOS RUEDAS

This dissertation was made at the Engineering Institute, UNAM.

THESIS ADVISOR:

Dr. César Angeles Camacho

---

Signature

---

## Abstract

---

The emerging technologies in renewable energy, specifically in wind energy, have increased their penetration not only at large scale but also in low generation wind projects. The International Energy Agency (IEA) Wind Extension Task 27, is specifically aimed at solving the problems of optimizing the use of the wind resource in turbulence zones, both urban and rural environments, through the application of innovative techniques like Computational Fluid Dynamics (CFD).

This thesis reports the development of an advanced methodology based on computational fluid dynamics analysis to assess the installation of small-scale wind turbines. The objective is to deliver an easy-to-follow methodology, which permits the application of diverse CFD methods and software. The optimal location of the SWTs, provided by the developed methodology, permitting to show the main advantages of small wind turbines in the urban/rural environments.

A Virtual Computational Domain (VCD) has superseded the unidirectional simulations in CFD analysis. Among the advantage, that the implementation of this VCD concedes, is the creation of wind resource maps with high resolution. This implementation allows determining new areas of interest with wind potential, which helps determine new zones or hot spot regions with higher wind incidence. The results show a great advantage of the CFD analysis thanks to its relative ease in the implementation and characterization of the wind resource. The proposed methodology has a cost reduction in the evaluation of the wind resource in turbulent areas in urban/rural environments, as compared with traditional experimental tests, such as wind tunnels.

---

## Resumen

---

Las tecnologías emergentes en energía renovable, específicamente la energía eólica, han aumentado su penetración no solo a gran escala, sino también en proyectos eólicos de baja generación. La Agencia Internacional de Energía (AIE) en la Tarea 27 está dirigida específicamente a resolver los problemas de optimización del uso del recurso eólico en zonas turbulentas, tanto en entornos urbanos como rurales, mediante la aplicación de técnicas innovadoras como la Dinámica de Fluidos Computacional (CFD).

La tesis informa sobre el desarrollo de una metodología avanzada basada en el análisis de dinámica de fluidos computacional, para evaluar la instalación de aerogeneradores de baja potencia. El objetivo es proporcionar una metodología fácil de seguir, que permita la aplicación de diversos métodos y software de CFD. La ubicación óptima de los SWT, proporcionada por la metodología desarrollada, permite mostrar las principales ventajas de los aerogeneradores de baja potencia en los entornos urbano/rural.

Un Dominio Computacional Virtual (DCV) ha sido reemplazado por las simulaciones unidireccionales en el análisis de CFD. Entre las ventajas, que concede la implementación de este DCV, está la creación de mapas de recursos eólicos con gran resolución, lo que permite determinar nuevas áreas de interés con potencial eólico, lo que ayuda a determinar nuevas zonas o regiones con mayor incidencia del viento. Los resultados muestran una gran ventaja del análisis de CFD gracias a su relativa facilidad de implementación y caracterización del recurso eólico. La metodología propuesta tiene una reducción de costos en la evaluación del recurso eólico en áreas turbulentas en entornos urbano/rural, en comparación con las pruebas experimentales tradicionales, como los túneles de viento.

## **Dedication**

***To my parents, brother, and sister***  
*for their unconditional support,*  
*limitless love and guidance*  
*through this journey of my professional life,*  
*and for the great moments and support*  
*that made this achievement possible.*

***To my co-workers and friends***  
*for their support, friendship, and good times at the power system laboratory.*

## **Acknowledgments**

*To Dr. César Angeles Camacho for his support, trust, and supervision during my formation as a PhD*

*To Dr. Francisco Bañuelos Ruedas for their suggestions and support as a PhD student.*

*To the committee members for their suggestions and supervision of my PhD studies.*

*To the National Autonomous University of Mexico for opening its doors and allowing me to fulfill my goals that make this project life possible.*

*To the National Council of Science and Technology CONACYT, for the financial support through doctoral grant CVU/Scholarship holder 472076/612090.*



---

## Table of contents

---

Abstract.....	ii
Resumen .....	iii
Dedication.....	iv
Acknowledgments .....	v
Table of contents.....	vi
List of Figures.....	xi
List of Tables.....	xix
Nomenclature .....	xxi
Acronyms .....	xxv
<b>CHAPTER 1 .....</b>	<b>1</b>
INTRODUCTION.....	1
1.1 Introduction.....	1
1.2 Background.....	2
1.3 Research motivation.....	5
1.4 Problem statement.....	5
1.5 Hypothesis.....	6
1.6 Objectives of the research.....	6
1.6.1 Main objective.....	6
1.6.2 Specific objectives.....	6
1.7 Main contributions .....	7
1.8 Publications.....	8
1.8.1 Journals .....	8
1.8.2 Congresses and conferences.....	8
1.9 Thesis structure .....	8
<b>CHAPTER 2 .....</b>	<b>10</b>
FUNDAMENTALS OF COMPUTATIONAL FLUID DYNAMICS (CFD).....	10
2.1 Background of Computational Fluid Dynamics .....	10
2.2 Definition of Computational Fluid Dynamics .....	11

2.3	Advantages and disadvantages of Computational Fluid Dynamics .....	12
2.4	Solution process of the Computational Fluid Dynamics .....	14
2.5	The solution to Computational Fluid Dynamics in SolidWorks® Flow Simulation .....	15
2.5.1	Navier-Stokes equations for laminar and turbulent flows.....	16
2.5.2	Boundary conditions models for laminar and turbulent flows .....	18
2.5.3	Boundary conditions for internal and external flows .....	18
2.5.4	Computational mesh.....	18
2.6	Internal flow example for Computational Fluid Dynamics analysis.....	20
2.6.1	Initial conditions - Pre-processing.....	20
2.6.2	CFD Solver - Numerical solution.....	23
2.6.3	Post-processing - Results, reports, and visualization.....	24
2.7	External flow example for Computational Fluid Dynamics analysis.....	28
2.7.1	Initial conditions - Pre-processing.....	28
2.7.2	CFD Solver - Numerical solution.....	31
2.7.3	Post-processing - Results, reports, and visualization.....	32
2.8	Computational Fluid Dynamics in wind energy engineering.....	36
2.8.1	Urban wind energy.....	38
2.9	Turbulence models in the CFD analysis .....	43
2.9.1	A general overview of numerical approaches of CFD.....	43
2.9.2	Direct Numerical Simulation (DNS) .....	43
2.9.3	Large Eddy Simulation (LES).....	44
2.9.4	Reynolds Averaged Navier-Stokes (RANS) model .....	45
<b>CHAPTER 3</b>	.....	<b>46</b>
	<b>ADVANCED METHODOLOGY FOR FEASIBILITY STUDIES ON BUILDING-MOUNTED WIND TURBINE INSTALLATION IN AN URBAN ENVIRONMENT: APPLYING CFD ANALYSIS.....</b>	<b>46</b>
3.1	Size domains definition for the CFD simulations.....	46
3.2	Model selection of the small wind turbines.....	48
3.3	CAD modeling of the proposed small wind turbines .....	50
3.4	General description of the methodology proposed .....	51
3.4.1	Site selection and feasibility - Stage 1 .....	55
3.4.2	Wind resource assessment - Stage 2.....	56
	Computational Fluid Dynamics analysis.....	56
3.4.3	CAD Development of the topographic model of the site/complex - Stage 3.....	56
3.4.4	CFD Analysis of the topographic model of the site/complex - Stage 4a .....	56

3.4.5	CFD Analysis of the building or structure of rural or urban zone - Stage 4b .....	57
3.4.6	CFD Analysis of SWT - Stage 5 .....	58
3.4.7	CFD Analysis of the integration of building - SWTs - Stage 6.....	58
3.4.8	CFD Post-processing - Stage 7.....	59
3.4.9	Technical-economic evaluation.....	59
3.4.10	Evaluation of electric consumption.....	59
3.4.11	Economic evaluation .....	59
3.4.12	Evaluation of emissions reduction of CO <sub>2</sub> .....	59
3.5	Evaluation of the wind potential in the Tecnológico de Estudios Superiores de Ecatepec (TESE) campus .....	60
3.5.1	Stage 1 – Selection of the site of interest .....	60
3.5.2	Stage 2 – Wind resource assessment.....	61
3.5.3	Stage 3 – CAD Modeling of the geographic and topographic conditions.....	66
3.5.4	Stage 4a – CFD Analysis of the site and urban complex .....	68
3.5.5	Stage 4b – CFD Simulation of the building or structure .....	77
3.5.6	Stage 5a – CFD Configuration of the small wind turbines (SWTs).....	80
3.5.7	Stage 5b – CFD Simulations of the small wind turbines (SWTs).....	83
3.5.8	Configuration matrix array of the proposed SWT.....	91
3.5.9	Stage 6 – CFD Analysis of the integration of building and SWTs .....	94
3.5.10	Stage 7 – CFD Post-processing.....	95
<b>CHAPTER 4</b>	.....	<b>98</b>
	<b>AN INNOVATIVE VIRTUAL COMPUTATIONAL DOMAIN (VCD) BASED ON A WIND ROSE BY APPLYING CFD.....</b>	<b>98</b>
4.1	Evaluation and application of the methodology at the Universidad Autónoma de Zacatecas Siglo XXI (UAZ) .....	99
4.1.1	Traditional CFD analysis with unidirectional simulation.....	101
4.2	Virtual Computational Domain (VCD) in CFD analysis.....	102
4.2.1	A Virtual Computational Domain Innovation of 16 segments.....	102
4.2.2	Validation of the Virtual Computational Domain in 16 Segments.....	107
4.2.3	A Virtual Computational Domain Innovation of 36 segments.....	109
4.2.4	Validation of the Virtual Computational Domain in 36 Segments.....	114
4.3	CFD Simulation of the building or structure .....	116
4.4	Selection of the small wind turbines SWTs based on a three-dimensional frequency histogram .....	122
4.5	CFD Analysis of the integration of building and SWTs domain .....	125

4.6	CFD Post-processing.....	127
4.7	Discussion and conclusions.....	131
<b>CHAPTER 5.....</b>		<b>133</b>
CONCLUSIONS AND FUTURE RESEARCH .....		133
5.1	Conclusions .....	133
5.2	Future research.....	134
5.3	References .....	136
<b>APPENDIX A .....</b>		<b>144</b>
FUNDAMENTAL EQUATIONS OF FLUID DYNAMICS .....		144
A.1	Introduction.....	144
A.2	Modeling of the flow .....	145
A.2.1	Finite control volume .....	145
A.2.2	Infinitesimal fluid element .....	146
A.3	The fundamental derivative (time rate change of a moving fluid element).....	147
A.4	Divergent velocity vector .....	150
A.5	The continuity equation.....	152
A.5.1	Principle of conservation of mass .....	152
A.6	The momentum equation.....	156
A.7	The energy equation.....	161
A.7.1	Principle of energy conservation.....	161
A.8	Equations for non-viscous fluids (Euler equations).....	165
A.8.1	Euler Energy equations.....	165
A.8.2	Euler Momentum equations .....	166
A.8.3	Euler Energy equations.....	166
<b>APPENDIX B .....</b>		<b>167</b>
SOLUTION FOR COMPUTATIONAL FLUID DYNAMICS.....		167
B.1	Solution methods for Computational Fluid Dynamics .....	167
B.1.1	Classification of the PDE processes.....	167
B.2	Introduction to numerical solution for ordinary and PDE's.....	168
B.2.1	Discretization approaches .....	168
B.3	Spatial discretization.....	169
B.3.1	Finite Difference Method (FDM).....	170
B.3.2	Finite Volume Method (FVM).....	170
B.3.3	Finite Element Method (FEM).....	172

B.4	Turbulence in the CFD analysis.....	172
<b>APPENDIX C</b>	.....	175
	3D TOPOGRAPHIC TERRAIN MODELING PROCEDURE.....	175
C.1	Modeling procedure for 3D modeling of topographic terrains.....	175
<b>APPENDIX D</b>	.....	181
	OPERATION PRINCIPLE OF THE ULTRASONIC ANEMOMETER WINDMASTER 3-AXIS .....	181
D.1	Ultrasonic anemometer WindMaster 3-Axis .....	181
<b>APPENDIX E</b>	.....	187
	DEVELOPMENT OF THE DATALOGGER FOR THE ULTRASONIC ANEMOMETER WINDMASTER 3-AXIS.....	187
E.1	Datalogger for anemometer WindMaster 3-Axis.....	187
E.1.1	Software development of the WindMaster Datalogger .....	188
E.1.2	Electrical diagram of the WindMaster Datalogger .....	190
E.1.3	Database and file generator of the WindMaster datalogger .....	191
E.2	Installation of the ultrasonic anemometer WindMaster.....	193
<b>APPENDIX F</b>	.....	195
	CFD COMPUTATIONAL RESOURCE.....	195
F.1	Computational resource .....	195
F.2	Computational time.....	195
F.3	Appendix References.....	196

---

## List of Figures

---

Figure 2.1 Disciplines that integrate CFD.....	11
Figure 2.2 Wind tunnel test of an automobile in Pininfarina Cambiano 2012.....	13
Figure 2.3 The interconnectivity functions of fundamental elements of CFD analysis.....	15
Figure 2.4 Computational meshing near the solid/liquid interface.....	19
Figure 2.5 Solid/liquid interface computational meshing procedure in SolidWorks.....	19
Figure 2.6 Computational domain of the nozzle model.....	20
Figure 2.7 Structural meshing of the nozzle model.....	21
Figure 2.8 Flowchart of the physical properties of fluids in CFD.....	22
Figure 2.9 Boundary conditions for the internal flow of the nozzle model.....	22
Figure 2.10. Flowchart of the CFD solution process.....	23
Figure 2.11 Representation of sections “A” and “B” of the nozzle model.....	24
Figure 2.12 Fluid temperature in sections “A” and “B” of the nozzle model.....	25
Figure 2.13 Speed vector graph of the nozzle model.....	26
Figure 2.14 Contour plot and iso-lines of velocity in the nozzle model.....	26
Figure 2.15 Contour plot and iso-lines of pressure in the nozzle model.....	27
Figure 2.16 Streamlines plot of velocity in the nozzle model.....	27
Figure 2.17 Velocity LIC graph in the nozzle model.....	28
Figure 2.18 Velocity trajectories flow graph in the nozzle model.....	28
Figure 2.19 Components of the NACA 4415 airfoil section.....	29
Figure 2.20 Example ii) of fluid passing through an aerodynamic profile NACA 4415.....	29
Figure 2.21 Mesh for a fluid that passes through an aerodynamic profile NACA 4415.....	30
Figure 2.22 Boundary conditions for external flow in the aerodynamic profile.....	31
Figure 2.23 Lift coefficient convergence of the NACA 4415 aerodynamic airfoil.....	31
Figure 2.24 Drag coefficient convergence of NACA 4415 aerodynamic airfoil.....	32
Figure 2.25 CFD simulation results of the aerodynamic profile of the NACA 4415 airfoil section.....	33

Figure 2.26 Lift and drag forces of an aerodynamic profile of a wind turbine.....	33
Figure 2.27 Lift coefficient compared to the attack angle for the NACA 4415 aerodynamic profile for laminar and turbulent flows. ....	34
Figure 2.28 Drag coefficient against the attack angle for the NACA 4415 aerodynamic profile for laminar and turbulent flows.....	35
Figure 2.29 Pressure coefficient along the length of the aerodynamic profile NACA 4415.....	36
Figure 2.30 Total small wind turbines installed worldwide (2017).....	40
Figure 2.31 CAD models of the building wind turbines configurations.....	41
Figure 2.32 Difference between the LES and DNS models, on a spatial scale.....	44
Figure 3.1 Size domain definition for the CFD simulations. ....	47
Figure 3.2 Power curves of the selected small wind turbines.....	49
Figure 3.3 3D CAD models of selected wind turbines: a) Bergey Excel 10 kW, b) XZERES Skystream 2.6kW, c) Aeolos V-10 kW and d) Aeolos V-5 kW .....	50
Figure 3.4 Proposed methodology for the optimization of the use of wind resource by applying CFD analysis.....	51
Figure 3.5 Flow diagram of the proposed methodology for the optimization of wind resource use applying CFD analysis for urban and rural areas.....	54
Figure 3.6 Griggs-Putnam scale for estimating wind speed from foliage and tree deformation. ....	55
Figure 3.7 Map of the location of the municipality of Ecatepec, and location of the study site and its respective SIMAT monitoring stations.....	61
Figure 3.8 San Agustín monitoring station of the SIMAT meteorological network.....	62
Figure 3.9 Wind rose and frequency distribution of the SAG station through WRPLOT View™. ....	62
Figure 3.10 Wind rose and frequency distribution of the SAG station through WAsP®.....	63
Figure 3.11 Xalostoc monitoring station of the SIMAT meteorological network.....	63
Figure 3.12 Wind rose and frequency distribution of the XAL station through WRPLOT View™. ....	64
Figure 3.13 Wind rose and frequency distribution of the XAL station through WAsP®.....	64
Figure 3.14 Wind rose and frequency distribution of SAG and XAL stations through WRPLOT View™ .....	65
Figure 3.15 Wind rose and frequency distribution of SAG and XAL stations through WAsP®..	65
Figure 3.16 Isometric view of the 3D topographic modeling of the case study site.....	66

Figure 3.17 a) Spatial distribution and b) 3D site of academic complex models of the interest site.....	67
Figure 3.18 Iso-metric 3D view of the site and academic complex model of the site of interest.....	68
Figure 3.19 CFD Simulation of the top view of the site and complex of the case study at 1.97 m/s.....	72
Figure 3.20 CFD Simulations of the top view of the site and academic complex at a) 1.9 m/s, b) 1.5 m/s and c) 1.0 m/s.....	73
Figure 3.21 CFD Simulation top view of the site and complex of the case study at 1.0 m/s.....	74
Figure 3.22 CFD Simulation of the isometric view of the site and complex contour plot at 1.5 m/s.....	74
Figure 3.23 CFD Simulation side view result comparison at a) 1.5 m/s and b) 1.0 m/s.....	75
Figure 3.24 Wind speed profiles and measurement comparison through weather station and CFD simulation.....	76
Figure 3.25 CAD modeling of the buildings Q and S in an isometric view.....	78
Figure 3.26 CFD Simulation of the top view of the buildings Q and S, contour plot at 0.8 m/s.....	78
Figure 3.27 CFD Simulation side view of the buildings Q and S, contour plot of the longitudinal and transversal cuts at 0.8 m/s.....	80
Figure 3.28 CFD Simulation isometric view of the buildings Q and S, contour plot of the longitudinal and transversal cuts at 0.8 m/s.....	80
Figure 3.29 Computational domain dimensions for Horizontal Axis Wind Turbine HAWT.....	82
Figure 3.30 Computational domain dimensions for Vertical Axis Wind Turbine VAWT.....	82
Figure 3.31 Steady-state CFD simulation of Bergey Excel 10 kW wind turbine – Cut plots: a) Side View and b) Top View.....	84
Figure 3.32 Steady-state CFD simulation of Bergey Excel 10 kW wind turbine – Flow streamlines: a) Front View and b) Isometric View.....	84
Figure 3.33 Rotational-state CFD simulation of Bergey Excel 10 kW wind turbine – Cut plot: Side View.....	85
Figure 3.34 Rotational-state CFD simulation of Bergey Excel 10 kW wind turbine – Cut plot: Top View.....	85
Figure 3.35 Rotational-state CFD simulation of Bergey Excel 10 kW wind turbine – Streamlines: a) Side View and b) Top View.....	86
Figure 3.36 Rotational-state CFD simulation of Bergey Excel 10 kW wind turbine – Streamlines: a) Isometric View and b) Front View.....	87
Figure 3.37 Steady-state CFD simulation of the Aeolos V-10 wind turbine – Cut plot: Side View.....	87



Figure 3.38 Steady-state CFD simulation of the Aeolos V-10 wind turbine – Cut plot: Top View. .....	88
Figure 3.39 Steady-state CFD simulation of the Aeolos V-10 wind turbine – Flow streamlines: a) Front View and b) Isometric View.....	88
Figure 3.40 Rotational-state CFD simulation side view of the Aeolos V-10 wind turbine – Cut plot. ....	89
Figure 3.41 Rotational-state CFD simulation top view of the Aeolos V-10 wind turbine – Cut plot. ....	89
Figure 3.42 Rotational-state CFD simulation of the Aeolos V-10 wind turbine – Streamlines: a) Side View and b) Top View.....	90
Figure 3.43 Rotational-state CFD simulation of the Aeolos V-10 wind turbine – Streamlines: a) Top View and b) Isometric View.....	91
Figure 3.44 Matrix scheme for the small wind emplacements. ....	93
Figure 3.45 a) Layout of the matrix arrangement of the SWTs and the b) 3D model design of the building - SWTs arrangement. ....	94
Figure 3.46 Rotational-state CFD simulation of the matrix array of the Aeolos V-10 wind turbine and the Building – Streamlines: a) Isometric, b) Side, c) Top, and d) Front views at 2.0 m/s. ....	95
Figure 3.47 CFD Simulation at total hub height of 30 m at a) 2.5 m/s and b) 2.0 m/s.....	96
Figure 3.48 CFD Streamlines of the Aeolos V-10 wind turbines layout of the Buildings Q and S. .....	96
Figure 4.1 Wind rose and frequency distribution of the station through WRPLOT View™ in 16 segments.....	100
Figure 4.2 Wind rose and frequency distribution of the station through WASP® in 16 segments.....	100
Figure 4.3 Unidirectional CFD simulations top view of the Site and Complex Domains of UAZ. .....	102
Figure 4.4 Representation of the Virtual Computational Domain (VCD) implemented in the 3D rural topographic model - a) Top View and b) Isometric View. ....	103
Figure 4.5 Representation of the wind rose in the hexadecagonal prism of the Virtual Computational Domain VCD with the initial and boundary conditions, a) Top View, and b) Isometric View.....	105
Figure 4.6 Comparison of CFD simulations - a) wind speed in the multidirectional direction of the hexadecagonal VCD and b) unidirectional wind speed. ....	105
Figure 4.7 CFD Simulations with the VCD of 16 Segments implementation of the Site and Complex Domains of the UAZ Siglo XXI campus, a) 2,329, and b) 2,319 m a.s.l. ....	106

Figure 4.8 CFD Simulations with the VCD of 16 Segments implementation of the Site and Complex Domains of the UAZ Siglo XXI campus, a) 2,309, and b) 2,299 m a.s.l. ....	107
Figure 4.9 CFD Simulations with the hexadecagonal VCD implementation of 16 individual wind speeds. ....	108
Figure 4.10 Wind rose and frequency distribution of the station trough WRPLOT View™ in 36 segments.....	109
Figure 4.11 Wind rose and frequency distribution of the station through WAsP® in 36 segments.....	110
Figure 4.12 Representation of the Virtual Computational Domain (VCD) 36 segments implemented in the 3D rural topographic model, a) Top View, and b) Isometric View.....	110
Figure 4.13 Representation of the wind rose in the triacontakaihexagonal prism of the Virtual Computational Domain VCD 36 Segments with the initial conditions, a) Top View, b) Isometric View.....	112
Figure 4.14 Comparison between CFD simulations - a) Multidirectional wind speed of the triacontakaihexagonal VCD and b) the traditional unidirectional wind direction.....	112
Figure 4.15 Comparison between CFD simulations - a) triacontakaihexagonal VCD, b) hexadecagonal VCD, and c) the unidirectional wind direction.....	113
Figure 4.16 CFD Simulations; triacontakaihexagonal VCD implementation 36 wind speeds (0°-170°).....	114
Figure 4.17 CFD Simulations; triacontakaihexagonal VCD implementation 36 wind speeds (180°-350°).....	115
Figure 4.18 Location of interest buildings based on the VCD 36 segments implementation a) Building Location and b) Buildings' Cut Plots.....	117
Figure 4.19 CFD Streamlines cut plots scanning along the y-axis (North to South). ....	117
Figure 4.20 CFD Streamlines cut plots scanning along the x-axis (East to West). ....	118
Figure 4.21 3D model of the UAZ building in the isometric view.....	119
Figure 4.22 CFD Simulation of the top view of the interest building, contour plot at 4.0 m/s. ....	120
Figure 4.23 CFD Simulation side view of the interest building, contour plot of the a) transversal, and b) longitudinal view at 4.0 m/s.....	121
Figure 4.24 CFD Simulation isometric view of the interest building, contour plot of the a) longitudinal, and b) transversal view at 4.0 m/s.....	121
Figure 4.25 Components of the wind speed of the WindMaster ultrasonic anemometer.....	122
Figure 4.26 Wind speed and wind direction of the wind resource data of the WindMaster station.....	123

Figure 4.27 Wind rose diagram and scatter plot for the one-year wind speed data in the UAZ case study.....	123
Figure 4.28 Three-dimensional frequency histogram a) and density graph b) for the velocity vectors.....	124
Figure 4.29 <i>K</i> -means clustering applied to the UAZ case study data with five clusters in a) 2D representation and b) 3D representation.....	124
Figure 4.30 <i>K</i> -means clustering applied to the UAZ case study data with two clusters in a) 2D representation and b) 3D representation.....	125
Figure 4.31 a) Layout of the matrix arrangement of the SWTs and b) 3D model design of the arrangement building - SWTs.....	126
Figure 4.32 Rotational-state CFD simulation of the matrix array for the Domain of the arrangement of the building - SWTs – Streamlines a) Isometric, b) Side, c) Front, and d) Top views at 4.0 m/s.....	127
Figure 4.33 CFD Simulation with the VCD 36 segments implementation at a total hub height of 32 m.....	128
Figure 4.34 a) Layout II of the matrix arrangement of the SWTs and b) the 3D model design of the arrangement building - SWTs.....	129
Figure 4.35 CFD Streamlines of the Aeolos V-10 SWTs layout I and the VCD integration of the seven buildings from a) to g).....	130
Figure 4.36 CFD Streamlines of the Aeolos V-10 SWTs layout II and the VCD integration of the interest buildings from e) to g). .....	131
Figure A.1 Computational Fluid Dynamics analysis roadmap CFD.....	144
Figure A.2 Flow models of fluid through the finite control volume.....	145
Figure A.3 Flow models of fluid through the infinitesimal fluid element.....	146
Figure A.4 Fluid element moving in the fluid flow.....	147
Figure A.5 Moving control volume for the representation of the divergence of velocity.....	151
Figure A.6 Finite control volume fixed in space.....	153
Figure A.7 Detailed view of the moving fluid element infinitesimal.....	156
Figure A.8 Element of the deformed fluid due to the surface forces.....	157
Figure A.9 Energy flows of the <i>x</i> -component of the infinitesimal fluid element.....	162

Figure B.1 Types of mesh generation a) Meshing coupled to the solid, b) Cartesian meshing. .....	169
Figure B.2 Types of meshing a) Structured meshing - solid tracking, b) Unstructured meshing - mixed mesh. ....	170
Figure B.3 Basic approaches FVM meshing a) Cell-centered control volume, b) Vertex cell control volume. ....	171
Figure B.4 Boundary layer over a flat surface. ....	173
Figure B.5 Hierarchy of turbulence models. ....	174
Figure C.1 Circle menu in Google Earth software. ....	175
Figure C.2 Polygon menu in Google Earth software. ....	175
Figure C.3 Right-click menu list in Google Earth software. ....	176
Figure C.4 Configuration projection menu in Global Mapper software. ....	176
Figure C.5 Source maps menu in Global Mapper software. ....	177
Figure C.6 Localization of the circle figure file in Global Mapper software. ....	177
Figure C.7 Export menu options in Global Mapper software. ....	177
Figure C.8 Export menu options in Global Mapper software. ....	178
Figure C.9 Development of the grid points with spline command in SolidWorks. ....	178
Figure C.10 Creation of the solid surface through splines. ....	179
Figure C.11 Results of the 3D topography surface in SolidWorks. ....	179
Figure C.12 Creation process of the 3D solid of the topography. ....	180
Figure C.13 Intersection operation of the 3D solid of the topography. ....	180
Figure C.14 Final results of the 3D modeled topography. ....	180
Figure D.1 Operation principle of the ultrasonic anemometer. ....	181
Figure D.2 Schematic diagram of WindMaster ultrasonic anemometer from Gill Instruments. ....	182
Figure D.3 Registration string in Mode 1 - ASCII, UVW (Continuous) ultrasonic anemometer. .....	184
Figure D.4 Registration string in Mode 2 - ASCII, (Polar) ultrasonic anemometer. ....	185

Figure E.1 Block diagram of the WindMaster datalogger.....190

Figure E.2 Components of the wind resource data in the MySQL database.....191

Figure E.3 Example .csv file generated with the WindMaster datalogger.....192

Figure E.4 Final installation of the WindMaster datalogger.....192

Figure E.5 Location of the S&C Building and the anemometer within the UAZ campus. ....193

Figure E.6 Process of manufacturing, assembling, and installing the WindMaster anemometer.  
.....194

Figure E.7 Final installation of the WindMaster ultrasonic anemometer.....194

---

## List of Tables

---

Table 2.1. Advantages of CFD on wind tunnel modeling.....	13
Table 2.2 Disadvantages of CFD in wind tunnel modeling.....	14
Table 2.3 Size classification of Small Wind Turbines (SWTs). .....	39
Table 3.1 Technical specifications of the operation of selected SWTs.....	49
Table 3.2 List of selected monitoring stations of the SIMAT network in Ecatepec.....	61
Table 3.3 Roughness classification and roughness length values for various land types.....	69
Table 3.4 Physical properties of air at different temperatures.....	71
Table 3.5 Initial and boundary conditions for the CFD simulations of the TESE case study.....	72
Table 3.6 Friction coefficient for various terrain characteristics.....	76
Table 3.7 Initial and boundary conditions for the CFD simulations ( $\mu S$ ) of the TESE case study. .....	79
Table 3.8 Initial and boundary conditions for the development of CFD simulations of SWTs..	83
Table 3.9 Comparison between CFD simulation and Jensen wake model under steady and rotational states .....	92
Table 3.10 Proposed distance between SWTs based on the CFD rotational simulations.....	93
Table 3.11 Configuration of the matrix arrangement dimension of the TESE case study.....	94
Table 4.1 Ultrasonic WindMaster station <i>in situ</i> measurement at Siglo XXI Campus.....	99
Table 4.2 Result parameters, UWIN station for the development of unidirectional CFD simulations.....	100
Table 4.3 Initial and boundary conditions for the unidirectional CFD simulation of the UAZ case study.....	101
Table 4.4 Initial and boundary conditions for the UAZ case study - Implementation of 16 segments in the Virtual Computational Domain.....	104
Table 4.5 Representation of 16 sectors of the wind rose of the wind speed and frequency in the intensity scale; red is higher.....	109

Table 4.6 Initial and boundary conditions for the UAZ case study - Implementation of 36 segments in the Virtual Computational Domain.....	111
Table 4.7 Representation of 36 sectors of the wind rose of the wind speed and frequency in the intensity scale; red is higher.....	115
Table 4.8 Initial and boundary conditions for the CFD simulations ( $\mu$ S) of the UAZ case study.....	119
Table 4.9 Configuration of the matrix arrangement dimension of the UAZ case study.....	125
Table 4.10 Initial and boundary conditions for the development of CFD simulations of SWTs.....	126
Table 4.11 Configuration of the matrix arrangement dimension of the UAZ case study.....	129
Table 4.12 Comparison between the VCD implementation and unidirectional CFD simulations.....	132
Table A.1 Operational, technical specifications of the WindMaster ultrasonic anemometer..	183
Table A.2 Characters string in ASCII format - Continuous recording of the ultrasonic anemometer.....	184
Table A.3 Characters string in ASCII- Polar format recording of the ultrasonic anemometer.....	186
Table E.1 Variables that make up the MySQL database for the WindMaster datalogger.....	189
Table E.2 Main components of the WindMaster datalogger block diagram.....	191

---

## Nomenclature

---

### Fundamental equations of fluid dynamics

$a$	Acceleration
$a_x$	Acceleration of the fluid in the x-direction
$S$	Control surface
$V$	Control volume
$\rho$	Density
$dV$	Differential volume
$\delta m$	Differential of mass
$\delta V$	Differential of volume
$dS$	Differential surface
$\vec{\nabla} \cdot \vec{v}$	Divergence of velocity
$F$	Force
$F_x$	Forces sum in the x-direction
$D/Dt$	Fundamental derivative
$\partial u/\partial x$	Gradient of normal velocity
$\dot{q}_x$	Heat transferred in the x-direction
$e$	Internal energy per unit mass
$V^2/2$	Kinetic energy per unit mass
$\partial/\partial t$	Local derivative
$m$	Mass of the fluid
$\tau_{xx}$	Normal stress
$\tau_{xy}$	Shear stress
$D\rho/Dt$	Speed of change of the density of the fluid element
$v$	Speed vector
$\tau_{ij}$	Surface forces
$k$	Thermal conductivity
$t$	Time
$\vec{i}$	Unit vector along the x-axis



$\vec{j}$	Unit vector along the y-axis
$\vec{k}$	Unit vector along the z-axis
$\vec{n}$	Unit vector perpendicular to control surface
$\dot{q}$	Velocity addition rate of volumetric heat per unit mass
$\vec{V}$	Velocity vector

### **Turbulent flow**

$\Omega$	Angular velocity
$g_i$	Component of gravitational acceleration along the i-coordinate
$q_i$	Diffusion heat flux
$\varepsilon$	Dissipation rate of turbulence
$C_\mu$	Dynamic viscosity coefficient
$S_i$	External force of mass distributed per unit mass
$F$	Flow
$P_B$	Generation of turbulence due to the lift force
$\delta_{ij}$	Kronecker delta function
$Le$	Lewis number
$M$	Molecular mass of the fluid
$Pr$	Prandtl number
$P$	Pressure
$Re$	Reynolds number
$\tau_{ij}$	Shear viscosity tensor
$Q_H$	Source of heat or dissipation per unit volume
$H$	Thermal enthalpy
$\mu_t$	Turbulent eddy viscosity coefficient
$\kappa$	Turbulent kinetic energy (TKE)
$R$	Universal gas constant
$u$	Velocity of the fluid
$f_\mu$	Viscous turbulence factor

## NACA Profiles

$D_C$	Drag coefficient
$\rho$	Free airflow density
$v_0$	Free flow velocity
$L_C$	Lift coefficient
$L$	Line of the aerodynamic profile
$P_c$	Pressure coefficient
$Re$	Reynolds number
$v$	Speed
$P$	Static pressure

## Case study analysis

$x$	Distance between turbines
$\mu$	Dynamic viscosity of the air
$U$	Fluid velocity
$\alpha$	Friction coefficient, wind shear exponent or Hellmann exponent
$H$	Height
$H_0$	Height at determined value
$h$	Hub height
$d_h$	Hydraulic diameter
$\nu_k$	Kinematic viscosity of the air
$L$	Length of the surface on which the fluid will flow
$u_{mean}$	Mean wind speed
$A$	Rotor area of the turbine
$D$	Rotor diameter
$z$	Roughness length
$z_0$	Roughness surface
$C_v$	Specific heat at a constant volume
$C_p$	Specific heat ratio at constant pressure
$\sigma_v$	Standard deviation
$C_T$	Thrust coefficient
$l$	Turbulence length scale
$\kappa$	Wake decay constant

$P_w$	Wind power
$v$	Wind speed
$u_1$	Wind speed at the first turbine in upwind direction
$u_2$	Wind speed at the second row of turbines
$u^3$	Wind speed cube
$v_0$	Wind speed to the height $H_0$

---

## Acronyms

---

<b>ABL</b>	Atmospheric Boundary Layer
<b>AIAA</b>	American Institute of Aeronautics and Astronautics
<b>ASTER</b>	Advanced Spaceborne Thermal Emission and Reflection Radiometer
<b>AWEA</b>	American Wind Energy Association
<b>AWS</b>	AWS Truepower
<b>BAWT</b>	Building Augmented Wind Turbine
<b>BIWT</b>	Building Integrated Wind Turbine
<b>BSI</b>	British Standards Institution
<b>BUWT</b>	Building Mounted Wind Turbine
<b>BWE</b>	Bundesverband Windenergie (German Wind Energy Association)
<b>BWEA</b>	British Wind Energy Association
<b>CAD</b>	Computer-Aided Design
<b>CFD</b>	Computational Fluid Dynamics
<b>DNS</b>	Direct Numerical Simulation
<b>DTM</b>	Digital Terrain Model
<b>EMAS</b>	Estaciones Meteorológicas Automáticas
<b>ENE</b>	East-northeast
<b>ESE</b>	East-southeast
<b>EWEC</b>	European Wind Energy Conference
<b>FDM</b>	Finite Difference Method
<b>FEM</b>	Finite Element Method
<b>FOWT</b>	Floating Offshore Wind Turbine
<b>FVM</b>	Finite Volume Method
<b>GDEM</b>	Global Data Explorer Map
<b>GIS</b>	Geographic Information System
<b>GUI</b>	Graphic User Interface
<b>HAWT</b>	Horizontal Axis Wind Turbine
<b>IEA</b>	International Energy Agency
<b>IEC</b>	International Electrotechnical Commission

<b>IER</b>	Instituto de Energías Renovables, UNAM
<b>IIUNAM</b>	Instituto de Ingeniería, UNAM
<b>LES</b>	Large-eddy simulation
<b>LIC</b>	Line Integral Convolution
<b>MEASNET</b>	Measuring Network of Wind Energy Institutes
<b>MIT</b>	Massachusetts Institute of Technology
<b>MSWT</b>	MARIN Stock Wind Turbine
<b>NACA</b>	National Advisory Committee for Aeronautics
<b>NASA</b>	National Aeronautics and Space Administration
<b>NNE</b>	North-northeast
<b>NNW</b>	North-northwest
<b>NOABL</b>	Numerical Objective Analysis Boundary Layer
<b>NREL</b>	National Renewable Energy Laboratory
<b>NYSERDA</b>	New York State Energy Research and Development Authority
<b>PDE</b>	Partial Differential Equation
<b>RAMA</b>	Red Automática de Monitoreo Atmosférico
<b>RANS</b>	Reynolds-averaged Navier-Stokes
<b>REDDA</b>	Red de Depósito Atmosférico
<b>REDMA</b>	Red Manual de Monitoreo Atmosférico
<b>REDMET</b>	Red de Meteorología y Radiación Solar
<b>RPM</b>	Revolution Per Minute
<b>SAG</b>	San Agustin
<b>SAM</b>	System Advisor Model
<b>SIMAT</b>	Sistema de Monitoreo Atmosférico
<b>SMN</b>	Sistema Meteorológico Nacional
<b>SODAR</b>	Sonic Detection and Ranging
<b>SSE</b>	South-southeast
<b>SSW</b>	South-southwest
<b>SWT</b>	Small Wind Turbine
<b>TKE</b>	Turbulent Kinetic Energy
<b>UAZ</b>	Universidad Autónoma de Zacatecas
<b>UBL</b>	Urban Boundary Layer
<b>UCE</b>	Unidad Campo Experimental Zacatecas, INIFAP
<b>UNAM</b>	Universidad Nacional Autónoma de México

<b>UNEVE</b>	Universidad Estatal del Valle de Ecatepec
<b>UPN</b>	Universidad Pedagógica Nacional
<b>USA</b>	United States of America
<b>UWIN</b>	Ultrasonic WindMaster Station
<b>VAWT</b>	Vertical Axis Wind Turbine
<b>VCD</b>	Virtual Computational Domain
<b>WDR</b>	Wind-Driven Rain
<b>WNW</b>	West-northwest
<b>WRPLOT</b>	Wind Rose Plots Software
<b>WSW</b>	West-southwest
<b>WTC</b>	World Trade Center
<b>WWEA</b>	World Wind Energy Association
<b>WVEC</b>	World Wind Energy Congress
<b>XAL</b>	Xalostoc

# CHAPTER 1



---

## INTRODUCTION

---

### 1.1 Introduction

In recent years the wind energy industry has been in continuous growth around the world to widely as well as energy consumption. The technology used in large-scale wind turbines has proven to be a reality. The installed capacity worldwide and their different applications, such as on land, offshore, or the use of low power wind projects. In the latter, the development of technologies that make possible the use of the available wind resource in urban areas and rural areas is distinguished. However, it is necessary to develop new methodologies that allow the optimal use of wind resource with Small Wind Turbines (SWTs), both in rural and urban areas. All the above mentioned is a niche opportunity that will be addressed in this project.

The creation of techniques and methodologies for maximizing the efficient use of the wind resource, by applying techniques such as computational fluid dynamics analysis, will allow to building structures to be used as support for the correct installation of these devices. Similarly, it will be possible to decrease the billing of the electrical consumption of the homes or buildings, even allowing them to participate in the recent electric market through carbon bonds or Clean Energy Certificates (CECs).

Small wind turbines can also be a source of energy for off-grid isolated communities. This technology permits the electrification and heating homes in rural areas, where there is good wind potential. The SWT can be integrated into hybrid systems where wind energy is combined, among other energy sources like solar power, to increase efficiency.

For this growing energy demand and the increase in the industry of SWTs, there is a need to optimize the use of the wind resource. When applying techniques, such as in this case the computational fluid dynamics analysis, because of the cost and engineering that nowadays involves modeling systems in wind tunnels, the CFD technique is viable for reducing these inputs.

On the other hand, this methodology to be developed, allows the use of the CFD analysis, as a tool for the evaluation of SWTs, to be used instead of wind tunnel modeling, which is generally accepted in the scientific and engineering community [1], [2]. It should be noted that the disadvantage of wind tunnel modeling requires the construction of physical models of the sites to be studied. In addition, the use of specialized equipment and equipped facilities of large dimensions that not every university or institution can dispose. It is also essential to indicate that the latter is representative of real-world situations when correctly modeling the characteristics of the atmosphere but with disadvantages. Among these are the performance of wind tunnels because of cost, a few measurement variables, and monochromatic results, etc.

Therefore, it is justifiable to consider and develop methodologies that allow the efficient use of the wind resource. Such is the case of the present doctoral project, which will allow this objective to be applied to sites of interest both in the urban and rural environments. Furthermore, it can optimize from a cost-benefit and even in the environmental aspect, the low power wind project sites.

## 1.2 Background

The analysis of computational fluid dynamics is a tool widely applied in most branches of engineering. In the field of the use of renewable energies, it has diverse applications, among which the following stand out: the analysis in the dispersion of pollutants, the study of airflow inside urban canyons, and the applications in wind energy projects.

In relation to the wind energy industry, it has benefited from the use of CFD techniques and analysis, which has been applied to the evaluation of wind resources for open land in the integration of large-scale wind turbines. This type of analysis is performed with commercial software specialized in wind resource estimation, such as WAsP CFD®, WindPRO®, Meteodyn®, and Openwind®. The use of specialized software presents the disadvantage that it uses a black box architecture, concerning the variables that are handled, which limits the development potential when using CFD simulations.

On the other hand, the use of nonspecialized CFD software has an open architecture that allows the development of 3D designs and models that help provide quick solutions avoiding high costs, predicting the properties of fluids in great detail. The methodology proposed in this doctoral research contemplates an open architecture software on which any type of complex topography can be modeled. Furthermore, this selection will allow the implementation of more computational domains to be solved by CFD.

Regarding the progress developed in CFD, several studies by diverse authors exist for the applications of wind energy engineering, which are described in the following paragraphs. For managing the present research work that focused on the development of wind energy using CFD analysis as a tool, it is proposed to classify these investigations into four main groups that will serve for the development of the proposed methodology.

The first group proposed is related to the study of the wind currents in the urban environment, regarding the analysis of the impact that the wind has at pedestrian level, concerning security and comfort. Commonly, CFD analysis and modeling in wind tunnels are used for the design of buildings. Allowing the evaluation of the impact of the wind currents of the new models on people at ground level, the analysis of the dispersion of pollutants, as well as the transportation of snow and dust [3]–[6].

Most CFD calculations are validated using *in situ* measurements, which would also allow analyzing levels of turbulence. In [7], CFD simulations are used in ANSYS Fluent® software for evaluating pedestrian wind comfort. In this same context, in [8], the CFD is used to make a comparison with wind-driven rain (WDR) methods of how the wind affects the displacement of rain on the facades of low-rise buildings. In addition, in [9], the wind is analyzed concerning concepts of safety and comfort for people when interacting with urban buildings, specifically on the Eindhoven University campus.



The second group of classification is related to the development of CFD studies in the aerodynamics area in wind energy. These studies have allowed not only for the simulation and modeling of the aerodynamic profiles, including their performance under overloads at operational conditions but also for the development and design of an aerodynamic airfoil of wind turbines. Regarding the study of airfoil profiles [10], [11] evaluates the typical NACA4412 airfoil using the ANSYS Fluent® software, observing the lift and drag coefficient for its efficiency. Meanwhile, in [12], the CFD is used as a tool for simulating a free stream using the  $\kappa - \varepsilon$  turbulence model over the NACA23024 airfoil.

In relation to the use of CFD as a design tool for small-scale to large-scale wind turbines, several works emerged, such as [13] that shows the CFD simulations of flow around the NREL Phase VI rotor using twelve turbulence models. This wind turbine model is usually used as a reference for validating new turbulence models and for studying the behavior and evaluation of structural properties of the large-scale wind turbines (LWTs) [14], [15]. Other studies proposing the use of CFD software as virtualization of wind tunnels in order to evaluate loads of wind turbine blades are presented in [16] and [17].

Other studies have emerged using the CFD for wind energy applications for evaluating and identifying the impact that has the nacelle of wind turbines. For example, the anemometers installed in the turbine and the possible issues of measuring wind speed at this height [18]. Other researches include the analyses of specialized software comparing Meteodyn WT® versus WAsP® for the location of wind turbines [19].

The CFD is not only applied to wind projects in open land (On-shore) but also Off-shore projects. One of them reports a CFD analysis applied to large wind turbines called floating marine wind turbines (FOWT). In this case, the wind turbine model of 5MW from the National Renewable Energy Laboratory (NREL) and the MARIN wind turbines (MSWTs), from which the effects of wind at these sites are analyzed, in relation to the power coefficient  $C_p$  and coefficient of thrust  $C_T$  [20].

In this context, emerge the third group that refers to the use of CFD in wind energy engineering for the analysis of complex terrains like the urban and rural environment, which are the object of study of the present doctoral project. In [3], the use of physical and statistical models for estimating wind speed over complex terrains is mentioned; some of these models are used in complex areas, such as WAsP, NOABL, AIOLOS, MCP, and MSFD. The WAsP model, for example, was not developed by taking into consideration the urban environment, so it does not provide good results for this type of site. In order to address the above in [21], wind modeling is performed in CFD with WindSim® software, which is validated through comparisons of wind measurements with SODAR anemometric equipment against the vertical wind profile.

Considering the feasibility studies for SWTs installation on buildings in references [22]–[24], improvement techniques are proposed for predicting wind behavior based on Building Augmented Wind Turbine (BAWT) building configurations, specifically analyzing the Bahrain WTC. In [25], a study is made regarding the aerodynamics of a wind turbine with a BAWT configuration of 110 kW with different wind directions.

In relation to the wind resource estimation, performing this task can be stated in different ways, including *in situ* measurement campaigns, wind tunnel analysis, and CFD techniques, including mathematical modeling [26]. Regarding the use of CFD for the installation of micro-turbines in the urban environment as a first approach, it is studied in [27]–[31], where the CFD is used for the evaluation of an array of the urban complex with different types of roofs [32], [33].

In reference [34], AWS Truepower LLC, presents a CFD analysis with 48 different wind conditions, for assessing a wind project in an urban area of New York. It uses the SWIFT wind turbine model of 1.5 kW, to be installed on the roof of the Erastus Corning building with a height of 180 m. It can be stated that it is part of an approach of a methodology for the installation of SWTs, which considers factors such as wind recirculation, horizontal wind flow inclination, and turbulence intensity.

The last group classification is related to the study of the development of methodologies using CFD to estimate the wind resource for installing small wind turbines in urban terrains. As shown in [35], which uses the specialized Virtualwind® CFD software to propose a methodology for estimating the performance of micro wind turbines in an urban district. The study has the limitation that CFD analysis only uses four directions of the average wind speed.

In relation to this topic, [36] is presented the estimation of the wind resource potential in a Greater London, UK region in order to install small wind turbines in urban terrain. Nevertheless, the maps presented are with 1 km<sup>2</sup> resolution, which implies a difficult location of SWT to be able to observe the behavior of the wind on individual buildings. This study includes a proposed thumb rule estimation of SWTs height from 5 to 10 meters above the mean building height. In addition, [37] presents another study but in a rural, microscale community, which shows CFD unidirectional simulations of the prominent wind. In [38], CFD simulations are performed with ANSYS CFX® and WAsP® software in order to characterize eight wind directions within an urban environment by analyzing the turbulence intensity parameter.

Recent publications, as in [39], where the methodology of mesoscale Urban Digital Terrain Model (U-DTM) is used, which is based on CFD simulations developed with the specialized WindSim® software, to generate two neighboring areas inside the city of Cascais, Portugal. This study is validated by LiDAR and anemometric stations measuring the wind speed and power density. In [38], a CFD analysis using the typical hub heights of commercial wind turbines, according to the maps for the best placements for wind farming, is proposed.

Other studies also present other methodologies, which use CFD simulations with ANSYS Fluent® software, that are validated using *in situ* measurements evaluating the wind speed, the power density, and the turbulence intensity [40], [41]. Finally, in [42], a methodology for the micro-location of wind turbines is presented using CFD simulations. Which only use two prominent wind directions, while considering the criteria of high turbulence and areas of wind acceleration.

Based on the International Energy Agency (IEA) and its specific Task 27 regarding small wind turbines in high turbulence sites [43], is currently innovating techniques for improving the wind resource assessment in urban areas. Which the objective of proposing and developing a methodology based on new techniques like CFD, the present project drives in that direction in order to have better performance and placement of SWTs.

These previous studies will serve as a fundament for the development of this doctoral research, allowing the observation of the behavior of small wind turbines for the localization of wind projects in the urban and rural environment through the development of the methodological tool proposed. The limit of these studies is that they only contemplate prominent wind direction, which loses the information of the typical wind rose. The present project proposes to include at least 36 wind directions in order to have a better representation of the wind in an urban or rural complex.

### **1.3 Research motivation**

Forms of clean, renewable energy, like wind power, are essential for stopping the problem of climate change. Renewable energy is vital for continuing the energy transition from polluting energy forms to clean energy, which reduces the threats to the health and benefits balance for sustainable environmental development in the coming years. Global climate change forces to stop polluting the environment; in this sense, the use of renewable wind energy becomes a necessary tool for this.

On the threshold of the XXI century, the world is experiencing a technological revolution that is transforming the global energy sector, including Mexico. The sustainable microgeneration will allow every citizen to take responsibility for their generation and power consumption, since each home can obtain the energy required through various renewable sources, such as small photovoltaic panels or small wind generators on roofs, without being connected to the supply networks.

The increased focus on reducing the CO<sub>2</sub> emissions attributable to buildings has stimulated small-scale generation, low carbon emission, electricity generation technologies designed to meet part of the local demand. Among these technologies, SWTs appear to be promising. Supported by policy stimulation, some established manufacturers are expanding into this market, and several new manufacturers and technologies are at various stages of market entry. However, many significant issues remain untreated, for in instance: planning procedure, structural, vibration, and safety issues in the case of a roof-mounted application and the effects of such devices on the electricity distribution system. That is the main motivation for developing a methodology for the installation of SWTs in complex terrains like urban and rural zones.

Another issue that motivates the present study is the limited access to electricity and the technological gap that people who live in remote areas have. An open-access tool that facilitates the installation of SWTs allows overcoming the electrical needs and thereby reducing the gap that exists in the society. In this sense, the need to create new methodologies used for a more significant impact of SWTs, having novel tools like CFD studies for the installation of SWTs in the urban and rural environments in an economical way, is necessary.

### **1.4 Problem statement**

Among the main problems that involve the use of SWTs in the urban and rural environment are the following: noise, aesthetics, integration in architectural systems and the efficient use of the available wind resource. The main disadvantages of this type of wind sites are the low wind speeds and the high turbulence intensity, which are currently the main research subjects.

Based on the specific tasks required in Task 27 by the IAE, it is necessary to develop methodologies and good practices for evaluating the wind resource in places of high turbulence intensity, such as urban and rural areas, by optimizing the energy production assessment of SWTs. Current approaches include wind tunnel analysis, micrometeorology, and computational fluid dynamics studies. In addition to the scarcity of tools for performing feasibility studies in urban and rural SWTs implementation, most of these current tools are commercial ones and expensive. The latter is part of this doctoral research, which will provide a solution to this task. The CFD analysis is the basic building block of the proposed methodology. It includes novel techniques for optimizing the use of wind resources and market studies of wind turbines to help spread the development of SWTs installations. The result is a novel methodology, which will present advantages compared with traditional techniques such as wind tunnels.

## **1.5 Hypothesis**

Having an easy-to-follow and economical open access methodology, which provides the assessment and optimization of the energy production of the wind resource as well as the cost-benefit analysis, will facilitate the penetration of low power wind sites in both urban and rural environments.

## **1.6 Objectives of the research**

### **1.6.1 Main objective**

The general objective of this doctoral project is to develop a tool that allows performing feasibility studies for the installation of low power wind turbines in a fast and economical way. The methodology will be based on a dynamic computational fluid analysis and will establish the optimal locations for the installation of low power wind turbines in urban and rural areas.

### **1.6.2 Specific objectives**

- Establishment of a technique for the preparation of topographic and geographic models of urban and rural environments.
- Identification of commercial software for performing simulations in CFD.
- Coupling of topographic and geographic models with the different CFD programs.
- Analysis of CFD results of the geography and topography of the urban and rural environment.
- Identification of optimal locations or with greater wind potential of the geography and topography of the urban and rural environment, through CFD.
- CFD modeling and the evaluation of small wind turbines of horizontal and vertical axis models in the national and international markets.
- Validation and analysis of the proposed methodology in various sites of interest.

- Validation of the methodology based on the comparison of existing measurements of the wind resource and modeling of the sites of interest, as well as the comparison of results with CFD simulations.

It is clear that the fulfillment of the previous objectives, until a proposed methodology is obtained, will allow replicating these studies without problems in other urban and rural areas wind projects, which will be benefited with the decrease of the costs of feasibility studies of a project of this type, as well as the implementation in projects of large-scale wind generators in the open field.

## 1.7 Main contributions

An advanced easy-to-follow methodology according to the specific Task 27 of the International Energy Agency (IEA), has been developed in order to improve the wind resource assessment in the urban environment by using computational fluid dynamics

In order to conceptualize this methodology, it was proposed and established the new definitions of domains that will be dealt with within the proposed methodology, as well as in CFD analysis. These definitions state from a general point of view (macro-siting MS) to a particular point of view (micro-siting  $\mu$ S), which represents the space area used in the CFD stages of the methodology.

An innovative Virtual Computational Domain (VCD) has been developed and is the basic building block of the proposed methodology. The VCD is based on the 3D model prism and increases the sides of the computational domain in the CFD analysis. The VCD analysis function is to have a higher representation of the wind resource simulations, and it is directly fitted with the 16, and 36 segments of the wind rose diagram, which summarizes the information about the wind at a particular location.

Additionally, to develop the wind resource assessment and the proper selection of the SWTs, an algorithm was developed using MATLAB® to estimate the wind variables used in the CFD simulations.

Historical data from meteorological stations were collected from the automatic stations of the Mexican national weather system located in Mexico City to be used in obtaining the wind resource assessment for any proposed geographic location and in employing the wind resource to the proper validation of the CFD simulations incorporated in the methodology.

As a parallel achievement, a wind data logger was developed for the WindMaster 3D ultrasonic anemometer to perform the wind resource assessment through *in situ* measurement campaigns, specifically used for case studies where there are no wind measurements available.

One of the stages of the proposed methodology allows the creation of a tool to select and implement matrices arrangements for the SWT, which pretend to delimit the best way to choose the correct small wind turbine and predict its behavior depending on the SWTs configuration in complex environments or wind conditions.

Finally, the methodology developed allowed to analyze different study cases both in urban and rural settings, making the developed methodology versatile and applicable to any environment or wind conditions, as well as capable of creating fully detailed wind resource maps in micro-siting locations.

## 1.8 Publications

The following publications have been generated as part of this research:

### 1.8.1 Journals

- **Arteaga-López, E.,** Angeles-Camacho C., and Bañuelos-Ruedas F., “Advanced methodology for feasibility studies on building-mounted wind turbines installation in urban environment: Applying CFD analysis”, *Energy*, Vol. 167, pp. 181–188, Jan. 2019. ELSEVIER SCI ISSN: 0360-5442. DOI: <https://doi.org/10.1016/j.energy.2018.10.191>
- **Arteaga-López, E.,** & Angeles-Camacho C., “An Innovative Wind Rose Virtual Computational Domain in CFD for Urban Wind Energy”, (In process), 2019.

### 1.8.2 Congresses and conferences

- Ashley-Grant, J., **Arteaga-López, E.,** & Angeles-Camacho C., “Design and Simulation of a DC microgrid for a small island in Belize”, WWEC 2018, 17<sup>th</sup> World Wind Energy Conference & Renewable Energy Exhibition. Pakistan, November 2018.
- **Arteaga-López, E.,** & Angeles-Camacho C., “Methodology Study for the Urban Wind Energy, Applying CFD: Study Case, Engineering Tower Building, II-UNAM.”, WWEC 2017, 16<sup>th</sup> World Wind Energy Conference & Renewable Energy Exhibition. Sweden, June 2017.

## 1.9 Thesis structure

The present thesis is structured in an easy-to-follow style for a better understanding of the reader. First, the purpose of this research is explained, including the problematic, objectives, and achievements. The second chapter states the background and fundamentals of Computational Fluid Dynamics. In addition, the chapter also includes two base cases for the implementation of CFD analysis in external and internal flows stating the fundamental process of CFD and its advantages that present the CFD versus wind tunnel techniques. Including the fundamental equations used in CFD and the system equations used by the SolidWorks Flow Simulation® software, which helps describe all CFD simulations of the present doctoral research.

The third chapter shows the development of an advanced methodology that uses the Computational Fluid Dynamics CFD as a tool for the assessment and location of small wind turbines both in urban and rural environments. In addition, in this same chapter, this methodology is evaluated and applied in the first case study, which corresponds to an urban academic complex.

It is important to mention that this case study only focuses on a traditional way to use CFD by employing only the prevailing wind direction, which limits the potential of the CFD analysis and reduces the representation of the wind resource and limits the location of wind hot spots.

Additionally, the market study of the SWTs used in the present methodology is shown, including their CFD simulations to be implemented in the recommended matrix configuration based on the CFD result analysis. These CFD analyses were performed in four different models of SWTs, based on two HAWTs and two VAWT wind turbine models, which allow determining the selection and layout configuration of the proper location of the SWTs.

The fourth chapter presents the innovation in the development of a wind rose Virtual Computational Domain (VCD), which is applied in the developed methodology. This VCD considers both the segments of the wind rose diagram that is applied in a new case study. This second case contemplates the use of VCD 16 and 36 segments in a rural environment, specifically at Campus Siglo XXI of the Universidad Autónoma de Zacatecas. In both cases, the CFD results and their respective validation of the implementation of the VCD compared with unidirectional CFD simulations are presented. Finally, the conclusions and future research are presented and placed in the fifth chapter.

# CHAPTER 2



---

## FUNDAMENTALS OF COMPUTATIONAL FLUID DYNAMICS (CFD)

---

### 2.1 Background of Computational Fluid Dynamics

The use of techniques in Computational Fluid Dynamics analysis was remote in the 1960s when the National Advisory Committee for Aeronautics (NACA), now the National Aeronautics and Space Administration (NASA), had to determine aerodynamic problems for the study of movement and aerodynamic heat of the ultra-ballistic missiles that entered the Earth's atmosphere at supersonic speeds. By using concepts known today as time-dependent variables to approach the steady-state, Moretti, and Abbett developed a differential-finite numerical solution for the problem posed [44], [45]. The above shows the importance of computational fluid dynamics in applications to the study of modern aerodynamics.

The first generation of computational fluid dynamics analysis appeared during the 1950s and early 1960s; where a large number of supersonic flows were compiled by solving differential equations (Taylor-Maccoll equations) in the Massachusetts Institute of Technology (MIT) that were related to the calculation of airflow behavior at the tips of projectile cones entering the Earth's surface at supersonic velocities [45], [46]. In 1970, CFD tools were already available, but computers at that time only allowed essential calculations in two-dimensional flows [47].

Some of the topics in which the CFD has had great importance are in high-temperature phenomena that include vibration analysis, chemical reactions in flow systems, and high speeds, even in the field of medicine or biomedicine. This is because they are phenomena that cannot be solved analytically because of their complexity. Examples of these computational calculations are the work of Fay, Riddell, and Blottner [48], [49] for boundary layers, as well as Hall for nonviscous flows [45], [50].

It was not until the 1990s, where thanks to the technological evolution of computers, flows modeled in CFD began in three dimensions because most of the problems in the environment require an analysis of this type and more so in the aeronautical industry.

The second generation of computational fluid dynamics analysis were those studies in which today they are generally descriptive, which includes fundamental equations applied to dynamic flow problems that require the use of computational resources. Examples of these are subsonic or supersonic flows and viscous flows, whether they are separate or recirculated flows. For the latter, the Navier-Stokes equations are required to give an exact solution to these systems [45].

Today the use of CFD analysis has grown in branches such as medicine, aeronautics, modern aerodynamics, environmental engineering applications, automotive engineering, design engineering or manufacturing, etc. [51].



The CFD gives support and complement to the experimental analyzes with the theory, helping to interpret and understand the theoretical and experimental results.

## 2.2 Definition of Computational Fluid Dynamics

Computational Fluid Dynamics, or CFD, is the branch of fluid dynamics that provides an economical way for simulating the behavior of fluids by numerical solutions of the fundamental equations of fluids or heat transfer [52]. In addition, CFD analysis allows testing under conditions that are not feasible or difficult for experimental measurements and are not suitable for analytical solutions. It can be said that CFD is a new branch of engineering that integrates not only fluid mechanics calculation, but also integrates computer science and mathematics, as seen in Figure 2.1.

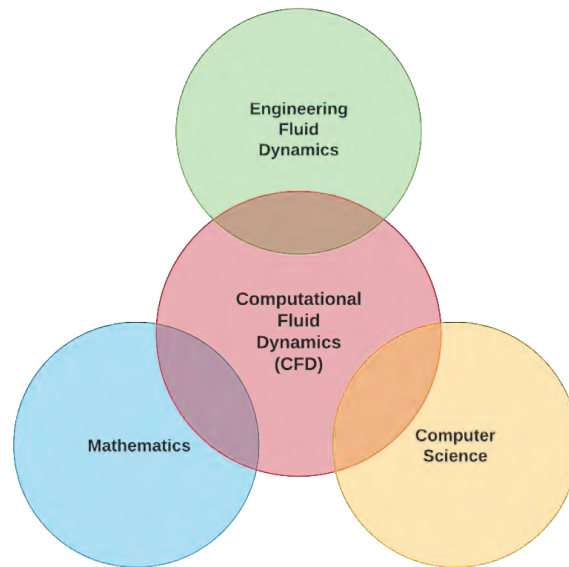


Figure 2.1 Disciplines that integrate CFD [5].

The main task of CFD is the manipulation of numbers and repetitive calculations of thousands or even millions of repetitions, which is a difficult task for humans. The CFD is one of the most viable and first used tools for preliminary design in the aeronautical and aerospace industry. The use of advanced computers with hardware that can process this large amount of data has facilitated the use of CFD analysis also in the wind industry. The results of the CFD analysis are directly analogous to the results provided by a wind tunnel analysis; both represent a series of fluid model data at different Mach numbers, Reynolds numbers, etc. [47].

However, the CFD represents an advantage in which one can access a computer and visualize the CFD models, while a wind tunnel would imply a large installation and transportation cost. In addition to the economic part, the CFD offers the opportunity to obtain detailed information on the flow field, which is more difficult to measure in a wind tunnel or is compromised by wall effects [45]. Even with the help of CFD analysis, this can understand and predict processes of interest in the field of wind engineering. Taking global warming and accelerated population growth into consideration, it is estimated that the use of CFD analysis techniques helps to reduce the cost of development and redesign in the field of wind engineering.

It should be mentioned that the results of a CFD analysis are as valid as the physical models, which are described by the fundamental equations and the boundary conditions, and therefore are subject also to errors, especially for turbulent flows. Discontinuity errors associated with the algorithm used to obtain a numerical solution, as well as rounding errors, could compromise the accuracy of the results of the CFD analysis.

However, CFD analysis is not the best option if one wants to characterize turbulent flow solutions. Most CFD solutions of turbulent flows contain turbulent models that are only approximations of real physics and depend on empirical data for several constants that are within turbulent models. Therefore, CFD solutions for turbulent flows are subject to inaccuracy, but there are currently works in calculating turbulent flows that take into account that all turbulent flows respond to the Navier-Stokes equations. If a proper technique of meshing is defined, with a large number of points in the grid, the aspects of turbulent flow can be calculated [45].

## **2.3 Advantages and disadvantages of Computational Fluid Dynamics**

Nowadays, the CFD analysis has a great acceptance in the scientific community because of several advantages over traditional techniques. Among these are the following:

- The opportunity to study specific characteristics of fluids through the fundamental equations that govern these fluids in a more detailed way.
- CFD allows complementing the experimental analysis with the analytical one, making it a useful tool to develop simulations of real flows.
- The ability to simulate flow conditions that are not possible to reproduce in physical tests, such as in the wind tunnel analysis or large dimension flows as scenarios of natural phenomena or nuclear accidents.
- It provides detailed, visual, and comprehensive information on better quality compared with analytical and experimental tests.
- CFD allows evaluations of dimensionless parameters such as the Reynolds number, Mach number, and Rayleigh number, as well as different flow orientations.

An experimental tool today is modeling in wind tunnels, which is generally accepted in the scientific and engineering community. The aerodynamic tunnels turn out to be representative of real-world situations, by correctly modeling the characteristics of the atmosphere, as well as the scale of the models. However, the cost of wind tunnel use is not as favorable, and it can be expensive to try to cover or develop a large wind tunnel.

A wind tunnel is a machine that allows modeling any object in an aerodynamic study in which airflow is passed to measure the flow conditions that could affect the scaled model. There are two types of wind tunnels; the first is open from both sides, as shown in Figure 2.2, while the second is a closed wind tunnel, with the airflow, is recirculated through it.



Figure 2.2 Wind tunnel test of an automobile in Pininfarina Cambiano 2012 [53].

Despite the numerous advantages offered by the CFD analysis, this does not suggest that this tool replaces the experimental tests. The CFD analysis can be considered as a viable alternative since it also includes a visualization of the 3D model. The wind measurement campaigns will be used in the present research topic as a comparison tool between CFD simulations, which will serve to evaluate the methodology to be proposed for the optimization of the use of the wind resource for the installation of small wind turbines in urban and rural environments.

In the CFD analysis, there may be a miscalculation, possibly resulting in differences between the calculations of the results and the experimental tests. In case the results are correct, these must be properly analyzed.

Some of the advantages of the application of analysis and modeling in computational fluid dynamics versus the development and analysis of a wind tunnel can be seen in Table 2.1

Table 2.1. Advantages of CFD on wind tunnel modeling [54].

Advantages	Discussion
Complete analysis	The CFD can define and register discrete points that calculate the fluid variables throughout the entire study domain.
Easy analysis	CAD design allows building modeling in the CFD domain and can be modified and remodeled immediately, while physical models require more time and cost for possible adjustment changes during initial modeling of the wind tunnel.
Low cost	It can have the same or a lower cost in producing the modeling.
Better visualization	The results will be shown in the output in a graphical color chart because photographs of the wind tunnel tests cannot give many details because sometimes the images of the results are monochromatic.
Measurement of wind parameters	The CFD is a tool that can measure and control some parameters like wind direction, the concentration of pollutants, chemical reactions, heat, and radiation, etc.
Few wind tunnels with good performance	The wind tunnels are only achieved by the large international companies and universities because of expense and excessive equipment dimensions for the development of studies in wind tunnels.

On the other hand, Table 2.2 shows some of the disadvantages that are found when using computational fluid dynamics analysis, compared to the use of wind tunnels.

Table 2.2 Disadvantages of CFD in wind tunnel modeling.

Disadvantages	Discussion
CFD is not recognized by a standard certification	CFD is a new tool for helping with the analysis construction. Some companies that use CFD modeling are <u>improving technology continuously</u> .
CFD results are subject to have errors	CFD results do not match those of the real world in specific parameters. The most common problems are as follows: <ul style="list-style-type: none"> <li>- An excess of turbulent kinetic energy in the wind flow.</li> <li>- Over/underprediction of the estimation of the pollutant's concentrations.</li> <li>- The incorrect manipulation of a vortex with the steady-state models.</li> </ul>
Only experienced staff makes use of the specialized software	The studies show that the results of CFD can vary significantly depending on the modeler, even using the same CFD software [55].
Projects cannot be complex	The size of the modeled project is limited by the calculation power and the software used for the mesh size of the project. On the other hand, a wind tunnel is not so limited in the size and complexity of the model.
The results are often better for less complex projects	The accuracy of wind tunnel results, this does not depend on the complexity of the geometry.
CFD provides a steady-state solution; a transient solution entails more time consuming	The average wind field is acceptable for specific applications, including turbulent kinetic energy. Transient primary wind tests are used to locate the time of the worst conditions for conservative results.

The CFD analysis can currently be considered as a research tool that helps the implementation of new codes for the solution of experimental tests in engineering, such as wind loads in structures and heat transfer. It can even be a teaching tool in the education of the basic principles of thermofluids and can serve as a tool for designing new prototypes or models in engineering, increasing the cost-benefit in the development of new products. The CFD analysis also allows modeling fluids that can reach speeds above the speed of sound (343 m/s or 1,234.8 km/h), commonly classified as supersonic, hypersonic, or transonic speeds.

## 2.4 Solution process of the Computational Fluid Dynamics

Recently, there is commercial and open-source software on the market that allows the CFD analysis. Some of the software may or may not include a graphical interface known as Graphic User Interface (GUI) to input the data of the problem or model for later examining the calculated results. This software or CFD code is composed of three fundamental elements: the pre-processing, the solver, and finalizing with the post-processing, as shown in Figure 2.3.

In the pre-processing, the geometry of the flow region and the model are defined and created, including the definition of the computational domain based on the observation of the physical problem to be studied.

Later, the mesh generation process is carried out, which includes the subdivision of the domain into a smaller number of cells in order to solve the flow physics in the model created. Also, the fluid properties and boundary conditions are considered in order to pass to the solver.

In the solver function, are calculated numerically the governing equations that describe the flow physics problems in the cells of the mesh, which will help to determine the behavior of the fluid represented. The final step, according to the CFD solution process, is post-processing, where it is developed the result analysis throughout the data visualization with graphical representation. These CFD steps will be explained in further sections.

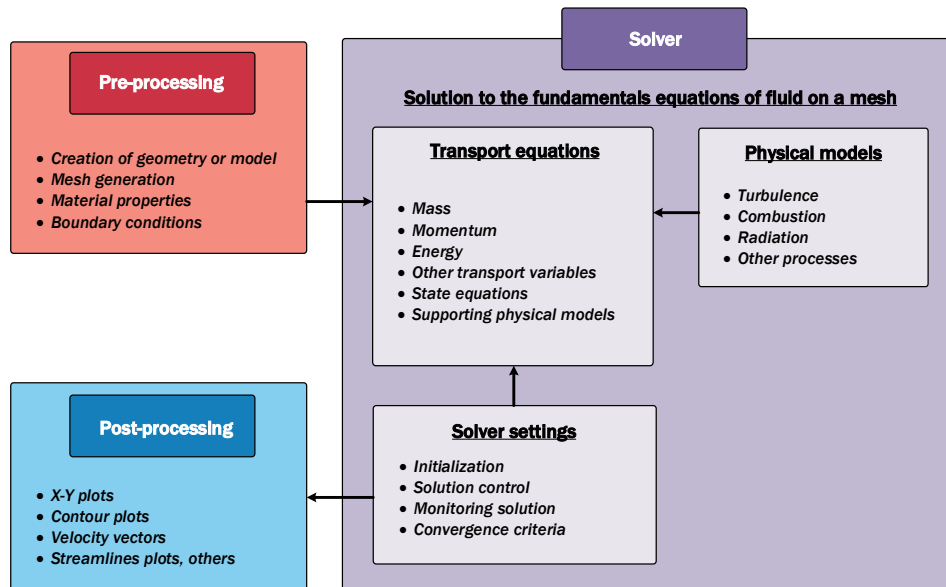


Figure 2.3 The interconnectivity functions of fundamental elements of CFD analysis [56].

## 2.5 The solution to Computational Fluid Dynamics in SolidWorks® Flow Simulation

According to previous sections, it is possible to analyze the different available software, including Siemens NX, Autodesk CFD, SolidWorks Flow Simulation, OpenFOAM, and ANSYS Fluent, etc. When analyzing the software, SolidWorks was selected because of its characteristics of the software and its easy GUI for simulating the fluids, allowing more excellent stability in the calculation processing of the proposed models.

Based on the above, SolidWorks Flow Simulation software uses computational fluid dynamics analysis to obtain a fast and efficient simulation of fluid flow and heat transfer models. This allows easily calculating the forces of a fluid’s flow and understanding the impact that these forces have on the models or analyses that are required, which in this case is the optimization of the use of the wind resource through the CFD analysis.

In the present research, the computational fluid dynamics analysis is the cornerstone for the methodologic proposal for the better installation of SWTs in urban and rural areas. The SolidWorks Flow Simulation software is used as an analytical tool.

This software handles the solutions of the Navier-Stokes equations that allow analyzing mass formulas, as well as moment and energy conservation laws for the fluids (gases and liquids). These equations are complemented by fluid state equations, which define the fluid's nature, density, viscosity, and thermal conductivity. The deduced fundamental equations that govern the fluids are described in detail in Appendix A.

Incompressible fluids are dependent on their dynamic viscosity in the flow of the cutting speed and temperature; moreover, compressible liquids are considered to have a dependence on their density on the pressure. A particularity here is the definition of the geometry, the boundary conditions, and the initial conditions in which the fluids are found.

On the other hand, fluids can behave in three ways according to the boundary and initial conditions they have, as well as the viscosity and the inertial forces they present: laminar flow, transient, and turbulent flow.

**Laminar or Poiseuille flow:** This flow behaves in an orderly manner since the fluid moves only in the direction of the current or in one direction only. These laminar flows occur at low Reynolds number values, which are defined as the product of scales representative of speed and length divided by kinematic viscosity. It can be said that a laminar flow has a Reynolds number less than 2,300.

**Transient Flow:** Flows in this range can fluctuate between laminar and turbulent flows. The fluid flow is about to become turbulent. It can be said that a transient flow has a Reynolds number between 2,300 and 4,000.

**Turbulent or Venturi flow:** This movement regime occurs when there is a disorderly movement with intensive mixing between the different layers of the fluid. When the Reynolds number exceeds a specific critical value, the flow is considered turbulent. Turbulent flow has a Reynolds number greater than 4,000.

For purposes of this doctoral research, air as fluid is considered to have a simple chemical structure and a compressible Newtonian fluid (the viscosity does not vary depending on the shear stress applied) and behaves as turbulent flow, under normal conditions of pressure and temperature.

### 2.5.1 Navier-Stokes equations for laminar and turbulent flows

For the estimation of these turbulent flows, the Favre-averaged Navier-Stokes equations are used where samples of the turbulent flow are taken in time averages on the flow parameters, while on a large scale, in time-dependent phenomena they are directly considered. Considering that the turbulence of a boundary layer is not influenced by density fluctuations if  $\partial\rho/\partial t \ll \rho$ , being generally true for wall-bounded flows up to a Mach number about five. Otherwise, in the case of hypersonic flows, the flows with heat transfer, and combustion, the density fluctuation has to be considered [57].

Through this procedure, additional terms known as Reynolds stresses appear in the equations for which additional information should be provided.

In order to close this system of equations, Flow Simulation uses transport equations for turbulent kinetic energy  $\kappa$  and its dissipation rate  $\varepsilon$ , which is called the  $\kappa - \varepsilon$  model. Flow Simulation software uses the same system of equations to describe both laminar and turbulent flows [58].

The laws of conservation of mass, angular momentum, and energy in the Cartesian coordinate system that rotates with an angular velocity  $\Omega$  around an axis that passes through the origin of the coordinate system can be written the Navier-Stokes equations simplified as follows:

### Mass conservation

$$\frac{\partial \rho}{\partial t} + \frac{\partial}{\partial x_i} (\rho u_i) = 0 \quad (2.1)$$

### Momentum conservation

$$\frac{\partial \rho u_i}{\partial t} + \frac{\partial}{\partial x_j} (\rho u_i u_j) + \frac{\partial \rho}{\partial x_i} = \frac{\partial}{\partial x_j} (\tau_{ij} + \tau_{ij}^R) + S_i; \quad \text{where } i = 1,2,3 \quad (2.2)$$

### Energy conservation

$$\frac{\partial \rho H}{\partial t} + \frac{\partial \rho u_i H}{\partial x_i} = \frac{\partial}{\partial x_i} (u_j (\tau_{ij} + \tau_{ij}^R) + q_i) + \frac{\partial \rho}{\partial t} - \tau_{ij}^R \frac{\partial u_i}{\partial x_j} + \rho \varepsilon + S_i u_i + Q_H; \quad (2.3)$$

$$\text{where } H \text{ is:} \quad H = h + \frac{u^2}{2}$$

where  $u$  is the velocity of the fluid,  $\rho$  is the density of the fluid,  $S_i$  is an external force of mass distributed per unit mass because of the resistance of porous media  $S_i^{porous}$ , a lift force ( $S_i^{gravity} = -\rho g_i$ ), where  $g_i$  is the component of gravitational acceleration along the direction of the  $i$ th-coordinate.

In the rotation of the system of coordinates  $S_i^{rotation}$ , for example,  $S_i = S_i^{porous} + S_i^{gravity} + S_i^{rotation}$ ,  $H$  is the thermal enthalpy,  $Q_H$  is a source of heat or dissipation per unit volume,  $\tau_{ij}$  is the shear viscosity tensor, and  $q_i$  is the diffusion heat flux. The subscripts are used to denote a sum over the three coordinate directions  $x$ ,  $y$ , and  $z$  [58].

For calculations with the high flow Mach<sup>1</sup> number enabled, the following equation is used:

$$\frac{\partial \rho E}{\partial t} + \frac{\partial \rho u_i (E + \frac{p}{\rho})}{\partial x_i} = \frac{\partial}{\partial x_i} (u_j (\tau_{ij} + \tau_{ij}^R) + q_i) - \tau_{ij}^R \frac{\partial u_i}{\partial x_j} + \rho \varepsilon + S_i u_i + Q_H \quad (2.4)$$

$$\text{where } E \text{ is:} \quad E = e + \frac{u^2}{2}$$

---

<sup>1</sup> The Mach number,  $M = u/c$  corresponds to the fluid velocity ratio  $u$ , for the speed of sound in that fluid,  $c$ . The Mach number measures the compressibility of the fluid.

## **2.5.2 Boundary conditions models for laminar and turbulent flows**

In SolidWorks, the boundary conditions for laminar and turbulent flows are used to describe regions of nearby walls. The model is based on the approximations of Modified Wall Functions. This model is used to describe the laminar and turbulent flows near the walls and to describe the transitions from laminar to turbulent flow and vice versa. The modified walls function uses the Van Driest profile instead of using a logarithmic profile. If the size of the grid cells is close to the wall and is more than the thickness of the boundary layer, the technology of the integral boundary layer is used. The model provides the precise conditions of speed and temperature limits for the conservation equations mentioned above [58].

## **2.5.3 Boundary conditions for internal and external flows**

Flow Simulation offers two options for specifying the boundary conditions: manually by placing the inputs and outputs of the system or by specifying them through a transfer of the results obtained from another CFD simulation in the same coordinate system [58]. With the first option, all openings in the model are classified into pressure outlets and flow outlets, depending on the boundary conditions of the flow that is intended to be specified.

A boundary condition of pressure outlets, which could be static pressure, total pressure, or atmospheric pressure, is imposed in general cases when the direction of flow and/or the magnitude in the open model is not known beforehand. Therefore, they are calculated as part of the solution. It should be mentioned that when an inflow occurs at the pressure outlets, the temperature, the composition of the fluid mixture, and the parameters of the turbulence have to be specified.

A boundary condition of flow outlets it is imposed when dynamic flow properties, such as the direction of flow and masses, the flow rate or volume, and the Mach number, are known in the opening. If the flow enters the model, then the temperature input, the composition of the fluid mixture, and the turbulence parameters will have to be specified. The pressure in the openings will be determined as part of the solution. For supersonic flows, the pressure inputs must be specified [58].

For external flow problems such as flow over an aircraft or a building, as is in the present study cases of this doctoral research, the parameters of the external incoming flows, also called ambient conditions, must be defined. Among them are the speed, pressure, temperature, the composition of the fluid mixture and the turbulence parameters, and must be specified when executing the external simulations [58].

## **2.5.4 Computational mesh**

Flow Simulation has a computational approach that is based on a thin rectangular mesh near the geometric boundaries. The cells of the mesh are rectangular parallelepiped with orthogonal faces for the specification of axes of the Cartesian coordinate system. However, near the borders of the mesh cells are more complex. The cells near the border are parts of the cells of the original parallelepipeds that intersect the boundary or the geometry boundary.

A geometric curved surface is approximated by sets of polygons with vertices that are points of intersections of the surface with the edges of the cell. These flat polygons cut the cells of the



original parallelepiped. Therefore, the resulting near-limit cells are polyhedral with both faces oriented to the axis and arbitrarily oriented to the plane, as shown in Figure 2.4. The cells of the original parallelepiped containing limits are divided into several control volumes that are referred to as only one fluid or solid medium. In the simplest case, there are only two control volumes in the parallelepiped; one for the solid and the other for the fluid.

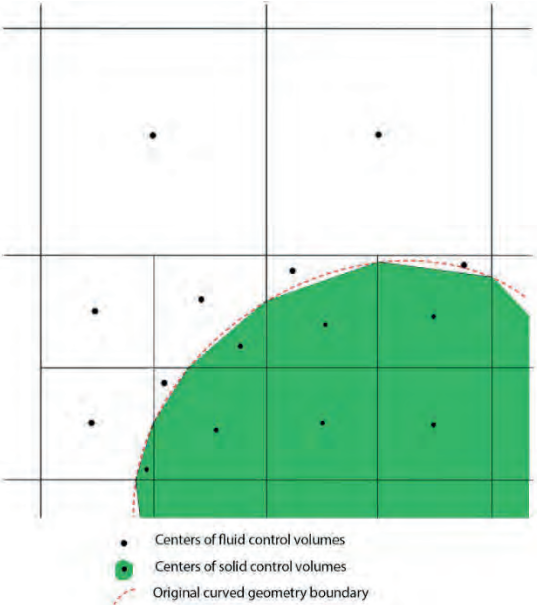


Figure 2.4 Computational meshing near the solid/liquid interface.

The fundamental part of the computational mesh is the rectangular computational domain that is constructed automatically by SolidWorks, so it encloses the solid body and has the boundary planes orthogonal to the axes specified in the Cartesian coordinate system. This rectangular computational domain presents a limitation in most of the CFD software to be applied to the present project. This limitation will be overcome by developing and proposing a Virtual Computational Domain (VCD), which will be explained further; otherwise, SolidWorks states a computational mesh constructed according to the following stages shown in Figure 2.5 [58].

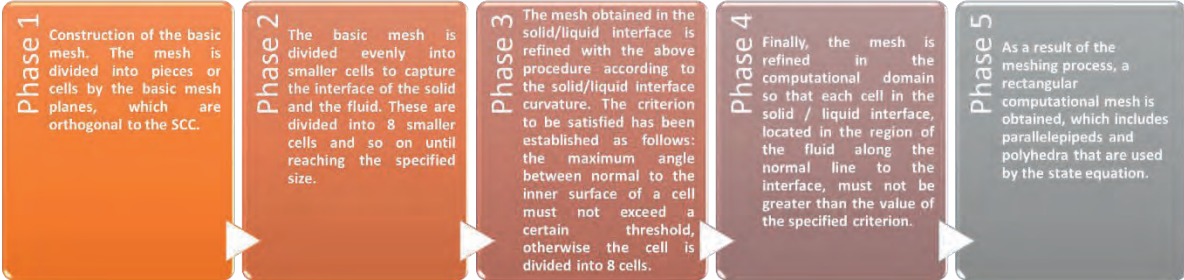


Figure 2.5 Solid/liquid interface computational meshing procedure in SolidWorks.

Since the procedure, as mentioned above, is performed before the calculation, the meshing can be further refined at the specified times during the calculation according to the spatial gradients of the solutions. As a result, the low-gradient regions of the cells merge, while the high-gradient regions are divided into smaller cells [58].

# 2.6 Internal flow example for Computational Fluid Dynamics analysis

## 2.6.1 Initial conditions - Pre-processing

### i) Development of the model or geometry

The first step of the CFD analysis is the definition and creation of the model of the region of the flow to be studied, which is known as the computational domain [56]. This computational domain is where the fluid is simulated in controlled conditions, adding the environmental settings or boundary conditions. Figure 2.6 shows the proposed first case of the CFD analysis for internal flows.

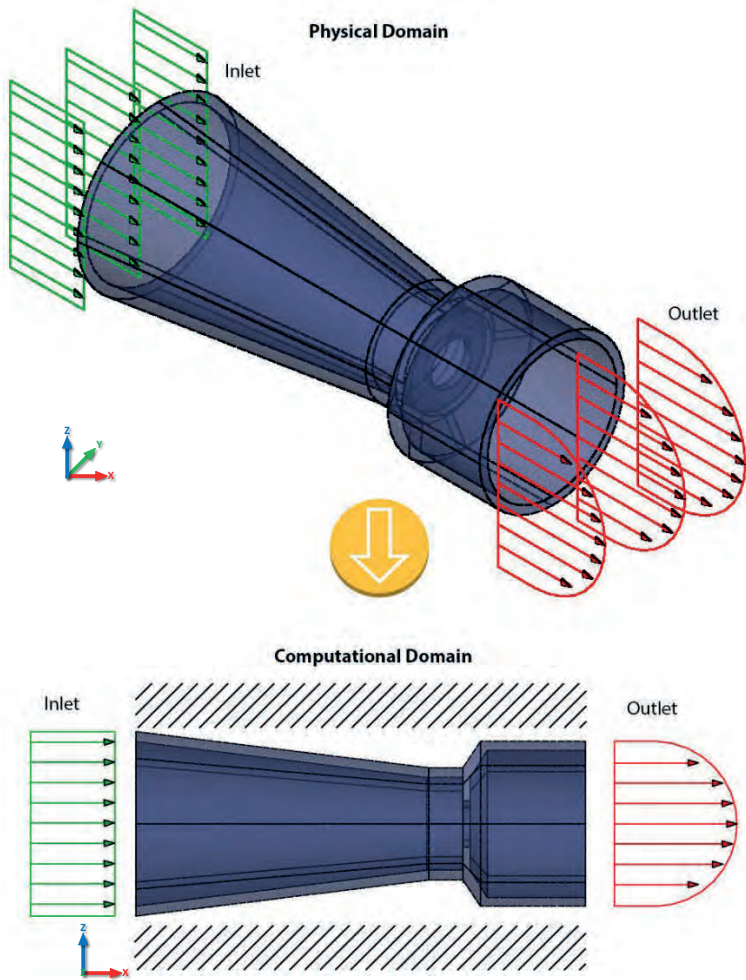


Figure 2.6 Computational domain of the nozzle model.

In the present example, the flow of the fluid is surrounded by a rigid wall domain, in this case, represented by the cylinder with the reduced nozzle. Additionally, the fluid enters from the left side of the contour or computational domain and leaves on the right side of the computational boundary domain.

## ii) Mesh generation

The second step is the creation of the mesh or grid. This step is one of the most important processes during the pre-processing phase after defining the domain geometry or model [56].

The CFD analysis requires subdividing the domain into smaller parts for solving the fundamental equations of fluid physics together with the domain geometry (model), which has already been created. This is the mesh of cells that can be called elements or control volumes.

The flow of the fluid is described throughout each cell in order to mathematically solve the model and, thus, the values of the flow properties, such as speed, pressure, temperature, and other properties that can be calculated. Depending on the number of cells in the mesh, the CFD analysis allows having greater precision in solving the problem. This is linked to computational cost and calculation time.

For simple geometries such as the one created for the reduced nozzle, a mesh of structural cells overlaps the model. Figure 2.7 shows a mesh of 78 (L) x 28 (H) cells, which gives a total of 2,184 cells for this case.

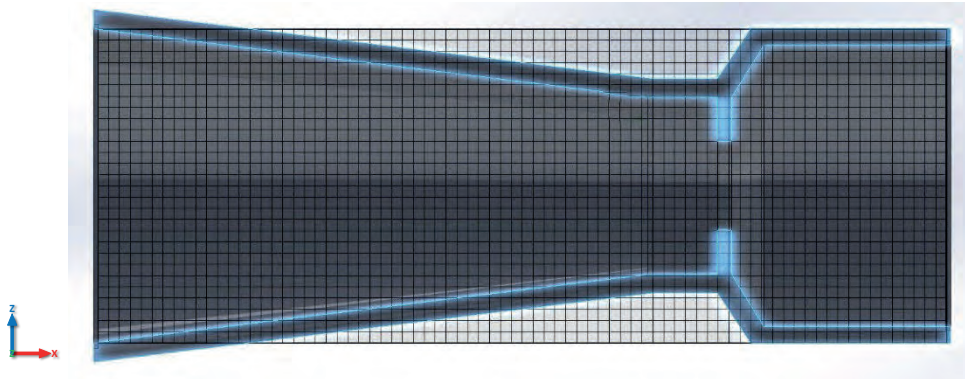


Figure 2.7 Structural meshing of the nozzle model.

## iii) Selection of physical and fluid properties

The third stage is the selection of the fluid and its physical properties, which are intended to be studied: selecting what type of fluid or fluids will pass through the model, as well as determining if the flow is of an unstable or stable type. It is then defined if the fluid is viscous or non-viscous; generally, non-viscous fluids are called compressible fluids.

On the other hand, viscous fluids can exist in a laminar or turbulent fluid, in which an important aspect that should be considered is the heat transfer of the fluid, which may be conduction, convection, or radiation. Convection will predominate in these types of heat transfer problems. For the reduced nozzle shown, water was selected as fluid. In the diagram of Figure 2.8, the physical characteristics of the flows types that are the object of the CFD study are shown in a general way.

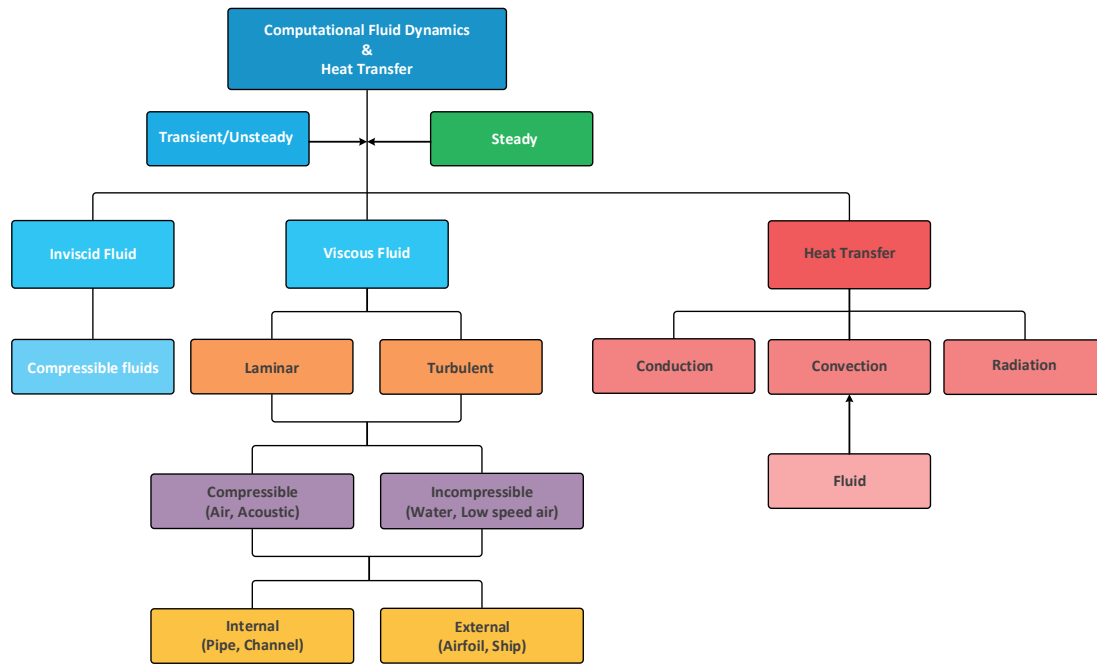


Figure 2.8 Flowchart of the physical properties of fluids in CFD [56].

#### iv) Specification of boundary conditions

The complexity of describing the physical properties of fluids and their behavior with the environment plays an important role in CFD analysis. Therefore, defining the boundary conditions that describe the actual physics of fluids in a CFD analysis system is necessary.

At this step, it is important to define the boundary conditions in which the physical input and output properties have influence, being these: the speed, the mass flow, the volumetric flow of the fluid, and the atmospheric pressure, which allow modeling the behavior of the fluid that overlaps the geometric body of study.

In Figure 2.9, some of the boundary conditions can be observed for the geometry of the nozzle. The density corresponding to a particular fluid flowing in the domains at the boundary of the inflow needs to be specified and is usually determined directly from the selected temperature and pressure.

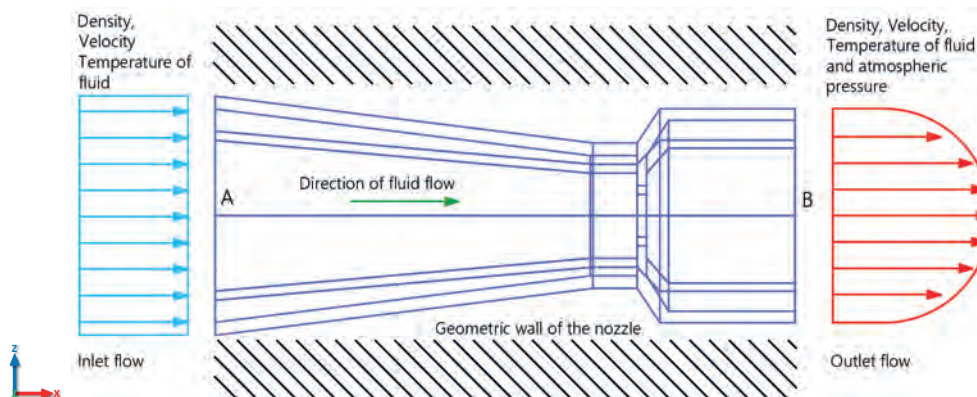


Figure 2.9 Boundary conditions for the internal flow of the nozzle model.

Until this step, it can be considered that the pre-processing element is finished in the CFD analysis, so in the next section, we will start with the numerical solution or solver phase.

## 2.6.2 CFD Solver - Numerical solution

In this element of the numerical solution, the CFD analysis focuses on the mathematical basis used to reach the solution or convergence of the problem proposed, which is as follows:

### i) Initialization and control of the solution

The numerical solution of the CFD analysis requires calculations through iterations, which contain discrete values of the properties of the flows and fluids, such as speed, pressure, density, temperature.

These were configured in the previous stage and must be correctly represented in order to calculate the solution of the CFD system. The initial conditions can be configured arbitrarily, but it can save computational time if the initial conditions are configured intelligently. In other words, the solution of the model or convergence is reached more quickly, allowing to reduce the possibility that the model is composed in an unstable manner.

Most commercially available CFD analysis software uses the Finite Volume Method (FVM), which will be studied later as a standard numerical solution. This CFD solution process can be summarized in the following flow diagram in Figure 2.10.

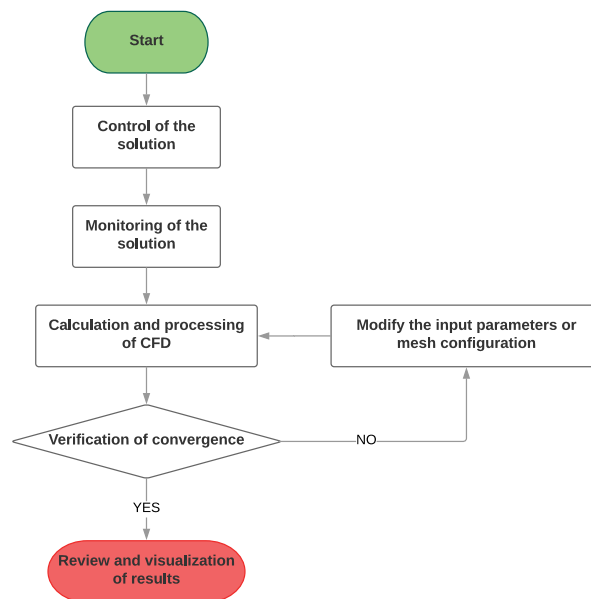


Figure 2.10. Flowchart of the CFD solution process [56].

### ii) Monitoring of the convergence of the system

This last process (verification of the convergence) permits following the numerical calculations of the fundamental equations that govern the fluids (Navier-Stokes equations) through each iteration when developing the CFD calculation and processing.

This parameter of convergence, or also called as the goals of the solution convergence, allows establishing if a good result will exist in the CFD analysis.

Different criteria exist for assessing CFD convergence, among which can be found the residual values, solution imbalances, and quantities of interest. The first is the most fundamental criterion used in the CFD area and directly measures the error in the solution of the equation system. In the iterative numerical solution, the residuals of the variables will never be zero even though the closer to zero value, the better it will be for the system solution.

The imbalances criterion is based on the conservation of the governing equations of the fluids. For a proper validation of the CFD results, the solution imbalances must be less than 1% as a starting point, although a more precise application may require rigid convergence.

The last criterion is referred to with the convergence of the system, using quantities of variables of interest, which allows monitoring values until a particular settled goal value of convergence is reached.

### 2.6.3 Post-processing - Results, reports, and visualization

The CFD analysis can generate graphs and images of the results obtained from the proposed problem and is an effective tool in the development of new products or processes. The results of CFD allow analyzing and visualizing the flow of the fluid through the model, which even can generate a video to see the behavior of the model. Most commercial and CFD open-source software have visualization tools for the post-processing element. The categories of the visualization of the results based on the flow through a nozzle are described below.

#### Cut plots X-Y

This type of visualization refers to two-dimensional graphs, which represent the variation of a dependent variable compared with an independent variable. This type of visualization is the most accurate and quantitative for presenting the numerical data of CFD results. The cut plots allow comparisons between the numerical data, with the experimental results of a wind tunnel analysis or another method of validation.

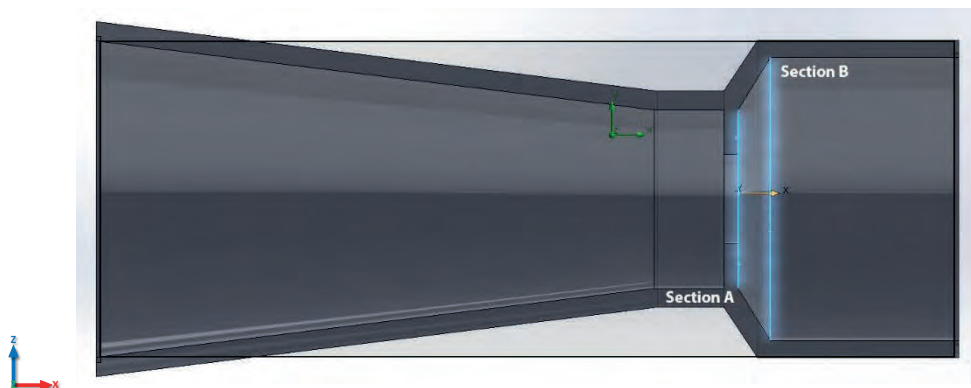


Figure 2.11 Representation of sections “A” and “B” of the nozzle model.

Among the results that these graphs represent is the use of speed profiles, or surface graphs with parameters such as density, pressure, temperature, and coefficients of friction, etc.

To exemplify these graphs, with the present example in Figure 2.11, sections “A” and “B” are presented, which are considered to graph the temperature of the fluid and its behavior along the length of the nozzle. Representing the section “A” in red color shown in the graph with a limit length of 0.065 m and for section “B” represented by the blue color with the maximum length of 0.1 m; both are shown in Figure 2.12.

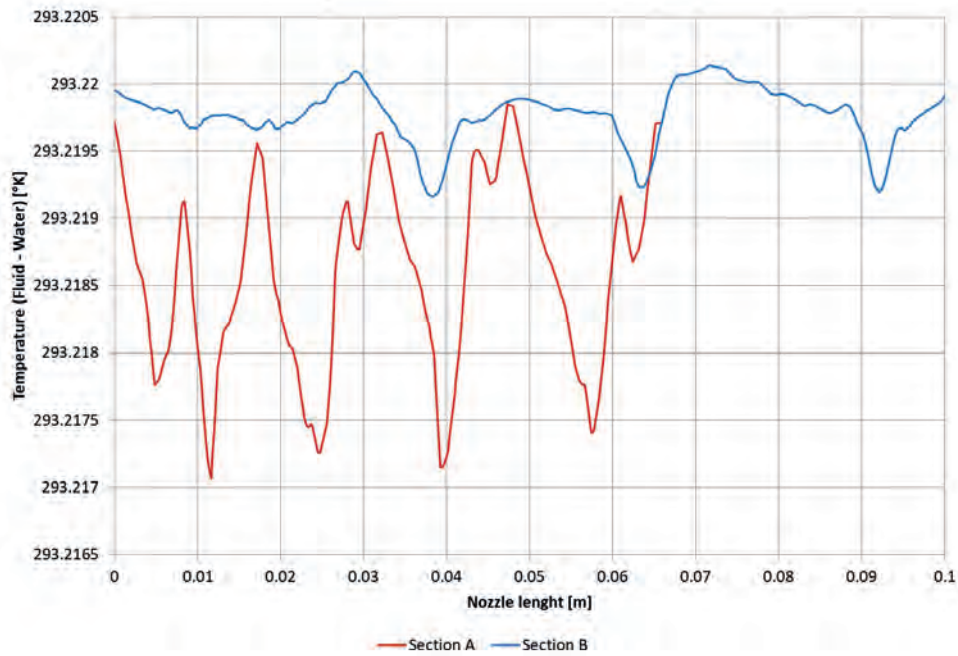


Figure 2.12 Fluid temperature in sections “A” and “B” of the nozzle model.

### Vector graphs

Another way to represent the CFD results is vector graphics. These commonly show discrete points of the velocity vectors of a fluid, indicating the direction and magnitude. Generally, this type of graphic is in two dimensions.

Figure 2.13 shows a typical vector graph, which represents the fluid flowing through the nozzle. The velocity vectors are shown in different sizes, which represent the intensity with which the fluid (water in this case) flows, showing how the bottleneck presented in this case represents speeds from 0 m/s to 186.6 m/s.

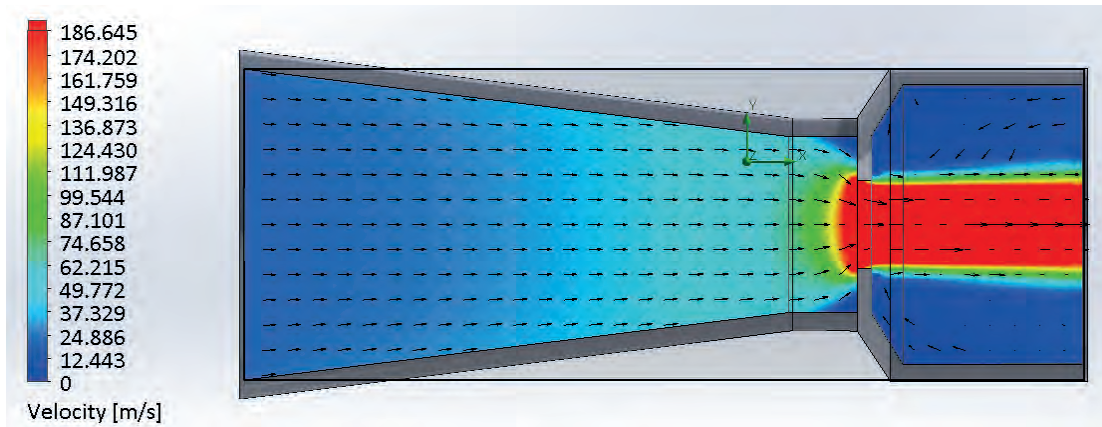


Figure 2.13 Speed vector graph of the nozzle model.

### Contour plots

The contour plots are another useful tool in the field of CFD analysis for data representation. A contour line or isoline indicates a property that is constant in space. In turn, the equivalent representation in three dimensions is the iso-surface [56]. This type of graphic operates so that it represents a constant value of the transport dependent variable and that it is a fixed value in a specific part of the fluid in relation to the proposed model. In addition, in the case where the intervals of the variable are the same, grouping these lines indicate a rapid change in the amount of the flow.

In Figure 2.14 and Figure 2.15, the contour plots for the fluid in the nozzle are represented, both for the velocity and the fluid pressure, respectively. It can be seen that the contour graphs can be represented either with isolines or with contours distributed along with the model, as well as in the speed contour plot.

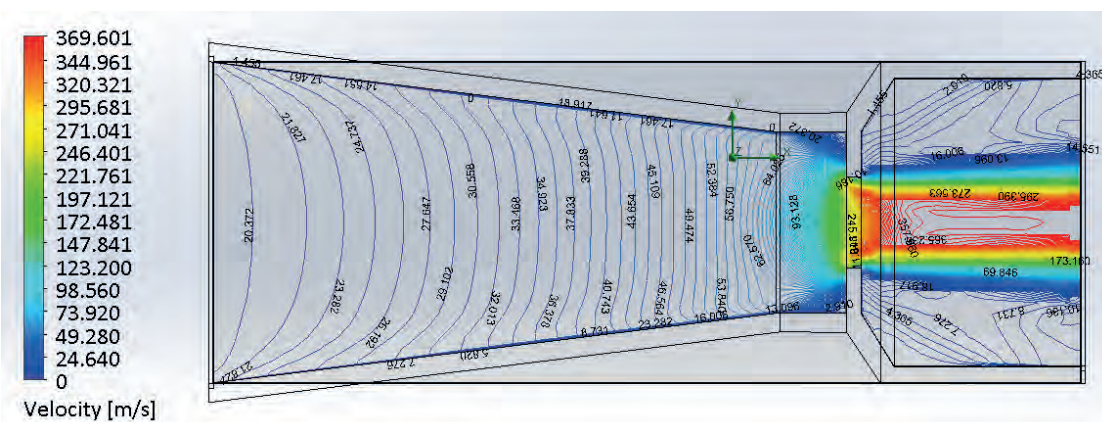


Figure 2.14 Contour plot and iso-lines of velocity in the nozzle model.

Figure 2.14 shows that where the lines they are closely grouped, which is around the bottleneck of the nozzle, clearly indicates a greater presence of activity in the velocity flow of the fluid passing through this narrow part of the nozzle. Something similar happens with the pressure in Figure 2.15.



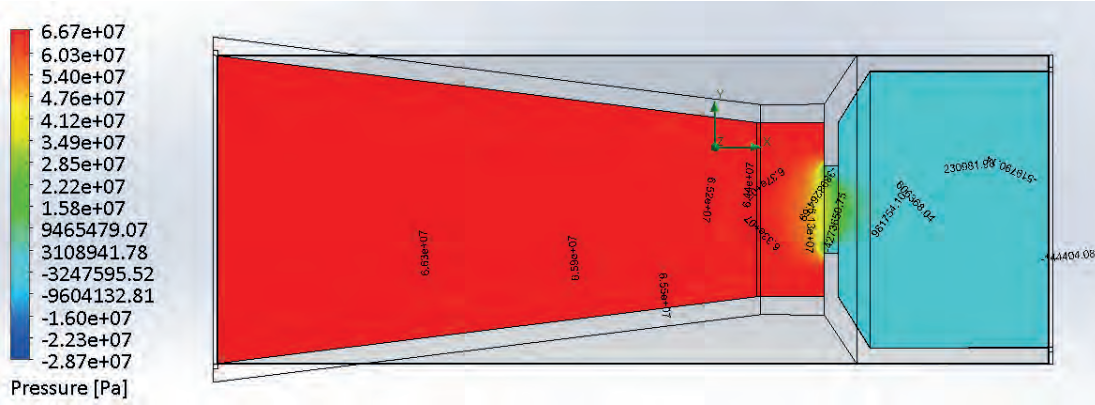


Figure 2.15 Contour plot and iso-lines of pressure in the nozzle model.

### Other types of graphics

A tool that allows examining the nature of the fluid in either two or three dimensions is the use of current line graphs (streamlines), and as the name says, they show the trajectory that the fluid will take within the proposed analysis model. In [56], a current line is defined as a line parallel to the velocity vector, where it traces the flow pattern using particles without masses, as shown in Figure 2.16. Where can be calculated integrating the spatial components of the velocity, expressed in a three-dimensional Cartesian plane as  $dx/dt = u$ ,  $dy/dt = v$ , and  $dz/dt = w$ .

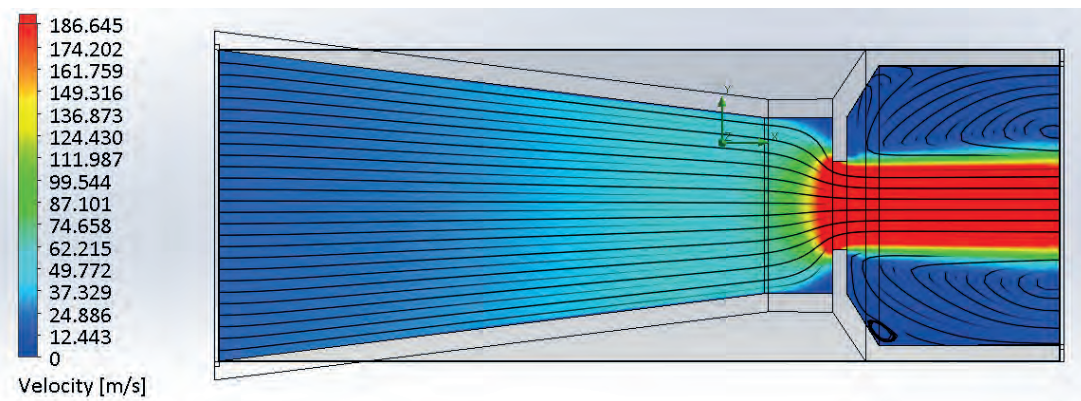


Figure 2.16 Streamlines plot of velocity in the nozzle model.

Examples of other types of graphs are shown in Figure 2.17 and Figure 2.18, in which the representation of the magnitude of the velocity along the nozzle is presented in two dimensions. These are LIC<sup>2</sup> (Line Integral Convolution), and finally, the trajectories flow graph is also shown.

<sup>2</sup> It is a technique proposed by B. Cabral and L. Leedom for the visualization of fluid dynamics, used mainly to identify the critical points of the flow.

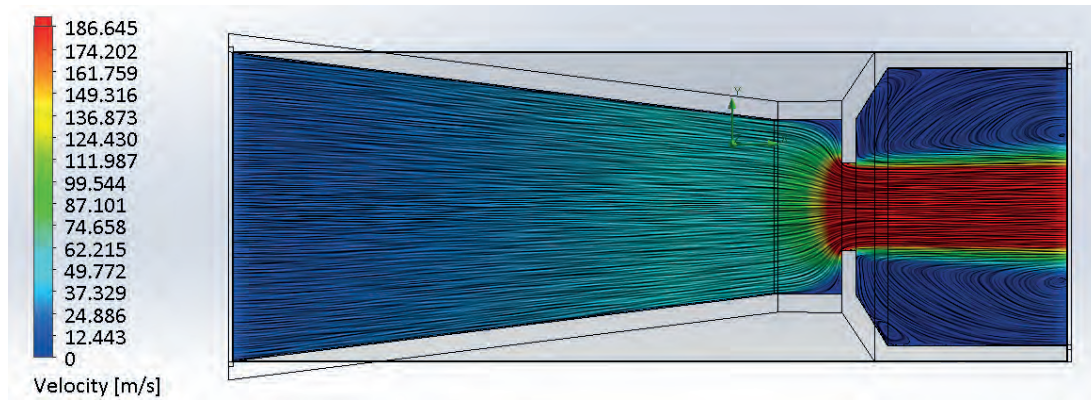


Figure 2.17 Velocity LIC graph in the nozzle model.

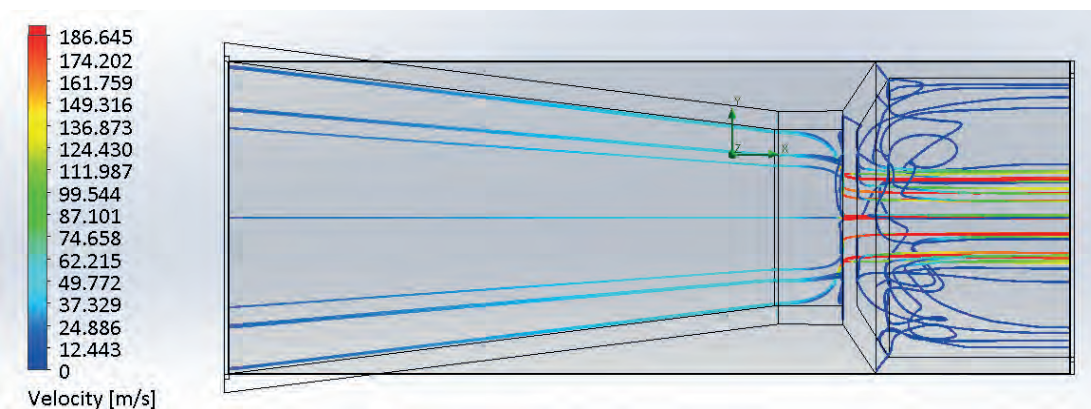


Figure 2.18 Velocity trajectories flow graph in the nozzle model.

## Animations or video

The animation is another useful tool that is implemented in CFD analysis, which represents the flow process of fluids, whether in the motion of particles, vectors, etc. This tool makes animated video recordings in multiple frames to present CFD simulations in color. It is essential to mention that this type of result representation requires a transient simulation.

## 2.7 External flow example for Computational Fluid Dynamics analysis

### 2.7.1 Initial conditions - Pre-processing

#### i) Development of the model or geometry

In order to show the external flow CFD analysis, an aerodynamic profile is used, which will allow knowing the advantages and limitations of the software selected for the CFD analysis. This software can calculate the viscosity and compressibility of the flow on an airfoil. This aerodynamic profile is depicted in Figure 2.19, where the main components are described.

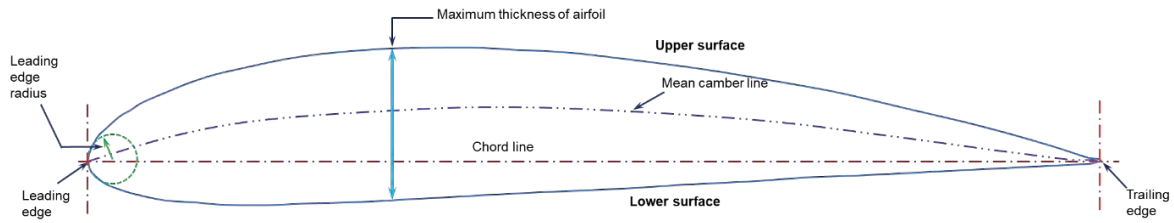


Figure 2.19 Components of the NACA 4415 airfoil section.

The development of CFD studies can be seen as computer software and is an easy matter to reproduce; this could be done as if turning on or off a button for determining which flow to reproduce, while in a wind tunnel, we could not perform this task easily and efficiently. Unlike the reduced nozzle example that has a rigid wall domain, in the aerodynamic profile, it is not presented since the fluid can pass above and below through the NACA 4415 profile limited by the computational contour domain. Figure 2.20 shows the computational domain of the model for external flow CFD analysis.

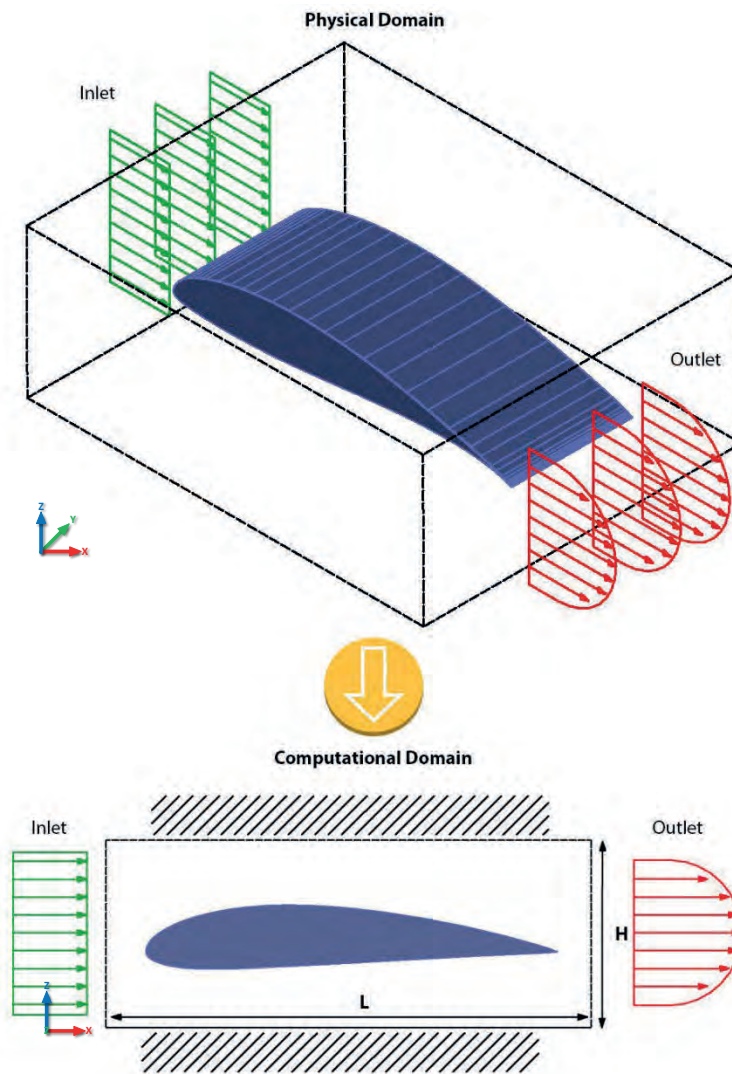


Figure 2.20 Example ii) of fluid passing through an aerodynamic profile NACA 4415.

In order to become familiar with the software and gain experience in this stage of the research, the use of the SolidWorks software was also implemented, where this airfoil profile was modeled, obtaining the CFD results for the NACA 4415 airfoil, both for laminar and turbulent flows. These studies consider an attack angle of  $0^\circ$  and a turbulence factor of 0.12%.

The above takes into account the computational domain as a tool or container of the fluid to be studied, so a sufficient distance between the model and the walls of the domain must be taken into consideration since this could cause wall effects in the flow of the fluid that surrounds the model to be studied.

## ii) Mesh generation and selection of physical fluid properties

Regarding the aerodynamic profile, for more complex geometries, the meshing can be performed by triangular cells or rectangular cells, allowing more complicated contour shapes, such as the structured mesh shown in Figure 2.21. In this case, a total of 15,656 cells constitute all the flow domain surrounding the NACA 4415 aerodynamic profile. For the aerodynamic profile, the air was selected as fluid, including all its physical properties.

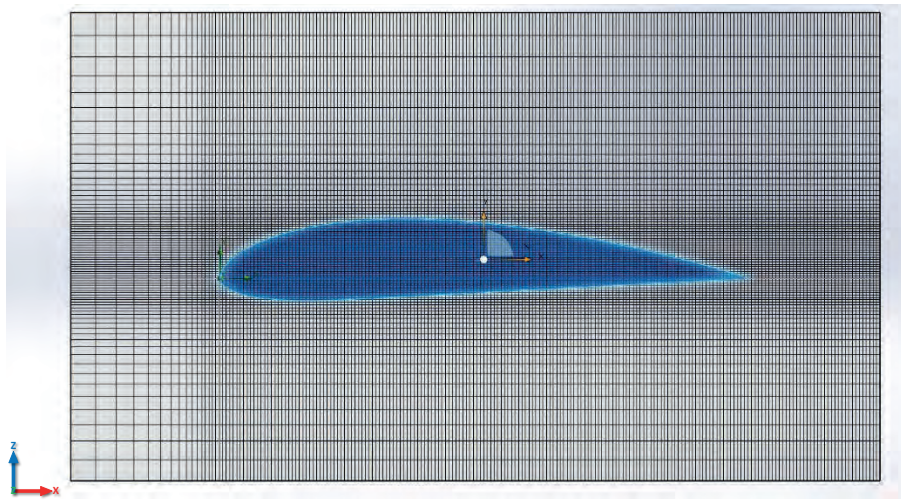


Figure 2.21 Mesh for a fluid that passes through an aerodynamic profile NACA 4415.

## iii) Specification of boundary conditions

The boundary conditions are essential for the problem definition; in this sense, Figure 2.22 illustrates these boundaries in order to characterize the airfoil example. The fluid moves around the airfoil, and for this reason, is considered as external fluid flow. Because of this flow, normal and parallel forces around the airfoil called drag and lift forces respectively are produced.

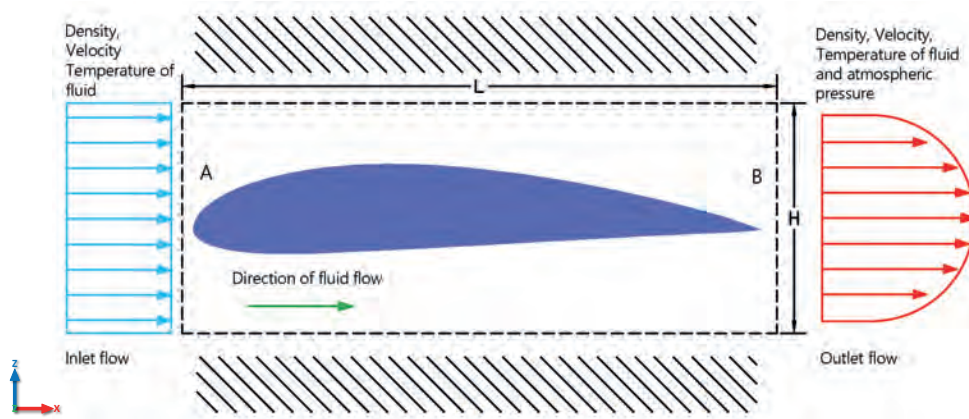


Figure 2.22 Boundary conditions for external flow in the aerodynamic profile.

In this step, it is considered the setup of the inlet and outlet conditions that describe the fluid that interacts with the geometric body. A compressible fluid (air) is considered in this aerodynamic profile, which will show what would be the differences between laminar flow and turbulent flow. The simulations were performed with an angle of attack of  $0^\circ$  for a Reynolds number of  $Re = 100,000$ .

## 2.7.2 CFD Solver - Numerical solution

In this step, the solution to the Navier-Stokes equations that describe the fluids in the model or desired geometry based on Section 2.5 is given.

### i) Initialization and solution control and Monitoring of convergence

As was described in the previous section, in this step, the convergence criteria are configured, as well as the numerical solution used to describe the behavior of the fluid flow. Regarding the proposed example of the airfoil, this convergence criterion can be verified with other variables in this process, such as lift and drag coefficients, momentum forces, or torque.

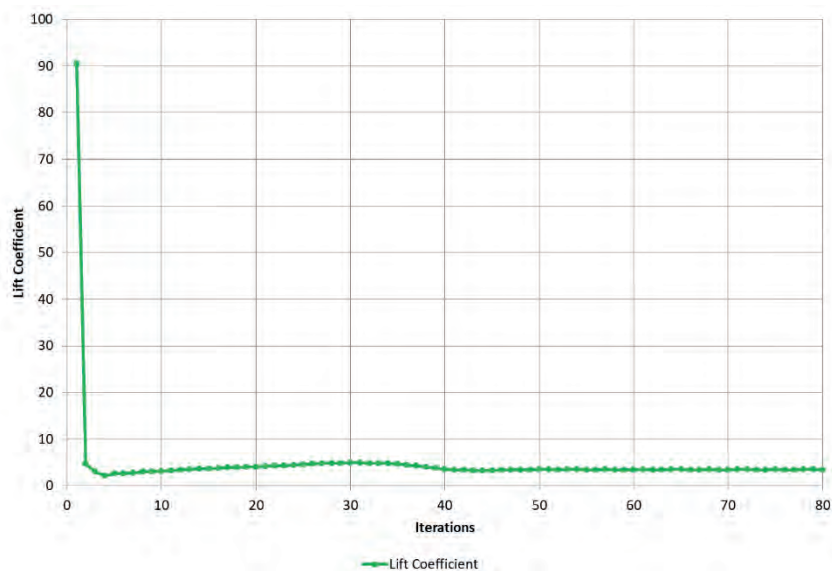


Figure 2.23 Lift coefficient convergence of the NACA 4415 aerodynamic airfoil.

In Figures 2.23 and 2.24, both the coefficient of lift and drag, respectively, and their convergence concerning the number of iterations are presented. In this case, the system convergence is reached in the 85<sup>th</sup> iteration.

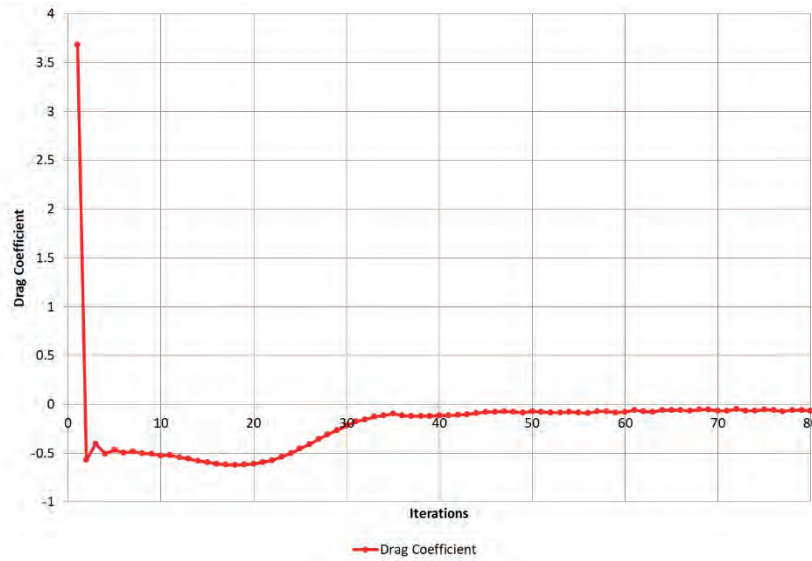


Figure 2.24 Drag coefficient convergence of NACA 4415 aerodynamic airfoil.

## 2.7.3 Post-processing - Results, reports, and visualization

### i) Post-processing

Figure 2.25 a) shows the current lines of the wind flow on the NACA 4415 profile, considering a laminar flow model, it can be appreciated that an unstable flow is obtained on the upper leakage edge, whereas, Figure 2.25 b) shows the current flow lines for the turbulent flow case. These current lines are parallel and subject to the aerodynamic profile, resulting in a stable current flow. Both simulations were obtained with the input parameters obtained from the Reynolds number equation:

$$Re = \frac{v\rho L}{\mu} \quad (3.5)$$

where  $Re$ , is the desired Reynolds number, which in this case is 100,000;  $v$  is the speed at which the aerodynamic profile is subjected;  $\rho$  the density of the fluid ( $\rho_{air} = 1.204 \text{ kg/m}^3$ );  $L$  is the line of the aerodynamic profile string being one meter and last;  $\mu$  which in this case is the viscosity of the fluid ( $\mu_{air} = 1.8 \times 10^{-5} \text{ Pa/s}$ ). The above results in a fluid velocity of 1.94 m/s.

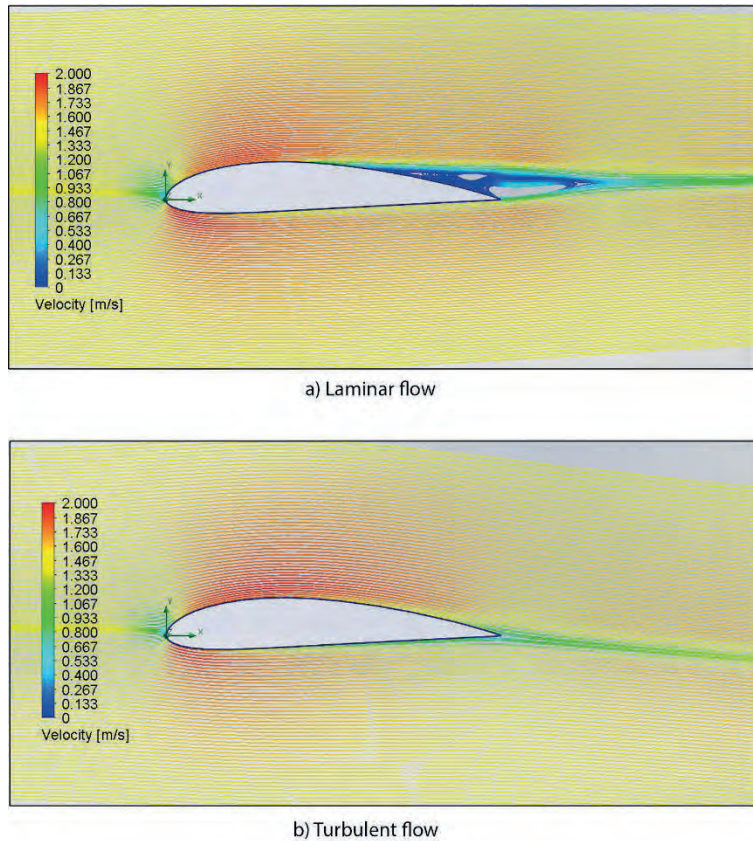


Figure 2.25 CFD simulation results of the aerodynamic profile of the NACA 4415 airfoil section.

By comparing both simulations of Figure 2.25 in a) and b), it can be observed that both laminar and turbulent flows are slightly different. In addition, this CFD analysis allows studying the physical differences between both flows with the same input conditions in detail, which, unlike a wind tunnel, would be difficult to reproduce. From these previous simulations, interesting concepts arise in the aerodynamics of the profile simulated by CFD. These are the lift and drag forces illustrated in Figure 2.26.

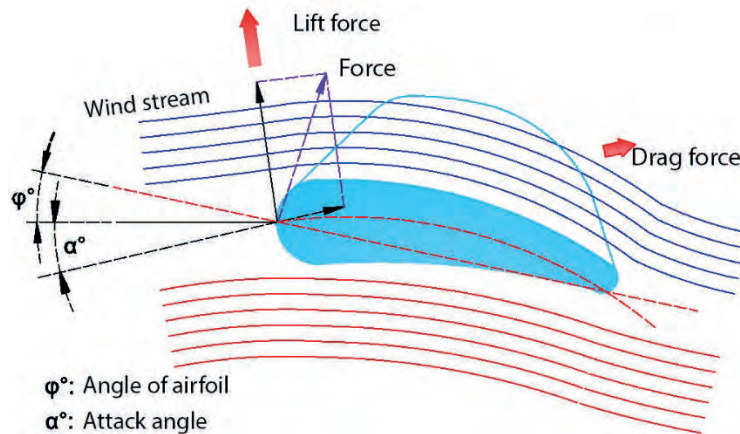


Figure 2.26 Lift and drag forces of an aerodynamic profile of a wind turbine.

Figure 2.27 represents a graph of the lift coefficient  $L_C$  from the CFD simulations results. Three lift coefficients can be observed: the green line for laminar flow, the blue line for turbulent flow, and the red line for a laminar and turbulent combined flow. All of them have the same Reynolds number ( $Re = 100,000$ ) and a turbulence factor of 12%. Note that this last type of flow represents a linear lift coefficient in relation to the attack angles.

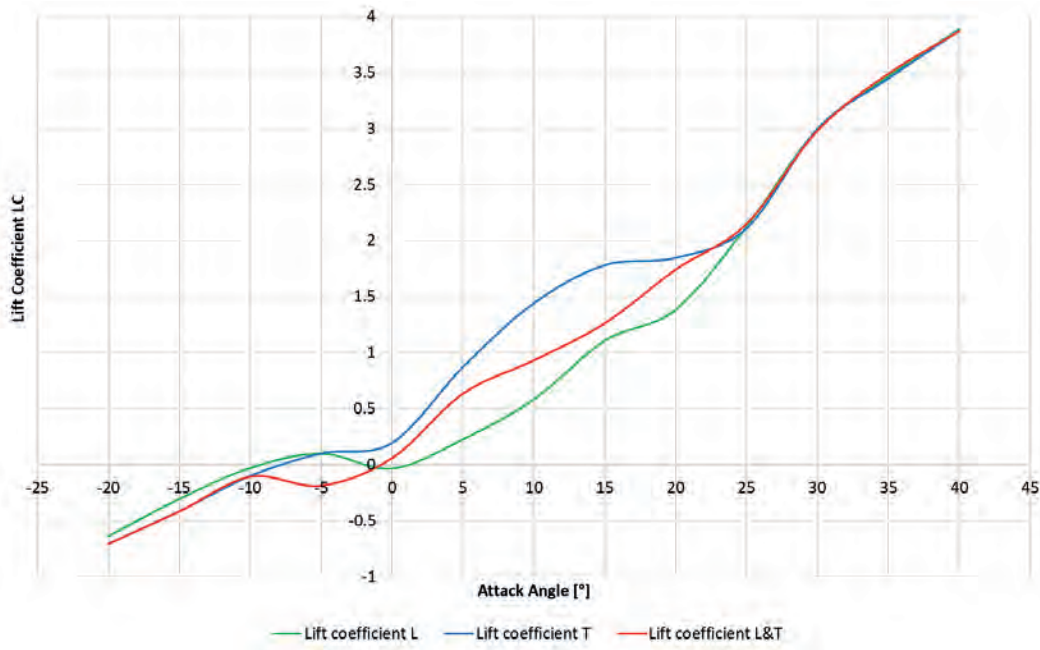


Figure 2.27 Lift coefficient compared to the attack angle for the NACA 4415 aerodynamic profile for laminar and turbulent flows.

On the other hand, Figure 2.28 represents a graph of the simulation where the drag coefficient  $D_C$  is shown as a function of the attack angle of the aerodynamic profile for different types of flow, with the same colored lines as Figure 2.27.

The lift coefficient and drag coefficient are respectively given by

$$L_c = \frac{2L}{\rho v^2 A} \quad (2.6)$$

$$D_c = \frac{2D}{\rho v^2 A} \quad (2.7)$$



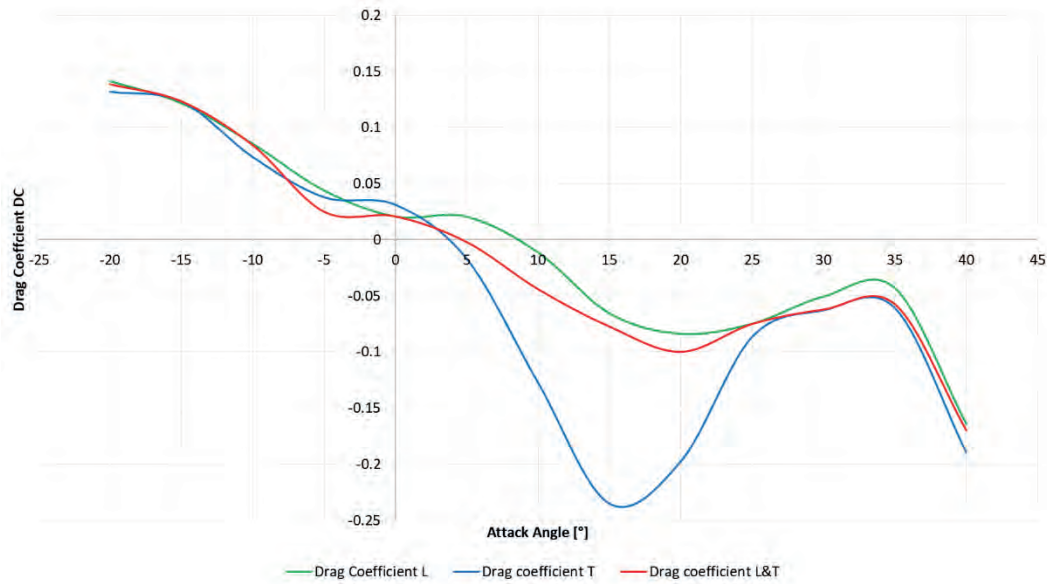


Figure 2.28 Drag coefficient against the attack angle for the NACA 4415 aerodynamic profile for laminar and turbulent flows.

where  $v$  is the wind speed on the aerodynamic surface of the blade;  $\rho$  is the density of the air;  $A$  is the surface of the blade;  $L_c$  is the lift coefficient and  $D_c$  is the drag coefficient.

Another aspect to consider is the distribution of pressure on the aerodynamic profile, which is a dimensionless parameter denoted by the pressure coefficient  $C_p$ :

$$C_p = \frac{P - P_0}{\frac{1}{2} \rho v_0^2} \quad (2.8)$$

where  $P$  is the static pressure at the point of interest;  $P_0$  refers to static free-flow pressure;  $v_0$  is the flow velocity and  $\rho$  the airflow density. The pressure distribution along the longitudinal section of the NACA 4415 aerodynamic profile could also be determined by the results of the simulations obtained by the CFD analysis. In Figure 2.29, the  $P_c$  pressure coefficient graph for the three flow types is shown: laminar, turbulent, and combined for an angle of attack of  $0^\circ$  and  $Re = 100,000$ .

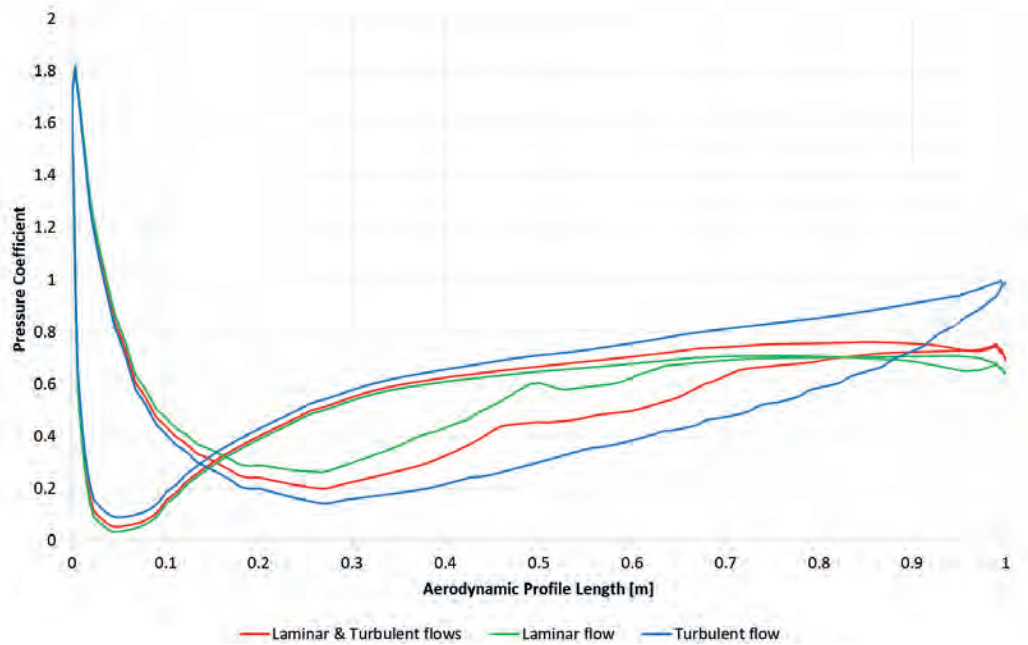


Figure 2.29 Pressure coefficient along the length of the aerodynamic profile NACA 4415.

Results show how CFD analysis can be of great help and how comparisons could be made with experimental simulations in a wind tunnel. CFD achieves the same results with greater efficiency at lower time and cost than traditional studies in wind tunnels. It can be said that CFD analysis plays a very important role as a design or research tool. For the present work, it is the fundamental tool for the optimization of the use of wind resource around urban and rural areas.

## 2.8 Computational Fluid Dynamics in wind energy engineering

The computational fluid dynamics has had an essential advance in the field of engineering and other sciences such as medicine, where it has been used for heart coronary diseases [59], [60], or the performance of artificial kidneys [61]. In relation to the use of CFD in wind energy applications, the analysis of the dispersion of pollutants in urban environments, both in external flows and in the bioclimatic design of buildings for internal flows, has benefited [6]. Other more recent studies about the application of CFD focus on the study of urban safety measures, demonstrating how safe and comfortable the wind is in the cities for the pedestrian, as presented in [9]. Another similar study focuses on the CFD analysis of the balconies of urban buildings and the effects of the wind at the pedestrian level [30], [62]. Another review related to the issue of pedestrian safety shows a CFD analysis with FLUENT software in the urban environment [63].

In the field of aerodynamic engineering regarding profiles with NACA nomenclature, several studies of these profiles have been performed, both in design and on their behavior in the lift and drag forces in two and three-dimensional simulations, previously analyzed by NREL in which the CFD analysis is used [64].

These advances have included CFD analysis in wind energy engineering. Although most focus on the aerodynamic analysis of both horizontal axis (HAWTs) and vertical axis wind turbines (VAWTs) and their performance using CFD analysis, others focus on the identification of devices installed in the wind turbine nacelle and their effects on them. These were also developed with FLUENT software [18].

Another review of the use of CFD in wind energy proposes a methodology for the simulation of wind conditions in open land for wind sites using FLUENT. This allows comparisons to be made of the turbulent flow models between Reynolds-averaged Navier-Stokes (RANS) and Large Eddy Simulations (LES) with the Monin-Obukhov's theory for determining of the wind speed profile [65].

In this sense, focusing on the estimation of the wind resource, revisions arise in which validations are made through other specialized commercial software for estimating the wind resource with CFD techniques, in this case, WindSim software. In this, comparisons are made between the vertical wind profile measurements with SODAR anemometers and their behavior in the modeling of complex terrain surfaces. Furthermore, it is mentioned that WindSim performs four different modeling techniques: meshing, nesting, sectoring, as well as climatology and weighting. However, WindSim presents some limitations when including obstacles like buildings and also has a low resolution in the development of wind resource maps [21].

Other works present comparisons between the different specialized software for CFD simulations in wind energy, as in this case: WAsP and MeteodynWT [66]. In [67], a case study related to the micro-siting wind turbines is presented, where a comparison of the finite differentiation method FDM is made against a CFD analysis, showing favorable results for the computational dynamics by using the ViziFlow software for two contiguous wind turbines.

By applying CFD for the installation of urban SWTs in [7], CFD is used for wind simulation around buildings. It is worth mentioning that this study is for the comfort of the pedestrian in the urban environment and not for determining the optimal positions of the wind turbines on the buildings. However, some aspects will be taken into account for the modeling in CFD, which could be applied to the present work.

Interesting work is done in [35], where the installation of vertical axis SWTs in urban areas using CFD is discussed, specifically in a small city in the center of Sicily, Italy. This article describes several CFD simulations, which use only four single wind directions of the case study.

Recent publications perform the use of CFD analysis, through the WAsP and ANSYS CFX software, in which a brief methodology is developed for the installation of wind turbines on buildings in an Australian community. In the model, a radius of 200 m is used, as well as a height of 200 m, which allows modeling the wind speed at this height and eight directions of the average wind speed. However, the case study showed, the optimal locations of the wind turbines on the building proposed are not discussed [38].

Other articles have emerged in recent years that are not only applied to open land wind sites, but also offshore sites, as in this case with a CFD analysis applied to large-scale wind turbines (LWTs) known as Floating Offshore Wind Turbine (FOWT), which use the NREL 5 MW and MARIN Stock Wind Turbine (MSWT) and their effects of the wind on them installed offshore,

where the power coefficient  $C_p$  and the thrust coefficient  $C_T$  are analyzed [20]. In addition, other studies arise for HAWTs, VAWTs, Buildings Integrated Wind Turbines (BIWTs), Buildings Augmentation Wind Turbines (BAWTs), and Building Mounted Wind Turbines in (BUWTs), as proposed to be studied in the present doctoral project [25], [68].

Another contribution is made in the estimation of the urban wind resource, taking into consideration the surface roughness layer, which is present in urban areas. In [26], several methods for estimating the urban wind resource are presented:

- The first of these are on-site measurements of wind speed. These measurements are made in three dimensions with the help of ultrasonic anemometers.
- The second is the tests carried out in controlled wind tunnels. These tests allow us to analyze the effects of wind turbulence on buildings, which is part of one of the activities of this research.
- The third method, which is the object of study of the present work, is the use of Computational Fluid Dynamics.

In the last 50 years, a large number of studies have been performed based on the CFD analysis of wind flow loads and their behavior in complex terrains. Regarding this, in a particular study of complex topographical terrains in [69] are performed CFD simulations in the Ria de Ferrol, Galicia Spain, at twelve different wind directions from, at 10 m above sea level. This study functions as a first approach for the wind resource assessment applied to the present methodology.

In particular, several publications talk about the application of CFD techniques in the field of wind energy, as well as comparisons of these techniques with wind tunnel analysis, observing the advantages and disadvantages that the CFD has over them [1]. These reviews and publications will support the development of this doctoral research. The present doctoral project allows taking advantage of the application of CFD analysis for the development of wind resource maps and the location of hot spots in an urban, academic, and rural complex.

### **2.8.1 Urban wind energy**

During the oil crisis of the 1970s, mini-wind technology emerged as an alternative to the generation of electricity, including devices connected to the electricity grid [70].

Later in the 1990s in the United States, SWTs were developed for particular applications, in the rural environment, such as for the water supply for homes that were not connected to national power grids [70]. In the first decades, the SWTs were used for power supply in remote areas. Sonner, these wind turbines disappeared because of the rural electrification that was carried out in that epoch.

The technology of small wind turbines in the last decade was growing despite the challenging market conditions; in countries such as China, the United Kingdom, and the United States, including the horizontal and the vertical axis configuration. In addition, the increasing number of companies around the world that manage the growing market emerged of both forms of application interconnected to the network and isolated from it [71],[72].

Different organisms establish the dimensions for small wind turbines. In accordance with the International Electrotechnical Commission (IEC) 61400-2 "Standard Design Requirements for Small Wind Turbines," the STWs are considered to have a power of 50 kW or less, with a rotor diameter of approximately 16 meters and a swept area less than 200 m<sup>2</sup>, and can generate a voltage below 1,000 V AC or 1,500 V DC [73], [74].

On the other hand, other organizations, such as the American Wind Energy Association (AWEA), define small wind turbines as devices with a nominal capacity of 100 kW or less [75]. However, the British Wind Energy Association (BWEA) stipulates that small wind turbines are those with a rated power below 50 kW, just to mention a few definitions stated by diverse organizations [76].

In order to resume the above size classification, in Table 2.3, the classification of small wind turbines is shown.

Table 2.3 Size classification of Small Wind Turbines (SWTs).

Wind Organization or Standard	Nominal Power & Size
American Wind Energy Association (AWEA)	Nominal Power of 100 kW and less
	<ul style="list-style-type: none"> <li>Residential Systems: 1kW to 10 kW</li> <li>Commercial Systems: 21 kW to 100 kW</li> </ul>
British Wind Energy Association (BWEA)	Nominal Power < 50 kW
	<ul style="list-style-type: none"> <li>Micro-wind turbines: Diameter of rotor less than 2.1 m (swept area less than 3.5 m<sup>2</sup>), being either independent or mounted on the side or upper part of the attached building, generally mounted from 3 m to 4 m above the ridgeline of the top of the building or up to 16 m for free systems.</li> <li>Small wind turbines: diameter of rotor greater than 2.1 m (a swept area greater than 3.5 m<sup>2</sup>), most of them in free configuration, reaching more than 30 m of total height.</li> </ul>
German Wind Energy Association (BWE)	Nominal Power up to 100 kW
IEC 61400-2	Rotor swept area smaller than 200 m <sup>2</sup> , generating a voltage below 1000 V AC or 1500 V DC.
	<ul style="list-style-type: none"> <li>For turbines with a rotor swept area smaller than 2 m<sup>2</sup>, the tower is not considered as part of the design.</li> <li>For turbines with a rotor swept area greater than or equal to 40 m<sup>2</sup>.</li> </ul>

According to the World Wind Energy Association (WWEA), the market for small wind turbines in the world has grown: in 2015 there were around 990,000 small wind turbines installed in the world, which represented an increase of 5% compared with 8% in 2014, with a total installed capacity of 948 MW [71], [72]. The total number of small wind turbines installed at the end of 2015 is shown in Figure 2.30 [72].

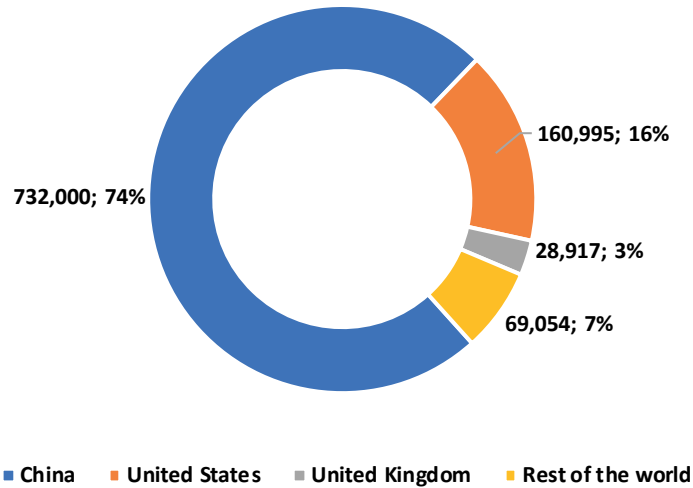


Figure 2.30 Total small wind turbines installed worldwide (2017).

The WWEA itself foresees that the total installed capacity of small generation wind power will reach almost 1.9 GW by 2020. Small wind turbines are defined as belonging to the range of nominal capacity up to 100 kW. To date, around 330 manufacturers of such turbines have been identified in 40 countries, including China, the United States, the United Kingdom, Canada, and Germany, where more than 50% of small wind power turbine producers are concentrated [72].

There are different types of configurations for the installation of small wind turbines in urban areas. The following configurations are highlighted.

**Building-Mounted Wind Turbines (BUWTs):** They are also called roof-mounted wind turbines; as their name says, they are wind turbines physically attached to the structure of the building. The building is used as a tower to install the system in a flow of desirable wind flow. Whatever the type of wind turbine installed on the buildings used, the structure must be capable of supporting the turbines in terms of load, noise, and vibration [3], [77].

**Building-Integrated Wind Turbines (BIWTs):** This configuration is designed from the planning or the design of the building with the wind requirements considered. Design and construction practices are taken into consideration, as are the energy costs and the environment for sustainable construction [23], [24], [77].

**Building-Augmented Wind Turbines (BAWTs):** These can be defined as those buildings in which the wind turbines were integrated into the building, which was modified to increase the wind flow in the turbine through a vortex structure. This modification can even be from the design of the building. These modifications are specifically for increasing the flow through the turbines [25], [27], [77], [78].

**Building-Environment Wind Turbines (BEWTs):** These wind turbines can be incorporated in an urban environment, without the need to place them on buildings; otherwise, the small wind turbine's tower is used to locate them in spaces of common areas or areas destined for a particular wind project within an urban or rural environment [79].

These small wind turbines installed on buildings can take many forms. These options are considered to take advantage of the wind streams, which are described below and observed in Figure 2.31.

*A) At the top of the buildings.-* This option allows taking advantage of accessing the highest quality winds because of the height. This wind has a relatively high energy content and less turbulence.

*B) In the upper part of rounded buildings.-* In this type of configuration, because of the height of the building, the wind quality is better and has an acceleration of 15% for the local wind caused by the rounded shape of the building.

*C) A concentrator in the upper part of the rounded building.-* In this type, the wind turbine can operate bidirectionally, increasing the acceleration of the wind speed by 20%.

*D) Square concentrator inside the facade of buildings.-* This configuration of wind turbines with an increase in buildings consider a local wind acceleration for the whole direction by 25%. However, this option requires much space for its construction and design.

*E) Circular concentrator on the façade of buildings.-* This configuration is similar to the square concentrator, but it is a cylindrical shape. These wind turbines present an increment in the local acceleration for the wind of uniform direction by 35%. This type can achieve a 50% increase for bidirectional winds.

*F) On the sides of the buildings.-* This configuration allows installing VAWT on the side of the building. The swept area can be maximized by using several wind turbines, and the building itself must be acoustically and thermally insulated.

*G) Between forms of multiple buildings.-* Architectural forms are possible when using this type of configuration. This allows the capacity of wind turbines to increase about 10% extra energy compared with a normal wind turbine.

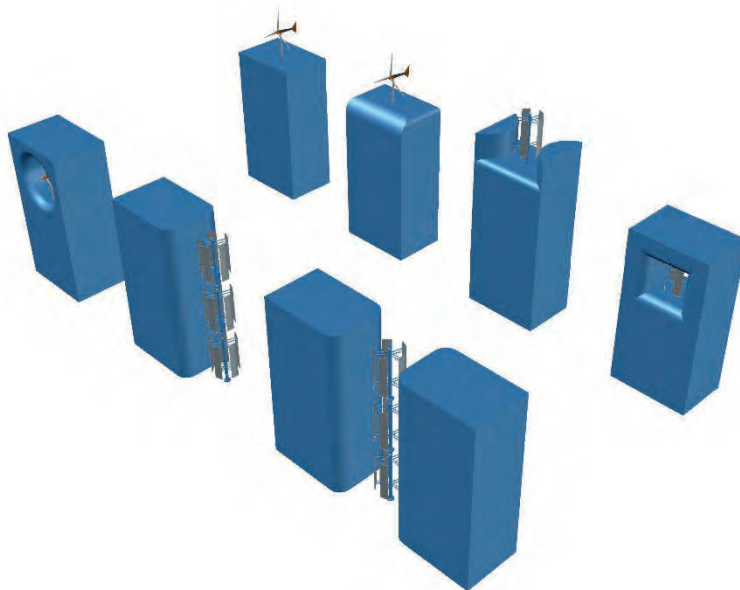


Figure 2.31 CAD models of the building wind turbines configurations.

According to the wind market, there is a wide variety of small wind turbines, which can be studied in the development of the methodology proposed in this project. In this sense, it is necessary to make a market study for determining which wind turbine is the best option for the wind project.

On the other hand, the economic benefit in kW/hr by reducing the electricity bill, together with the environmental benefit and the evaluation of the impact on the electricity grid, especially on the distribution side, can be useful in the development of smart grids, both in urban and rural areas.

Among the main problems that involve the use of low-power wind turbines in the urban and rural environment are the following: noise, aesthetics, integration in architectural systems, and the efficient use of the available wind resource [80]. The main disadvantages of these types of wind sites are the low wind speeds and the high intensity of turbulence, which are the main research tasks today [28].

In addition to the scarcity of tools for improvement, for the realization of feasibility studies in the implementation of small wind turbines in urban and rural areas, including novel techniques for optimizing the use of wind resources, it is one of the basic needs that will be addressed in the next chapter.

Based on the specific tasks required in Task 27 by the International Energy Agency (IEA) [43], it is considered necessary to formulate and recommended practices for the location and evaluation of the wind resource in places of high turbulence such as urban and rural areas using low power wind generation technology. Current approaches include wind tunnel analysis, micrometeorology, and computational fluid dynamics studies.

The fundamental part is to provide a solution to this task by using the CFD as a tool within a methodology to help the installation of small wind turbines. This will present advantages compared with traditional techniques such as wind tunnels.

The industry of small wind turbines has been in continuous growth around the world to a large extent. Currently, the development of technologies that make feasible the use of the available wind resource in urban and rural areas is remarkable. However, it is necessary to develop new tools that allow the optimal use of wind resource with small wind turbines, both in rural and urban areas.

When applying techniques, in this case, CFD analysis, compared to other technologies, the CFD reduces the costs of feasibility studies, which will encourage the application of SWTs and more than justifies research in this field. In particular, it is expected that the methodology to be obtained will replace or complement the modeling in wind tunnels, which is widely in the scientific and engineering community. It should be noted that the disadvantage of wind tunnel modeling, requires the construction of physical models of the sites to be studied, as well as the use of specialized equipment and equipped facilities of large dimensions, of which not many universities or institutions can provide.

The wind tunnel tests are representative of real-world situations when modeling the characteristics of the atmosphere, but with disadvantages, such as the performance of wind tunnels because of cost, few measurement variables, and monochromatic results, etc.



Therefore, it is justifiable that innovative methodologies that permit an economic study and efficient use of the wind resource be studied and developed. Such is the case of the present chapter, which will allow this objective to be applied to sites of interest both in the urban and rural environments, which can optimize from a cost-benefit and environmental point of view of the low power wind sites.

## **2.9 Turbulence models in the CFD analysis**

### **2.9.1 A general overview of numerical approaches of CFD**

The numerical approaches to turbulent flow analysis can be divided into two groups: first, the simulations, and the second the modeled. Within the groups of the simulations, current flow visualization is calculated: the behavior of the fluid is simulated within an environment. The methods of this group are the Direct Numerical Simulation (DNS) and the Large Eddy Simulations (LES) [52]. The hierarchy of the turbulence model is shown in Appendix B.

The DNS method gives a solution to the Navier-Stokes equations, without modifications or assumptions of modeling. The result is a complete picture of the evolution of the fluid, dependent on time. One of this method's disadvantages is that in the case of turbulent flows, where an accurate approximation of the flow on a small scales is required, it leads to a large unrealistic computational mesh, which results in a non-effective simulation [52].

The LES method allows solving the equations, so spatially filtered variables represent a time-dependent behavior of the flow characteristics with a large and moderate length scale.

The effects of small-scale fluctuations appear in the form of additional terms of the equations, which cannot be calculated directly and must be replaced by modeling approaches or models.

On the other hand, in the modeling group, the current display of the flows is not calculated. The problem instead incurs a system of equations for averaged flow quantities, such as average velocity and pressure, as well as Reynolds tensions, among others. This allows for obtaining the characteristics of the fluid. This approach is called the method of the Reynolds-averaged Navier-Stokes equations (RANS) [52].

### **2.9.2 Direct Numerical Simulation (DNS)**

The DNS method is the most straightforward approach of all turbulence models in CFD analysis. This appeared in the year of 1972, shown by Orszag and Patterson [52]. It can be said that it is the most precise approach in the simulation of turbulence because it gives a solution to the Navier-Stokes equations without averaging or approximating the discrete numerical values, which have errors that can be estimated and controlled [81]. The methods used for discretization are shown in Appendix B.

Among the considerations to take into account is that the domain where the computational work is developed must be at least as large as the physical domain to be able to consider the large flows of turbulence.

The direct numerical simulation allows simulating, only flows with a low Reynolds number and geometrically simple domains. On the other hand, it is also possible, thanks to the computational advance, to perform turbulent flow studies with Reynolds numbers in the order of hundreds [81].

It also obtains detailed information about the flows studied, such as speed, pressure, and other variables of interest in a significant number of points of the mesh or network. These results can be studied to produce statistical information or create numerical visualization graphs.

### 2.9.3 Large Eddy Simulation (LES)

This model of turbulence used in computational fluid dynamics can be applied to engineering applications, such as combustion, acoustics, and simulations of the atmospheric boundary layer. It was proposed in 1963 by Joseph Smagorinsky for simulating atmospheric air currents [81].

The turbulent flows characterized by the abovementioned DNS model allows showing that these flows have a variation in the spatial and temporal scales. In this sense, the model that makes the simulations of large eddies called Large Eddy Simulation (LES) arises. In Figure 2.32, the focus of these two models is represented: both the DNS and the LES, in relation to the spatial scale.

Compared with Direct Numerical Simulation, LES is a computationally more economical model, and therefore the cost allows simulations of practical engineering systems with complex geometries or configurations of complex flows, such as aircraft, vehicles, and missiles [82].

This LES model ignores the small scales of turbulent flows, which are more computationally expensive to solve. This model allows reducing computational cost. This is done with a low pass filter of the Navier-Stokes equations. A recent research area focuses on the small scale of turbulent flows, thus addressing problems such as reaction flows, multiphase flows, and flows near the boundary walls [82]. In contrast to the DNS model, LES allows solutions to flows where the Reynolds number is very high, or the geometry of the model is too complex to allow the application of the DNS model.

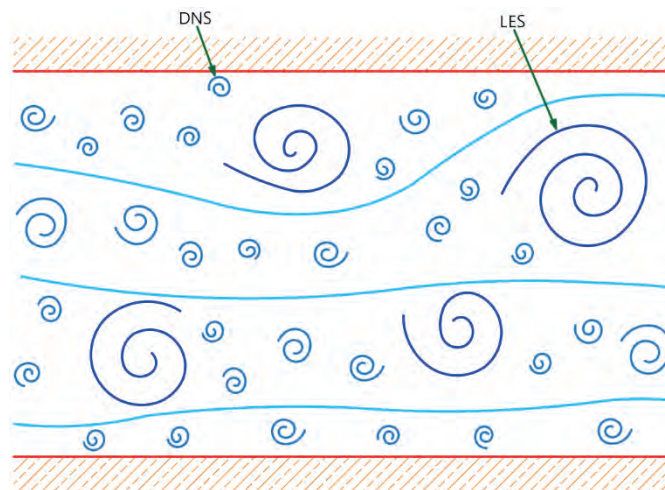


Figure 2.32 Difference between the LES and DNS models, on a spatial scale.

## 2.9.4 Reynolds Averaged Navier-Stokes (RANS) model

This approach was proposed by Reynolds in 1895, which is based on the decomposition of the flow variables into an average value. The RANS method is one of the first to appear and remains a practical first-use tool for CFD analysis cases, as well as widely used for the calculation of industrial flows. Among the advantages of this method are its relative simplicity and modeling in all the spatial scales of turbulent flows, its low computational cost compared with the DNS and LES methods, as well as its significant experience in the application of different types of turbulent flows. On the other hand, some of the disadvantages of the RANS method are that there is no information available beyond the characteristics of the flow, as well as that present a modeling error in the considerable turbulent flows [52].

Two considerations must be taken into account when the RANS model is going to be applied:

1. Consider the way in which the model captures the physical flow.
2. The precision of the quantitative predictions obtained in the analysis.

The RANS model is averaged equations of the flow movement of turbulent fluids. These equations, including the Reynolds stress tensor  $\tau_{ij}$ , can be used with approximations based on the turbulent flow properties, with solutions that can be given to the Navier-Stokes equations with precision.

# CHAPTER 3



---

## ADVANCED METHODOLOGY FOR FEASIBILITY STUDIES ON BUILDING-MOUNTED WIND TURBINE INSTALLATION IN AN URBAN ENVIRONMENT: APPLYING CFD ANALYSIS

---

At present, it has been estimated that there is great potential for wind resource in the world. In this sense, Mexico is one of the most potential areas in the world, specifically in the state of Oaxaca. However, there are also other areas distributed throughout the country with great potential, such as Zacatecas, Tamaulipas, and Baja California Norte, only to mention some of the Mexican states with this available resource. From this estimated wind potential in these regions, it has been predicted that the wind resource can also be used in urban areas for the reduction in electricity consumption, as well as in rural areas outside the National Electric System, as a means for their electrification. Therefore, tools that allow extending or help to increase the use of the wind resource are required, relying on novel CFD analysis techniques that allow the increment of the cost-benefit when implementing low power wind projects.

Considering a methodology that uses both the CFD analysis and an efficiency study of small wind turbines can be a useful tool for maximizing the use of the wind resource in urban and rural areas and solving these issues. In this context, this chapter's content is based on the published article "Advanced methodology for feasibility studies on building-mounted wind turbines installation in urban environment: Applying CFD analysis," where the methodology was systematically integrated and is only complemented with the following sections that give a detailed view of the methodology developed.

### 3.1 Size domains definition for the CFD simulations

From the point of view of the CFD solution process, it is necessary to define the problem of the implementation of the CFD techniques in the study area of wind energy by applying CFD analysis. Some main issues arise, which include the selection and location of the site, the selection of the wind turbine model, and including also the evaluation of wind potential. It is, therefore, convenient to propose some definitions to conceptualize the size domains.

The definitions of the domains that will be used in the methodology will allow understanding and facilitating the process of the same. The following domains are used in the proposed methodology, as well as in the CFD simulations.

**Domain of the Site.-** This includes the space of the land or place for implementing the low generation wind project, within the urban or rural environment. It is understood as the geographic and topographic location within a radius of 500 m from the interest zone. This domain of the site will be generated from databases of topographic maps.

**Domain of the Complex or Zone.-** It refers to the sizing and modeling in CAD of the geographical areas, including structures or buildings where the low power wind project will be implemented. This allows delimiting the spaces that will influence the wind resource directly on the structures or buildings to be selected and obtain the maximum potential of the wind resource. This domain is also part of the macro-siting (MS) dimensioning.

**Domain of the Structure or Building.-** This domain is based on the CAD modeling of the structure or selected building, where the low power wind project will be implemented. This allows delimiting the flows of the wind resource that will directly influence the structure or building selected from the previous CFD simulations of both the site and the complex domains, for the optimal use of the wind resource. This domain is part of the micro-siting ( $\mu$ S).

**Domain of the SWT.-** It includes the modeling in CAD and its respective CFD simulation of the selected wind turbine, based on the available space of the proposed structure or building and the market study performed, to obtain its correct installation.

**Domain of the Arrangement of the Structure or Building - SWTs.-** This domain is the modeling of the CAD arrangement of the building or structure with the SWT and will be selected based on the results of the CFD simulations of the MS,  $\mu$ S, and SWT. This domain is part of the micro-siting SWTs ( $\mu$ S-SWTs).

In order to specify the terms that will be used to determine the sites of interest within the methodology, Figure 3.1 shows the general view of the size domains for the proposed methodology.

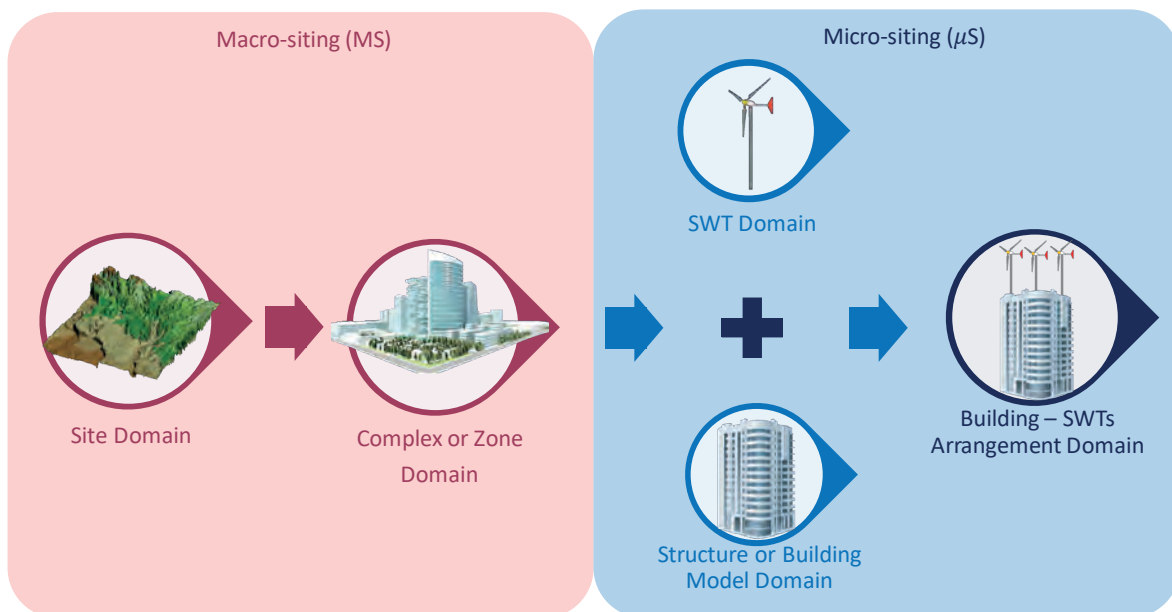


Figure 3.1 Size domain definition for the CFD simulations.

## 3.2 Model selection of the small wind turbines

Another issue to be solved is that in the market, multiple varieties of SWTs exist, from which the consumer can choose the right one for the type of application and the energy consumption that it is required. Small wind turbines have some advantages, including the following: they permit the supply of electrical energy in isolated and remote places away from the electrical grid, they generate energy in a distributed way, reducing the losses of transport and distribution, and they can be combined with photovoltaic modules or other technology like fuel cells in hybrid installations.

Within the proposed methodology presented here, the selection of the proper SWTs is necessary based on the conditions of the interest site selected and the availability of the wind turbines in the world and Mexico. In this context, the three-dimensional modeling of cited wind turbines and their respective CFD simulations can be developed. It is important to mention that these CFD simulations will only serve as a reference for the location of wind turbines and not for aerodynamic performance tests of them.

The work performed during the stages of the methodology includes the selection and modeling of small wind turbines. This selection was made based on the market availability of the SWTs, as well as the available information on the technical characteristics of the wind turbines themselves. The selection of SWTs includes the configurations for both horizontal axis wind turbines (HAWT) and vertical axis wind turbines (VAWT), in order to study the behavior in the urban and rural environments of both configurations.

As initially established in the scope of the doctoral project, the analysis of the aerodynamic study of SWTs is beyond the scope of the research project. The analysis performed in CFD of the small wind turbines is properly in terms of their behavior when subjected to the nominal wind speeds in two conditions, in a steady-state and rotational-state, for analyzing the wind wake regeneration and thus determining the possible matrix arrangements and their correct location in the case studies presented. It should be mentioned that for the steady-state simulations, the rotating region is not included in the CFD study.

The small wind turbines from the international market to be compared will be selected according to the wind resource assessment of case studies, the CFD simulation results, the diameter size according to the available space on the building's rooftop, and the availability and possibility of acquiring the SWTs in Mexico. The first company considered for providing the wind turbines for the small wind project is an American company named as Bergey Wind Power.

The Excel 10 kW wind turbine of Bergey Wind Power, a company with more than 30 years in the wind market, is one of the wind turbine models selected for the feasibility study of the small wind project. This wind turbine has a rated wind power of 8.9 kW, a cut-in wind speed of 2.5 m/s, and 7 m of rotor diameter [83].

Another selected company, dedicated to producing small wind turbines is XZERES Wind. This company provides a wind model called Skystream 3.7, which has a rated power of 2.6 kW at 13 m/s, a rotor diameter of 3.7 m, and a cut-in speed of 3.2 m/s [84]. The last SWTs selected were the Aeolos V-5 and Aeolos V-10, with a rated power of 5 kW and 10 kW, and rotor diameters of 4.2 m and 5.5 m, respectively.

Table 3.1 shows the main operating technical specifications of the wind turbine models for the CFD study.

Table 3.1 Technical specifications of the operation of selected SWTs.

SWTs	Type	Nominal power	Rotor diameter	Tower & Rotor heights	Cut in speed	Cut out speed	Nominal RPM
					[m/s]		
Bergey Excel	HAWT	10 kW @ 12 m/s	7.0 m	18 m & -	2.5	60	400 rpm
XZERES Skystream	HAWT	2.6 kW @ 13 m/s	3.7 m	10 m & -	3.2	63	325 rpm
Aeolos V-10	VAWT - Daerrius	10 kW @ 11 m/s	5.5 m	18 m & 6 m	2.5	52.5	150 rpm
Aeolos V-5	VAWT - Helical	5 kW @ 11 m/s	4.2 m	18 m & 5 m	2.8	50	100 rpm

Not only are the abovementioned characteristics important, but the power curve is another key factor that must be considered for having an overview of the performance of any wind turbine. This power curve is different from each wind speed and every wind turbine, and with this power curve, it is possible to predict the energy production of the wind turbines by considering the technical details of their components.

The comparison between the power curves of the selected wind turbines is shown in Figure 3.2. Among the main features that are immersed in the power curve are the cut-in and the cut-out speeds, as well as the maximum output power that the SWTs can generate.

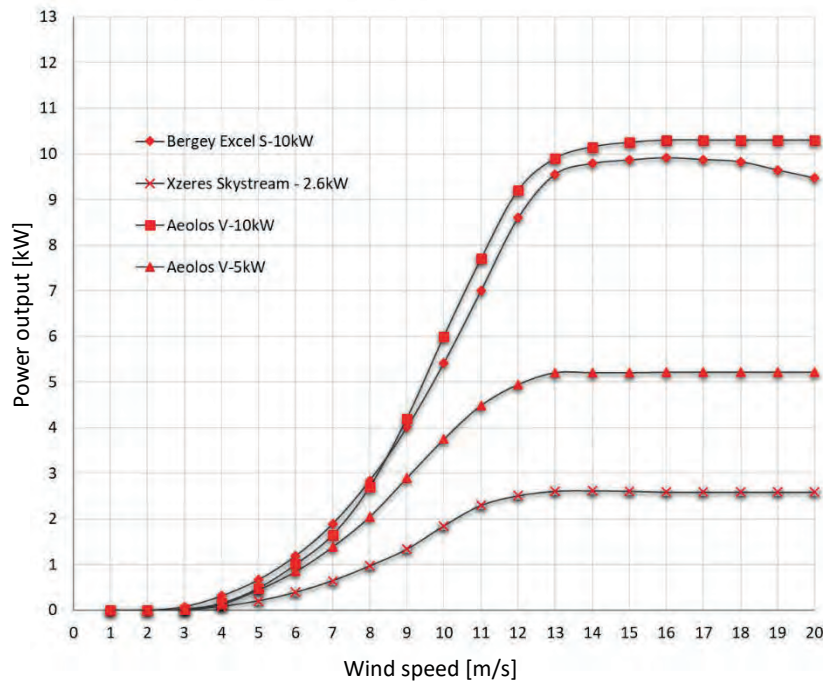


Figure 3.2 Power curves of the selected small wind turbines.

### 3.3 CAD modeling of the proposed small wind turbines

By considering the technical data sheets available, as well as images of the selected wind turbines, the three-dimensional models in CAD tools have been developed. These models will later be incorporated in the model of the buildings of the proposed case studies for their correct location. It is worth mentioning that the aerodynamic profile used for these models corresponds to the NACA 63415 profile for homogenizing the models because this information from manufactures is in confidential treatment.

One of the advantages in this stage of the methodology proposed, and with respect to the use of CAD modeling, is that the models of SWTs can be improved to change the settings of the airfoil for improving the performance of the wind turbines. These models will permit the development of matrix arrangements of small wind turbines for the proper installation in the further case studies to be proposed. In further sections, these models will be used for their implementation in the Stage 5 CFD analysis of the methodology proposed.

Figure 3.3 shows the three-dimensional models developed from the four wind turbines selected, which will serve as the basis for the analysis of CFD in steady-state and rotational-state simulations.

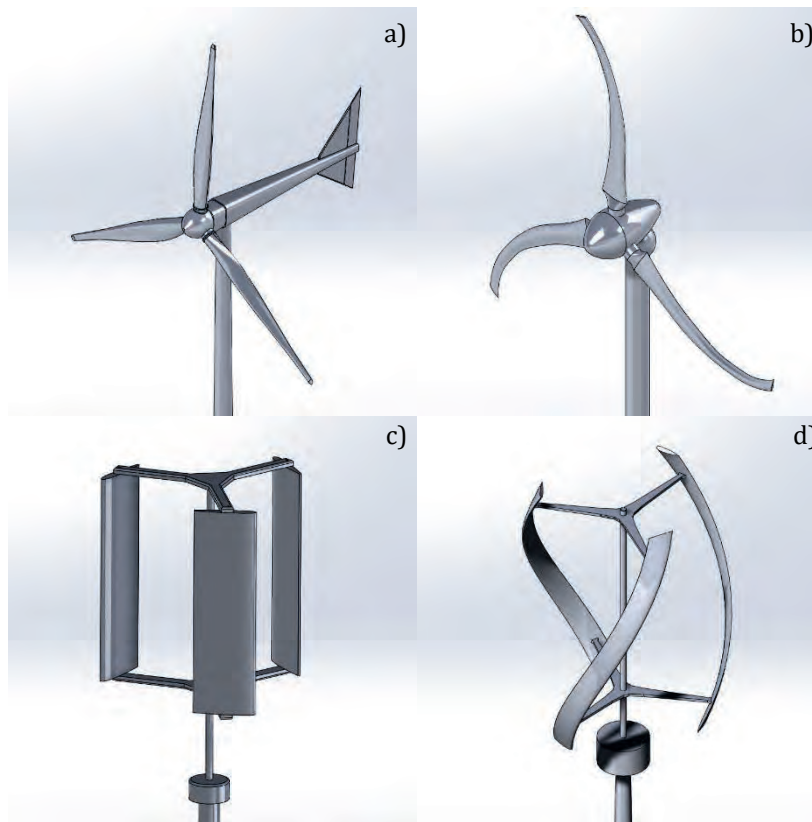


Figure 3.3 3D CAD models of selected wind turbines: a) Bergey Excel 10 kW, b) XZERES Skystream 2.6kW, c) Aeolos V-10 kW and d) Aeolos V-5 kW



### 3.4 General description of the methodology proposed

In general terms, the proposed methodology that is intended to be followed for the development of low power wind sites, including the optimization of the use of wind resource, performing the analysis of computational fluid dynamics in the urban and rural environment, is summarized in the stages shown in Figure 3.4. This methodology proposes a better approach in the development of this type of wind projects, which reduces the time and cost in feasibility studies, according to the IEA in its Task 27.

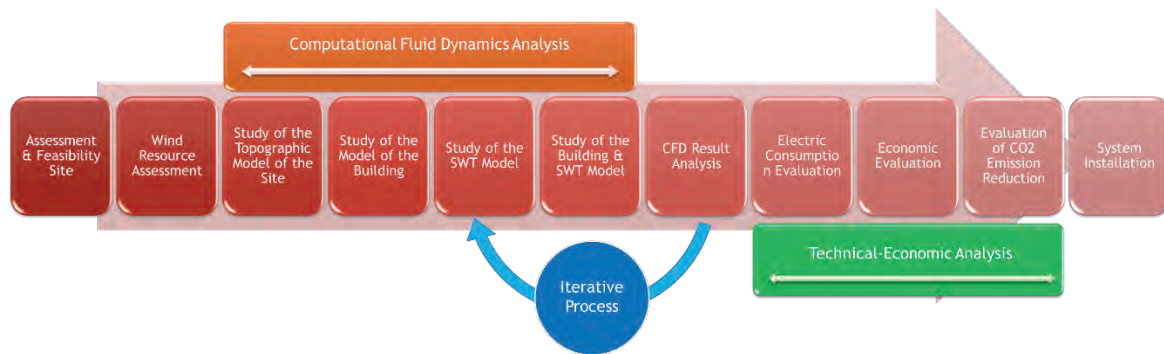


Figure 3.4 Proposed methodology for the optimization of the use of wind resource by applying CFD analysis.

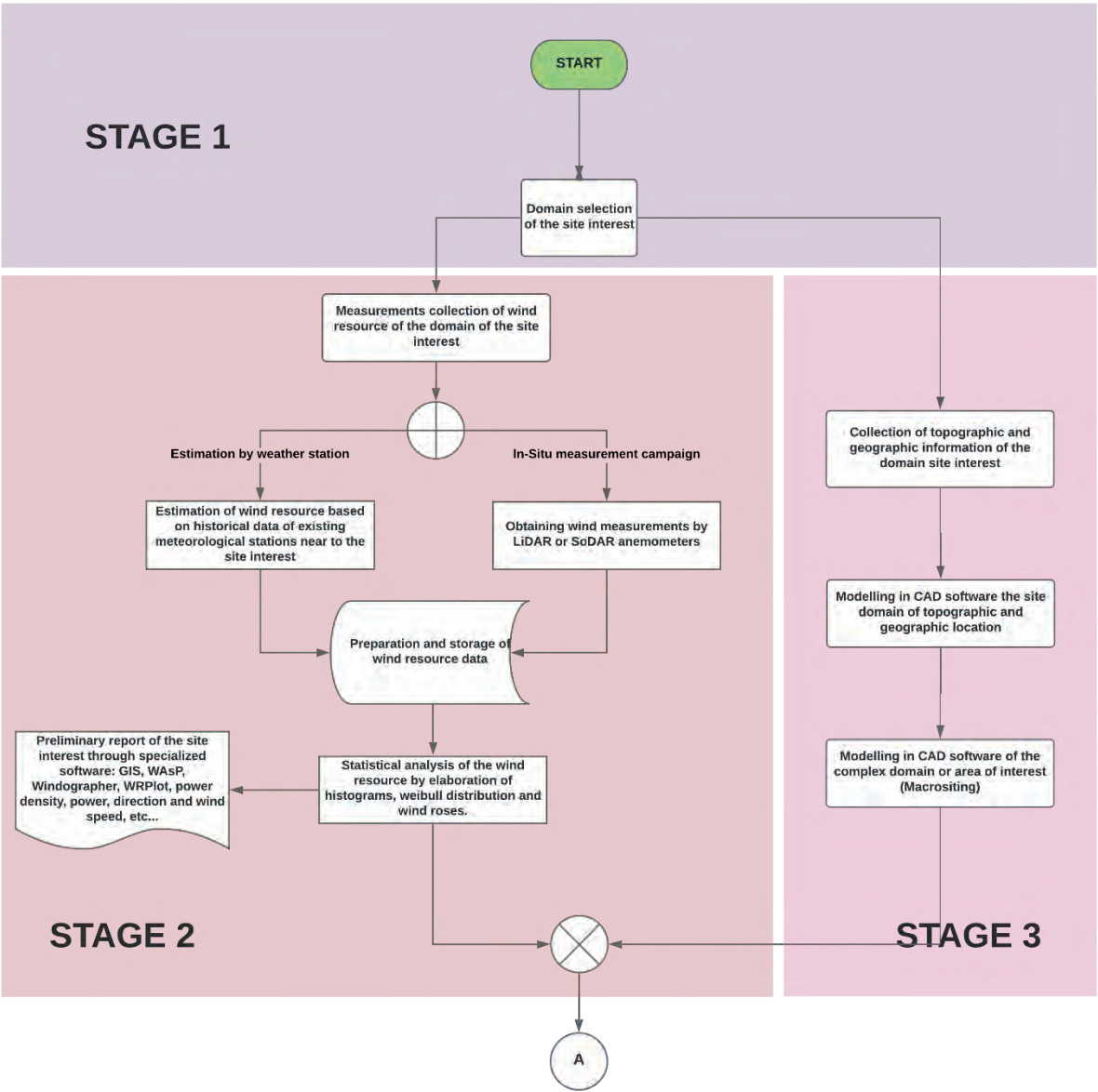
According to the general scheme shown in Figure 3.4 and the size domain definitions, the first stage of the methodology is to delimit the site domain of the project location and the domain of the complex or zone, to estimate the project site’s feasibility. Subsequently, to develop a study of the wind potential of the area of interest are considered the wind resource maps, wind resource databases, wind speed profiles, and wind roses.

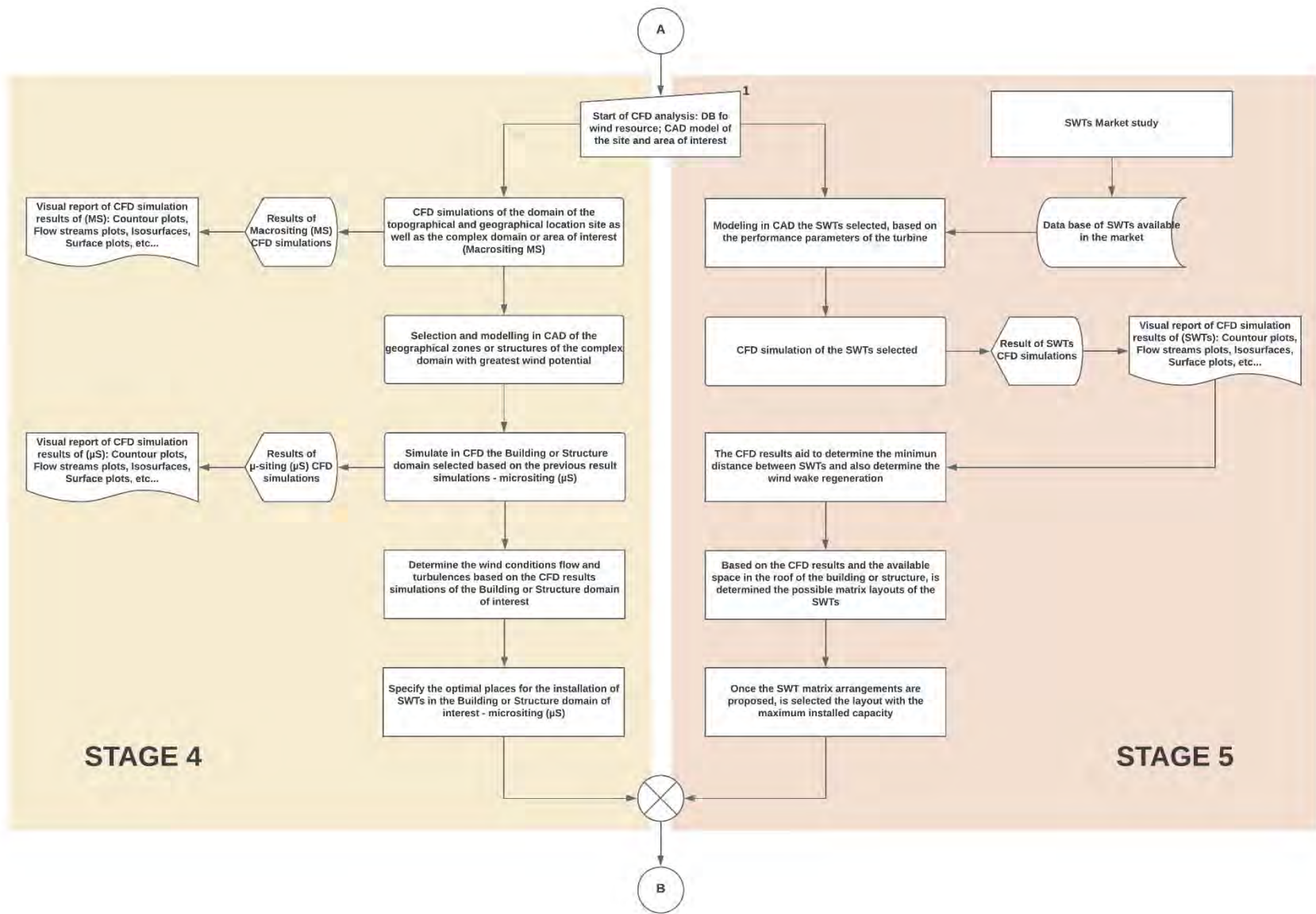
After the site is selected, a conventional wind resource assessment is performed, using statistical and historical data from on-site measurements, which will serve as input parameters for developing the CFD simulations.

The next step is the CFD analysis, which includes four phases: *i)* the evaluation of the site, *ii)* the study of the structure of the building of interest, *iii)* the study of the SWT and *iv)* the study of the Building-SWT arrangement. In these steps, the three-dimensional models of the **Domain of the Site** and the **Domain of the Complex** are developed, including the buildings and the surrounding areas of interest for CFD analysis. This analysis will allow selecting the type of SWT to be installed.

After selecting the type of SWT, it will be subject to performance studies using CFD analysis. Finally, the models that correspond to the **Domain of the Arrangement of the Structure or Building – SWTs** are developed. It comprises the building and the appropriate SWTs. The results of this final analysis using the integral model will define the viability of the project in terms of technical performance.

Figure 3.5 shows the methodology in a flow diagram, showing the steps to follow for optimizing the use of the wind resource by applying CFD computational fluid dynamics analysis for the installation of SWTs. Within the seven stages, certain activities that structure this methodology to be implemented in the case studies for the urban and rural environments can be developed in a parallel process in some cases, as is depicted.





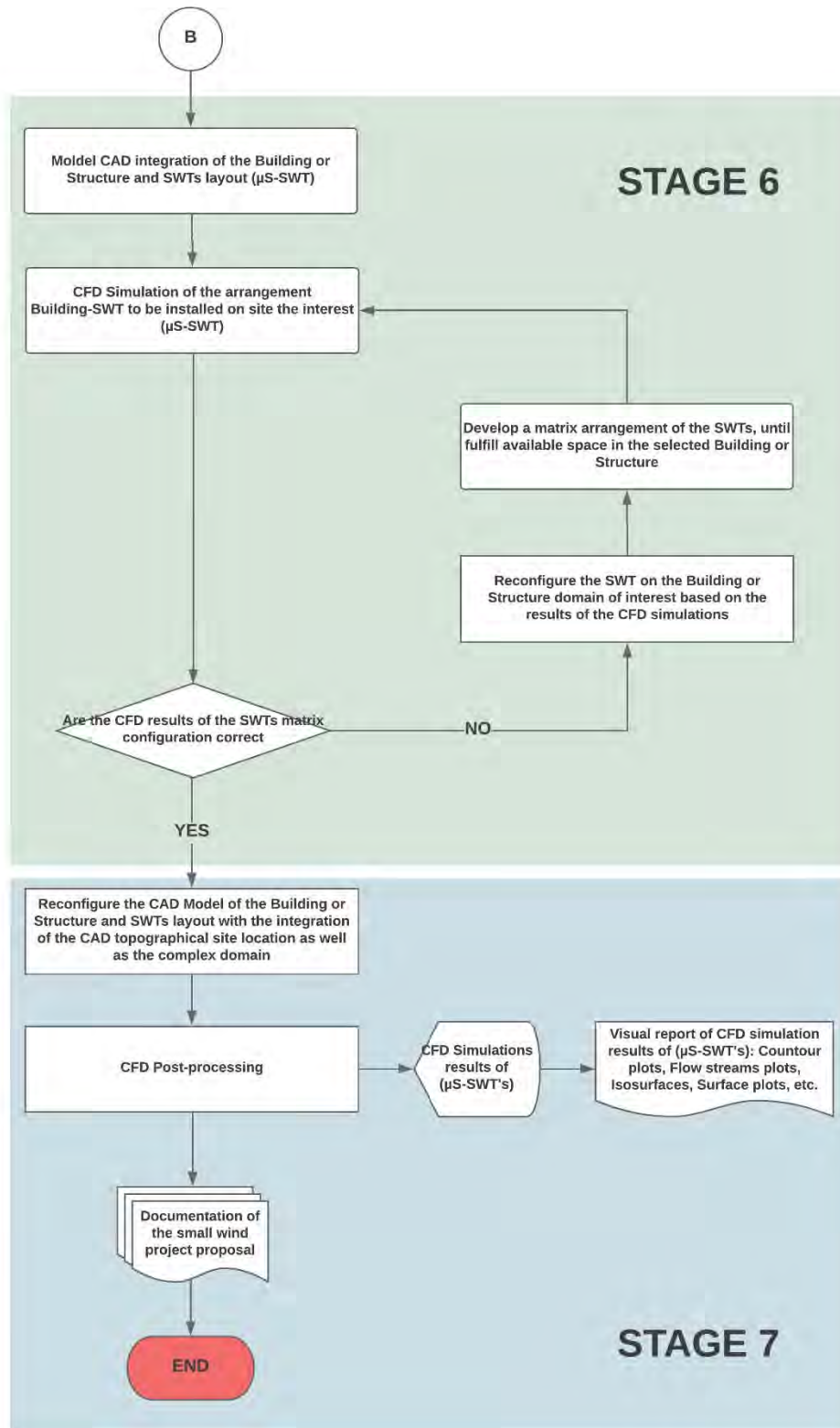


Figure 3.5 Flow diagram of the proposed methodology for the optimization of wind resource use applying CFD analysis for urban and rural areas.

In the following section, the seven stages will be described in detail. Note that the last steps of the proposed methodology are the technical-economic evaluations, which include the following: the evaluation of the electrical consumption, the economic evaluation, and the CO<sub>2</sub> emissions reduction evaluation. It should be noted that these technical-economic evaluations will be outside the scope of the present doctoral project.

### 3.4.1 Site selection and feasibility - Stage 1

In Stage 1, referring to the evaluation and selection of the domain of the site of interest, a preliminary study is necessary, based on the observation of the urban or rural environment. This visual inspection of indicators or physical evidence, as well as surveys, will allow the determination and estimation of areas with wind potential, leading to the feasibility of exploiting the existing wind resource. These parameters to be taken into account can be divided into two types, based on what is shown in [85].

- Geological Indicators.- These are based on the erosion produced by the wind in the geographical environment and can be observed on hills, slopes, or rugged coastlines. This type of erosion arises from the continuous wind in the same direction and the intensity of the wind.
- Ecological Indicators.- These are based on the erosion produced by the wind in the environment of the vegetation and include foliage, shrubs, and trees deformed by the intensity of the wind, which allows determining the wind's speed and direction. These indicators are represented in the Griggs-Putnam scale, shown in Figure 3.6, which can be used to estimate the wind speed based on the deformation presented by the trees according to the ecological signs visible in a certain area. This way of estimating the wind resource is known as flagging or the flag effect. [85], [86].

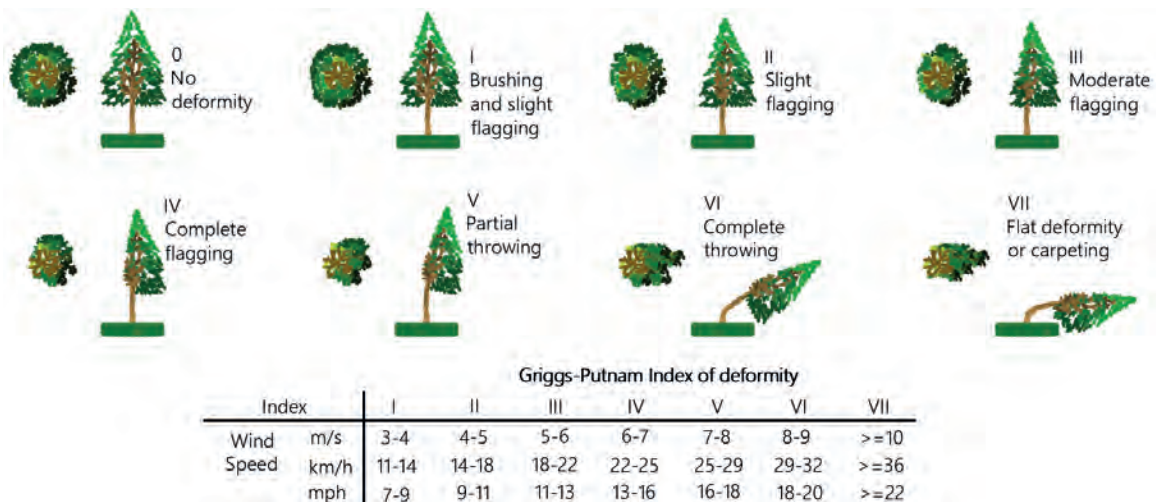


Figure 3.6 Griggs-Putnam scale for estimating wind speed from foliage and tree deformation.

### **3.4.2 Wind resource assessment - Stage 2**

Secondly, data from the wind resource measurements will be acquired and processed. Whether they are obtained by existing anemometric or meteorological stations, these data will be processed to be used in CFD studies. On the other hand, it should be noted that regarding the case studies of the selected sites and in the absence of measurements these will be obtained by extrapolating measurements from the meteorological stations around the site or by taking measurements of the wind resource with ultrasonic anemometric equipment: LiDAR or SoDAR [87]. This would be done through *in situ* measuring campaigns. The parameters of interest of the wind resource data obtained will be the profiles of wind speed, speed, and direction.

Based on the above, the power and density of the available wind at the site of interest will be estimated. The wind resource measurements obtained will be prepared and stored in databases for later use in the statistical analysis. This will be done through the elaboration of wind frequency histograms, Weibull and Rayleigh distributions, as well as the generation of wind roses.

Finally, within this stage, there is the development of a preliminary report of the site of interest selected through specialized software like WASP<sup>®</sup>, Windographer<sup>®</sup>, WRPLOT View<sup>™</sup> and through tools such as Geographic Information System (GIS) for the representation of the wind resource or maps of the wind potential of the selected site.

### **Computational Fluid Dynamics analysis**

#### **3.4.3 CAD Development of the topographic model of the site/complex - Stage 3**

In a parallel way, Stage 2 and Stage 3 (Wind resource assessment and development of the topographic model in CAD) will be developed. This stage is focused on the modeling of the geographical and topographic location of the macro-siting (MS) interest site domain, based on topographic maps for the realization of models with CAD tools, to start with an overview of the flow patterns of wind currents and thus determine the places with the highest wind flow or hot spots within the studied sites.

Afterward, the topographic models will include the modeling of the buildings, structures, and natural obstacles of the sites of interest defined in this methodology as the domain of the Complex or macro-siting zone. In order to obtain a specific vision of the patterns of wind flow currents, the realization of CFD simulations around the buildings and rural areas will be performed.

This stage will allow determining the best location based on the wind resource, specifying the Structure or Building of the micro-siting ( $\mu S$ ), from both the data obtained from the wind resource and the CFD simulations' results

#### **3.4.4 CFD Analysis of the topographic model of the site/complex - Stage 4a**

Once the CAD model is developed, both the domain of the Site and the Domain of the Complex, Stage 4 (CFD Analysis of the Site and the Complex), will be developed. This comprises the analysis of computational fluid dynamics with the initial conditions, based on the results obtained in Stage 2 (Wind resource evaluation).

These initial conditions are of utmost importance since they will allow defining and describing the turbulence phenomena that will be represented in the computational domain of the CFD analysis and thus obtain a better representation of the environment in which the wind site will take place.

In the first place, these initial conditions will be represented and used in each of the simulations to be performed in the present methodology, and the following phases can be defined within the initial conditions.

**a) Type of Analysis.-** In this methodological proposal, an external type of fluid analysis is defined since it is necessary to observe the behavior on an open surface; that, in this case, is the topographic surface of the Site and the Complex. In this same phase, the use of gravitational force on the z-component is defined.

**b) Type of Fluid.-** This phase requires defining the type and characteristics of the fluid to be used. For this purpose, in this project, all CFD simulations will use the air as fluid and turbulent characteristics with their respective humidity.

**c) Contour or Wall Conditions.-** Within this phase, the roughness length will be defined. This is a factor to consider since it will allow describing the surface of the Site and Complex, considering the existing vegetation, where the small-scale wind project is to be built.

**d) Initial and Boundary Conditions.-** This phase allows defining the thermodynamic parameters and the subdomain of the fluid, which in this case are the atmospheric pressure and the temperature. Included in this phase are also the parameters of speed, turbulence, and humidity, which are registered. On the other hand, the speed parameters will be considered based on the results obtained from Stage 2 regarding the evaluation of the wind resource. This stage considers the average speed of the wind, obtained from the wind rose diagrams, and also considering the prevailing direction of the wind.

**e) Mesh Configuration.-** This phase generates the meshing in which each of the cells or control volumes the fundamental equations of the fluid will be solved. There is a relationship between the size of the cell and the computational cost: when there is a better definition of the cells, the greater the cost and computational time. However, it will have a result with a better approximation of the environment that it is simulated in CFD.

### **3.4.5 CFD Analysis of the building or structure of rural or urban zone - Stage 4b**

Up to this stage, the identification of the best locations for the wind sites will be fulfilled so that a proposal will be developed for establishing and measuring the space available and the electricity consumption needs of the site of interest where the wind project will be developed.

Considering the above, it is possible to model the specific site where the small wind turbines will be assembled; in other words, the CAD model and its respective CFD simulation of the building or structure in question are developed.

This stage will help to specify the optimal location of the wind turbines on the selected building, considered as Building Mounted Wind Turbine (BUWT), based on the post-processing stage of the CFD analysis, showing the wind flow currents and their behavior around the building. This permit to estimating in this way the micro-siting ( $\mu S$ ) of SWTs.

#### **3.4.6 CFD Analysis of SWT - Stage 5**

Once the optimum location of the hot spot around the building has been determined in the previous stage, in Stage 5, a search strategy will be developed for the SWTs commercially available. The representative selection of small wind turbines will be based on the criteria of market availability, turbine certification, nominal power, cut-in and cut-out wind speed, and the structure available for their installation.

In addition, the small wind turbine has been selected, based on the space available on the building selected and for the energy consumption of the building or community. The appropriate location and sizing within the BUWT configuration, it will be required to have the CAD model of the wind turbines, and later its respective CFD analysis of the selected wind turbine.

For determining the SWT's behavior, according to the conditions of the wind resource, and thus being able to estimate the energy potential generated by the SWTs. Moreover, observing their behavior and their wind wake produced when it is subjected to the parameters of the nominal speed of the selected turbine, will be allowed to determine the dimensioning and spacing within the selected building or structure space available.

In other words, in this stage, based on the CFD results of the SWTs, the possible matrix arrangements that the roof size of the building or structure will have been proposed, contemplating a maximum installed capacity for the small wind emplacement.

#### **3.4.7 CFD Analysis of the integration of building - SWTs - Stage 6**

With these inputs, in Stage 6, the CAD models will be modified to perform the new CFD simulations. Later will be modified the CAD model of the small wind turbines integrated on the domain of the building or structure selected for the sites of interest. This will give a specific view of the wind flow patterns on the buildings and wind turbines where the wind project is intended, as well as the matrix arrangement of the wind turbines.

In this stage, several simulations of CFD will be performed, integrating the small wind turbines' domain, which allows determining the correct distance between wind turbines and also the hub height, by optimizing both the wind resource and the available space that the wind turbines on the BUWT building will occupy.

This number of simulations will be based on the dimensioning of the project: the space available on the building and the result of the CFD simulations, as well as the behavior of the wind turbines, considered.



### **3.4.8 CFD Post-processing - Stage 7**

Stage 7 can be considered as a final stage of the proposed methodology since the CFD simulations necessary for the feasibility study for the low power wind site are completed. In this stage, one last CFD simulation is performed, which integrates the CAD model of the Building or Structure arrangement and the matrix layout of the SWTs proposed with the topography and complex CAD models.

These CFD results allow observing the behavior of the wind speed at the hub height of the SWTs, indicating if the proposed wind site is the correct location for the wind emplacement. In this post-processing stage, a visual report of the CFD simulations' results of  $\mu$ S-SWT's will be included, contemplating the analysis of the contour plots, streamlines, or flows, iso-surfaces, and surfaces of the wind speed, wind power, and turbulence intensity, etc. In addition, it is possible for the development of wind resource maps of the interest site by applying CFD techniques.

### **3.4.9 Technical-economic evaluation**

On the other hand, but not limiting, a technical-economic evaluation is proposed, for complementing the results of these CFD simulations, with the selected wind turbines. This stage considers an evaluation in the reduction of electricity consumption billing, an evaluation of emissions reduction, and also a cost-benefit evaluation of the wind generation arrangement.

It can be argued that this stage is outside the scope of the present doctoral research project, but the evaluations that are believed to be pertinent are described below, in order to have greater certainty in the development of these types of projects.

#### **3.4.10 Evaluation of electric consumption**

In order to complement the results of these simulations in CFD, with the selected wind turbines, a cost-benefit evaluation of the wind generation arrangement will be carried out, as well as an evaluation in the reduction of the billing of the electricity consumption.

An evaluation of the electricity consumption of the wind generation project will be analyzed and developed, which will allow observing the economic benefit of installing a wind project, by reducing electricity consumption and also consumer electric energy bills in urban areas, as well in rural areas the benefit of the electrification of communities without access to this service.

#### **3.4.11 Economic evaluation**

This study will include an economic evaluation of the selected wind turbines, which can calculate the annual cash flow during the life cycle of the wind project. This allows delimiting the internal rate of return and other aspects to take into consideration in the decision-making for the development of small wind projects.

#### **3.4.12 Evaluation of emissions reduction of CO<sub>2</sub>**

Furthermore, an environmental impact assessment can be performed based on the CO<sub>2</sub> emissions of the low power wind generation project and founded on the production of

electricity compared to fossil energy source technologies. In this case, the benefit of reducing greenhouse gas emissions can be observed during the total life cycle of the project by analyzing unconventional energy sources against conventional ones.

Finally, the methodology will be evaluated both in urban and rural areas, which allows the proposal's validation in various case studies. It is important to point out that the validation of the methodology will be performed with the comparison of results of the CFD study compared to the conventional method of *in situ* measurement validation or with another CFD software.

The following sections will be showing the application of the proposed methodology in two different study cases analyzed in diverse wind conditions and different topography, which will help to observe the advantages of conducting feasibility studies for rural and urban SWT installation by applying CFD analysis.

### **3.5 Evaluation of the wind potential in the Tecnológico de Estudios Superiores de Ecatepec (TESE) campus**

#### **3.5.1 Stage 1 – Selection of the site of interest**

In order to show the effectiveness of the methodology proposed in this doctoral research, an easy feasibility approach for evaluating the installation of SWT's in an urban area is presented in this section. The interest site and location of the project are in the Northwest of the metropolitan area of Mexico State, specifically considering the campus of the Tecnológico de Estudios Superiores de Ecatepec.

The feasibility study of the wind project will be performed at Av. Tecnológico S / N, Valle de Anáhuac, C.P. 55210, Ecatepec de Morelos, in the state of Mexico, with the coordinates 19° 30' 43" N and 99° 02' 32" W. This site has measurements of the wind resource provided by anemometric stations.

As already mentioned, acquiring this data from the wind resource is necessary; therefore, it has had an approach with the Secretary of the Environment of Mexico City, whose website includes an air quality monitoring section. In Mexico City, the Sistema de Monitoreo Atmosférico (SIMAT) is responsible for the permanent measurement of air pollutants. The SIMAT has more than 40 monitoring stations around Mexico City and the metropolitan area of the state of Mexico, which provide information on pollutants, and among other meteorological variables that these monitoring stations generate, are wind speed and direction, which are variables required by the present methodology [88].

The SIMAT is structured by four subnetworks, and one of them is the **Red de Meteorología y Radiación Solar (REDMET)**. It is integrated by 19 sites for the measurement of surface meteorological variables, such as temperature, relative humidity, direction and wind speed, solar radiation, and barometric pressure. Figure 3.7 shows the map with the 19 meteorological stations. The stations San Agustín and Xalostoc will be used, which serve as a reference for the evaluation of the required wind resource assessment stated in the methodology proposed.

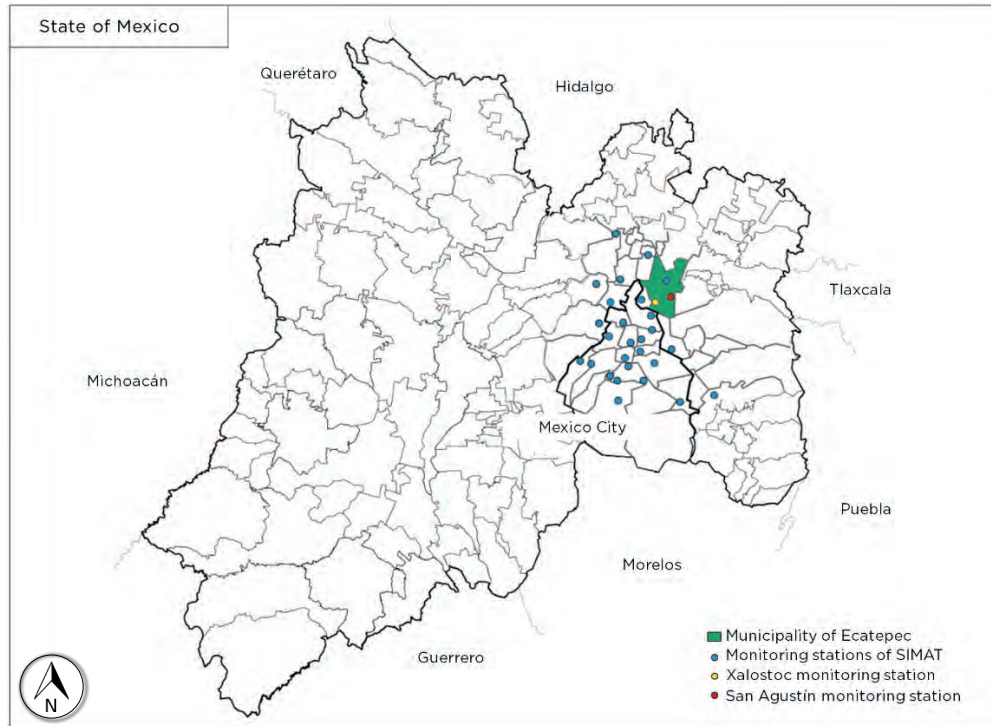


Figure 3.7 Map of the location of the municipality of Ecatepec, and location of the study site and its respective SIMAT monitoring stations.

These two monitoring stations correspond to the information presented in Table 3.2, which shows the parameters of the stations according to the SIMAT network, as well as the location, altitude, and height of each meteorological station.

Table 3.2 List of selected monitoring stations of the SIMAT network in Ecatepec.

Key	Monitoring Station	Address	Coordinates	Altitude (m a.s.l.)	Station Height
SAG	San Agustín	Av. Santa Rita y Sur 92, Col. San Agustín 3a sección, C.P. 55130, Ecatepec, Edo Mex.	19° 31' 58.68" N -99° 1' 49.17" W	2,241 m	9 m
XAL	Xalostoc	Vía Morelos km 12.5, Col. Xalostoc, entre López Rayón y Av. Benito Juárez, C.P. 54190, Ecatepec, Edo Mex.	19° 31' 33.58" N -99° 4' 56.64" W	2,269 m	25 m

### 3.5.2 Stage 2 – Wind resource assessment

After the site selection and the database availability, the next stage is the wind resource assessment. It is worth mentioning that in the wind resource databases managed by SIMAT, the sampling period is hourly. This is because a large number of monitoring stations are managed, which would present a disadvantage in the historical wind database. On the other hand, an advantage of selecting these weather stations is that their records of these measurements are provided from 1986, so important data for developing an efficient evaluation of the wind resource is presented. This analysis will allow a preliminary evaluation for determining the prevailing wind speeds and direction.

## Wind rose construction

### A) The San Agustín meteorological station

The development of wind roses is built on the records of the meteorological station of San Agustín SAG, which belongs to the REDMET subnetwork and is 3 km away from the interest site. In Figure 3.8, the SAG weather station is shown.



Figure 3.8 San Agustín monitoring station of the SIMAT meteorological network.

The development of the wind roses will be performed through the WRPLOT View™ and WASP® software. This data analysis will be carried out from 2006 to 2016, on a single wind rose diagram with its respective frequency distribution. These diagrams will allow determining the direction of the prevailing wind (resultant vector), as well as its respective speed in that direction. The result of this analysis is shown in Figure 3.9.

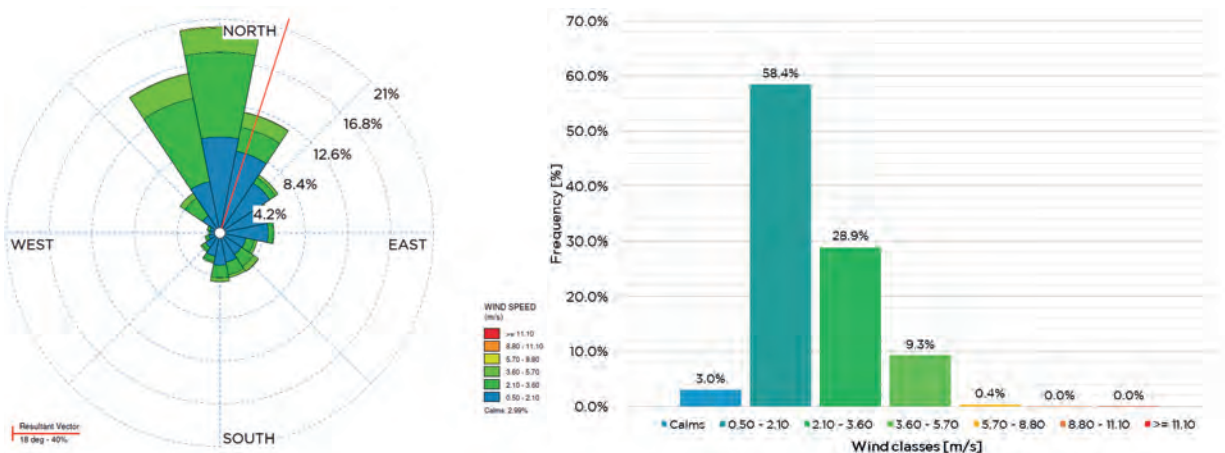


Figure 3.9 Wind rose and frequency distribution of the SAG station through WRPLOT View™.

In Figure 3.10, the results of the wind rose diagram with the WASP® software are shown. Here the average speed of each segment of the wind rose can be observed in detail, as well as the general average speed, comprising all the wind directions of the 16 segments of the wind rose diagram.

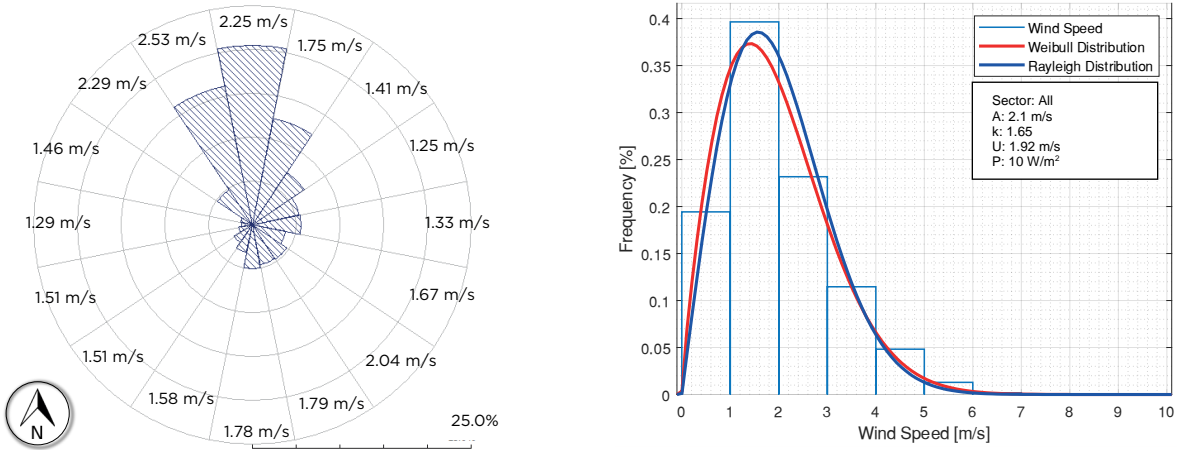


Figure 3.10 Wind rose and frequency distribution of the SAG station through WASP®.

**B) The Xalostoc meteorological station**

The other meteorological station, selected from the SIMAT network, is the XAL weather station, which is located 5.4 km away from the selected site of interest. This station is 25 m high above ground level, allowing a reliable wind resource analysis because there are no obstructions that limit the wind resource at this height. Figure 3.11 shows the images of the XAL weather station.



Figure 3.11 Xalostoc monitoring station of the SIMAT meteorological network.

The wind rose diagrams for this station were also developed, which are shown in Figure 3.12, where the wind rose with its respective Weibull frequency distribution histogram can be observed, resulting from the analysis of the wind resource in the XAL weather station, with the WRPLOT View™ software, also including a sampling period from 2006 to 2016.

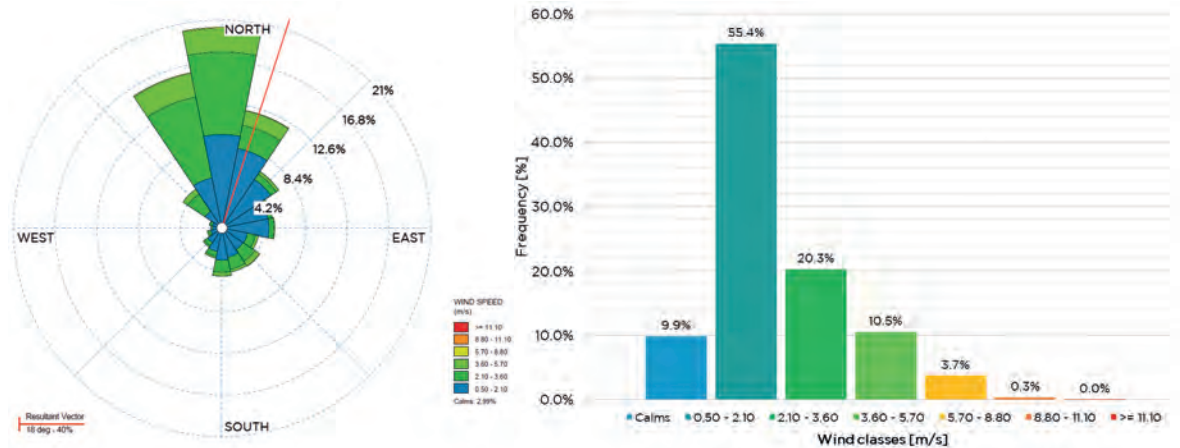


Figure 3.12 Wind rose and frequency distribution of the XAL station through WRPLOT View™.

In Figure 3.13 below, the wind rose diagram with its respective frequency distribution of the XAL monitoring station, developed with the WASP® software, is shown.

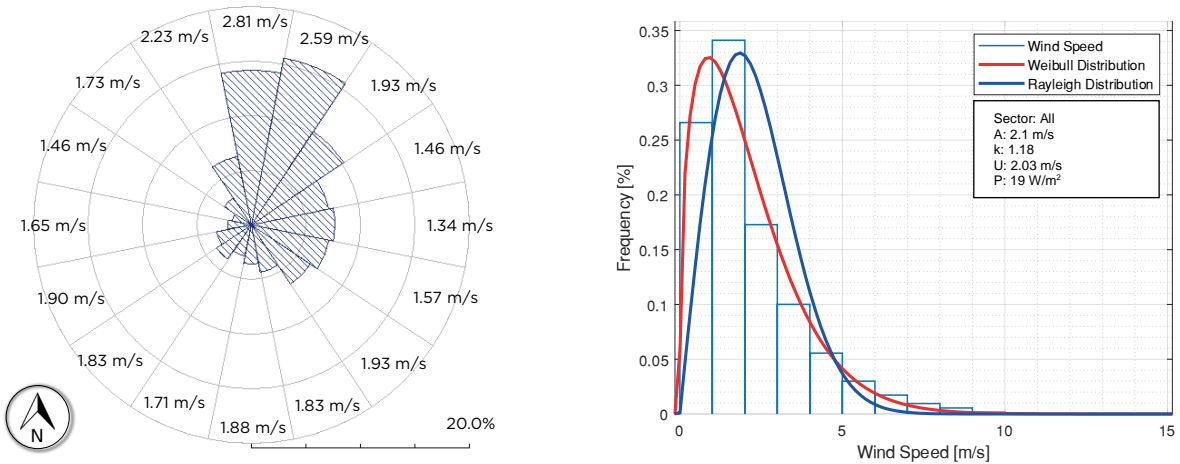


Figure 3.13 Wind rose and frequency distribution of the XAL station through WASP®.

Is worth to mention that both meteorological stations were considered for the representative radius stated by the Measuring Network of Wind Energy Institutes (MEASNET), which state a radius for simple flat terrain of 10 km of maximum distance from any wind turbines to the next mast and for complex terrain it is 2 km [89], [90]. Finally, in the following section, the two selected meteorological stations will be analyzed together to obtain the average analysis for later use in the CFD simulations.

### C) Conjunction of the wind rose diagrams of the SAG and XAL meteorological stations

In order to obtain a better interpretation, as well as wind resource results evaluation, both meteorological stations will be considered, to obtain the average speeds, as well as the vector resulting from the wind direction. In Figure 3.14, the results of the wind rose made with the WRPLOT View™ software is shown.

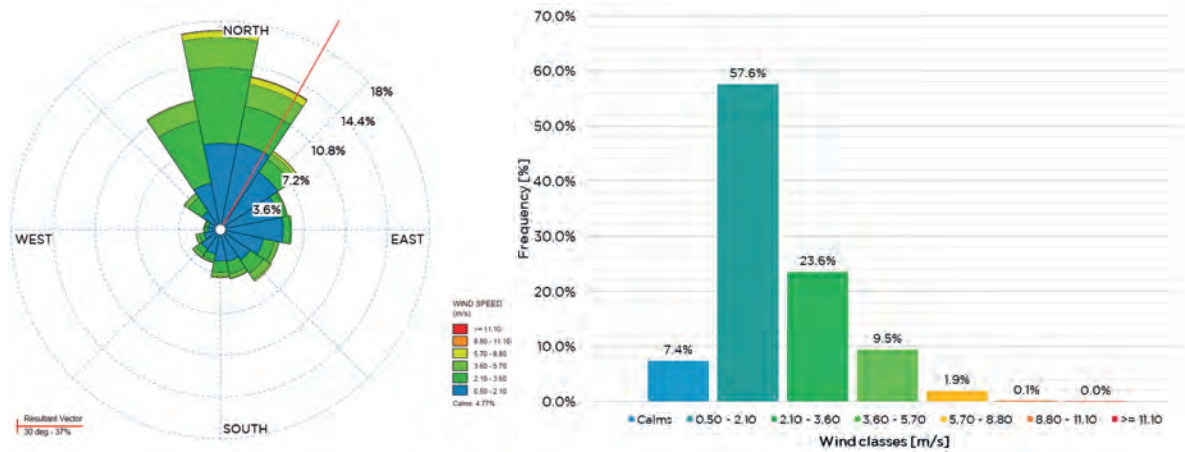


Figure 3.14 Wind rose and frequency distribution of SAG and XAL stations through WRPLOT View™.

In Figure 3.15, the wind rose diagram with its respective frequency distribution prepared with the WASP® software is then shown. This analysis will allow determining the initial conditions represented by the environmental conditions of the case study raised in the urban environment. Later these data will be used for the analysis of computational fluid dynamics.

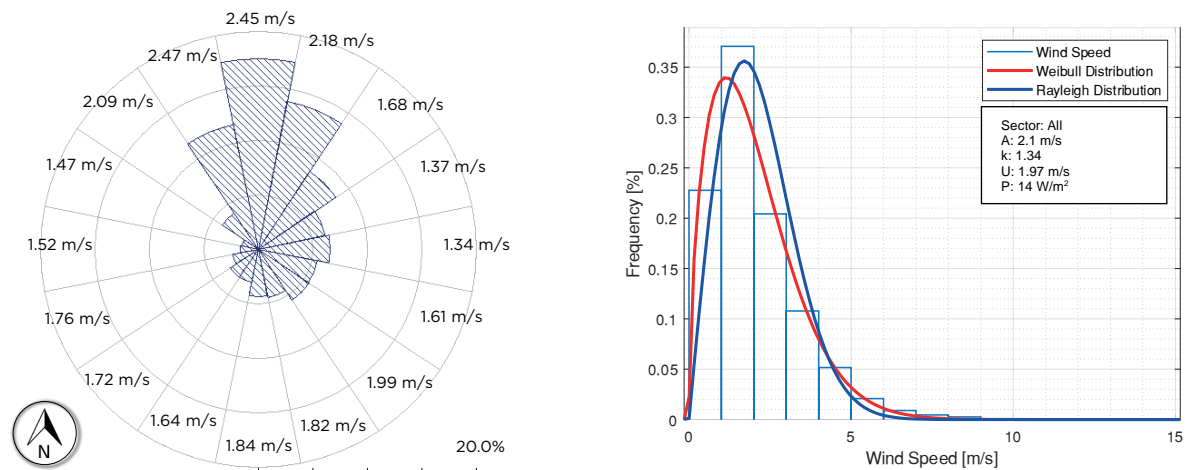


Figure 3.15 Wind rose and frequency distribution of SAG and XAL stations through WASP®.

#### Interpretation of wind rose diagrams

Once the wind rose diagrams have been developed, it is necessary to analyze the results obtained from both meteorological stations selected, based on their proximity to the selected interest site. The wind rose diagrams of Figure 3.14 and Figure 3.15 will be taken into consideration because the results of the XAL and SAG meteorological stations are adjacent to the wind project proposal.

From the wind rose diagram of Figure 3.14 (WRPLOT View™), the resulting vector with the highest incidence of the wind resource is 30° with a frequency of 37%. On the other hand, from the graph of frequency distribution, it can be determined that the speed with the highest incidence is in the range of 0.5 m/s to 2.1 m/s with a frequency of 57.56%. These results help determine that most of the wind comes from the North-northeast (NNE) cardinal direction.

For its part, the wind rose of Figure 3.15 (WAsP©) shows that the highest wind speed occurs in the northern cardinal point with an intensity of 2.45 m/s, and the frequency distribution diagram shows an average speed of 1.97 m/s. Although the average wind speed obtainable at the TESE site is not adequate for the cut-in speeds of the SWTs, it will continue with the methodology for observing the wind's behavior and establish the optimal location for the low power wind project could have.

### 3.5.3 Stage 3 – CAD Modeling of the geographic and topographic conditions

For this stage of the proposed methodology, the **Domain of the Site** corresponding to the topographic modeling of the site will be developed. These models will be performed with CAD software, as well as existing topographic map sources such as Google Earth and the topographic database ASTER GDEM v2 of the Global Mapper software [91].

For developing this stage, the topographic model is created. Figure 3.16 shows the three-dimensional topographic model of the site in an isometric view. The orientation of the coordinate system in the Y-vector is the North cardinal point. This CAD model will be part of the macro-siting (MS) of the proposed methodology and will be used to incorporate the three-dimensional model of the academic complex. The modeling process of the topography is developed through a process design with different software, which is detailed in Appendix C.

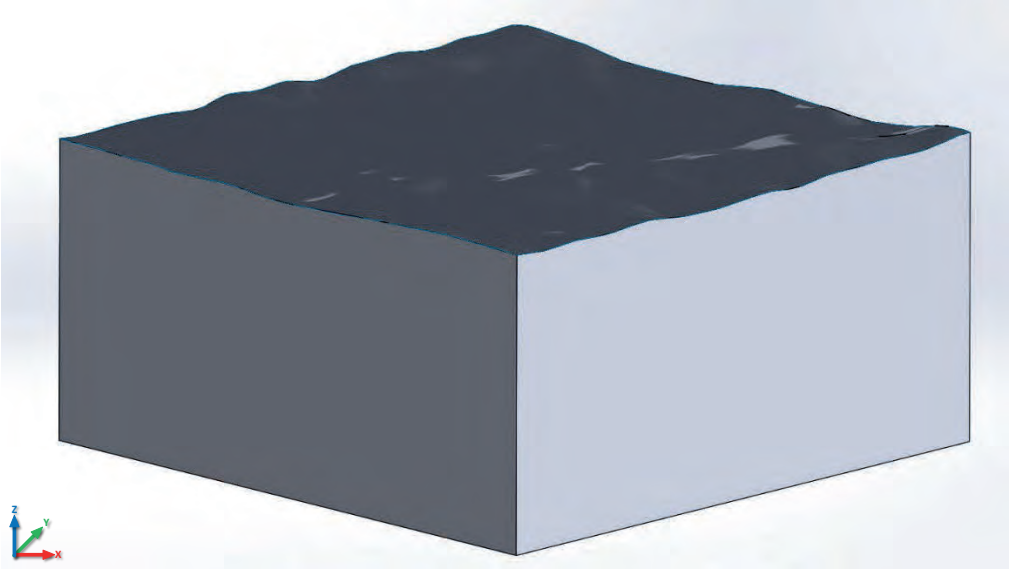


Figure 3.16 Isometric view of the 3D topographic modeling of the case study site.

This CAD model shows the terrain's rugosity according to the contour lines and considers the characterization of the terrain and its influence on the wind resource in the urban environment or any other type of terrain.



In addition to taking into account the model of the terrain, the parameter of the roughness length will be taken into consideration according to the type of terrain, which in this case focuses on the classification of cities with tall buildings.

After the development of the topographic model in CAD, the CAD model of the urban environment must be performed, known in this methodology, as the complex domain. This academic complex is developed with all the structures and buildings within a 500 m radius. Delimiting the study area based on the recommendations of New York State Energy Research and Development Authority (NYSERDA) representativeness, for developing computational fluid dynamics simulations [89], [90], [92].

The CAD model of the complex is also part of the MS, which, once having both domains, can be continued with the first CFD analysis of the proposed methodology.

Figure 3.17 a) shows the neighborhoods surrounding the proposed case study. Figure 3.17 b) shows the three-dimensional top view of the complex model, together with the associated buildings of the TESE campus, which are marked in dashed lines. In this model, other complexes appear to the North of TESE, such as the campus of the Universidad Estatal del Valle de Ecatepec (UNEVE), the Dr. José María Rodríguez General Hospital and next to it, the Universidad Pedagógica Nacional (UPN) No. 153 Ecatepec. In the same way, the model of the complex is oriented to the coordinate system in the Y-component, towards the North direction.

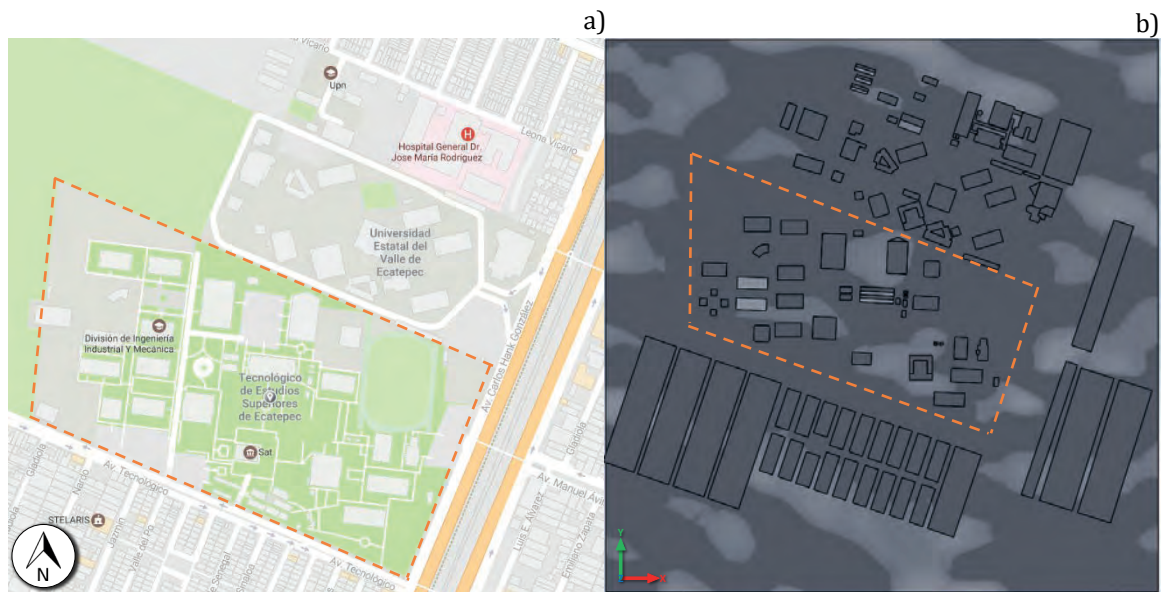


Figure 3.17 a) Spatial distribution and b) 3D site of academic complex models of the interest site.

Similarly, in Figure 3.18, the location of the site of interest is shown within the 500 m previously established radius, in which the three-dimensional model of the TESE academic complex and the other abovementioned complexes and structures can be observed.

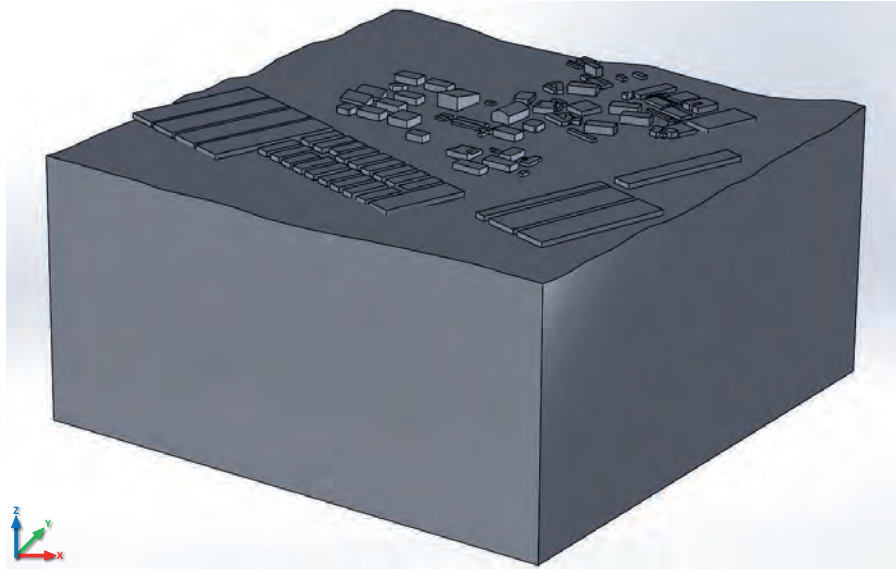


Figure 3.18 Iso-metric 3D view of the site and academic complex model of the site of interest.

### 3.5.4 Stage 4a – CFD Analysis of the site and urban complex

Once the model of the site and the complex domains have been taken into consideration, the computational fluid dynamics analysis will be performed. In this case, the initial conditions that will allow the CFD analysis are required. The following describes each of the initial conditions selected based on the development of Stages 1 to 3, which correspond to the feasibility study including the selection of the site of interest, the evaluation of the wind resource, and the development of both the CAD model of the site of interest and the complex domains. In this sense, there are five phases that comprise the CFD analysis, and each one of them will be analyzed with the proposed case study.

**1.- Type of Analysis.-** As already mentioned, the analyzes required for the present methodology are of the external flow type because the behavior of the fluid around the surfaces of the topographic domain, as well as the academic complex, must be analyzed.

**2.- Type of Fluid.-** The type of fluid to be analyzed in the present methodology is air. The properties of the air with which the CFD simulations are developed will be the specific heat ratio at constant pressure ( $C_p$ ), with the specific heat at a constant volume ( $C_v$ ) of 1.399 and the molecular mass of the air of 0.02896 kg/mol. In the same way, in this phase, the type of flow is defined, which for this case study will be a turbulent flow with its respective humidity.

**3.- Contour or Wall Conditions.-** The wall conditions are important since the topographic model surfaces describe and define the roughness of the land and the bushes or buildings that are around the site of interest. According to the classification of the roughness lengths based on the type of terrain, in this phase, the roughness length is defined.

This length will allow describing the urban environment, as well as the characteristics of the vegetation that surrounds the MS of the selected site of interest. Based on this classification, a roughness length of 1.6 meters is selected, being equivalent to 1,600,000  $\mu\text{m}$ , which describes the classification for large cities with tall buildings and forests [85].

This roughness length of the terrain is based on the classification of roughness. This classification, usually used in Europe, is represented by:

$$\frac{v}{v_0} = \frac{\ln\left(\frac{H}{z}\right)}{\ln\left(\frac{H_0}{z}\right)} \quad (3.1)$$

where  $z$  is the roughness length,  $v$  and  $v_0$  are the wind speeds to the heights  $H$  and  $H_0$  respectively. Table 3.3 presents the classification of rugosities with their respective lengths [85], [93]–[95].

Table 3.3 Roughness classification and roughness length values for various land types.

Roughness Classification	Description	Roughness Length $z$ [m]
0	Water surface	0.0002
1	Open lands with few windbreaks	0.03
2	Farmlands with some windbreaks more than 1 km	0.1
3	Urban districts and farmlands with many windbreaks	0.4
4	Dense urban areas or forest	1.6

**4.- Initial and Boundary Conditions.**- This phase, also known as the subdomain phase of the fluid, allows characterizing the fluid in question (air). Within the specified properties, four types stand out:

*a) Thermodynamic parameters.* - In this parameter, the temperature, and pressure to which the CFD simulations will be subjected. For this case study, the recording of the temperatures of the SIMAT network in Mexico City is used. Thanks to the historical records of ambient temperature, it is possible to obtain the average and enter this value in the specifications of the CFD simulations.

By obtaining the average of both the SAG and XAL stations, it is assumed that the XAL station has a temperature of 17.5 °C and the SAG station it has an ambient temperature of 17.3 °C, with an average temperature of both stations of 17.4 °C, which is equivalent to 290.5 °K.

On the other hand, the atmospheric pressure was obtained, which is given in millimeters of mercury (mmHg). The average of the atmospheric pressure of the XAL station is 584.36 mmHg, which is equivalent to 77,908 Pa with a conversion factor of 1 mmHg → 133.32 Pa.

*b) Velocity parameters.*- In this, the air velocity vector is defined, which will be used in CFD simulations. By taking into consideration, the evaluation of the wind resource, an average speed of 1.97 m/s and a wind direction with a greater frequency of 30° with respect to the northern cardinal point were estimated. This requires a decomposition of the average velocity vector in the velocity of the “ $x$ ” and “ $y$ ” components.

This results in a wind speed of 1.70 m/s for the  $x$ -component and wind speed of 0.985 m/s for the  $y$ -component. This describes the average speed that will include CFD simulations. Both components of the velocity vector are of negative value because these velocities enter the coordinate system of the CAD model. In this same phase, the gravitational force is defined as  $-9.81 \text{ m/s}^2$ , which acts on the  $z$ -component of the three-dimensional coordinate system of the model.

*c) Turbulence parameters.*- The turbulence intensity and turbulence length to which the model will be subjected in the CFD simulations are defined. These simulations were selected for a turbulence length of 38 m and a turbulence intensity of 0.040%. These parameters were calculated based on the turbulence length scale  $l$ , which is a physical quantity that describes the size of the eddies with high energy content in a turbulent flow. This turbulence length scale is usually used to estimate turbulent properties under the input conditions of a CFD simulation. Typically, the turbulence length scale is proposed as a percentage. By taking into consideration the model of the proposed site of interest as a flow over a pipeline, the turbulence length scale can be estimated from the hydraulic diameter, which is defined as in a flow of a pipe the turbulence length is 3.8% of the hydraulic diameter [96]. Thus,

$$l = 0.038d_h \quad (3.2)$$

where  $d_h$  is the hydraulic diameter [97] and is calculated with the following expression for rectangular pipes as is the case with a width of  $a$  and a height of  $b$  is:

$$d_h = \frac{2ab}{a + b} \quad (3.3)$$

In this sense, for the developed three-dimensional model, it has a width of 1000 m with a length of 1000 m. Therefore, a hydraulic diameter of 1000 m and a turbulence length of 38 m are obtained.

Regarding turbulence intensity, it is based on the parameters of the Reynolds number  $Re$ , the fluid velocity  $U$ , the length of the surface on which the fluid will flow  $L$  and the kinematic viscosity of the air  $\nu_k$ . It is determined by the following equation:

$$Re = \frac{UL}{\nu_k} \quad (3.4)$$

Table 3.4 shows the physical properties of air at the atmospheric pressure, from which the kinematic viscosity of air  $\nu_k$  for the selected temperature of 17.4 °C based on the meteorological stations of SIMAT will be used.

Table 3.4 Physical properties of air at different temperatures.

Temperature °C	Density $\rho$ [kg/m <sup>3</sup> ]	Dynamic viscosity $\mu$ [N.s/m <sup>2</sup> ] 10 <sup>-5</sup>	Kinematic viscosity $\nu_k$ [m <sup>2</sup> /s] 10 <sup>-5</sup>
-10	1.342	1.67	1.24
0	1.292	1.72	1.33
10	1.247	1.76	1.42
20	1.204	1.81	1.51
30	1.164	1.86	1.60
40	1.127	1.91	1.69
50	1.092	1.95	1.79
60	1.060	2.00	1.89

Therefore, by making a linear interpolation for the temperature of 17.4 °C, is obtained the kinematic viscosity value, which is equal to  $1.486 \times 10^{-5}$  m<sup>2</sup>/s.

By calculating the Reynolds number  $Re$  with this kinematic viscosity, it has:

$$Re = \frac{1.97(1000)}{1.486 \times 10^{-5}} = 132,570,659.5$$

Thus, according to the classification of flow type, based on the Reynolds number obtained, it corresponds to turbulent flow because it is greater than 4,000 units. Based on the equation for determining the intensity of turbulence in a square pipe, we have the following expression [98], [99]:

$$I = 0.317Re^{-0.110} \quad (3.5)$$

In this sense, it is obtained a turbulence intensity of 0.040%, which will be applied to the CFD simulations of the present case study.

*d) Humidity parameters.*- The initial conditions for the relative humidity that occurs in the environment are also required. With the average of the relative humidity of the SAG station of 54.28% and for the XAL station of 51.18%, an average of the relative humidity of 52.73% for both stations is determined.

**5.- Mesh Configuration.**- This last phase determines the size of the refinement of the mesh, which will delimit the precision with which the CFD simulations will be developed. While there is a mesh with less space between the grid, the greater the definition of the post-processing of the CFD. This configuration should be considered since the greater refinement of the mesh will be the time and computational cost [100].

For these CFD simulations, an automatic mesh configuration is selected, with a high level of refinement: with the largest number of cells with possible rectangular parallelepipeds, which in each of the cells defines the control volumes, to solve the equations that govern the fluids. In this case, the TESE campus case study has 28,993 cells that integrate the mesh, of which 9,426 are in contact with the solid modeled in three-dimension with the fluid.

These five phases allow determining the parameters of the initial conditions, which can be summarized in Table 3.5, which shows the characteristics and conditions that allow describing the environment of the CFD simulations of the present case study.

Table 3.5 Initial and boundary conditions for the CFD simulations of the TESE case study.

Analysis Type	Fluid Type	Boundary Conditions	Initial and Environment Conditions	Mesh Configuration
Type of flow: external	Air with all its physical properties	Roughness length: 1,600,000 $\mu\text{m}$	a) <i>Thermodynamic parameters:</i> -Temperature environment: 17.4 °C = 290.5 °K. -Atmospheric pressure of 77,908 Pa	Automatic mesh with 28,993 control volume cells
Gravitational force: -9.81 m/s <sup>2</sup>	Turbulent flow		b) <i>Velocity parameters:</i> Average wind speed of 1.97 m/s at 30°. It comprises 1.70 m/s in the "x" component and speed of 0.985 m/s for "y" component. c) <i>Turbulence parameters:</i> -Length of turbulence of 38 m -Turbulence intensity of 0.040%. d) <i>Humidity parameters:</i> -Average relative humidity of 52.73%.	

Taking into consideration these initial conditions and once the CAD models of the site of interest and the three-dimensional complex have been developed corresponding to the macro-siting (MS), the first CFD analysis based on the proposed methodology was developed. This case study focuses on the use of turbulent models to represent the characteristics of the urban wind flow for predicting the characteristics that the wind will take around the site and the complex (MS) of the TESE. Figure 3.19 shows the top view of the CAD model, with its longitudinal cut of the contour plot of the velocity parameter.

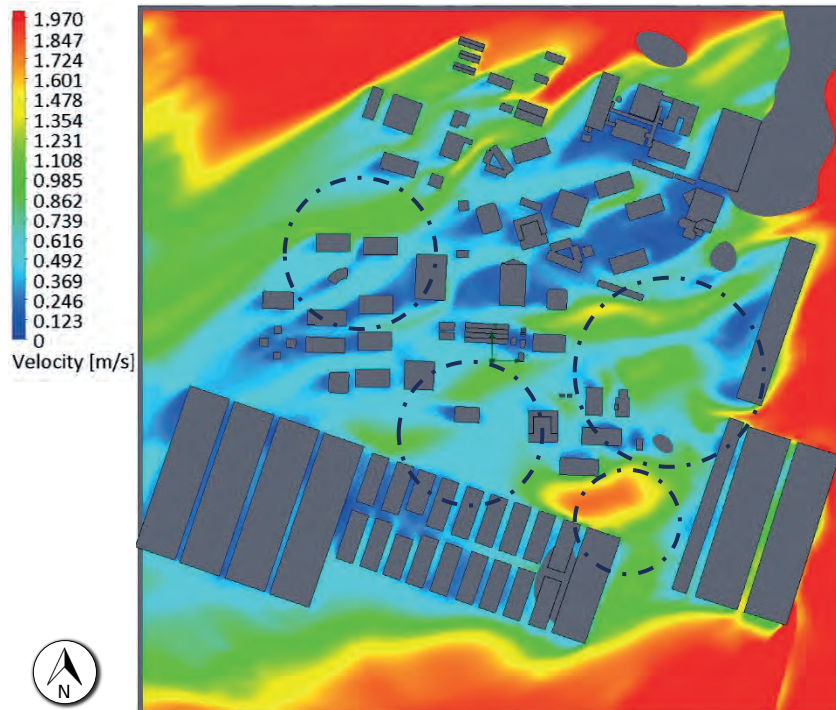


Figure 3.19 CFD Simulation of the top view of the site and complex of the case study at 1.97 m/s.

In the previous figure, the wind speed variable can be seen in the model of the site and the complex (MS) of the case study. The wind speed with which this simulation is represented is 1.97 m/s. When analyzing the figure, and considering the wind direction from the North-northeast (NNE) cardinal point, there is a decrease in the wind resource caused by the buildings around the campus. The green color is indicating the zones with an average speed of 1.1 m/s to 1.2 m/s. Meanwhile, where there could be a greater wind potential is indicated in circles, only in case the interest site had a better wind resource available in the buildings.

In Figure 3.20, a comparison of contour graphs at different wind speeds can be observed on different resolution scale. In Figure 3.20 a), the full wind speed of 1.97 m/s is presented; in Figure 3.20 b) a wind speed of 1.5 m/s is shown, and in Figure 3.20 c) a wind speed of 1.0 m/s is also shown respectively. In the latter, the areas shown in the circles represent the highest wind incidence over the buildings and can be observed clearly.

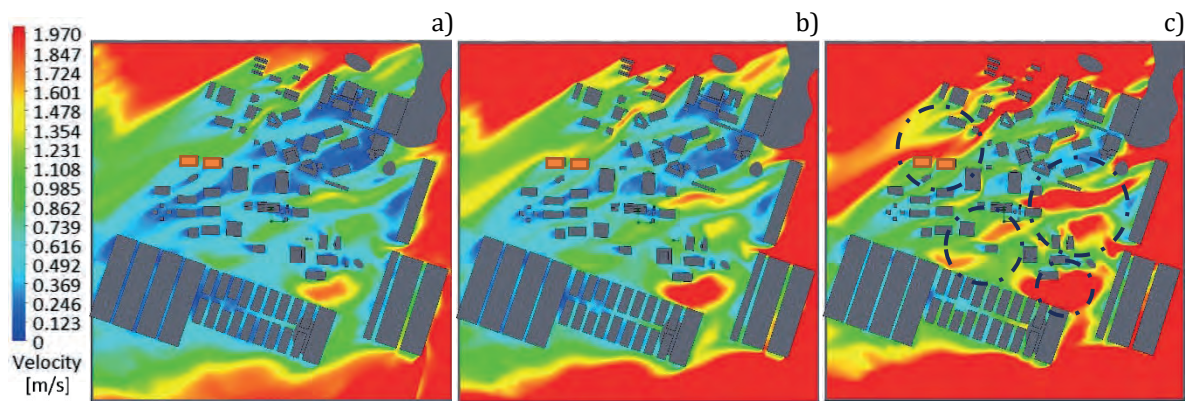


Figure 3.20 CFD Simulations of the top view of the site and academic complex at a) 1.9 m/s, b) 1.5 m/s and c) 1.0 m/s.

In the area of the site of interest, the buildings within the TESE university campus with greater wind potential in their surroundings include those located in the northwestern area of campus, which are presented in Figure 3.21, being able to appreciate the Buildings “Q” and “S”. These buildings have a greater wind incidence and could be considered as the best buildings for the installation of small wind turbines.

By observing the results of the CFD simulations, it is possible to verify the behavior of the wind speed around the buildings in order to evaluate the correct location of the wind turbines on the top of the Building Mounted Wind Turbine (BUWTs) buildings. In Figure 3.21, the wind speed ranges from 0 m/s to 1.0 m/s and above can be seen, with a wind speed of about 0.8 m/s over the buildings’ facades.

These simulations of this stage of the methodology allow identifying the buildings (Building Q and Building S), with higher wind incidence, which are dedicated to the Computational Systems and Information Technology buildings, respectively. It can be determined that in case there would be a good wind potential higher than 3 m/s for overcoming the cut-in wind speed of small wind turbines, the feasibility of the installation of a small wind project on the university campus could be achievable.

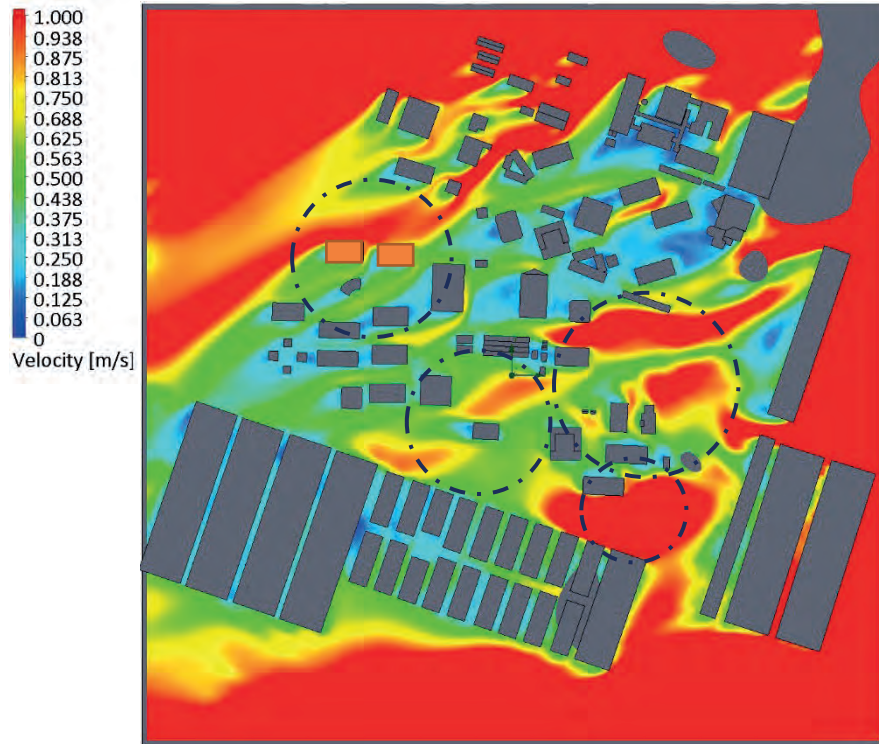


Figure 3.21 CFD Simulation top view of the site and complex of the case study at 1.0 m/s.

On the other hand, in Figure 3.22, the results of the CFD simulations of the site and the complex are shown in the isometric view of the graph of the contour of the wind speed in order to define the estimated hub height and the available wind speeds over the building selected in the university complex.

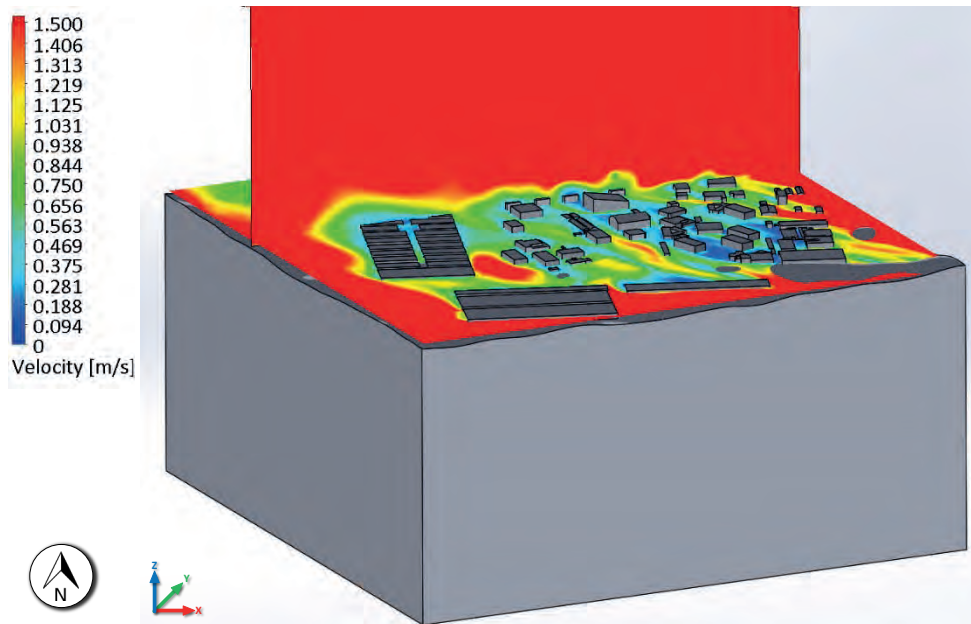


Figure 3.22 CFD Simulation of the isometric view of the site and complex contour plot at 1.5 m/s.



The advantage of CFD simulations is that the graphical representation of any parameter in a three-dimensional form of the fluids simulated can be obtained. In this case, the velocity parameter is analyzed with a resolution scale of 1.5 m/s for providing a guideline to analyze the z-component of the wind speed in order to estimate the hub height of the wind emplacement to be installed.

Based on the previous isometric view, a height can be estimated in which the wind resource shows consistency in the wind flow, as shown in red, which determines that at that height, there is a wind speed of 1.5 m/s or higher. The estimated hub height for the small wind turbines installation is approximately 40 m from the base of the building within the Atmospheric Boundary Layer (ABL) for extracting the wind speed of 1.5 m/s.

When performing this analysis, it can be determined that at lower altitudes, the wind speed is much lower, according to the law of the logarithmic profile of the wind or the Hellmann exponential law. For example, if it wants to acquire an average speed of 1.0 m/s at the height hub of the nacelle, this height will be 25 m.

This analysis can be seen in Figure 3.23 a) and Figure 3.23b), which show the corresponding hub heights of 40 m and 25 m based on their respective wind speeds reaching 1.53 m/s and 1.07 m/s respectively, which indicates the optimal height for the installation of wind turbines for this case study in case of having a good wind potential.

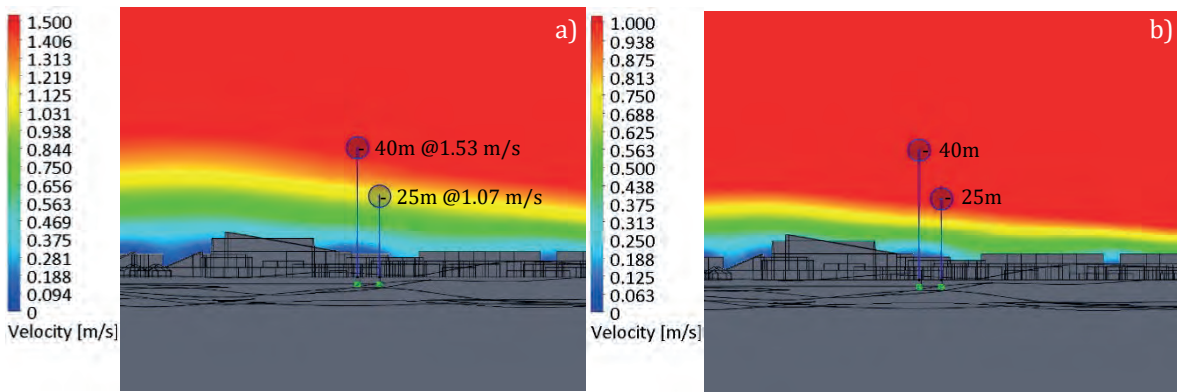


Figure 3.23 CFD Simulation side view result comparison at a) 1.5 m/s and b) 1.0 m/s.

By taking into consideration the Hellmann's exponential law, which is represented by:

$$\frac{v}{v_0} = \left(\frac{H}{H_0}\right)^\alpha \quad (3.6)$$

where  $v$  is the wind speed at height  $H$ ,  $v_0$  the speed at a height  $H_0$ , which frequently is referred to a height of 10 m and the parameter  $\alpha$  which is the wind shear exponent or also called friction coefficient of the Hellmann exponent, and is directly related to the height and nature of the terrain [85], [95].

Table 3.6 shows the values that Hellmann exponent takes for different types of terrain [93]. In addition, for this case, it will take the value of 0.40 on the basis that the case study is in the urban environment.

Table 3.6 Friction coefficient for various terrain characteristics.

Terrain type	Friction coefficient $\alpha$
Smooth hard ground, calm water	0.10
Grass on level ground	0.15
Crops, hedges, and shrubs	0.20
Forest wooded countryside, many trees	0.25
Small towns with trees and shrubs	0.30
Large city with tall buildings	0.40

By analyzing Figure 3.23, in the CFD results' simulation it is possible to determine that it has a wind speed of 1.5 m/s at the height of 40 meters, therefore, for a height of 25 m, considering  $\alpha$  as the friction coefficient of 0.40 because to the case study is considered in an urban area. It would represent a wind speed of 1.24 m/s based on Hellmann's exponential law.

This friction coefficient  $\alpha$  is determined empirically, and the equation can be used to adjust the data in a range from 10 to 150 meters in height if there are no significant obstacles on the terrain's surface. This exponent  $\alpha$  varies with different factors such as height, time of day, time of year, nature of the terrain, wind speeds, and temperature [85], [93].

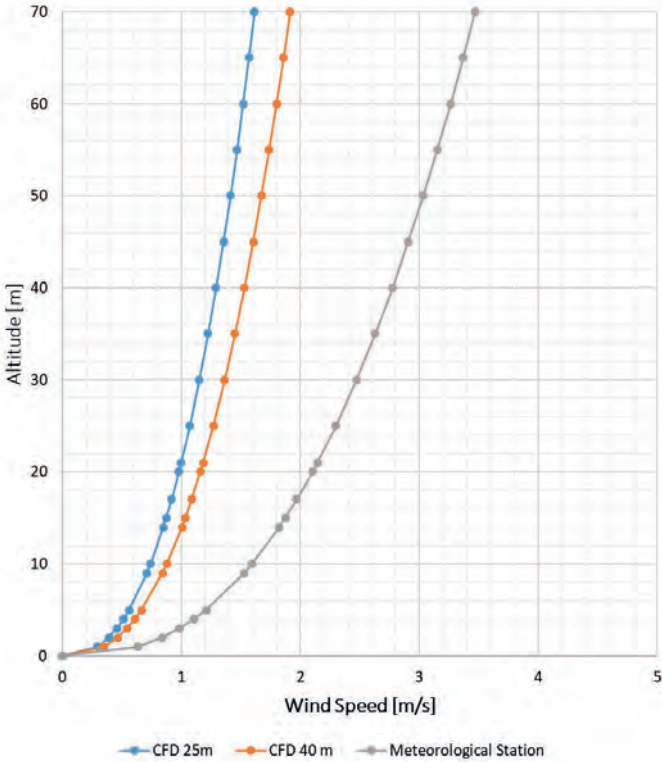


Figure 3.24 Wind speed profiles and measurement comparison through weather station and CFD simulation.

This coefficient is a function of the topography of the terrain where the wind speed and direction are being measured, which takes the value of  $1/7$  for open terrain without obstacles. When this coefficient takes this value, it is known as the one-seventh power law. However, it must be considered that this exponent can vary for the same place from a value of  $1/7$  during the day, up to values of  $1/2$  during the night [85], [93].

Figure 3.24 compares the wind profiles obtained by measuring data of the average wind speed obtained from the REDMET stations at a single height, which in this case is  $1.97$  m/s to  $17$  m in height compared to the wind speed measurement points resulting from the CFD simulations of the case study, where at the height of  $40$  m there is a wind speed of  $1.53$  m/s.

These previous results give an overview of the behavior of the wind resource. In this three-dimensional simulation, it is possible to identify the aerodynamics of the different geometries that comprise the university complex in different physical scenarios. In order to obtain the wind speed at which the structures are subjected and to observe how wind energy technologies behave at different heights. This CFD model allows the evaluation of wind energy efficiency and even the estimation of the generation of output power that small wind turbines will have, depending on their optimal location.

### **3.5.5 Stage 4b – CFD Simulation of the building or structure**

Considering the results of the previous CFD simulations of the site of interest and the complex, it is convenient, despite the scarce wind resource, continuing with the proposed methodology. In order to develop the methodology is taken into consideration this case study as a base case for the application of the new implementation of the VCD in the other proposed case studies.

The CFD simulations helped determine the buildings with the highest wind incidence. In this sense, the three-dimensional modeling will be performed with CAD tools of the selected buildings in question for performing the new CFD simulations of the building or structure. These results, together with this stage, permit the location of the small wind turbines to be installed. The structure and configuration of both buildings are the same, so only one building will be modeled to see the behavior of the wind resource on the building and determine the optimal locations for the installation of wind turbines.

These buildings Q and S are rectangular and are  $23.5$  m wide,  $45.5$  m long, and  $7.2$  m high. In Figure 3.25, the three-dimensional CAD modeling of these buildings can be observed, as well as the composition of their structure.

Once the three-dimensional model of the selected building is developed, based on the previous CFD simulations and according to the methodology, performing a computational fluid dynamics analysis on the structure in question is considered. This simulation of CFD will be part of the micro-siting ( $\mu$ S), which will allow the optimal location of the small wind turbines on the building.

These CFD simulations are useful to locate the exact position of the small wind turbines on the roofs of the building or interest structure. The results include the wind flow behavior in the boundaries around the building, allow determining the turbulent zones with its respective turbulent intensity.

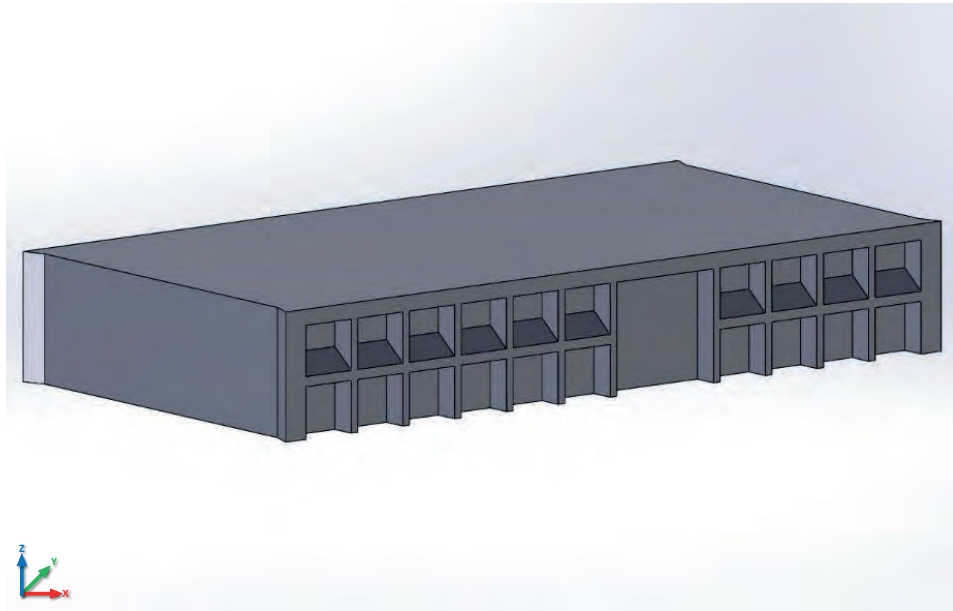


Figure 3.25 CAD modeling of the buildings Q and S in an isometric view.

Figure 3.26 shows the result of this CFD simulation, in which the contour graphs of the velocity parameter are seen at different heights of the building, which are detailed. This allows specifying the behavior of the wind around the building, with prevailing winds from the Northeast cardinal direction.

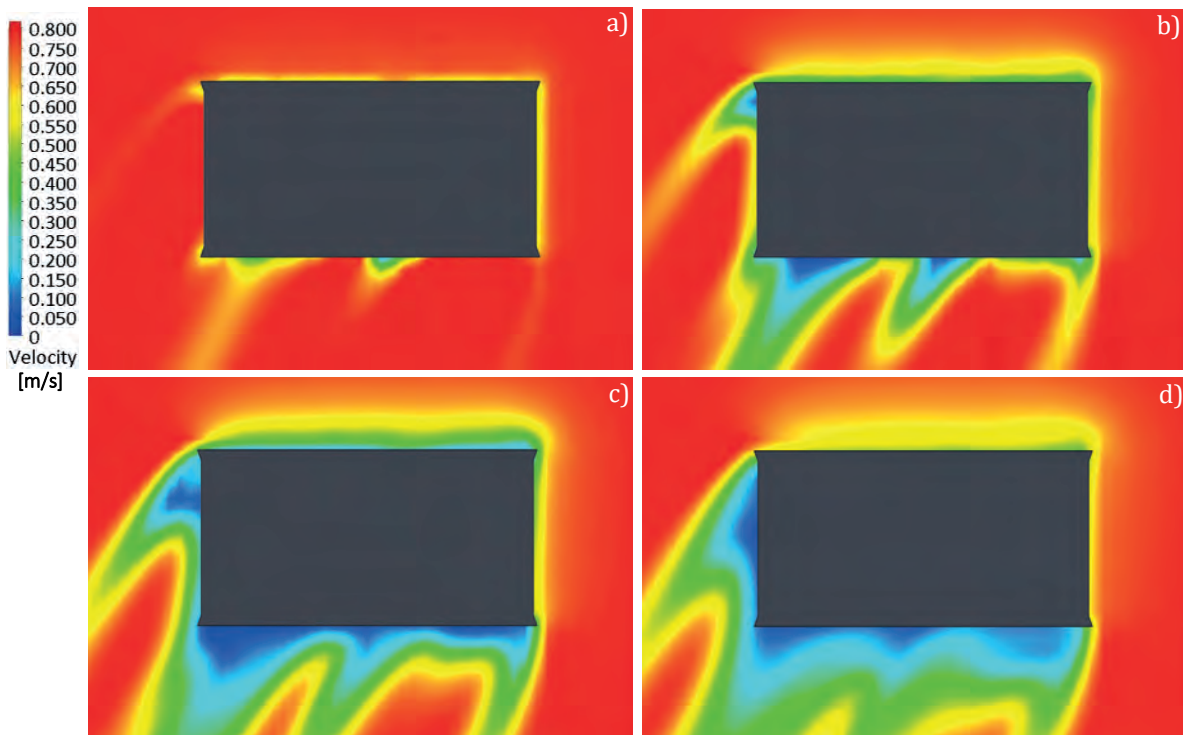


Figure 3.26 CFD Simulation of the top view of the buildings Q and S, contour plot at 0.8 m/s.

Figure 3.26 a) shows the behavior of the wind speed at the height of 0 m at the base of the building, and Figure 3.26 b) shows the wind speed at the height of 2.4 m. Furthermore, Figure 3.26 shows the same velocity parameter at the height of 4.8 m, and finally, Figure 3.26 d) shows the CFD simulation at the height of 7.2 m, which corresponds to the total height of the building.

In addition, these simulations can determine that a turbulence zone in the South backward part of the building exists and has an incremental behavior in relation to the wind speed parameter with the height of the building. This can be noted because of the reduction of the wind velocity from the initial condition of 0.8 m/s to 0.15 m/s. It can be concluded that at this rear point of the building, the installation of SWTs for side-mounted configuration cannot be considered.

In these simulations, the initial conditions and computational domains of CFD are those shown in Table 3.7, which follow the configuration of the computational fluid dynamics in relation to the wind flow characteristics.

Table 3.7 Initial and boundary conditions for the CFD simulations ( $\mu S$ ) of the TESE case study.

Analysis Type	Fluid Type	Boundary Conditions	Initial and Environment Conditions	Mesh Configuration
Type of flow: external	Air with all its physical properties	Roughness length: 1,600,000 $\mu m$	<i>a) Thermodynamic parameters:</i> -Temperature environment: 17.4 °C = 290.5 °K. -Atmospheric pressure of 77,908 Pa	Automatic mesh with 2,205,818 control volume cells
Gravitational force: -9.81 m/s <sup>2</sup>	Turbulent flow		<i>b) Velocity parameters:</i> Average wind speed of 0.8 m/s at 30°. It comprises 0.69 m/s in the "x" component and speed of 0.4 m/s for "y" component.	
			<i>c) Turbulence parameters:</i> -Length of turbulence of 38 m -Turbulence intensity of 0.040%.	
			<i>d) Humidity parameters:</i> -Average relative humidity of 52.73%.	

When the CFD analysis of Figure 3.21 is reviewed, the wind speed parameter, that reaches the buildings Q and S is 0.8 m/s, which determines the new wind speed to which the new CFD analysis will be performed. Similarly, the mesh of this analysis increases to show a higher detail around the building, with a total of 2,205,818 cells of the control volume.

Similarly, by making a cross-section of the three-dimensional building model, the result of the CFD simulations can be analyzed, as shown in Figure 3.27, which depicts the transversal a) and longitudinal b) cut plots. In these are detailed the cross-sectional side views, where can be observed the wind wake of the wind speed in the upper part of the building, forming an area with turbulence that extends to the rear of the building to about 21 m.

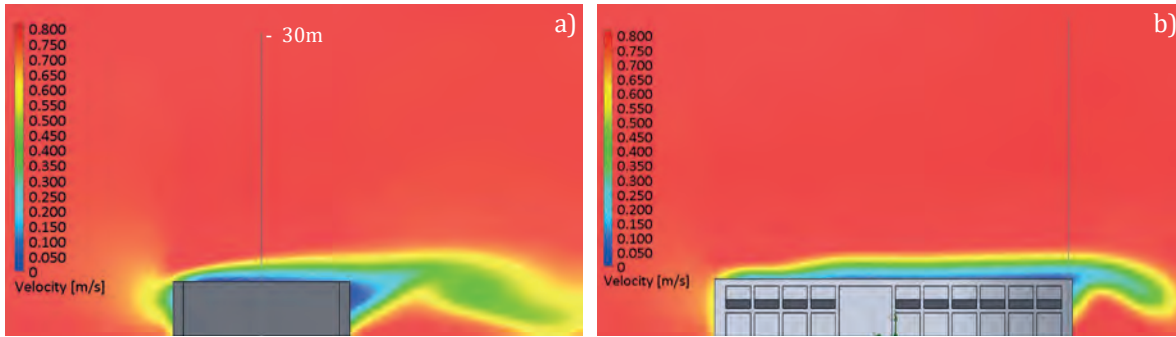


Figure 3.27 CFD Simulation side view of the buildings Q and S, contour plot of the longitudinal and transversal cuts at 0.8 m/s.

In addition, Figure 3.28 shows the transversal a) and longitudinal b) cuts of the isometric view of CFD simulations, determining that around 30 m in height would be an optimum hub height for the SWTs' installation. This CFD analysis shows that it can be determined that there is no problem with the turbulence parameter when placing the SWTs at that height because of the interaction of the wind flow with the building.

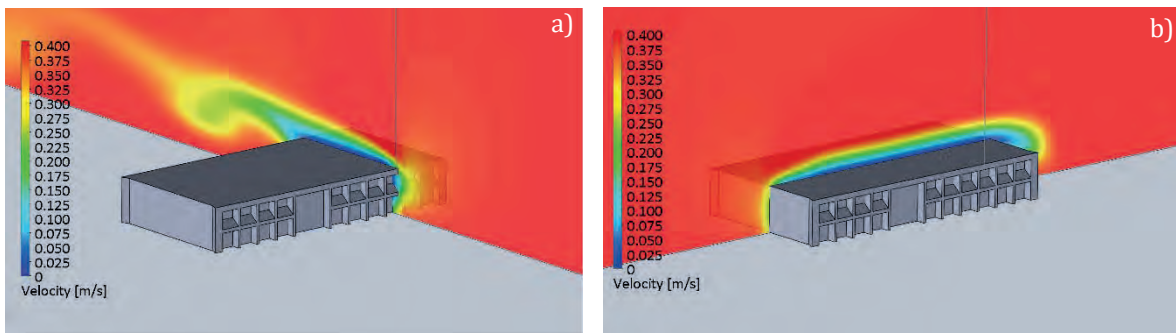


Figure 3.28 CFD Simulation isometric view of the buildings Q and S, contour plot of the longitudinal and transversal cuts at 0.8 m/s.

With these previous simulations, it is possible to determine the optimal hub height of the wind turbines, allowing to reduce the feasibility study time when using previous models for wind energy engineering applications. The optimal proposed tower height of 30 m that the small wind turbines have determined by the CFD simulation also corresponds to 4.16 times the height of the building. The use of CFD techniques allows assisting the design process for the installation of wind turbines, corresponding to the CFD analysis of the SWTs, which is the next stage of the proposed methodology.

### 3.5.6 Stage 5a – CFD Configuration of the small wind turbines (SWTs).

Once the three-dimensional models were selected and developed in CAD presented in Section 3.2 and Section 3.3, respectively. The CFD simulations are performed with the initial and boundary conditions based on the technical characteristics of the turbines, including parameters that will define the study such as the nominal speed, the flow, and fluid type, thermodynamic variables, and turbulence parameters.

The following five phases of the configuration of the CFD analysis for the proposed wind turbines are detailed. These phases will serve to determine the behavior and specify the optimal places or determine the matrix arrays of the SWTs to be installed.

**1.- Type of Analysis.-** The type of flow, in this case, is internal because analyzing the behavior of the fluid within the calculated computational domain is required. In this same phase, the gravitational force that acts on the z-component of the three-dimensional model's coordinate system is defined

**2.- Type of Fluid.-** The type of fluid to be analyzed in the present methodology is air, including all the properties that characterize it. The fluid used defines the type of turbulent flow with its respective humidity.

**3.- Contour or Wall Conditions.-** In this phase, the roughness length is defined. This length will allow describing the urban environment, as well as the characteristics of the trees and shrubs that surround the macro-siting. In addition, a roughness length of 1.6 meters is selected, which is equivalent to 1,600,000  $\mu\text{m}$  that describes the classification for large cities with tall buildings and forests. This is based on the roughness classification and its respective lengths.

**4.- Computational Domain.-** In this phase, it is possible to characterize the space that will occupy the fluid in question (air). This computational domain allows proposing the boundary and initial conditions to which small wind turbines will be subjected. The computational domain can be designed in different shapes. In this case, the parameters of the fluid velocity will be the nominal speeds at which the wind turbines operate, as shown in Table 3.1, and includes a computational domain of a rectangular prism, which will be analyzed and used.

Extensive research was developed in relation to the computational domain used in CFD simulations for the aerodynamic study of wind turbines. This allowed determining the ideal size that allows assuring the minimum interference of the boundary or contour conditions of the aerodynamic forces on the selected wind turbines. On the other hand, the computational domain also does not exceed the appropriate dimensions because it directly influences the computational time and cost [100].

In relation to the computational domain, depending on the CFD software and the type of analysis to develop, the shape of this domain is different and must be large enough to assure the minimum interference between the boundaries and the aerodynamic forces over the model studied. The most common computational domain shape is rectangular, and other domain shapes used are cylindrical and spherical.

Various research shows different dimensions in the use of the rectangular prism computational domain for the wind turbines analysis. This domain has a specific size for HAWTs [100]–[104] and other dimensions for the VAWTs [81], [105]–[109]. In Figure 3.29 and Figure 3.30, the dimensions of the computational domain are shown based on the diameter of the horizontal axis and vertical axis wind turbine, respectively for a CFD analysis.

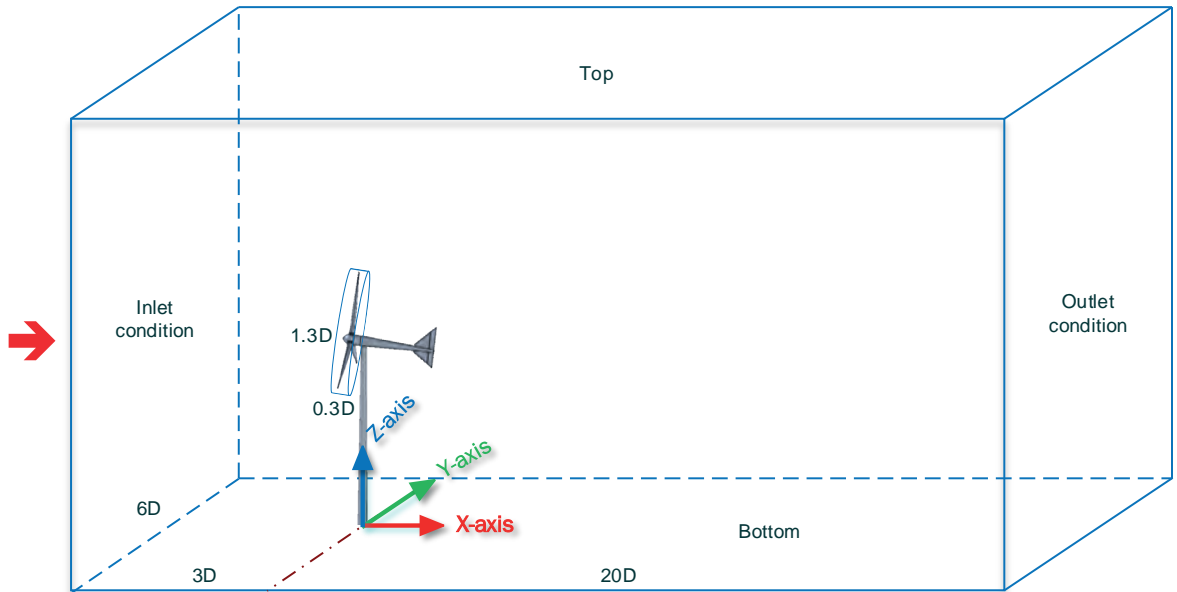


Figure 3.29 Computational domain dimensions for Horizontal Axis Wind Turbine HAWT.

As can be seen in Figure 3.29, there is an inlet condition located at three times the rotor diameter of the wind turbine, which corresponds to the input of nominal wind speed. On the other hand, the outlet condition is expected to be 20 times the diameter after the wind turbine. Finally, six times the diameter, three per side, are required at sides of the wind turbine. Regarding the computational domain of the VAWT turbines in Figure 3.30, the wind turbine is placed at a distance of 6D away from the inlet condition and a distance greater than 20D from the outlet condition. In this case, six times the diameter per side is required. The rotating region is presented in both figures with their respective dimensions. The nominal rotational speed of the turbines to which the simulations will be subjected is shown in Table 3.1.

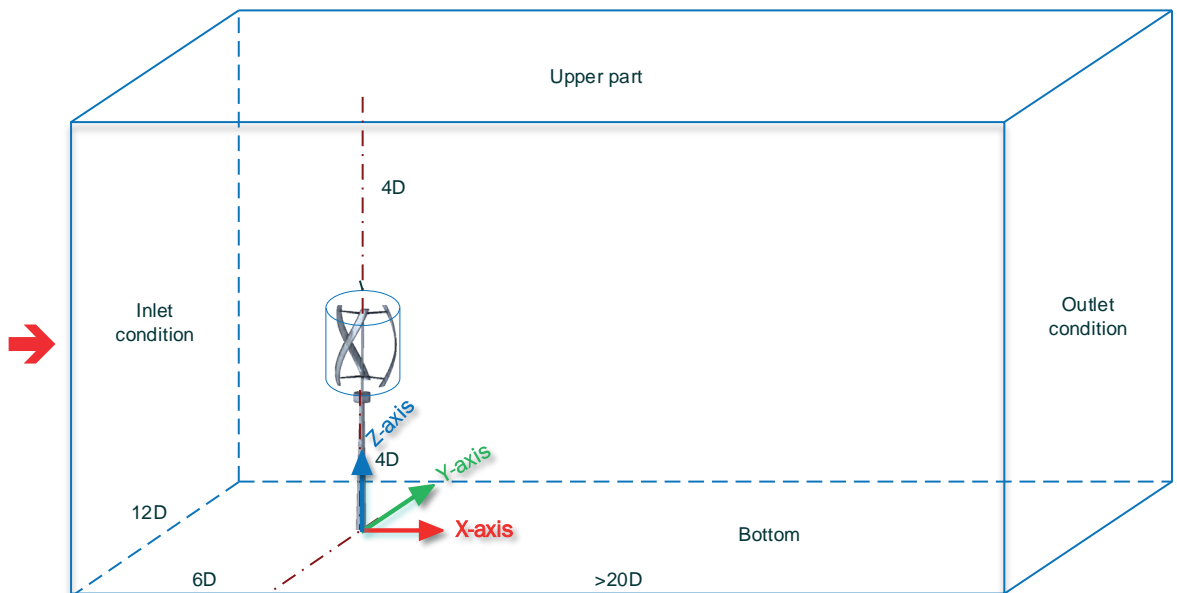


Figure 3.30 Computational domain dimensions for Vertical Axis Wind Turbine VAWT.



**5.- Mesh Configuration.-** For these CFD simulations, a manual mesh configuration is selected, with a high level of refinement, and the largest possible number of rectangular cells, in constraint with the computational time and cost. In summary, the previous phases determine the parameters of the initial and boundary conditions, which can be summarized in Table 3.8, which shows the characteristics and conditions that allow describing the environment of the CFD simulations of wind turbines. For the study of wind turbines, there is an average of 2,116,718 cells that make up the mesh, with 112,879 cells of the fluid in contact with the solid.

Table 3.8 Initial and boundary conditions for the development of CFD simulations of SWTs.

Analysis Type	Fluid Type	Boundary Conditions	Initial and Environment Conditions	Mesh Configuration
Type of flow: internal	Air with all its physical properties	Roughness length: 1,600,000 $\mu\text{m}$	<i>a) Thermodynamic parameters:</i> -Temperature environment: 17.4 °C = 290.5 °K. -Atmospheric pressure of 77,908 Pa	a. Bergey Excel -2,117,682 cells -Cells in contact with the solid 114,108
Gravitational force: -9.81 m/s <sup>2</sup>	Turbulent flow		<i>b) Velocity parameters:</i> Nominal wind speed of small wind turbines: <b>-HAWTs</b> a. Bergey Excel – 12 m/s @400rpm b. Skystream 3.7 – 11 m/s @325rpm <b>-VAWTs</b> c. Aeolos V-10 kW – 11 m/s @150rpm d. Aeolos V-5 kW – 11 m/s @100rpm	b. XZERES Skystream -2,117,634 cells -Cells in contact with the solid 114,005
			<i>c) Turbulence parameters:</i> -Length of turbulence of 38 m -Turbulence intensity of 0.040%.	c. Aeolos V-10 kW -2,114,118 cells -Cells in contact with the solid 109,502
			<i>d) Humidity parameters:</i> -Average relative humidity of 52.73%.	d. Aeolos V-5 kW -2,117,438 -Cells in contact with solid 113,900

### 3.5.7 Stage 5b – CFD Simulations of the small wind turbines (SWTs).

In this stage, the CFD simulations are performed for the four SWTs models proposed. As a representative manner of the CFD simulation, only two of the four models selected will be presented. This corresponds to the Bergey Excel wind turbine model in a HAWT configuration, and the Aeolos V-10 model in a VAWT configuration, both with a rated power of 10 kW. In both cases, the steady-state and the rotational-state CFD simulations have been performed.

#### A1) Bergey Excel 10 kW wind turbine – Steady-state simulation

Figure 3.31 shows the results of this first simulation, which represents the prevailing wind direction on the  $x$ -axis with its respective nominal speed at which the wind turbine operates. This simulation is part of the micro-siting ( $\mu\text{S}$ ) process.

These simulations show the surface wind speed in the a) side view and b) top view of the wind turbine CAD model at the height of the nacelle. As seen with these simulations, there is no fast wind wake regeneration, even after the 140 m that corresponds 20 times the diameter (7m) backward of the wind turbine.

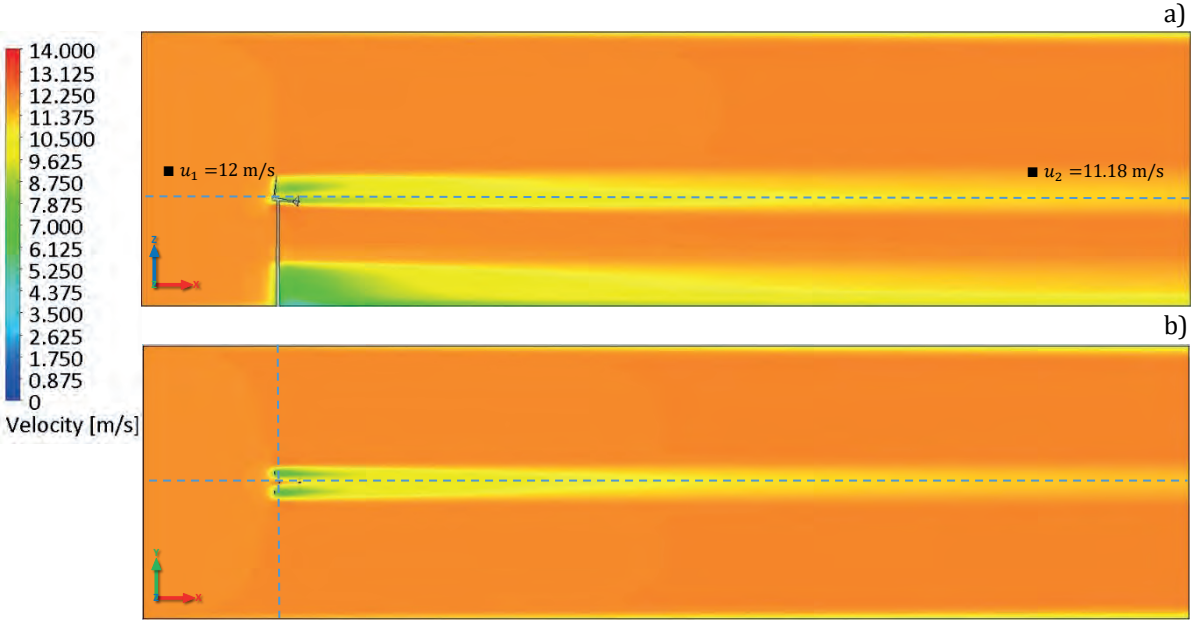


Figure 3.31 Steady-state CFD simulation of Bergey Excel 10 kW wind turbine – Cut plots: a) Side View and b) Top View.

By taking into account the same initial and boundary conditions, Figure 3.32 presents the a) front view and b) isometric view of the Bergey Excel turbine in which the streamlines are generated when subjected to the nominal speed of 12 m/s.

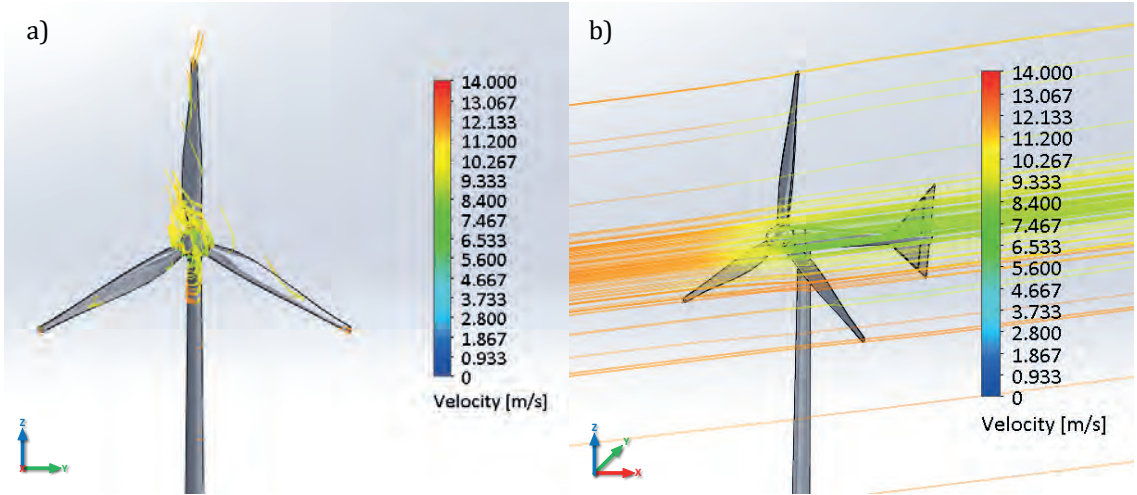


Figure 3.32 Steady-state CFD simulation of Bergey Excel 10 kW wind turbine – Flow streamlines: a) Front View and b) Isometric View.

## A2) Bergey Excel 10 kW wind turbine – Rotational-state simulation

In this type of CFD simulation, the rotation of the turbine blades is considered at the nominal speed at which the wind turbine operates. Unlike the stationary simulation, in this simulation, a rotating region is considered, that has dimensions that are based on the diameter of the rotor. This rotating region is 1.3 times the diameter of the turbine and a thickness of 0.3 times the diameter shown in the computational domain diagram of Figure 3.29, for the analysis of horizontal axis wind turbines [101].

This rotational simulation will allow obtaining a better approximation of the behavior of the wind wake behind the wind turbine at nominal operation. In addition, this CFD simulation will allow proposing the matrix arrangement for the location of the SWTs on the building-mounted wind turbine configuration. In Figure 3.33, the rotational CFD simulation side view of the selected wind turbine is shown.

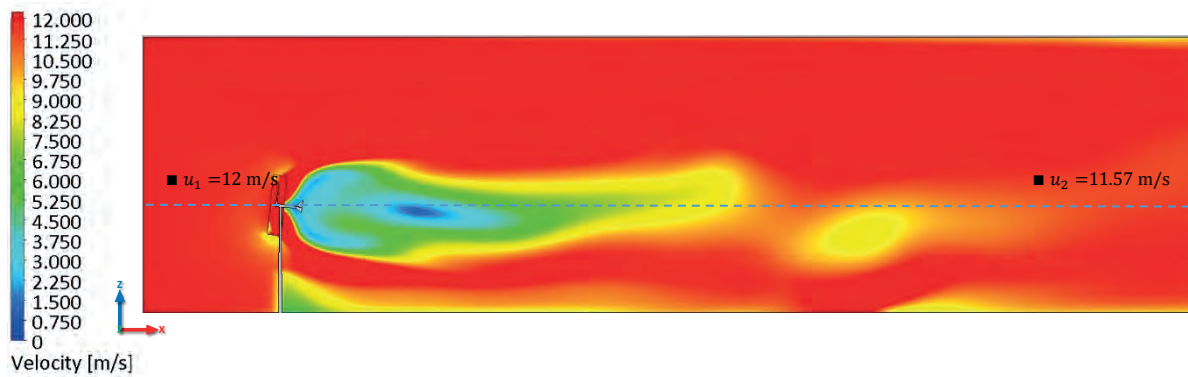


Figure 3.33 Rotational-state CFD simulation of Bergey Excel 10 kW wind turbine – Cut plot: Side View.

In addition, the top view is included, as shown in Figure 3.34, where the prevailing wind direction in the  $x$ -axis is represented. This simulation was performed at its respective nominal speed of 400 rpm at which the wind turbine operates.

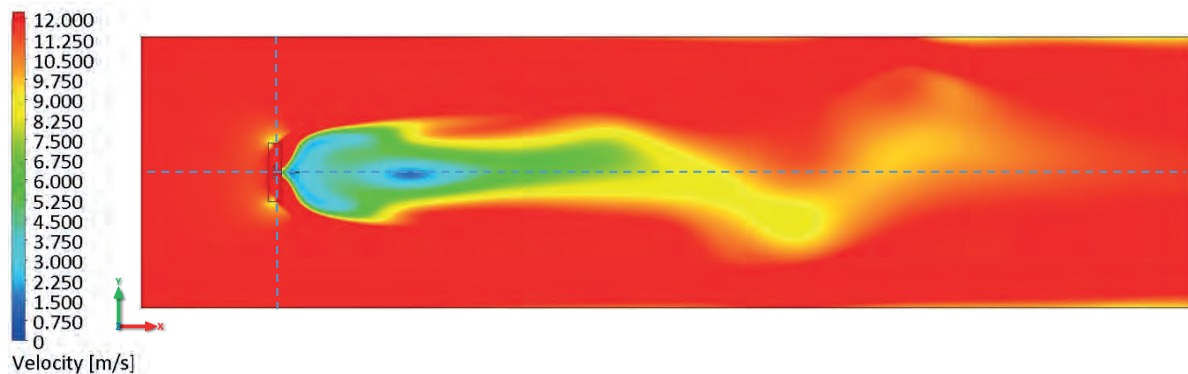


Figure 3.34 Rotational-state CFD simulation of Bergey Excel 10 kW wind turbine – Cut plot: Top View.

It can be observed that the wind regeneration through the  $x$ -axis is more efficient and faster in a rotational-state simulation than in the steady-state one. This simulation results in a distance approximately 15 times the diameter of the Bergey Excel wind turbine, considering the nominal angular and linear speed at which it operates.

If the wind turbine is installed with lower wind conditions, however, considering an average speed lower than 12 m/s, the regeneration of the wind through the turbine will be much faster, and the effect of the wind wake regeneration will improve. In Figure 3.35, the a) side view and b) top view of the wind streamlines passing through the turbine are shown, indicating the angular velocity that is formed when the turbine is in operation. This allows affirming that the regeneration of the wind wake is presented at a minor distance compared with the steady-state CFD simulation. This wake behind the SWT is considered as a turbulent wake, which is derived from the conservation of the energy momentum downstream of the wind turbine.

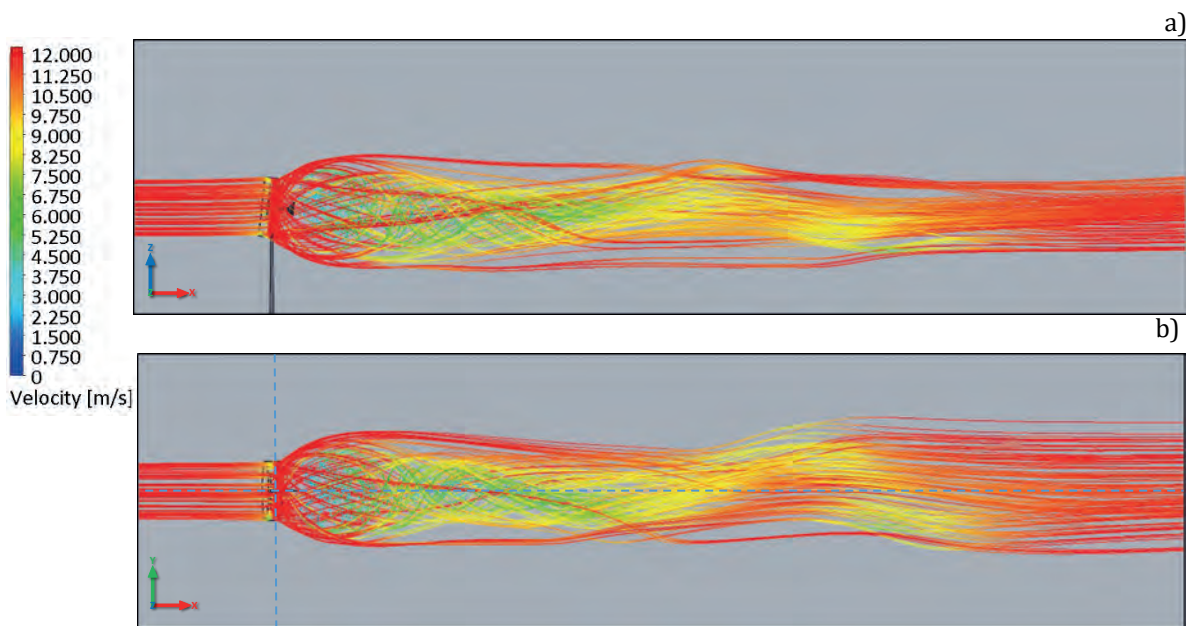


Figure 3.35 Rotational-state CFD simulation of Bergey Excel 10 kW wind turbine – Streamlines: a) Side View and b) Top View.

To complete this analysis, Figure 3.36 shows the a) isometric view and b) front view of the turbine in which are shown the streamlines that are generated when subjected to the nominal angular speed.

With these simulations, it is possible to determine the lateral spacing that the matrix arrays of the SWTs should have on the roofs of the buildings. For this wind turbine specifically, it is considered the nominal speed, resulting in a distance between towers of 22 meters equivalent to 3.15 times the diameter. These results show a first approximation for the proper selection of wind turbines for their optimal location within urban and rural small wind projects.

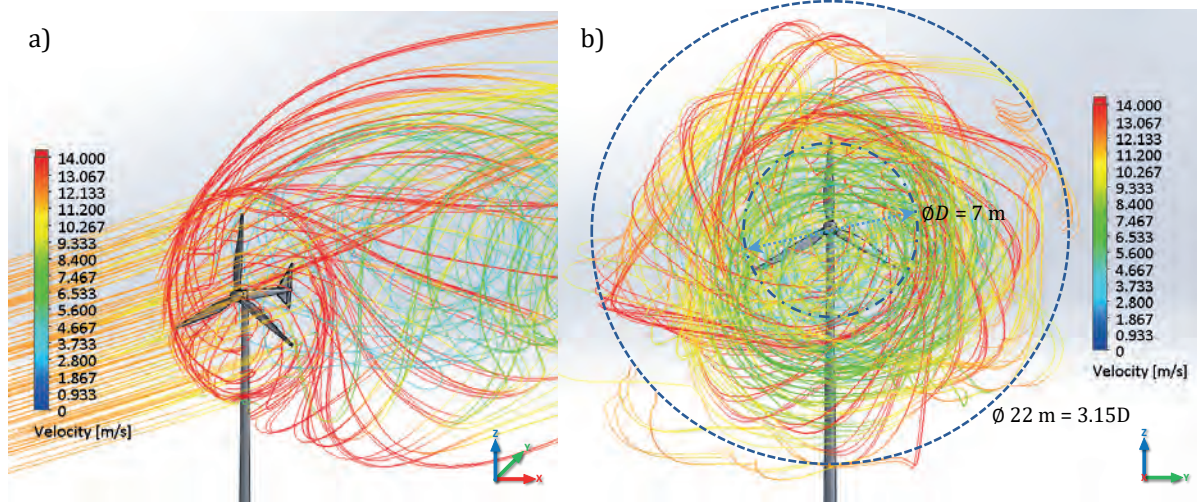


Figure 3.36 Rotational-state CFD simulation of Bergy Excel 10 kW wind turbine – Streamlines: a) Isometric View and b) Front View.

### B1) Aeolos-V 10 kW wind turbine – Steady-state simulation

The second wind turbine corresponds to the Aeolos V-10 model, which is a vertical axis wind turbine (VAWT) with a rated power range from 9.9 kW to 12 kW. This wind turbine model could start at 2.5 m/s wind speed. According to the American Wind Energy Association (AWEA) standard, the Aeolos V-10 has an annual output of 7.1 MWh at 5 m/s wind speed. The annual output at 10 m/s is around 60.4 MWh. In addition, this model offers a remote monitoring system in order to review the operation of the wind turbine.

Figure 3.37 shows the steady-state CFD result of the wind turbine with a prevailing wind direction in the  $x$ -axis. These simulations show the surface wind speed in a side view of the wind turbine CAD model.

The Aeolos V-10 wind turbine presents a slow wind wake regeneration with a turbulence zone in the back of the wind turbine. This wind speed decreases from 11 m/s to 10.55 m/s, representing a loss of 4.09%.

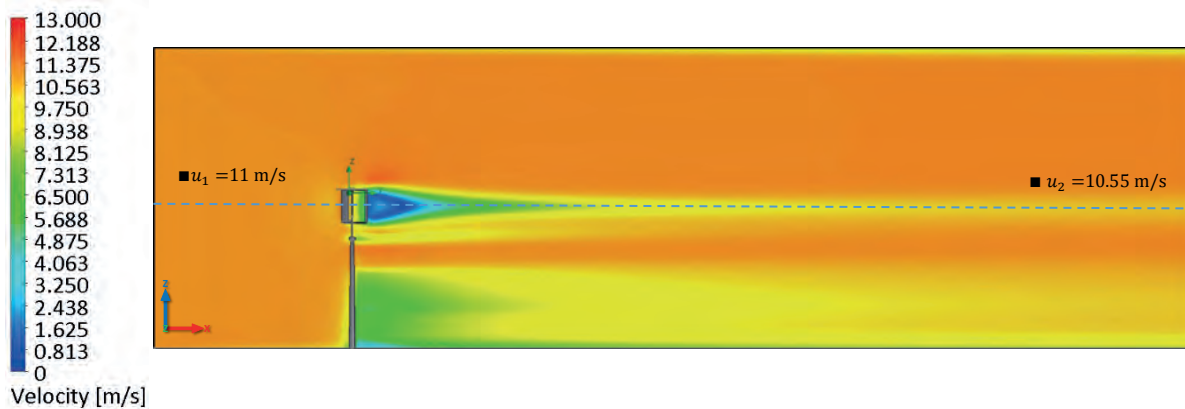


Figure 3.37 Steady-state CFD simulation of the Aeolos V-10 wind turbine – Cut plot: Side View.

Figure 3.38 presents the top view and both a turbulence zone and a wind speed decrease because of the arm of the airfoil, which is subjected perpendicularly to the wind flow can be observed in the CAD model. In addition, a small deviation of the flow in wind currents occurs with a wind speed of around 7.3 m/s.

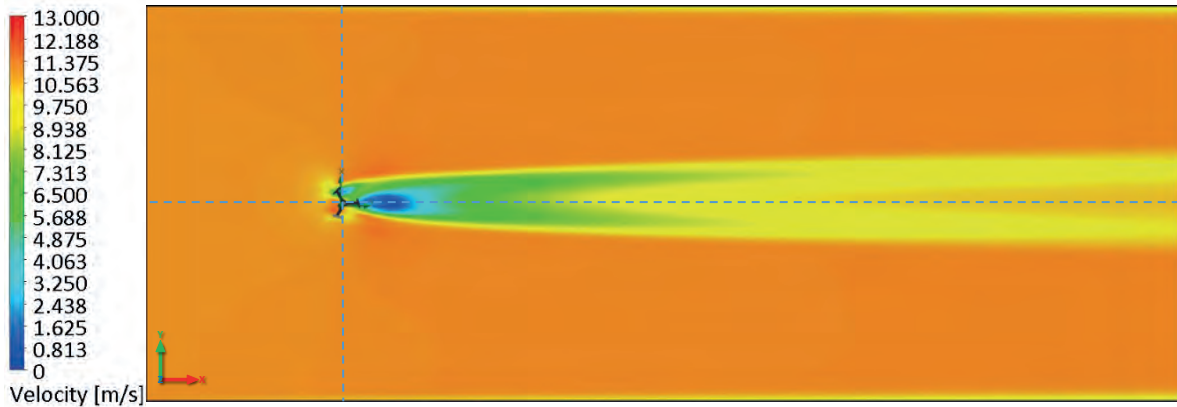


Figure 3.38 Steady-state CFD simulation of the Aeolos V-10 wind turbine – Cut plot: Top View.

Figure 3.39 presents the a) front view and b) isometric view of the Aeolos V-10 turbine in which the streamlines are generated when subjected to the nominal speed of 11 m/s. This allows observing the wind currents' behavior around the SWTs and gives an overview of the spacing location of wind turbines.

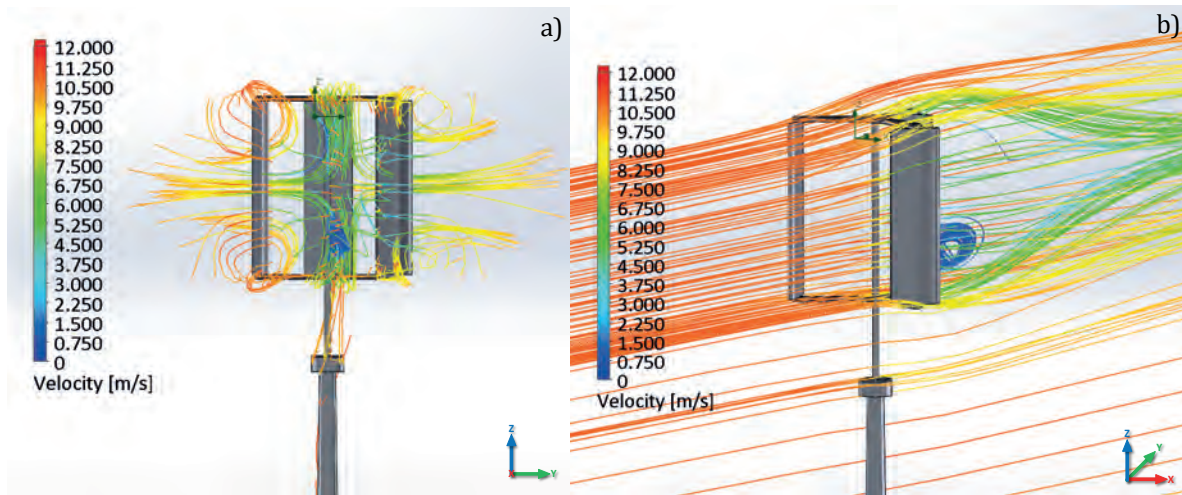


Figure 3.39 Steady-state CFD simulation of the Aeolos V-10 wind turbine – Flow streamlines: a) Front View and b) Isometric View.

## B2) Aeolos-V 10 kW wind turbine – Rotational-state simulation

Moving to the CFD simulations of the Aeolos V-10 wind turbine in the rotational state, Figure 3.40 presents the side view result of the simulation. Unlike the steady-state simulation, this simulation has a wind wake with a higher turbulence zone in the back of the wind turbine and an increment of wind speed around the wind turbine caused by the rotational speed to which it is subjected.

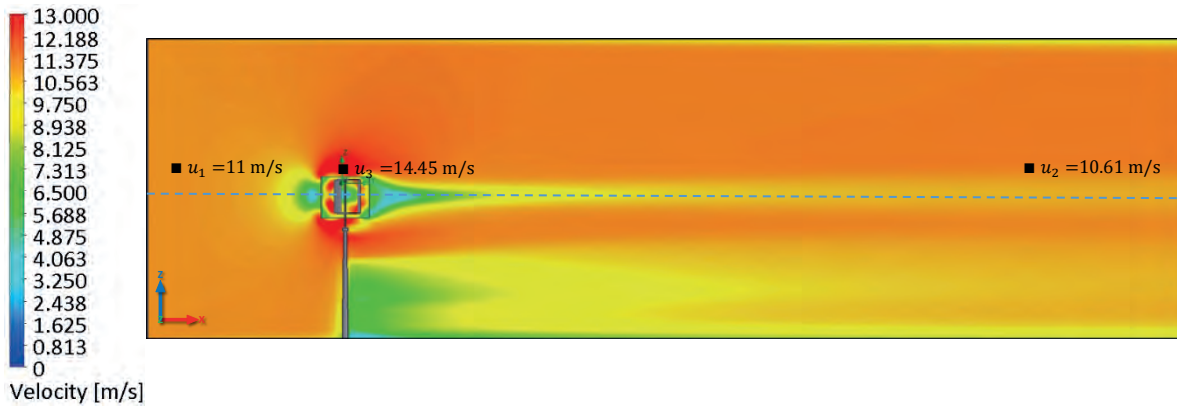


Figure 3.40 Rotational-state CFD simulation side view of the Aeolos V-10 wind turbine – Cut plot.

The CFD simulation allows showing a wind speed decrease from 11 m/s to 10.61 m/s, representing a loss of 3.54%, which indicates a lower loss than the steady-state CFD simulation. The region at the top and bottom of the circumference of the wind turbine presents an increment of the wind speed caused by the simulated rotational region having wind speeds of around 14.45 m/s.

Furthermore, the CFD simulation represented in Figure 3.41 shows the top view, which has a rotational region of the fluid with a higher area than the steady-state CFD simulation. In addition, from this top view, a flow bifurcation of the wind stream can be observed, which also indicates a slow regeneration and the presence of high turbulence in the back of the wind turbine compared with the steady-state CFD simulation. If the wind speed is measured at the inlet condition of the simulation and compared with the outlet condition, this manages a slightly lower wind wake regeneration presented in Figure 3.40 before the wind turbine.

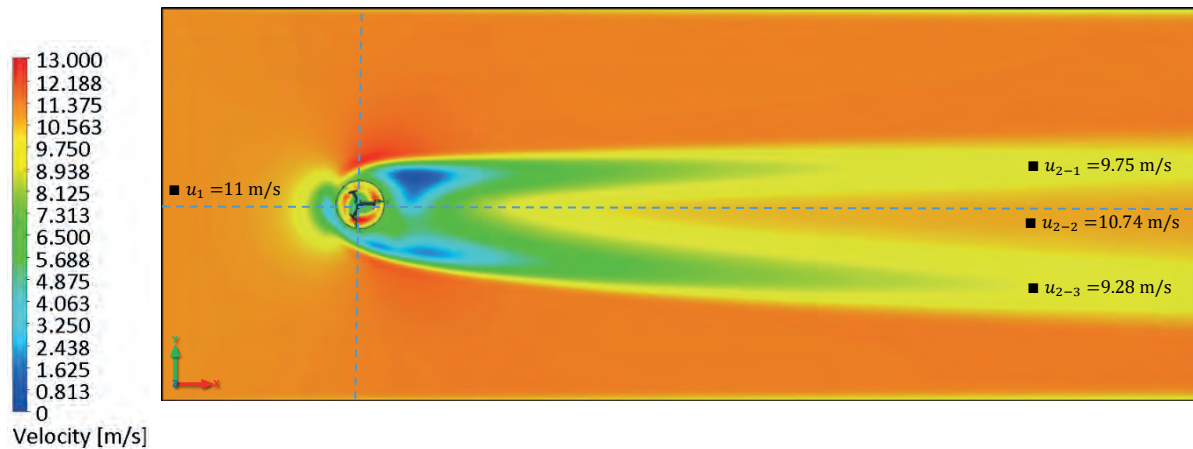


Figure 3.41 Rotational-state CFD simulation top view of the Aeolos V-10 wind turbine – Cut plot.

The same behavior is presented in Figure 3.42, where the streamlines depict the turbulent wind flow of the wind turbine in both the side view and top view. Clearly, in Figure 3.42 a), the turbulence zone and a reduction of wind stream in the back of the wind turbine can be observed.

The increment of the wind speed above and below the small wind turbine is also corroborated. In addition, the wind wake regeneration starts to recover after 25 m but does not recover completely for again reaching the inlet condition of 11 m/s even after the 140 m at which the computational domain is established

On the other hand, Figure 3.42 b) illustrates the top view, which includes the wind streamlines formed when the air passes through the wind turbine. Clearly, there is a light flow bifurcation of the wind stream in the *y*-axis caused by the interaction of the fluid with the wind turbine, allowing the presence of turbulence.

This bifurcation presented in the CFD simulation permits showing at the outlet condition three different wind speeds along the *y*-axis. These wind speeds are 9.75 m/s, 10.74 m/s, and 9.28 m/s, which correspond to losses of 11.36%, 2.36%, and 15.63%, respectively.

Based on the above, it is possible to estimate the location of the SWT directly aligned to the tower from the first column after the computational domain simulated at 140 m for this case.

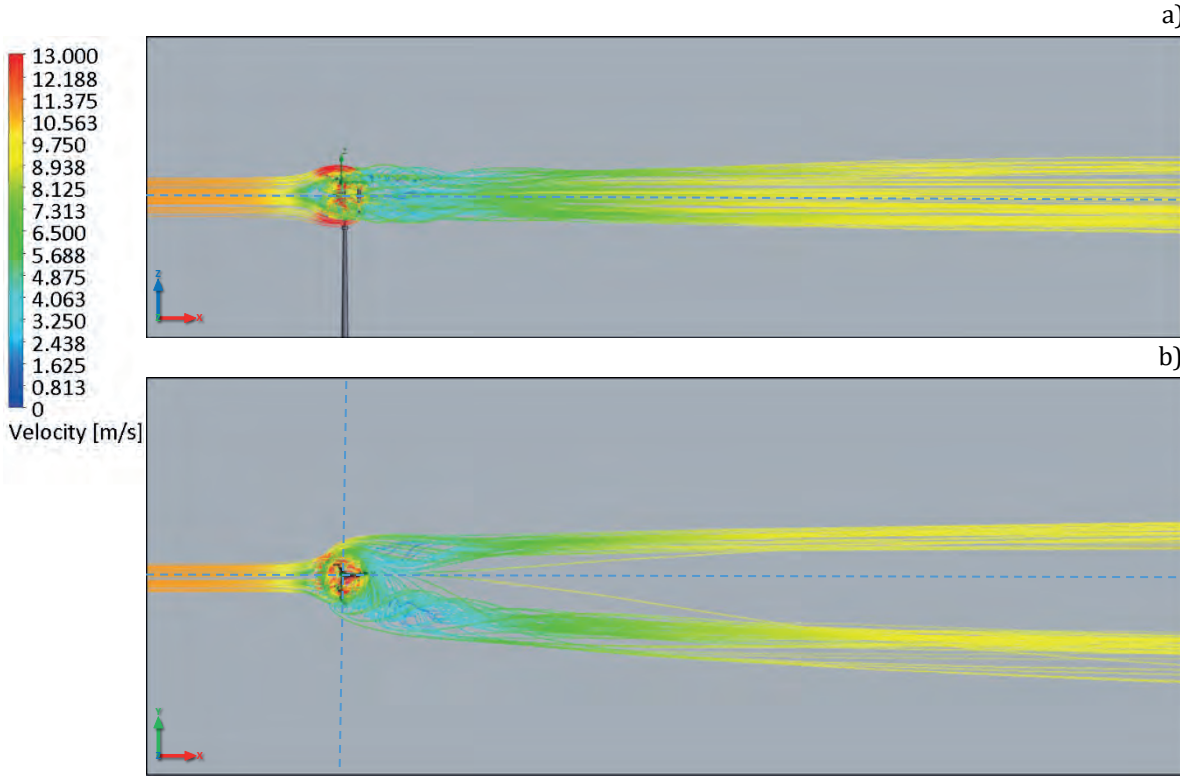


Figure 3.42 Rotational-state CFD simulation of the Aeolos V-10 wind turbine – Streamlines: a) Side View and b) Top View.

To determine the separation of rows and columns of the SWTs matrix arrangements, Figure 3.43 is presented, which depicts the top view a) and the isometric view b) of the same rotational CFD simulation showing the operation of the VAWTs' configuration and how the wind turbine receives the wind resource.



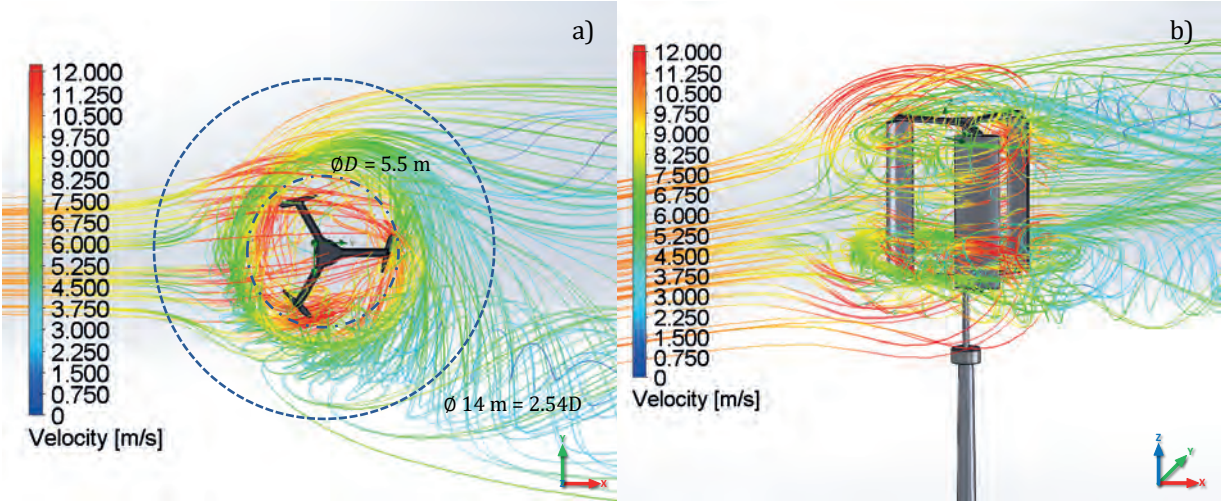


Figure 3.43 Rotational-state CFD simulation of the Aeolos V-10 wind turbine – Streamlines: a) Top View and b) Isometric View.

Based also in the previous CFD simulation, it is possible to determine the lateral spacing that the matrix arrays of the vertical axis SWTs should have. For the Aeolos V-10 model and considering the nominal rotational speed of 150 rpm, the turbines would have to be located at a distance between towers of 14 meters equivalent to 2.54 times the diameter (5.5m) of the wind turbine. In the following section, the matrix arrangements based on the CFD simulations performed for both cases of the SWTs will be proposed.

### 3.5.8 Configuration matrix array of the proposed SWT

In a feasibility study for the proper installation of a wind project, that each wind turbine extracts the kinetic energy from the wind resource is considered, resulting in lower speeds behind every SWTs, as shown in the CFD simulations' results. In this case, having less energy available for the downstream turbines in the wind project.

For this reason, the CFD results of the proposed SWTs and using the Jensen wake model, also referred to as Park Model [110], a proper distance behind the rotor of the SWTs installed in the first row of the matrix array can be estimated.

The Jensen wake model is based on the conservation of momentum, which assumes a uniform velocity profile and linear expansion of the wake. If the wind is flowing perpendicularly to a row of SWTs, the wind speed  $u_2$  in the second row can be determined using Eq. 3.7 from [110]–[112], where  $u_1$  is the wind speed at the first turbine in the upwind direction:

$$u_2 = u_1 \left[ 1 - \frac{D^2(1 - \sqrt{1 - C_T})}{(1 + 2\kappa x)^2} \right] \quad (3.7)$$

where  $C_T$  is the thrust coefficient,  $D$  is the rotor diameter, and  $x$  is the distance between turbines. The variable  $\kappa$  is the wake decay constant, which determines how fast the wake expands with the distance. The wake decay is based on ambient turbulence and atmospheric stability [111]. This wake decay can be calculated with the expression:

$$\kappa = \frac{\alpha}{\ln\left(\frac{h}{z_0}\right)} \quad (3.8)$$

where the variable  $\alpha \cong 0.5$ ,  $h$  is the hub height of the wind turbine and,  $z_0$  represents the surface roughness of the wind project. The parameter  $z_0$  is crucial in the decay coefficient calculation. The constant decay  $\kappa$  has a default value of 0.075 in most terrain cases. For offshore applications, using a  $\kappa$  value of 0.04 is recommended [111].

Regarding the  $C_T$ , the maximum value would be when  $a = 1/2$ , corresponding to  $u_2 = 0$  but a more realistic value, correspond to Betz criterion occurs when  $a = 1/3$ , leading to a thrust coefficient of  $C_T = 8/9$ , based on the Eq. 3.9: [110]

$$C_T = 4a(1 - a) \quad (3.9)$$

With these equations bear in mind, and the previous CFD simulations of the SWTs, the proper matrix arrays for each wind turbine model for the dimension between rows and columns of the wind project can be developed.

The wake losses were calculated with the Jensen model according to the previous CFD results. These wind speeds are based on the dynamic display of the inlet and outlet conditions of the air velocity parameter. The wind velocity  $u_2$  in the Jensen wake model is calculated based on the inlet conditions  $u_1$  (nominal wind speeds) configured at the CFD simulations both in steady-state and rotational-state simulations of all the SWTs. Table 3.9 shows a comparison between the CFD simulations and the Jensen wake model. The wind turbine with fewer losses is the Aeolos V-5 wind turbine model with 0.18%.

Table 3.9 Comparison between CFD simulation and Jensen wake model under steady and rotational states.

SWTs models	CFD Simulation @ 140 m		Jensen wake model calculated		
	Inlet & Outlet Steady	Inlet & Outlet Rotational	$u_2$	Percentage Steady	Percentage Rotational
Bergey Excel	12 m/s & 11.18 m/s	12 m/s & 11.57 m/s	11.80 m/s	5.16 %	1.91 %
Skystream 3.7	13 m/s & 12.67 m/s	13 m/s & 11.10 m/s	12.94 m/s	2.07 %	14.15 %
Aeolos V-10	11 m/s & 10.55 m/s	11 m/s & 10.61 m/s	10.94 m/s	3.54 %	3.0 %
Aeolos V-5	11 m/s & 10.35 m/s	11 m/s & 10.91 m/s	10.89 m/s	4.90 %	0.18 %

By analyzing the SWTs selected, the configuration of the matrices' arrangements considers only one row with multiple columns. Taking into account that the row is located perpendicularly to the prevailing wind direction. On the other hand, the distance between columns (wind turbines' tower) of the matrices will be determined only by the rotational-state CFD simulations of the SWTs presented in the previous section.

Table 3.10 below shows the distance that the matrix arrangements' columns will have between small wind turbines based on the rotational CFD results. It can be noticed that this distance is related to the size of the rotor diameter.

Table 3.10 Proposed distance between SWTs based on the CFD rotational simulations.

SWTs	Type	Nominal power	Rotor diameter	Tower height	Distance between wind turbines
Bergey Excel	HAWT	10 kW @ 12 m/s	7.0 m	18 m	22 m or 3.15D
XZERES Skystream	HAWT	2.6 kW @ 13 m/s	3.7 m	10 m	8 m or 2.16D
Aeolos V-10	VAWT - Daerrius	10 kW @ 11 m/s	5.5 m	18 m	14 m or 2.54D
Aeolos V-5	VAWT - Helical	5 kW @ 11 m/s	4.0 m	18 m	8 m or 2D

According to these results and the micro-siting ( $\mu S$ ), it is important to know the wind power from the energy available in the wind resource. The wind leaving the wind turbine has a lower energy content as can be appreciated in the SWTs CFD simulations. The wind wake causes this energy reduction in a wind project. This loss of wind potential can range from 2% to 30%, depending on the distances between turbines and turbulence [113].

For minimizing this wind wake effect in an area of small wind emplacement, and according to the CFD results previously shown, a spacing 20 times the rotor diameter within rows in the directions of prevailing winds is stated. On the other hand, the spacing between columns depends on the diameter and nominal rotational speed ranging from 2D to 3.15D in the direction parallel to the prevailing wind.

In Figure 3.44, the layout diagram of a small wind emplacement, taking into consideration only the scheme non-staggered array, can be observed. This figure shows the possible distance at which the SWTs will be located depending on the wind resource, the location of the building or structure of interest, and the diameter of wind turbines, etc. It is important to remark that because the BUWT configuration is used, only the first row of the turbine arrangement is considered. The crosswind spacing will be determined based on the SWTs selected for each case study.

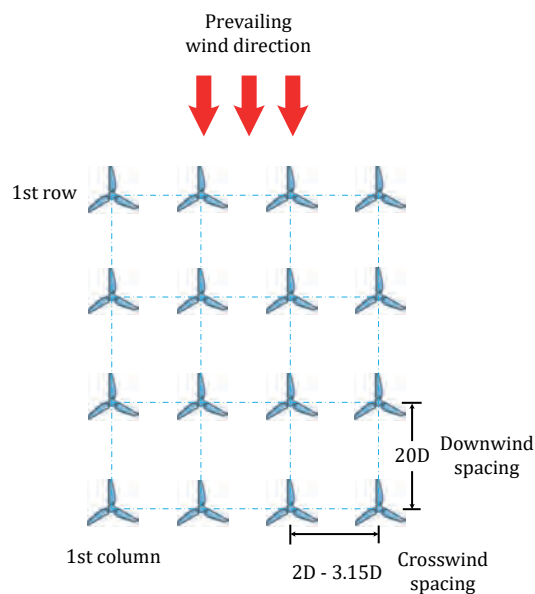


Figure 3.44 Matrix scheme for the small wind emplacements.

### 3.5.9 Stage 6 – CFD Analysis of the integration of building and SWTs

Stage 6 corresponds to the integration of the SWT and the building selected at TESE. The configuration of the small wind emplacement will be determined. The matrix arrangement and distance between turbines permit determining the final selection of the SWTs in the project. Several matrix arrays of the wind turbines are presented in Table 3.11, which represents the exact number of SWTs to be located on Building Q and the maximum capacity of the wind emplacement. Because of the characteristics of the selected building, the matrices comprise only one row and multiple columns. For the present case study and based on the dimensions of the building selected, the wind turbine selected is the Aeolus V-10 model.

Table 3.11 Configuration of the matrix arrangement dimension of the TESE case study.

SWT Model	1 <sup>st</sup> SWT	2 <sup>nd</sup> SWT	3 <sup>rd</sup> SWT	4 <sup>th</sup> SWT	5 <sup>th</sup> SWT	6 <sup>th</sup> SWT	Total capacity
Bergey 10 kW	0 m	22 m	44 m	-	-	-	30 kW
XZERES 2.6 kW	0 m	8 m	16 m	24 m	32 m	40 m	15.6 kW
A-V <sub>10</sub> 10 kW	0 m	14 m	28 m	42 m	-	-	40 kW
A-V <sub>5</sub> 5 kW	0 m	8 m	16 m	24 m	32 m	40 m	30 kW

The layout of the Aeolus V-10 wind turbine model proposes a matrix arrangement dimension with one row and four columns (1x4) positioned at every 14 meters. This layout is depicted in Figure 3.45 a), where the exact position of the Aeolus V-10 wind turbine model is marked on the roof of the building. Based on the CFD simulation process, a domain of the arrangement of the building and the SWTs is designed for this specific case study, which is shown in Figure 3.45 b).

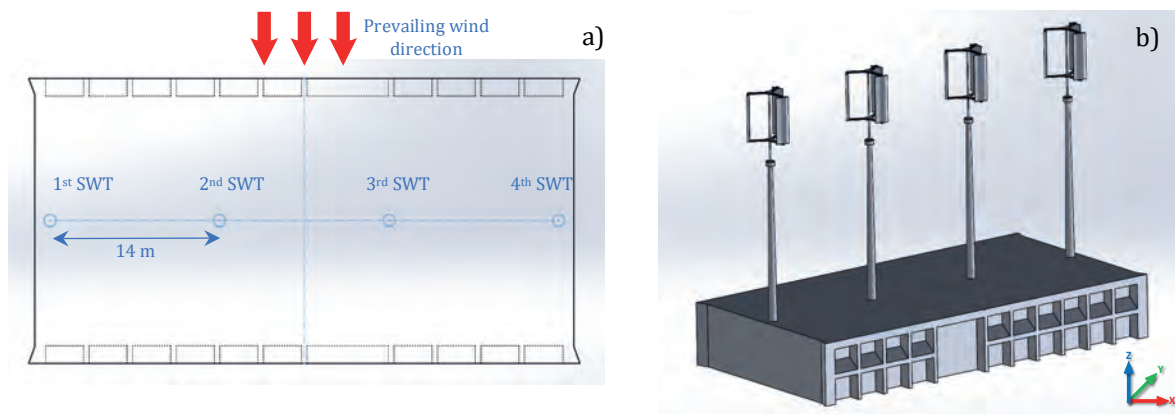


Figure 3.45 a) Layout of the matrix arrangement of the SWTs and the b) 3D model design of the building - SWTs arrangement.

Another important aspect is that the location of the SWTs and the CFD simulation of the integration of the building and the SWTs are based on the prevailing wind direction. In this case, the wind speed of 1.97 m/s corresponds to an angular speed of 6.84 rpm; a meshing with 2,204,090 cells and 106,459 cells in contact with the solid is used.

The proposed arrangement considers a 30 m hub height based on the CFD simulations of Section 3.5.7

### 3.5.10 Stage 7 – CFD Post-processing

The CFD results consider a rotational state of the wind emplacement, making it possible to determine the wind flow's behavior through the four small wind turbines, which correspond to the vertical axis Aeolos V-10 model. All the following CFD simulations are represented at 2.0 m/s resolution.

Based on Stage 4, a and b, the tower height of the SWTs was estimated at 23 m. Figure 3.46 shows the results of this CFD simulation, the a) isometric view, b) side view, c) top view and d) front view of the wind streamlines. These results show the interaction of the Aeolos V-10 wind turbines and the building of the proposed case study.

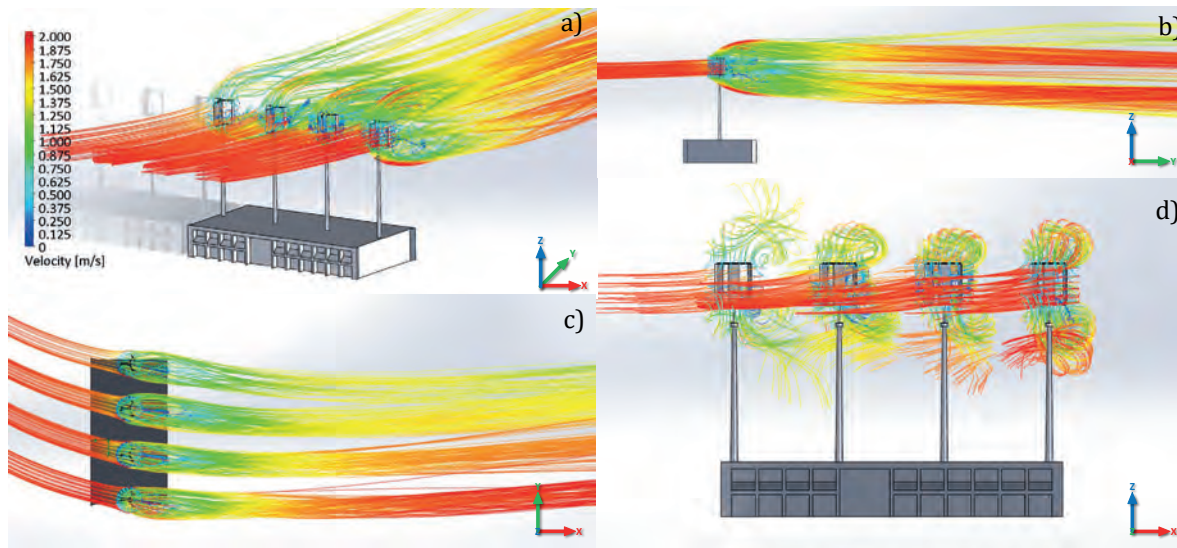


Figure 3.46 Rotational-state CFD simulation of the matrix array of the Aeolos V-10 wind turbine and the Building – Streamlines: a) Isometric, b) Side, c) Top, and d) Front views at 2.0 m/s.

In Figure 3.46 a), it can be observed that the isometric view of the CFD simulations in which behavior of the streamlines are similar between SWTs using an inlet condition of the wind speed along the  $xy$ -axis. In addition to this analysis, Figure 3.46 b) presents similar results for the standalone CFD simulation of the rotational state of the Aeolos V-10 wind turbine and also presents the flow bifurcation along the  $z$ -axis.

Similarly, Figure 3.46 c) shows the top view of the CFD simulation, which demonstrates a faster wind wake regeneration in the fourth wind turbine. A decreasing of the wind wake regeneration towards the first small wind turbine of the matrix array, however, is noticeable. Figure 3.46 d) indicates that the stated separation of 14 m between turbines is the appropriate distance for harnessing the optimal wind power. In conclusion, the SWTs do not interfere with each other, taking advantage of the maximum wind power extractable from the wind resource.

In order to complete the current case study, a final CFD simulation is performed that includes the proposed layout of four Aeolos V-10 wind turbines model in a rotational state simulation on both the Building Q and Building S, respectively.

It is important to mention that the wind flow found in the campus does not present a wind resource potential, because it has an average wind speed of 1.97 m/s. These CFD simulations are presented in Figure 3.47, which shows the wind speed at the proposed hub height of 30 m, considering the prevailing wind direction at a) 2.5 m/s and b) 2.0 m/s resolution scale.

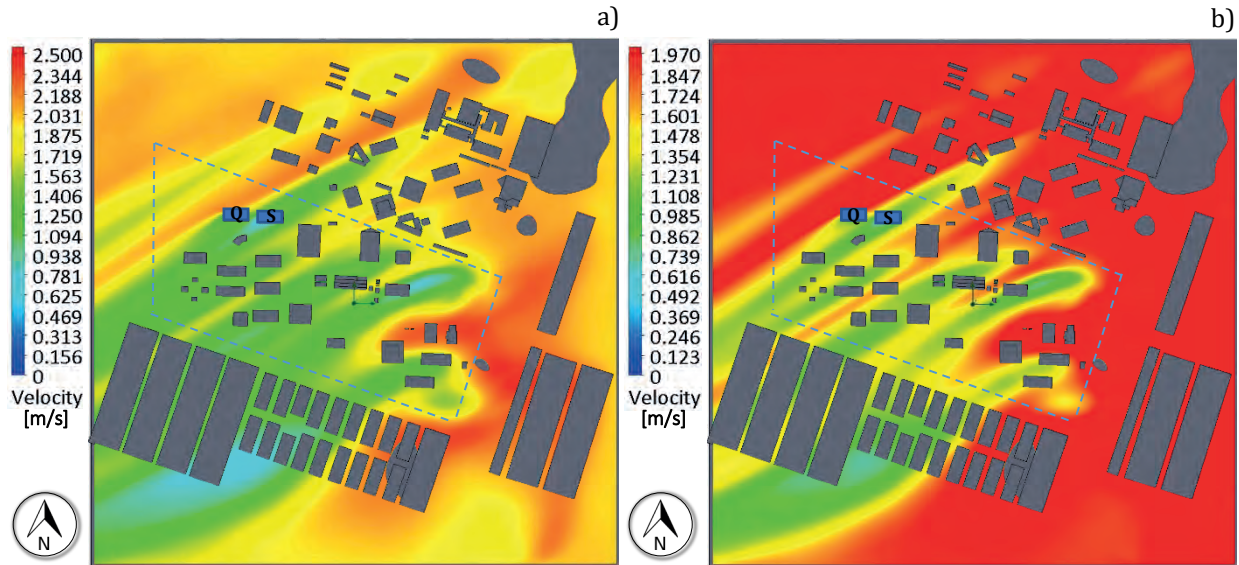


Figure 3.47 CFD Simulation at total hub height of 30 m at a) 2.5 m/s and b) 2.0 m/s.

As seen in Figure 3.47 a) and confirmed in Figure 3.47 b), Building S presents a low wind speed between 0.8 m/s and 1.5 m/s. Because of this condition, Building S cannot be considered a proper location for SWTs installation in a BUWTs configuration. Based on the previous simulations and considering the proposed SWTs' layout for the two buildings with a total installed capacity of 40 kW per building, Figure 3.48 is presented, which illustrates the streamlines of the velocity parameter that interact with the Aeolos V-10 SWTs.

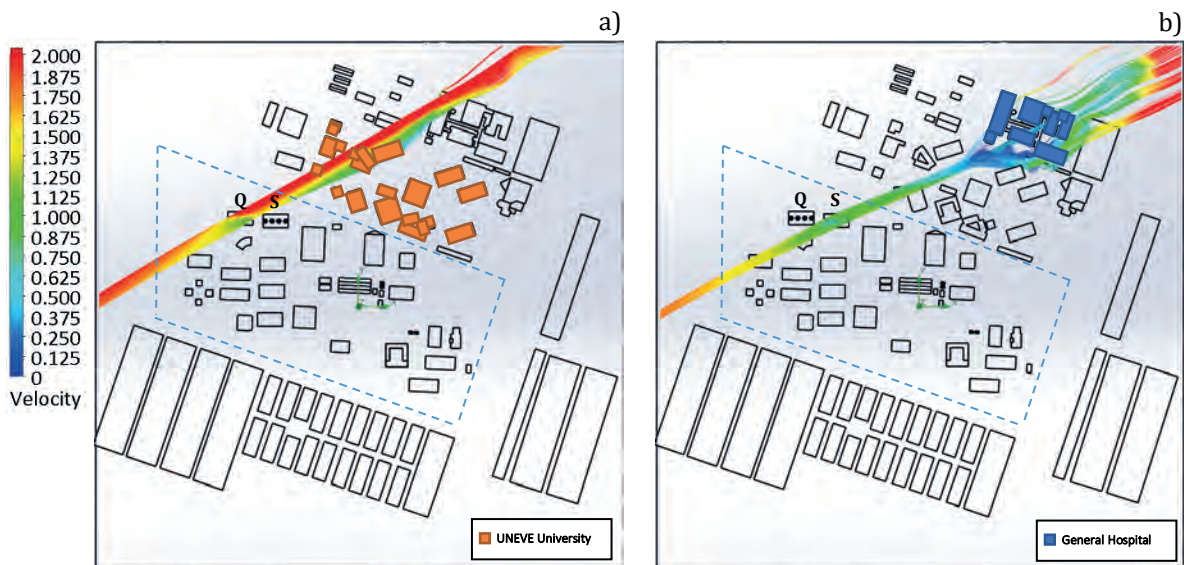


Figure 3.48 CFD Streamlines of the Aeolos V-10 wind turbines layout of the Buildings Q and S.

Furthermore, Building Q, shown in Figure 3.48 a) with the proposed layout of the four Aeolos V-10 wind turbines, receives a full wind speed than Building S. This wind speed ranges from 1.5 m/s to 1.97 m/s, and this slight decrease is due to the previous interaction of the wind flow with the buildings of the UNEVE campus. This decrease is more noticeable in the 4<sup>th</sup> SWT of the proposed layout than the other SWTs.

On the other hand, in Figure 3.48b) with the same proposed SWTs' layout, the wind speed decreases from the inlet condition of 1.97 m/s to 0.87 m/s. This reduction is due to the wind flow before arriving at the TESE campus, which interacts with the Dr. José María Rodríguez General Hospital buildings, which presents a reduction of 55.8% of the wind flow. On the other hand, the CFD simulation of Figure 3.48 a) presents a reduction of 23.8%.

With the previous information and the proposed methodology in mind, Building Q of the TESE campus is the uniquely proper location for a wind project using SWTs. The final results cast a total installed capacity of 40 kW, using the Aeolos V-10 wind turbine model. It is important to remark that this case study only considers the prevailing wind direction and not the other wind directions that compose the wind rose. Therefore, applying the proposed methodology for the implementation of SWTs has good results for the current case study. An advantage of this proposed methodology is that it can be improved, which in further cases, a Virtual Computational Domain (VCD) can be implemented. This innovation includes all the wind sectors from wind rose in order to represent in better conditions the behavior of the wind resource potential.

It is important to remark that based on this implementation of the VCD, the wind resource can be represented in a good manner and obtain a better representation of the wind flow over the proposed sites. This VCD allows having more wind hot spots or locations with wind potential that are affordable for the SWTs' installations that are not present in the prevailing wind direction CFD simulations.

The present case study only considers the traditional method used for the scientific community for the CFD analysis that determines the location or hot spots with higher wind potential through unidirectional simulations. These traditional CFD analyses use the prevailing wind direction of the wind resource. The next chapters will discuss and propose the innovative implementation of a Virtual Computational Domain VCD for performing the CFD simulations in multidirectional wind speeds embracing the 16 and 36 segments of a wind rose diagram.

# CHAPTER 4



---

## AN INNOVATIVE VIRTUAL COMPUTATIONAL DOMAIN (VCD) BASED ON A WIND ROSE BY APPLYING CFD

---

The CFD analysis applied to the study of the construction or dispersion of pollutants is usually used in a conventional manner using only single wind speed and direction. For most studies, this is suitable and sufficient, within the wind industry, however, if the analysis of the wind resources is performed through a wind rose diagram and has been accepted by the scientific community, why not to develop a CFD analysis in this frame of reference.

In the performed CFD simulations under this thesis's proposed methodology until now, the selected complex domains have worked with a conventional computational domain; however, in wind applications, they do not have adequate wind characterization. This computational domain has proven to be limited because of its rectangular prism shape that only allows unidirectional fluid velocities, contemplating prevailing wind directions.

The CFD results shown in this thesis, state that the methodology is efficient and adequate, with a balance between efficiency and computational speed. Nevertheless, it is required beyond the traditional methods, in this case proposing a new computational domain. The innovative proposal is to perform CFD simulations that characterize the wind resource more closely, eliminating unidirectional simulations.

In this chapter, a Virtual Computational Domain (VCD) is proposed. This new technique allows the characterization of the wind resource in such a way that it represents and contains at least the 16 segments that constitute the wind rose diagrams. This will allow CFD simulations with greater representation and fidelity to the wind's behavior in the environment, therefore, allowing a more optimal location of small wind emplacements and, thus, of the SWTs on the buildings.

The innovative VCD is applied under the complete proposed methodology presented in Chapter 3. For the documentation of this research work, only the methodology's stages of the CFD analyses are presented. The selected case study is the Campus Siglo XXI of Universidad Autónoma de Zacatecas. For a better evaluation of the methodology, including the VCD, a measurement campaign was performed, including its respective wind resource assessment. Results show the advantages of using the Virtual Computational Domain versus the conventional unidirectional CFD studies.



## 4.1 Evaluation and application of the methodology at the Universidad Autónoma de Zacatecas Siglo XXI (UAZ)

Based on Mexican wind resource maps, which reveal a high wind energy potential for the state of Zacatecas, a feasibility study is proposed for the installation of SWTs by applying the proposed methodology. A micro-localization shows that the Autonomous University of Zacatecas Siglo XXI campus in a rural area is an ideal site for applying a real case study. The campus is located to the west of the city of Zacatecas, with an address on the Zacatecas - Villanueva highway, La Escondida, Campus City Siglo XXI, C.P. 98160, Zacatecas, Zacatecas; with the latitude coordinates 22° 46' 15" N and longitude coordinates -102° 38' 38" W.

Once the place was selected, ultrasonic anemometric equipment (3D WindMaster) by Gill Instruments Ltd. was installed to develop a wind measurement campaign [114]. It is important to mention that a datalogger required for the 3D WindMaster was developed in the work team of the power electronics laboratory of the Institute of Engineering of UNAM. The development and installation work are described in Appendix E. The geographical data and characteristics of the meteorological station are represented in Table 4.1.

Table 4.1 Ultrasonic WindMaster station *in situ* measurement at Siglo XXI Campus.

Key	Monitoring Station	Coordinates	Altitude (m a.s.l.)	Station Height	Recording Interval
UWIN	WindMaster	22° 46' 23.3" N -102° 38' 38.8" O	2,311 m	16.5 m	1 min

### Wind resource assessment from the *in-situ* measurement campaign

Once the WindMaster ultrasonic anemometer was installed and set into operation, including the data from the wind resource *in situ* measurement campaign, the wind roses of the case study were built. The registry period of this station includes more than one year beginning in September 2017 and ending in December 2018.

As previously mentioned, the recording period of the WindMaster station is every minute, resulting in approximately 1,440 registers stored per day, allowing a high resolution in the measurements of the wind resource having a total record data of more than 525,600 registers. The results analyzed from the wind resource assessment in this *in situ* campaign comprise only one year from September 2017 to September 2018.

The quality of the measurement campaign will depend on its representativeness, accuracy, and the percentage of captured data. In case there is a loss of information or no recording of the wind resource measurements, the wind data must be at least 90% of the total information captured, based on the NREL Wind Resource Assessment Program Principles Guide [92].

The wind rose diagrams were developed with WRPLOT View™ software, as shown in Figure 4.1, detailing the 16 segments. In addition, its respective wind frequency distribution histogram is shown, and its resulting vector and wind speed of the UWIN station are described.

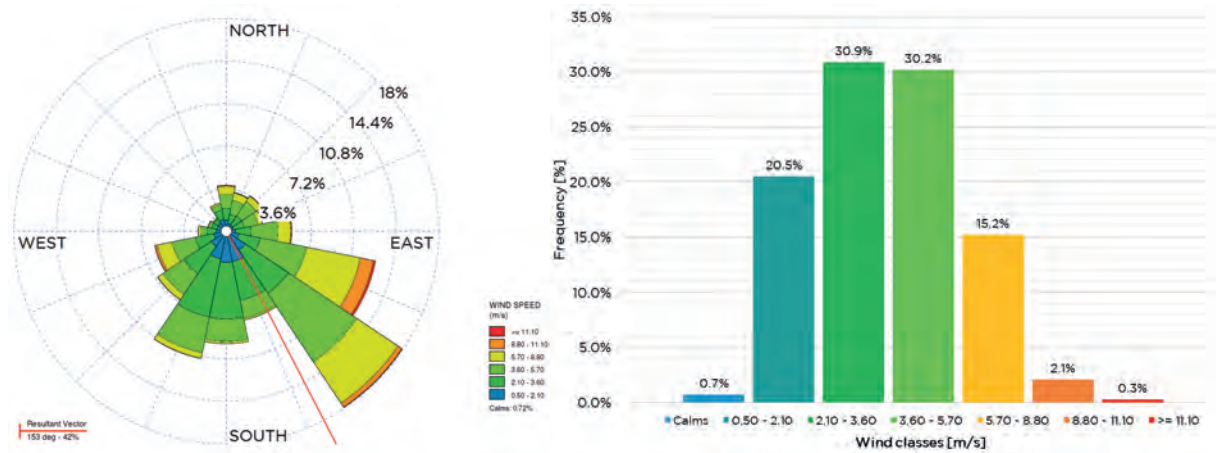


Figure 4.1 Wind rose and frequency distribution of the station through WRPLOT View™ in 16 segments.

On the other hand, Figure 4.2 shows the development of the wind rose diagram developed with WAsP® software, also showing the 16 segments that conventionally compose the wind roses. The respective Weibull and Rayleigh distributions of the UWIN station are also shown.

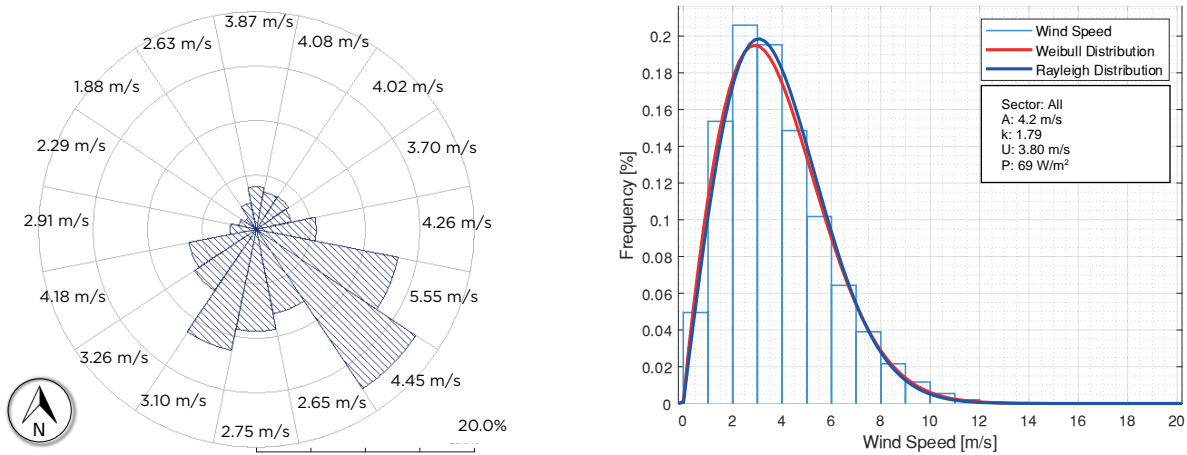


Figure 4.2 Wind rose and frequency distribution of the station through WAsP® in 16 segments.

Table 4.2 shows the summary of the wind resource assessment of the *in-situ* measurement campaign, which will be used for the unidirectional CFD simulation. In these data presented, it can be observed that the prevailing wind direction is located in the second quadrant of the wind rose diagram.

Table 4.2 Result parameters, UWIN station for the development of unidirectional CFD simulations.

Parameter	Averaged value 16 Segments
Wind speed	3.80 m/s
Wind direction	153° SSE – South-southeast
Temperature	20.37 °C
Atmospheric pressure	78,010 Pa

This analysis allows determining the initial conditions of the CFD simulations, fixing the optimal location of the wind site that can be installed within the UAZ campus.

#### 4.1.1 Traditional CFD analysis with unidirectional simulation

The first four stages of the methodology in the UAZ case study were performed as in the previous case study shown in Chapter 3. In this sense, the five phases based on the CFD analysis with the results of the wind resource assessment are presented.

In order to summarize the configuration phases, the parameters of the initial and boundary conditions are determined in Table 4.3, which shows the characteristics and conditions that allow describing the environment of the unidirectional CFD simulations of the present case study.

Table 4.3 Initial and boundary conditions for the unidirectional CFD simulation of the UAZ case study.

Analysis Type	Fluid Type	Boundary Conditions	Initial and Environment Conditions	Mesh Configuration
Type of flow: external	Air with all its physical properties	Roughness length: 400,000 $\mu\text{m}$	<i>a) Thermodynamic parameters:</i> -Temperature environment: 20.37 °C = 293.52 °K. -Atmospheric pressure of 78,010 Pa	Automatic mesh with 607,595 control volume cells
Gravitational force: -9.81 m/s <sup>2</sup>	Turbulent flow		<i>b) Velocity parameters:</i> Average wind speed of 3.8 m/s at 153°. It comprises 3.38 m/s in the "x" component and speed of 1.72 m/s for the "y" component.	
			<i>c) Turbulence parameters:</i> -Length of turbulence of 38 m -Turbulence intensity of 0.0377%.	
			<i>d) Humidity parameters:</i> -Average relative humidity of 50.16%.	

The CFD results are shown in Figure 4.3, which describes the unidirectional average wind speed. It is important to mention that the roughness length and the topographical unevenness conditions of this case study were considered at the same wind speed resolution of 4.0 m/s but at different heights.

The range of the highest height corresponds to a 2,329 m a.s.l., whereas the lowest height is 2,299 m a.s.l. with an existing terrain difference of around  $\pm 30$  m. In this sense, Figure 4.3 presents the CFD simulations at different heights to show the wind speed behavior around the academic buildings. These heights are represented by Figure 4.3 a) 2,329 b) 2,319 c) 2,309 and d) 2,299 m a.s.l.

In the university complex domain of Siglo XXI, it can be observed that some buildings have a better wind resource caused by the wind currents through the buildings coming from the South-southeast. These simulations give an overview of the possible wind potential zones and buildings for the SWTs' installation, which are marked in circles with dotted lines in Figure 4.3.

In the CFD simulations, that the lower altitude of the buildings at the rear of the campus university has a greater wind stream decrease is noticeable. On the other hand, the front of the

campus has a better wind resource, which permits determining the buildings of interest with greater wind potential.

These potential buildings show the possible installation of SWTs with desirable wind speed from 2.5 m/s to 4.0 m/s.

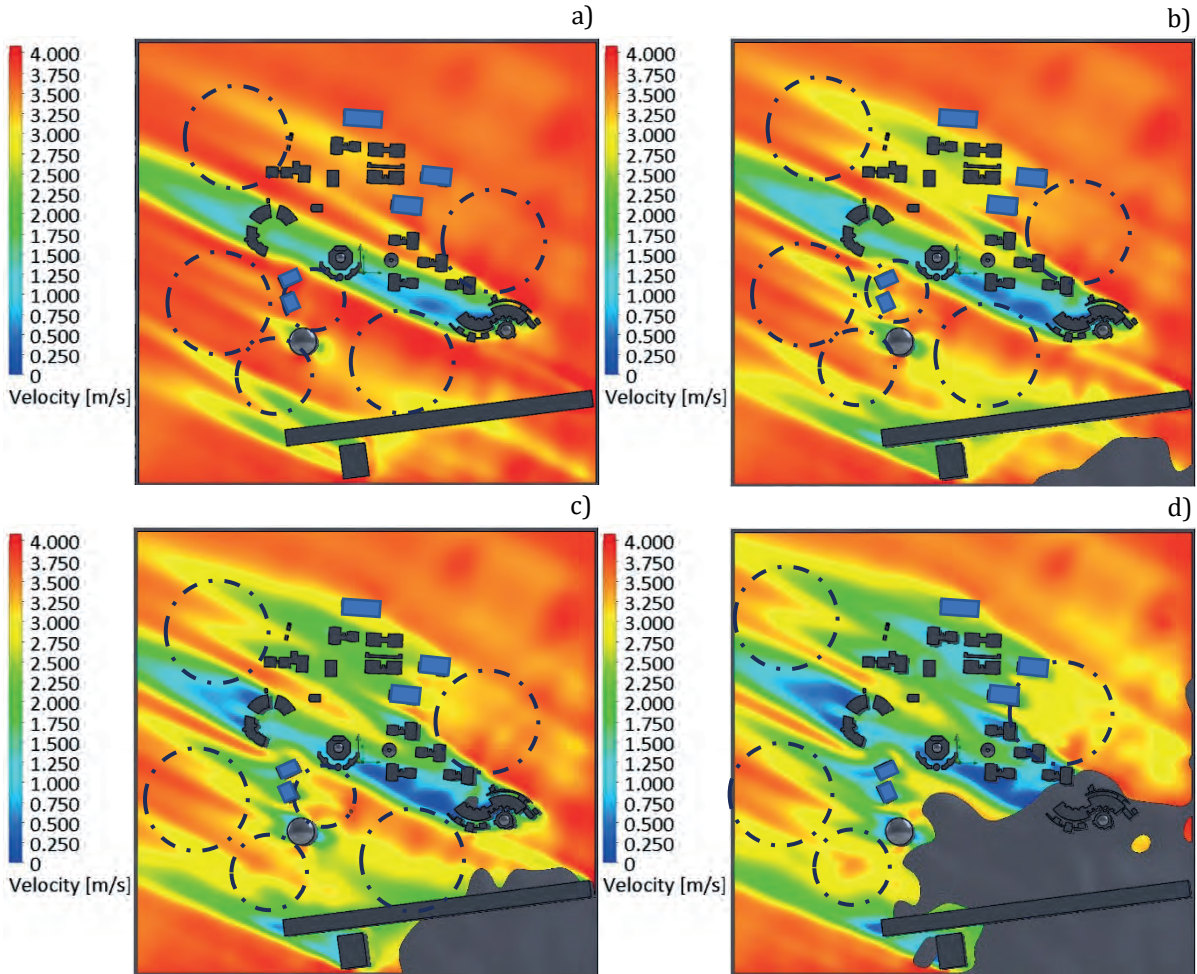


Figure 4.3 Unidirectional CFD simulations top view of the Site and Complex Domains of UAZ.

In the following section, the VCD of 16 segments will be implemented for determining the building or structure for the wind project according to the wind rose diagram. In addition, a comparison with the single domain case is made.

## 4.2 Virtual Computational Domain (VCD) in CFD analysis

### 4.2.1 A Virtual Computational Domain Innovation of 16 segments

The traditional CFD includes only the prevailing wind speed; this is because the Flow Simulation software only considers a rectangular prism computational domain. Only a unidirectional flow is considered limiting the simulations in one direction or a single fluid velocity with a 90° phase shift angle between them.

As an innovative proposal in this research work, a computational domain of the physical characteristics of a hexadecagonal prism, which will allow CFD simulations to be performed in the 16 directions, is proposed. The proposal is based on the standard representation of how wind speed and directions are typically distributed at a particular location, i.e., the wind rose.

Meteorologists and wind power engineers use this graphical tool to estimate the wind potential. The Virtual Computational Domain proposed is also based on the wind rose diagrams. In order to have represented all the magnitudes of the wind speed with their respective directions every  $22.5^\circ$ , interacting with the Complex Domain model of the selected location.

Note that in the first phase of the CFD simulation, the wind sector with the greatest potential is used, removing the other sectors; another technique is to perform single CFD analysis for a  $90^\circ$  shift angle of the wind rose. In both cases, the analysis increases the time and the need for additional computational resources. In the proposed methodology (Chapter 3), both cases will increase the execution time.

The VCD includes the requirement for building a hexadecagonal prism that surrounds the selected location, rather than a cube. This prism can have on each side the parameter of the corresponding sector of the wind rose, including the direction and wind speed as input conditions. This new technique allows greater precision and representativeness of the wind resource, because of to the same orientation of the wind rose's diagram according to the cardinal points and directly coupled to this doctoral research's proposed methodology.

The Site and Complex Domain models were obtained in order to implement the hexadecagonal VCD. This three-dimensional model is shown in Figure 4.4. The prism diameter used is 455 m and is 80 m high immersed in the Urban Boundary Layer (UBL). This UBL is represented with a height from 1 to 2 km above ground level [1], [36], [115]. The creation of this new computational domain is inserted into the three-dimensional topographic model with a dimension of 1,000 meters per side, centering the hexadecagonal prism within the building structure of interest.

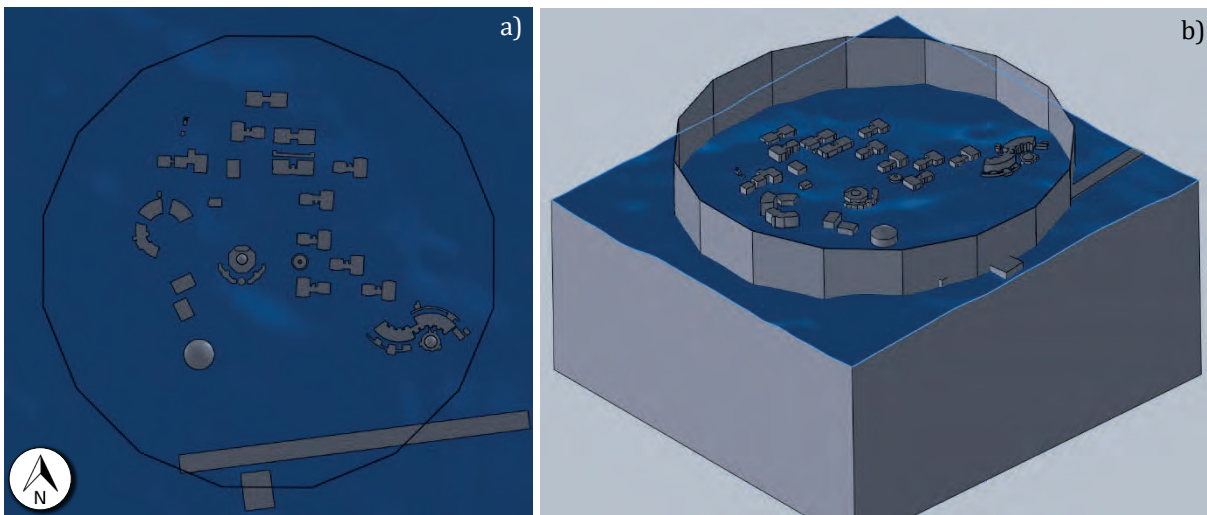


Figure 4.4 Representation of the Virtual Computational Domain (VCD) implemented in the 3D rural topographic model - a) Top View and b) Isometric View.

The wind resource assessment is used to select the initial and boundary conditions for the CFD simulations. These inlet and outlet conditions for the selected case of the UAZ university Complex Domain are shown in Table 4.4.

Table 4.4 Initial and boundary conditions for the UAZ case study - Implementation of 16 segments in the Virtual Computational Domain.

Analysis Type	Fluid Type	Boundary Conditions	Initial and Environment Conditions	Mesh Configuration																																		
Type of flow: external	Air with all its physical properties	Roughness length: 400,000 $\mu\text{m}$	<p><i>a) Thermodynamic parameters:</i>            -Temperature: 20.37 °C = 293.52 °K.            -Atmospheric pressure: 78,010 Pa</p>	Automatic mesh with 797,526 control volume cells																																		
Gravitational force: -9.81 m/s <sup>2</sup>	Turbulent flow		<p><i>b) Velocity parameters:</i> Average wind speed of 3.8 m/s at 153°. That includes the following wind speeds in each cardinal point of the wind rose with its respective frequency.</p> <table border="1"> <thead> <tr> <th>Wind direction</th> <th>Wind speed [m/s]</th> </tr> </thead> <tbody> <tr><td>N</td><td>3.87 m/s - 3.9%</td></tr> <tr><td>NNE</td><td>4.08 m/s - 3.5%</td></tr> <tr><td>NE</td><td>4.02 m/s - 3.5%</td></tr> <tr><td>ENE</td><td>3.70 m/s - 3.2%</td></tr> <tr><td>E</td><td>4.26 m/s - 5.5%</td></tr> <tr><td>ESE</td><td>5.55 m/s - 13.2%</td></tr> <tr><td>SE</td><td>4.45 m/s - 17.5%</td></tr> <tr><td>SSE</td><td>2.65 m/s - 7.9%</td></tr> <tr><td>S</td><td>2.75 m/s - 9.4%</td></tr> <tr><td>SSW</td><td>3.10 m/s - 11.3%</td></tr> <tr><td>SW</td><td>3.26 m/s - 6.8%</td></tr> <tr><td>WSW</td><td>4.18 m/s - 6.3%</td></tr> <tr><td>W</td><td>2.91 m/s - 2.4%</td></tr> <tr><td>WNW</td><td>2.29 m/s - 1.7%</td></tr> <tr><td>NW</td><td>1.88 m/s - 1.4%</td></tr> <tr><td>NNW</td><td>2.63 m/s - 2.5%</td></tr> </tbody> </table>	Wind direction	Wind speed [m/s]	N	3.87 m/s - 3.9%	NNE	4.08 m/s - 3.5%	NE	4.02 m/s - 3.5%	ENE	3.70 m/s - 3.2%	E	4.26 m/s - 5.5%	ESE	5.55 m/s - 13.2%	SE	4.45 m/s - 17.5%	SSE	2.65 m/s - 7.9%	S	2.75 m/s - 9.4%	SSW	3.10 m/s - 11.3%	SW	3.26 m/s - 6.8%	WSW	4.18 m/s - 6.3%	W	2.91 m/s - 2.4%	WNW	2.29 m/s - 1.7%	NW	1.88 m/s - 1.4%	NNW	2.63 m/s - 2.5%	
Wind direction	Wind speed [m/s]																																					
N	3.87 m/s - 3.9%																																					
NNE	4.08 m/s - 3.5%																																					
NE	4.02 m/s - 3.5%																																					
ENE	3.70 m/s - 3.2%																																					
E	4.26 m/s - 5.5%																																					
ESE	5.55 m/s - 13.2%																																					
SE	4.45 m/s - 17.5%																																					
SSE	2.65 m/s - 7.9%																																					
S	2.75 m/s - 9.4%																																					
SSW	3.10 m/s - 11.3%																																					
SW	3.26 m/s - 6.8%																																					
WSW	4.18 m/s - 6.3%																																					
W	2.91 m/s - 2.4%																																					
WNW	2.29 m/s - 1.7%																																					
NW	1.88 m/s - 1.4%																																					
NNW	2.63 m/s - 2.5%																																					
			<p><i>c) Turbulence parameters:</i>            -Length of turbulence of 38 m            -Turbulence intensity of 0.0377%.</p>																																			
			<p><i>d) Humidity parameters:</i>            -Average relative humidity of 50.16%.</p>																																			

For completeness, the initial and boundary conditions are represented in the VCD in Figure 4.5, in which the red and blue arrows interact with the faces of the VCD hexadecagonal prism describing the results of the wind resource assessment that represents part of Stage 2 of the methodology.

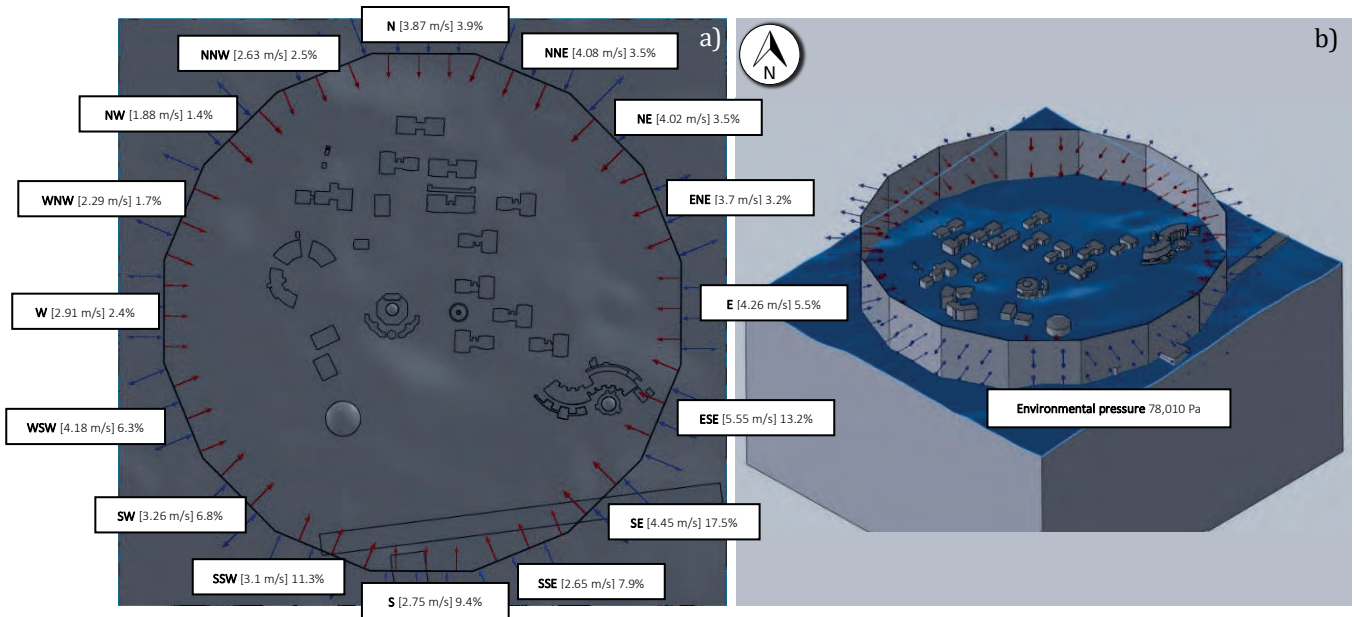


Figure 4.5 Representation of the wind rose in the hexadecagonal prism of the Virtual Computational Domain VCD with the initial and boundary conditions, a) Top View, and b) Isometric View.

The result of the CFD simulation with the implementation of the VCD of 16 segments is highlighted in Figure 4.6 a). The VCD 16 segments CFD simulation is depicted at merged heights for detecting all the possible wind streams that interact with the structures and buildings around the academic Complex Domain. For a better comparison, the unidirectional CFD simulation is shown in Figure 4.6 b). In both CFD simulations, the academic Complex Domain is superimposed in order to determine the buildings or structures that are subject to wind potential and to locate the SWTs.

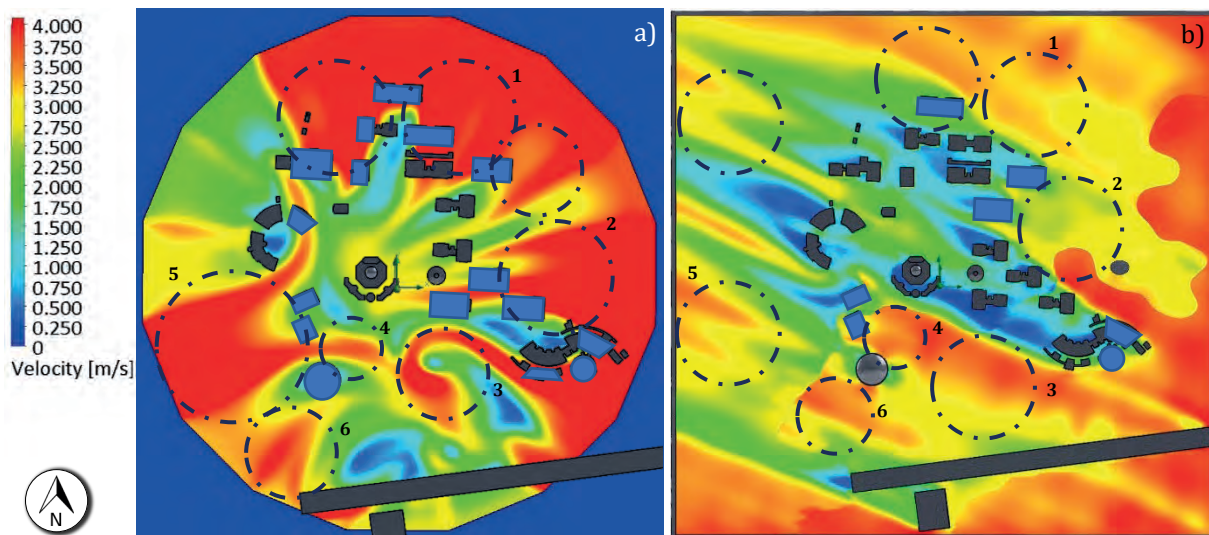


Figure 4.6 Comparison of CFD simulations - a) wind speed in the multidirectional direction of the hexadecagonal VCD and b) unidirectional wind speed.

Based on the previous comparison in Figure 4.6, a certain similitude in the presence of moderate wind streamlines is observed. The CFD simulation with the VCD of 16 segments implementation depicted in Figure 4.6 a), however, presents an increment of the number of potential buildings, compared with the potential buildings with the wind resource presented in the unidirectional CFD simulation of Figure 4.6 b).

The wind resource assessment shows that most of the hot spots consider a wind speed range of 2.7 m/s to 3.8 m/s, making the UAZ case study feasible for the SWTs installation in the rural environment.

Additionally, in the center of Figure 4.6 b), of the unidirectional CFD simulation shows a high reduction of the wind zones decreasing to 0.25 m/s in comparison with the multidirectional CFD simulation, which presents a reduction to 2.0 m/s. That represents a decrease of around 87.5% in the unidirectional simulation compared with a decrease of 45% in the VCD implementation.

Another comparison is with the multidirectional CFD simulation. Because of the frequency with which the wind blows from all directions, it is possible to estimate that the wind speeds with greater intensity and more frequently are those found in the first to third quadrants from the wind rose. Conversely, in the unidirectional CFD simulation, only the first and second quadrants present moderate wind speeds.

For completeness, Figure 4.7 and Figure 4.8 show the individual CFD simulations contemplating the different heights according to the roughness of the terrain. By observing these CFD simulations, it is possible to determine new buildings with opportunities for developing wind emplacements.

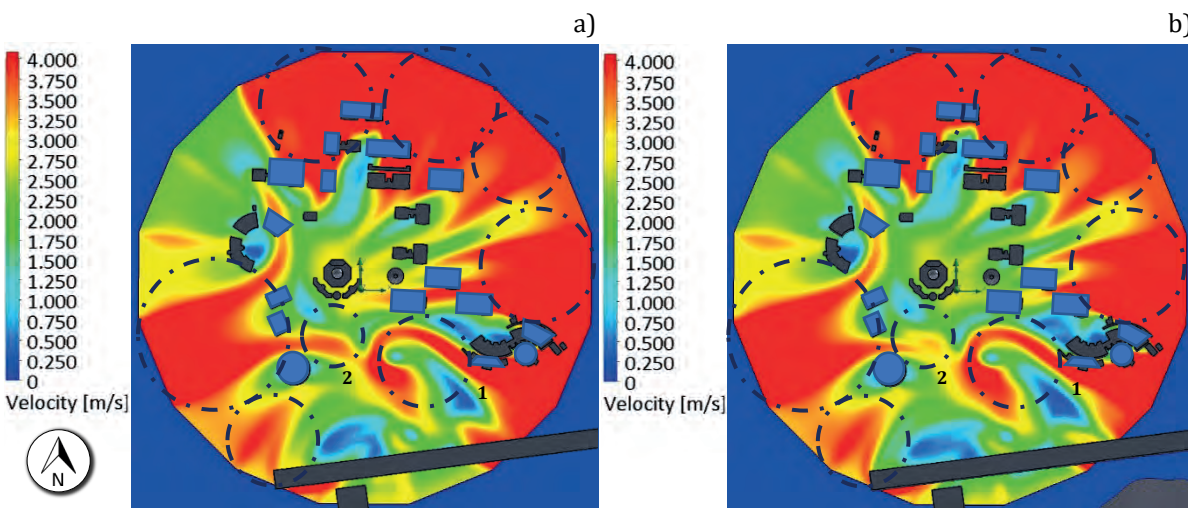


Figure 4.7 CFD Simulations with the VCD of 16 Segments implementation of the Site and Complex Domains of the UAZ Siglo XXI campus, a) 2,329, and b) 2,319 m a.s.l.



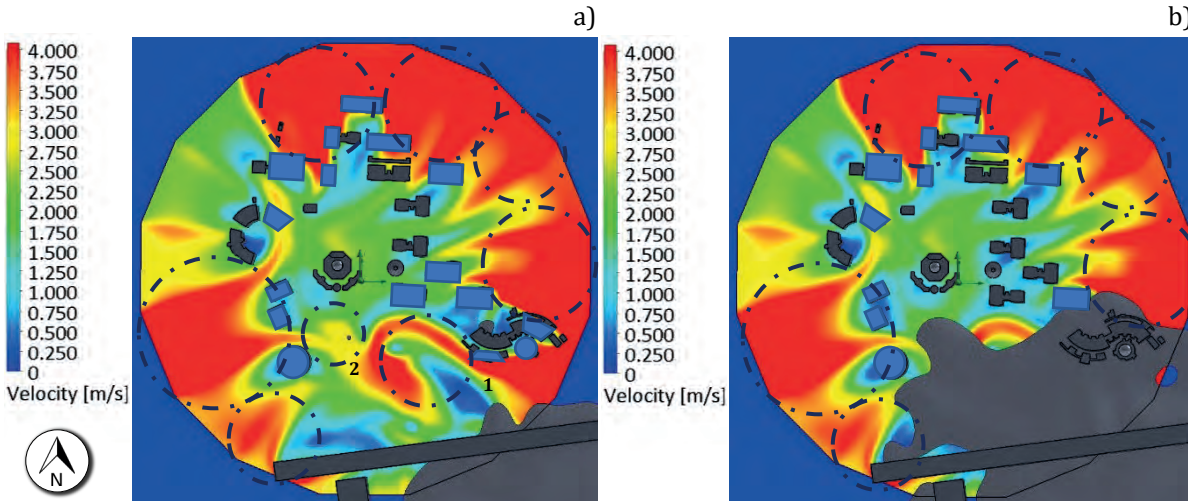


Figure 4.8 CFD Simulations with the VCD of 16 Segments implementation of the Site and Complex Domains of the UAZ Siglo XXI campus, a) 2,309, and b) 2,299 m a.s.l.

The CFD simulation results in Figure 4.7 shows the wind streams at different heights, which comprise the same terrain unevenness of  $\pm 30$  m of 2,329 m and 2,319 m a.s.l. As seen from Figure 4.7 a), b) and Figure 4.8 a) in the hot spot circles 1 and 2, a region with a wind potential ranging from 2.5 m/s to 3.8 m/s is shown, but this region corresponds to a location of SWT in the BEWTs' configuration because in these areas there are no buildings or structures that can support the SWTs.

The other remaining circles show the hot spots with wind potential ranging from 2.7 m/s to 4.0 m/s, which indicates a good opportunity for the location of the SWTs in the BUWTs' configuration, corresponding to a wind emplacement that takes the advantage of the proper height of the building for installing the SWTs.

The previous information shows that the implementation of the hexadecagonal virtual computational domain allows determining that the wind current flows tend to increase when they converge in the same simulation. This is an advantage for the possibility of determining the location with good wind potential for installing the SWTs, which could be installed on the building (s) or structure (s) studied in each of the 16 segments of the wind rose, which is compared with researches that only comprises a single prevailing wind speed.

#### 4.2.2 Validation of the Virtual Computational Domain in 16 Segments

In order to perform the validation of the CFD simulations, this section presents a comparison between the VCD of 16 segments against and a one-by-one wind rose sector of individual CFD simulations. These series of simulations also consider the same inlet and boundary conditions shown in Table 4.4, taking into account the individual wind speed and wind direction of the wind rose.

It is important to notice that this implementation of individual CFD simulations is similar to the techniques used in traditional wind tunnels, which use rotational models for observing the wind behavior in different wind directions. Figure 4.9 shows these individual CFD simulations for the wind flow over the UAZ Siglo XXI campus buildings.

The CFD simulations demonstrate that the best wind potential corresponds to the first and part of the second quadrant of the wind rose, which are represented by the N, NNE, NE, ENE, E, ESE and SE cardinal points. Furthermore, it is obtained a wind speed in the average range of 2.7 m/s to 4.0 m/s. On the other hand, the directions represented by SSE, S, W, WNW, and NW cardinal points have an average wind speed range of 1.75 m/s to 3.0 m/s, which corresponds to similar wind speed results presented in the VCD simulation of Figure 4.7 a).

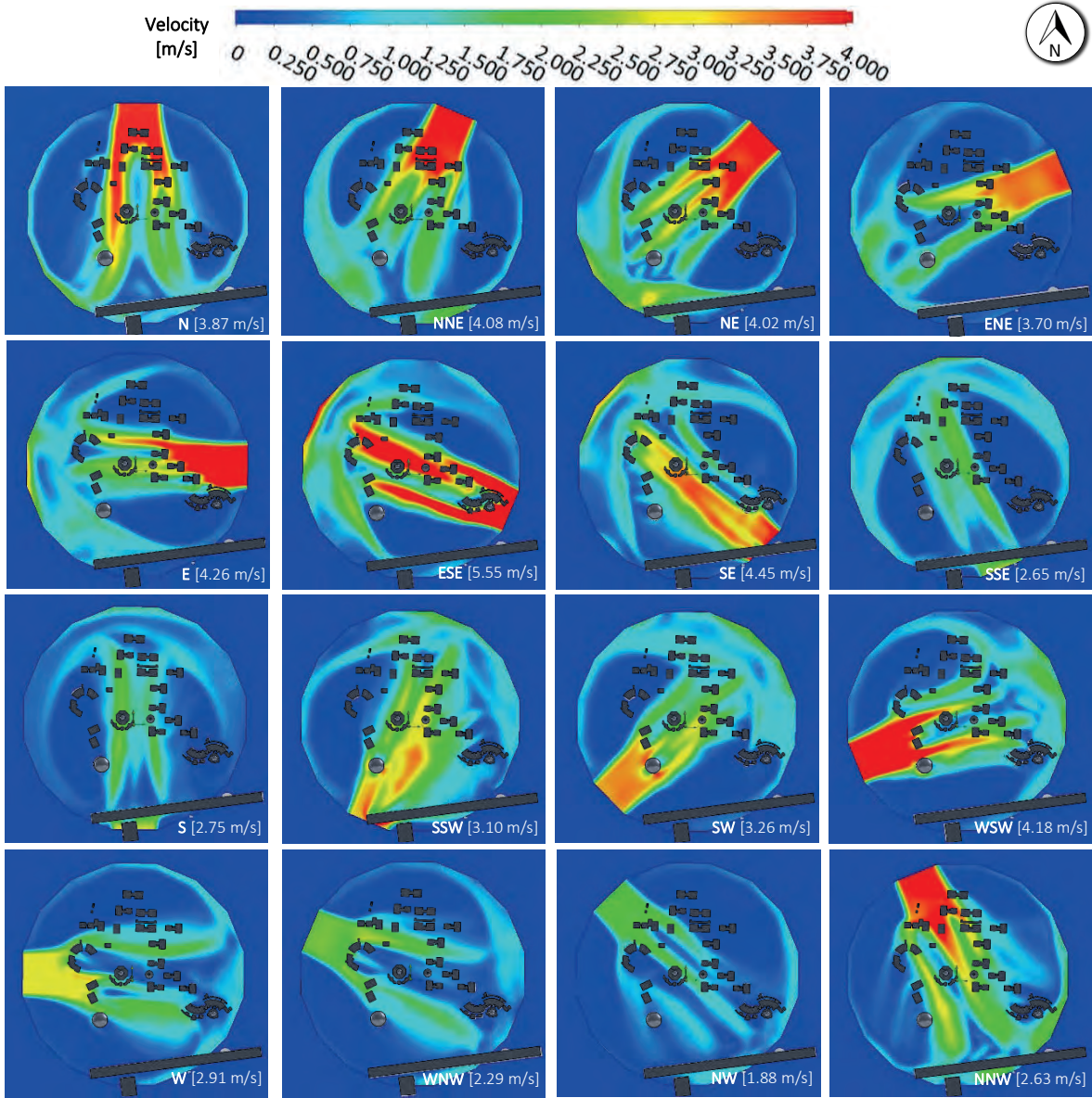


Figure 4.9 CFD Simulations with the hexadecagonal VCD implementation of 16 individual wind speeds.

The remaining cardinal points corresponding to SSW, SW, WSW, and NNW present a wind speed range averaged of 1.75 m/s to 4.0 m/s. The intensity scale developed with the wind speeds with their respective wind frequency is shown in Table 4.5. This analysis permits evaluating and performing a validation of the individual CFD simulations and comparing them with the VCD implementation.

Table 4.5 Representation of 16 sectors of the wind rose of the wind speed and frequency in the intensity scale; red is higher.

	0°	22.5°	45°	67.5°	90°	112.5°	135°	157.5°	180°	202.5°	225°	247.5°	270°	292.5°	315°	337.5°
<b>Wind directions</b>	N	NNE	NE	ENE	E	ESE	SE	SSE	S	SSW	SW	WSW	W	WNW	NW	NNW
<b>Wind speed [m/s]</b>	3.87	4.08	4.02	3.70	4.26	5.55	4.45	2.65	2.75	3.10	3.26	4.18	2.91	2.29	1.88	2.63
<b>Frequency %</b>	3.9%	3.5%	3.5%	3.2%	5.5%	13.2%	17.5%	7.9%	9.4%	11.3%	6.8%	6.3%	2.4%	1.7%	1.4%	2.5%

Based on the table mentioned above, the three main cardinal points to take into account are ESE, SE, SSW, which present a wind speed range from 3.1 m/s to 5.55 m/s, corresponding to moderate wind speeds in order to be considered for the implementation of small rural wind emplacement.

Based on the results of the VCD analysis, it can be stated that 87.5% of the wind speed and the direction of the case study selected correspond into a Wind Class IV according to the IEC 61400-1 [116]. In this sense, this case study is considered affordable for the implementation of wind emplacements in the UAZ campus.

### 4.2.3 A Virtual Computational Domain Innovation of 36 segments

As seen, the VCD of 16 segments implementation fitted into a traditional wind rose diagram has shown a noticeable increase in the wind potential zones of the wind resource maps compared with the traditional computational domain. In this context and by taking advantage of the three-dimensional modeling improvement, it is attempted further to increase the wind resource maps' resolution.

For observing the behavior of the wind streamlines with higher reliability and fidelity of the wind resource mapping, a VCD of 36 segments is implemented, increasing the wind sectors from the wind rose.

In this context, a new wind resource assessment is developed, now considering a wind rose diagram in 36 segments. These diagrams are shown in Figure 4.10, detailing the 36 segments and showing the respective wind frequency distribution histogram.

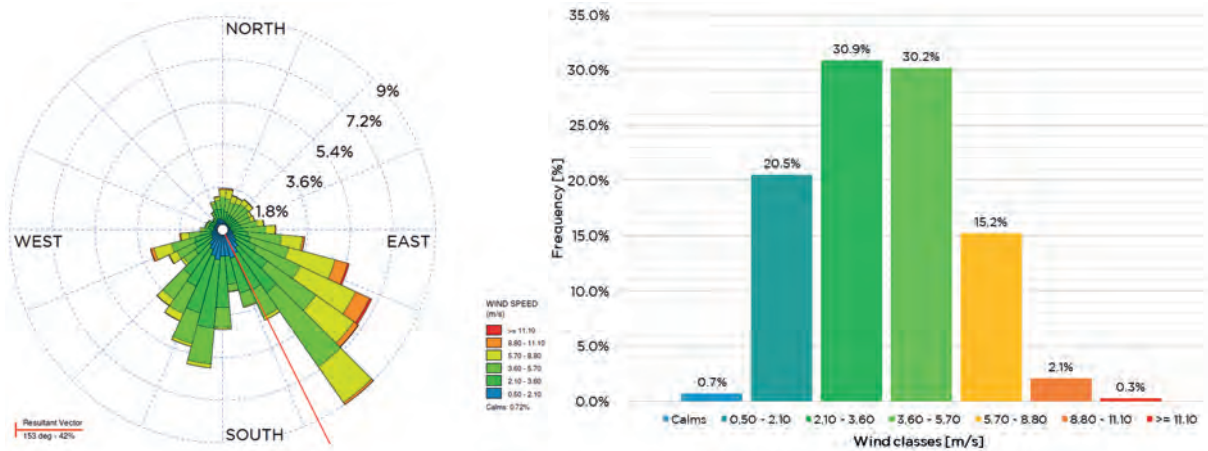


Figure 4.10 Wind rose and frequency distribution of the station trough WRPLOT View™ in 36 segments.

On the other hand, Figure 4.11 shows the development of the wind rose diagram developed with the WASP® software. In addition, the respective Weibull and Rayleigh distributions and wind frequency are shown. This analysis results in an average wind speed of 3.81 m/s with the same ambient conditions as in Table 4.2.

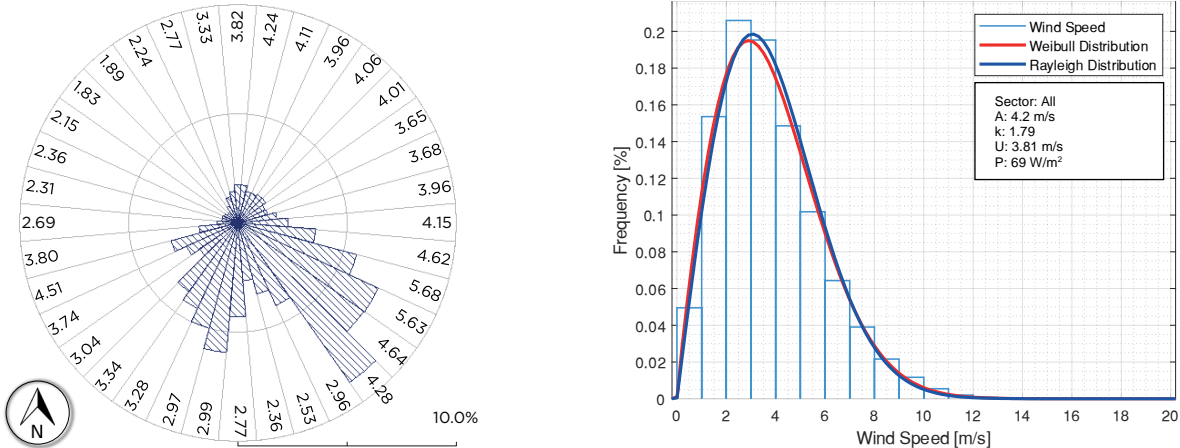


Figure 4.11 Wind rose and frequency distribution of the station through WASP® in 36 segments.

This analysis will allow determining the initial conditions of the CFD simulations to determine the optimal location of the wind site that could be installed within the UAZ campus.

Following the same process as the VCD of 16 segments, a Virtual Computational Domain of 36 segments (triacontakaihexagonal prism) was modeled and implemented in the Site Domain and the Complex Domain three-dimensional models of the UAZ Siglo XXI campus. Figure 4.12 shows this developed model, which allows having less information loss of the wind rose diagrams; the wind sector dimensions are established every 10°, with a quasi-circular representation of the wind rose sectors.

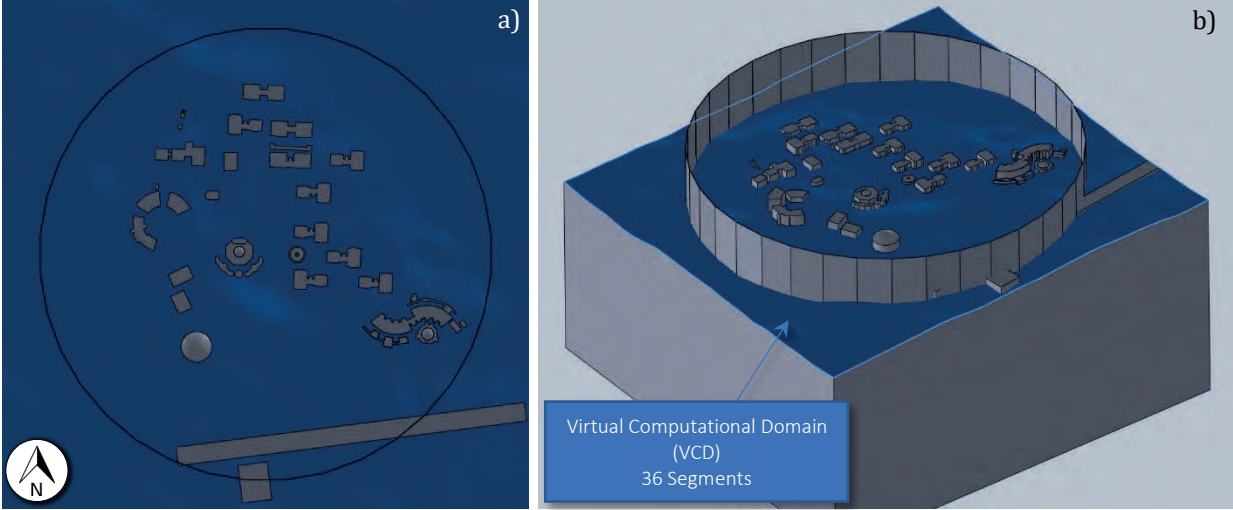


Figure 4.12 Representation of the Virtual Computational Domain (VCD) 36 segments implemented in the 3D rural topographic model, a) Top View, and b) Isometric View.

The initial and boundary conditions of the VCD of 36 segments simulation are based on the wind roses developed in the wind resource assessment shown in Figure 4.10 and Figure 4.11. These initial settings are shown in Table 4.6, which permit describing the physical settings of the fluid and its behavior to which the CFD simulations will be performed. In addition, the mesh configuration considers an automatic meshing with 797,440 control volume cells.

Table 4.6 Initial and boundary conditions for the UAZ case study - Implementation of 36 segments in the Virtual Computational Domain.

Analysis Type	Fluid Type	Boundary Conditions	Initial and Environment Conditions	Mesh Configuration																																																																												
Flow Type: external	Air with all its physical properties	Roughness length: 400,000 $\mu\text{m}$	<p><i>a) Thermodynamic parameters:</i>            -Temperature: 20.37 °C = 293.52 °K            -Atmospheric pressure: 78,010 Pa</p>	Automatic meshing with 797,440 control volume cells																																																																												
Gravity force: -9.81 m/s <sup>2</sup>	Turbulent Flow		<p><i>b) Velocity Parameters:</i> Average wind speed of 3.81 m/s at 153°. That includes the following wind speeds in each cardinal point degree of the wind rose with its respective frequency.</p> <table border="1"> <thead> <tr> <th>Wind dir.</th> <th>Wind speed [m/s]</th> <th>Wind dir.</th> <th>Wind speed [m/s]</th> </tr> </thead> <tbody> <tr><td>0°</td><td>3.82 - 1.8%</td><td>180°</td><td>2.77 - 4.3%</td></tr> <tr><td>10°</td><td>4.24 - 1.8%</td><td>190°</td><td>2.99 - 6.0%</td></tr> <tr><td>20°</td><td>4.11 - 1.5%</td><td>200°</td><td>2.97 - 5.0%</td></tr> <tr><td>30°</td><td>3.96 - 1.5%</td><td>210°</td><td>3.28 - 4.3%</td></tr> <tr><td>40°</td><td>4.06 - 1.6%</td><td>220°</td><td>3.34 - 3.9%</td></tr> <tr><td>50°</td><td>4.01 - 1.6%</td><td>230°</td><td>3.04 - 2.1%</td></tr> <tr><td>60°</td><td>3.65 - 1.4%</td><td>240°</td><td>3.74 - 2.6%</td></tr> <tr><td>70°</td><td>3.68 - 1.4%</td><td>250°</td><td>4.51 - 3.2%</td></tr> <tr><td>80°</td><td>3.96 - 1.8%</td><td>260°</td><td>3.80 - 1.8%</td></tr> <tr><td>90°</td><td>4.15 - 2.3%</td><td>270°</td><td>2.69 - 1.0%</td></tr> <tr><td>100°</td><td>4.62 - 3.6%</td><td>280°</td><td>2.31 - 0.8%</td></tr> <tr><td>110°</td><td>5.68 - 5.6%</td><td>290°</td><td>2.36 - 0.7%</td></tr> <tr><td>120°</td><td>5.63 - 7.1%</td><td>300°</td><td>2.15 - 0.7%</td></tr> <tr><td>130°</td><td>4.64 - 7.0%</td><td>310°</td><td>1.83 - 0.6%</td></tr> <tr><td>140°</td><td>4.28 - 8.9%</td><td>320°</td><td>1.89 - 0.6%</td></tr> <tr><td>150°</td><td>2.96 - 4.2%</td><td>330°</td><td>2.24 - 0.9%</td></tr> <tr><td>160°</td><td>2.53 - 3.4%</td><td>340°</td><td>2.77 - 1.3%</td></tr> <tr><td>170°</td><td>2.36 - 2.7%</td><td>350°</td><td>3.33 - 1.5%</td></tr> </tbody> </table>	Wind dir.	Wind speed [m/s]	Wind dir.	Wind speed [m/s]	0°	3.82 - 1.8%	180°	2.77 - 4.3%	10°	4.24 - 1.8%	190°	2.99 - 6.0%	20°	4.11 - 1.5%	200°	2.97 - 5.0%	30°	3.96 - 1.5%	210°	3.28 - 4.3%	40°	4.06 - 1.6%	220°	3.34 - 3.9%	50°	4.01 - 1.6%	230°	3.04 - 2.1%	60°	3.65 - 1.4%	240°	3.74 - 2.6%	70°	3.68 - 1.4%	250°	4.51 - 3.2%	80°	3.96 - 1.8%	260°	3.80 - 1.8%	90°	4.15 - 2.3%	270°	2.69 - 1.0%	100°	4.62 - 3.6%	280°	2.31 - 0.8%	110°	5.68 - 5.6%	290°	2.36 - 0.7%	120°	5.63 - 7.1%	300°	2.15 - 0.7%	130°	4.64 - 7.0%	310°	1.83 - 0.6%	140°	4.28 - 8.9%	320°	1.89 - 0.6%	150°	2.96 - 4.2%	330°	2.24 - 0.9%	160°	2.53 - 3.4%	340°	2.77 - 1.3%	170°	2.36 - 2.7%	350°	3.33 - 1.5%	
			Wind dir.	Wind speed [m/s]	Wind dir.	Wind speed [m/s]																																																																										
			0°	3.82 - 1.8%	180°	2.77 - 4.3%																																																																										
			10°	4.24 - 1.8%	190°	2.99 - 6.0%																																																																										
			20°	4.11 - 1.5%	200°	2.97 - 5.0%																																																																										
			30°	3.96 - 1.5%	210°	3.28 - 4.3%																																																																										
			40°	4.06 - 1.6%	220°	3.34 - 3.9%																																																																										
			50°	4.01 - 1.6%	230°	3.04 - 2.1%																																																																										
			60°	3.65 - 1.4%	240°	3.74 - 2.6%																																																																										
			70°	3.68 - 1.4%	250°	4.51 - 3.2%																																																																										
			80°	3.96 - 1.8%	260°	3.80 - 1.8%																																																																										
			90°	4.15 - 2.3%	270°	2.69 - 1.0%																																																																										
			100°	4.62 - 3.6%	280°	2.31 - 0.8%																																																																										
			110°	5.68 - 5.6%	290°	2.36 - 0.7%																																																																										
			120°	5.63 - 7.1%	300°	2.15 - 0.7%																																																																										
			130°	4.64 - 7.0%	310°	1.83 - 0.6%																																																																										
			140°	4.28 - 8.9%	320°	1.89 - 0.6%																																																																										
150°	2.96 - 4.2%	330°	2.24 - 0.9%																																																																													
160°	2.53 - 3.4%	340°	2.77 - 1.3%																																																																													
170°	2.36 - 2.7%	350°	3.33 - 1.5%																																																																													
			<p><i>c) Turbulence parameters:</i>            -Length of turbulence of 38 m            -Turbulence intensity of 0.0377%.</p>																																																																													
			<p><i>d) Humidity parameters:</i>            -Average relative humidity of 50.16%.</p>																																																																													

The implementation of the VCD of 36 segments in the Site and Complex Domains models is illustrated in Figure 4.13, which includes the inlet and outlet conditions for developing the CFD simulation. In this case, only half of the wind speeds and directions are shown; nevertheless, this new CFD simulation is achieved by considering the VCD and the 36 wind speeds and directions in order to converge into a single simulation. The initial and boundary conditions are represented with the 36 wind speeds at their respective wind directions used in the CFD simulation around the VCD represented by the red arrows entering the model, as well as the ambient pressure on each of the faces of the prism represented by blue arrows entering and leaving the VCD, respectively.

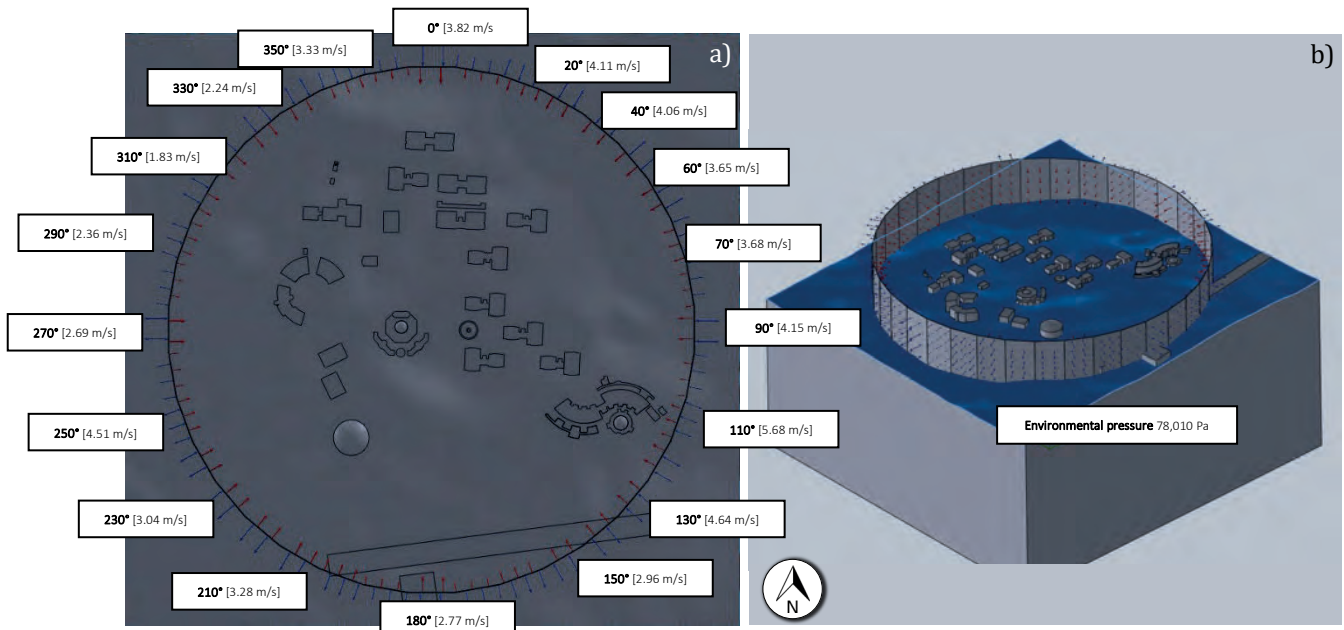


Figure 4.13 Representation of the wind rose in the triacontakaihexagonal prism of the Virtual Computational Domain VCD of 36 Segments with the initial conditions, a) Top View, b) Isometric View.

Figure 4.14 a) shows the result of the CFD simulation and b) the unidirectional CFD simulation. As can be seen, the wind streams formed in the simulation permit determining the potential buildings on which the SWTs can be installed. In this sense, hot spots have been drawn in both a) and b), and by observing circles 1 and 2, clearly, the 36 segments' analysis shows better potential than the unidirectional one. The same as occurs in the 16 segments VCD simulation, the 36 VCD simulation hot spots are marked in circles 3 and 4, which are the ones where the SWTs can be installed at ground level considered as BEWTs configuration.

On the other hand, in the central region, the simulations both in Figure 4.14 a) and b), there is a wind speed decrease caused by the building configuration of the UAZ Siglo XXI campus.

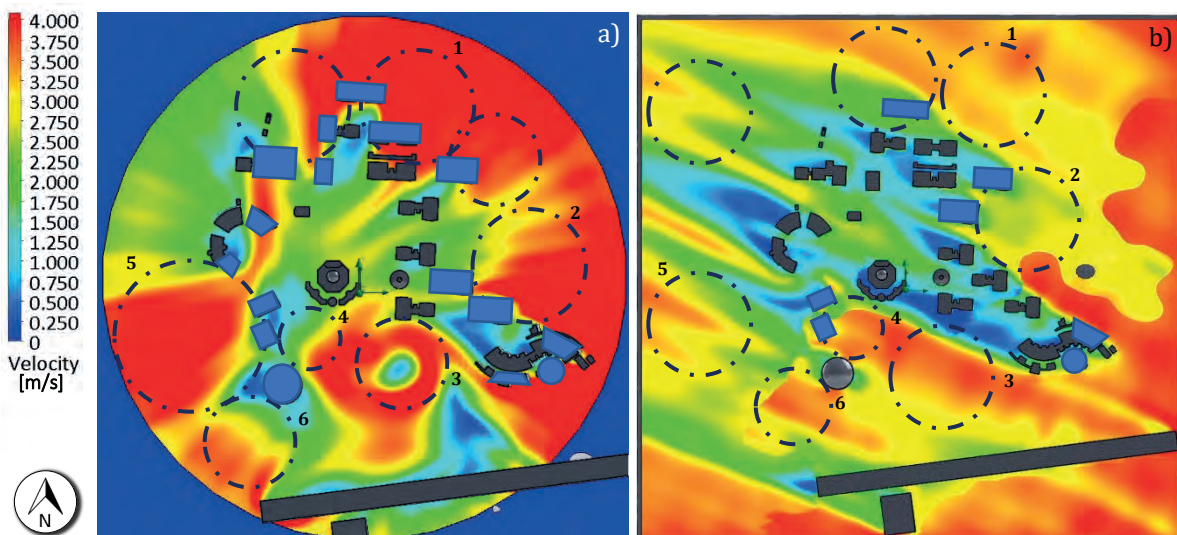


Figure 4.14 Comparison between CFD simulations - a) Multidirectional wind speed of the triacontakaihexagonal VCD and b) the traditional unidirectional wind direction.

Based on the results of the CFD simulations in Figure 4.9 a) and b) focusing on the central location of the simulations, where there exists a decrease in wind speed exist because of the buildings' location, a 30% increase in relation to the unidirectional CFD simulation can be observed, which corresponds to an increase in wind speed from 2.0 m/s to 3.2 m/s compared with both CFD simulations shown in Figure 4.14.

In addition, the wind current tunnels around buildings at the southern cardinal point represented by circles 3 and 4 are also presented in both CFD simulations. In Figure 4.14 a), an average wind speed of 4.0 m/s is notable with a high vortex presence formed in circle 3. Furthermore, it is remarkable that the wind speed formed in the third quadrant of the CFD simulation represented by circle 5 has a high potential hot spot with a wind speed of around 4.0 m/s, compared with the unidirectional CFD simulation in Figure 4.14 b) with wind speeds around 2.75 m/s.

Complementing the interpretation of the CFD simulation' results, Figure 4.15 shows the comparison of the results of the CFD simulations, implementing the following: a) Virtual Computational Domain 36 segments, b) VCD 16 segments, and c) the unidirectional simulation.

By comparing the CFD simulations of Figure 4.15 a) and b), a similarity of the wind potential zones can be observed, in the first and second quadrants of the wind rose, marking the potential buildings where the SWTs installation could be possible.

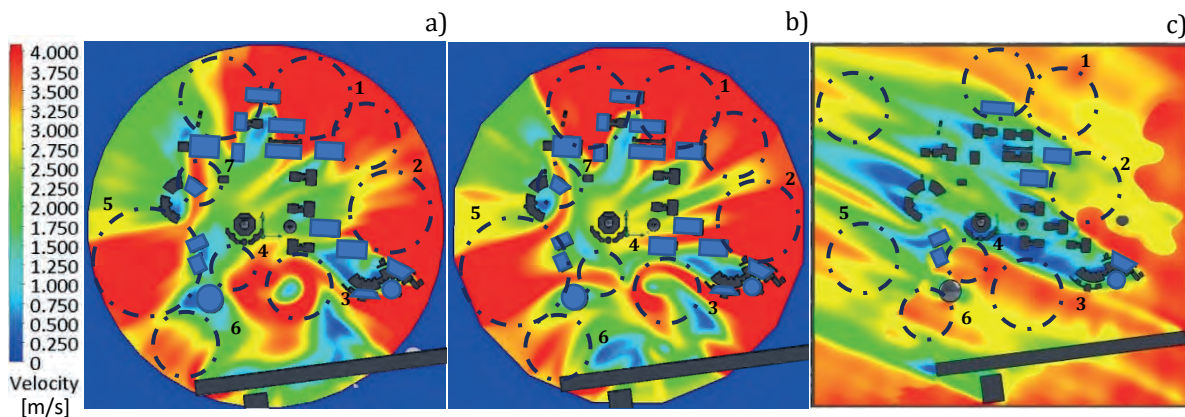


Figure 4.15 Comparison between CFD simulations - a) triacontakaihexagonal VCD, b) hexadecagonal VCD, and c) the unidirectional wind direction.

In addition, a slight penetration of the wind stream coming from the third quadrant towards the fourth quadrant exists, with an average wind speed of 4.0 m/s represented by circle 7. The clear notable difference between the implementation of the VCD of 16 and 36 segments is represented by circles 3 and 4, where a vortex exists formed in this hot spot, also with average wind speeds range from 2.7 m/s to 4.0 m/s.

These previous simulations give an overview of the behavior when the wind flow interacts with the buildings or structures of the academic Complex Domains. This results in a modification of the wind flow around these buildings with the interaction of the 36 wind speeds and directions of the CFD simulations.

#### 4.2.4 Validation of the Virtual Computational Domain in 36 Segments

The validation of the previous simulation is performed with the implementation of individual CFD simulations by taking the VCD into account. This validation considers the same initial and boundary conditions for the development of CFD simulations of the case study.

Figure 4.16 and Figure 4.17 show the results of each simulation developed at each wind speed and wind direction of the wind rose. For determining the behavior of the wind flow when interacting with the university Complex Domain buildings.

Derived from the individual simulations, the segments of the wind rose that have a higher incidence on the potential buildings of UAZ campus can be determined. These can be identified and represented in the wind directions ranging from  $0^\circ$  to  $140^\circ$  of the VCD corresponding to the first and the half of the second quadrant, with a wind speed that varies from 4.0 m/s to 1.5 m/s towards the center of the CFD simulations.

The sectors from  $150^\circ$  to  $200^\circ$  that corresponds to the second half of the second quadrant have less incidence in the site of interest, with wind speeds from 0.25 m/s to 2.75 m/s. The third quadrant, corresponding to wind sectors from  $200^\circ$  to  $260^\circ$ , has an increase in the wind speed ranging from 3.25 m/s to 4.0 m/s.

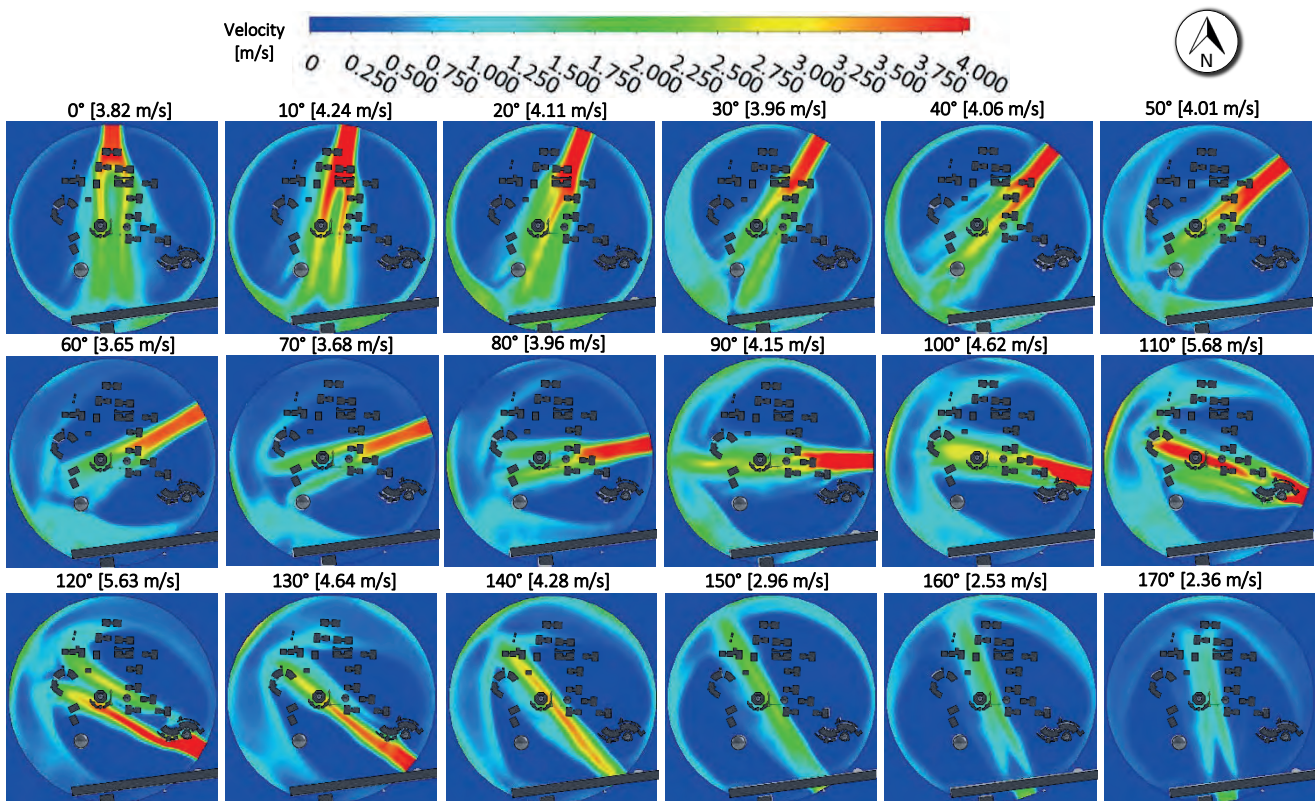


Figure 4.16 CFD Simulations; triacontakaihexagonal VCD implementation 36 wind speeds ( $0^\circ$ - $170^\circ$ ).



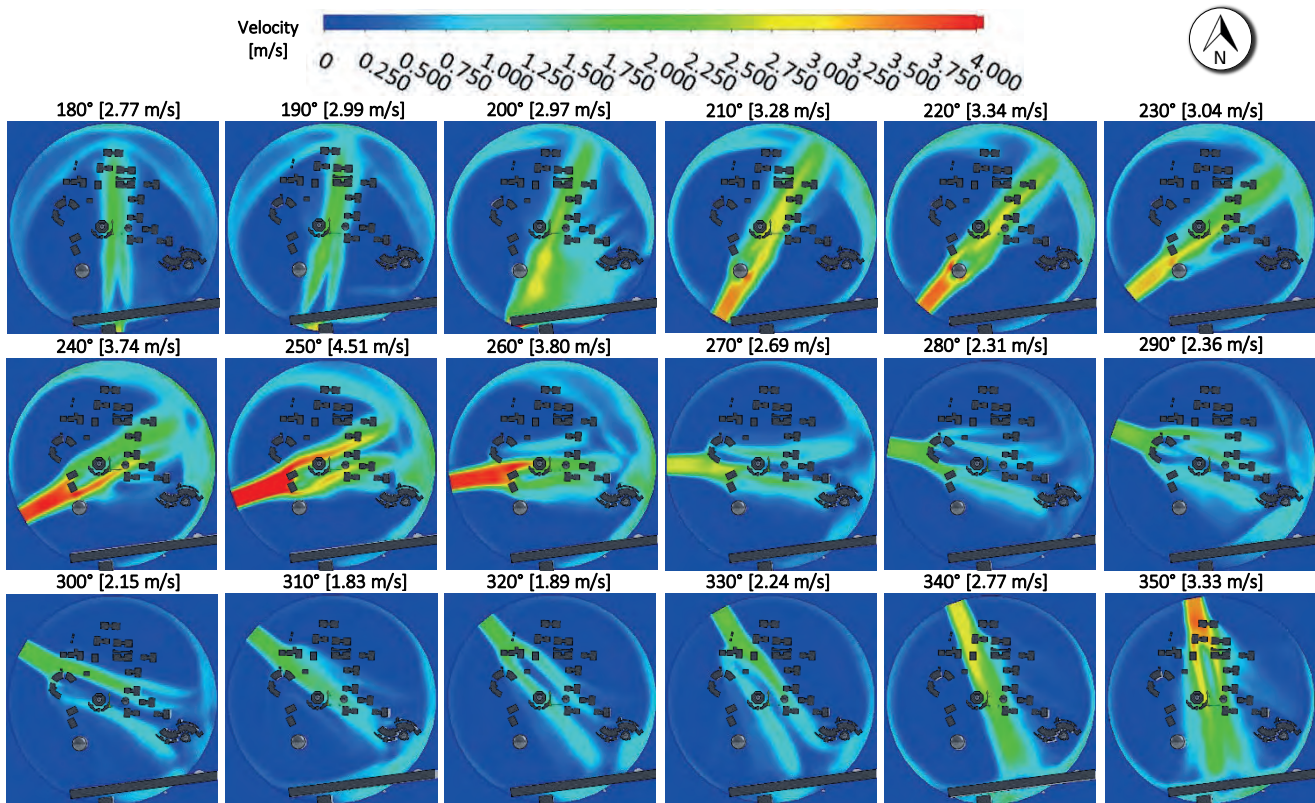


Figure 4.17 CFD Simulations; triacontakaihexagonal VCD implementation 36 wind speeds (180°-350°).

A zone of wind resource recession is presented in the fourth quadrant and corresponds to the sectors from 270° to 330°, with wind speeds from 0.75 m/s to 2.5 m/s. This zone can be considered as no wind potential affordable for the installation of SWTs. The following 340° and 350° wind sectors, an increment of the wind speed, can be observed, which is linked with the first quadrant having wind speeds from 2.5m/s to 3.5 m/s.

The results of the 36 individual CFD simulations are shown in Table 4.7, which shows the intensity scale of the average wind speed, and its respective frequency for each sector of the wind rose as a result of the wind resource assessment.

Table 4.7 Representation of 36 sectors of the wind rose of the wind speed and frequency in the intensity scale; red is higher.

	Wind rose sectors																	
	0°	10°	20°	30°	40°	50°	60°	70°	80°	90°	100°	110°	120°	130°	140°	150°	160°	170°
<b>Wind speed [m/s]</b>	3.82	4.24	4.11	3.96	4.06	4.01	3.65	3.68	3.96	4.15	4.62	5.68	5.63	4.64	4.28	2.96	2.53	2.36
<b>Frequency %</b>	1.8%	1.8%	1.5%	1.5%	1.6%	1.6%	1.4%	1.4%	1.8%	2.3%	3.6%	5.6%	7.1%	7.0%	8.9%	4.2%	3.4%	2.7%
	180°	190°	200°	210°	220°	230°	240°	250°	260°	270°	280°	290°	300°	310°	320°	330°	340°	350°
<b>Wind speed [m/s]</b>	2.77	2.99	2.97	3.28	3.34	3.04	3.74	4.51	3.8	2.69	2.31	2.36	2.15	1.83	1.89	2.24	2.77	3.33
<b>Frequency %</b>	4.3%	6.0%	5.0%	4.3%	3.9%	2.1%	2.6%	3.2%	1.8%	1.0%	0.8%	0.7%	0.7%	0.6%	0.6%	0.9%	1.3%	1.5%

As a comparison between Table 4.5 and Table 4.7, where the 16 and 36 segments are depicted, both present similar results with the higher incidence of the wind resource and frequency in the second quadrant. Generally, from the VCD of 36 segments implementation, wind speeds ranging from 1.83 to 5.68 m/s can be observed.

In this case, from the 110° to 140° wind sectors, correspond to wind speeds of 4.28 m/s to 5.68 m/s. On the other hand, the VCD of 16 segments implementation in the 90° to 135° wind sectors (E, ESE, SE cardinal points) corresponds to a similar wind speed ranging from 4.26 m/s to 5.55 m/s.

In summary, for this case study, the wind resource assessment and the VCD implementation in the CFD simulations allow corroborating the following. From the first to the third quadrant, a high incidence of the wind resource is presented, but with less frequency than the fourth quadrant of the wind rose diagram.

The implementation of the Virtual Computational Domain in the CFD simulations allows determining a better wind resource and hot spots. This new solution allows observing all the possibilities of installing wind turbines on buildings or structures by considering all the wind sectors of traditional wind roses. This methodology could also be used both for the small-scale wind emplacement or for large wind projects in any location having the proper wind resource assessment.

### **4.3 CFD Simulation of the building or structure**

Based on the previous sections and the implementation of the VCD, determining the potential buildings or structures inside the UAZ campus is possible. This section includes the CFD simulation of the buildings or structures to be analyzed with the VCD of 36 segments. Based on the previous results where a greater resolution exists in the wind maps and more hot spots compared with VCD of 16 segments' implementation and the unidirectional CFD simulation, the VCD of 36 segments is used in the present and further sections.

With the above CFD results and the campus' physical inspections, a building type with suitable characteristics for implementing SWTs in a BUWTs configuration has been identified. This type of building is located in seven different locations around the campus.

These seven buildings can be observed in Figure 4.18 a), which are marked from "a" to "g", in the VCD of 36 segments' implementation. These buildings are located in the first and second quadrant of the wind rose, which is an area with good wind potential. Buildings "a", "b", "e", "f", and "g" present an average wind speed of around 4 m/s. On the other hand, other buildings listed from I to XI are also presented, which also have good wind potential. These buildings can also be considered for the BUWTs installation, but there is less area available on the buildings' roof for placing the SWTs.

In order to determine which of the seven buildings selected are the best option for the implementation of the wind emplacement, it is necessary to develop a scanning along the *xy*-axis with cut plots of the CFD result on the *z*-axis. These cut plots will be implemented in the center of each building to measure which of the buildings have better wind conditions. Figure 4.18 b) shows the cut plots where the CFD simulations on each building are analyzed.

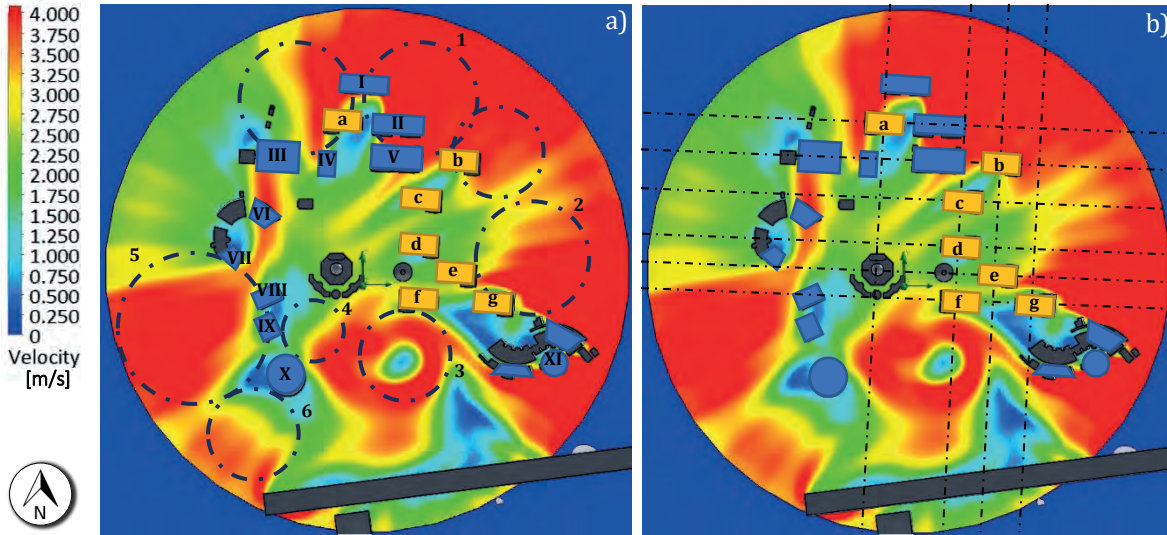


Figure 4.18 Location of interest buildings based on the VCD 36 segments implementation a) Building Location and b) Buildings' Cut Plots.

The following CFD results present the streamlines cut plots, which correspond to the best buildings for implementing the wind emplacement. The side views of the CFD simulations are shown, where the wind speed around the selected buildings is around 0 to 4.0 m/s inside the Urban Boundary Layer (UBL). This UBL is represented with a height of 1 to 2 km above ground level [1], [36], [115].

Figure 4.19 shows the streamlines cut plots of the CFD results over the seven buildings. The wind resource is presented by coming from the North towards the South cardinal point. These CFD simulations indicate the proper height for reaching the maximum wind potential. Furthermore, backward of the buildings, a high turbulence zone with low wind speeds can be observed.

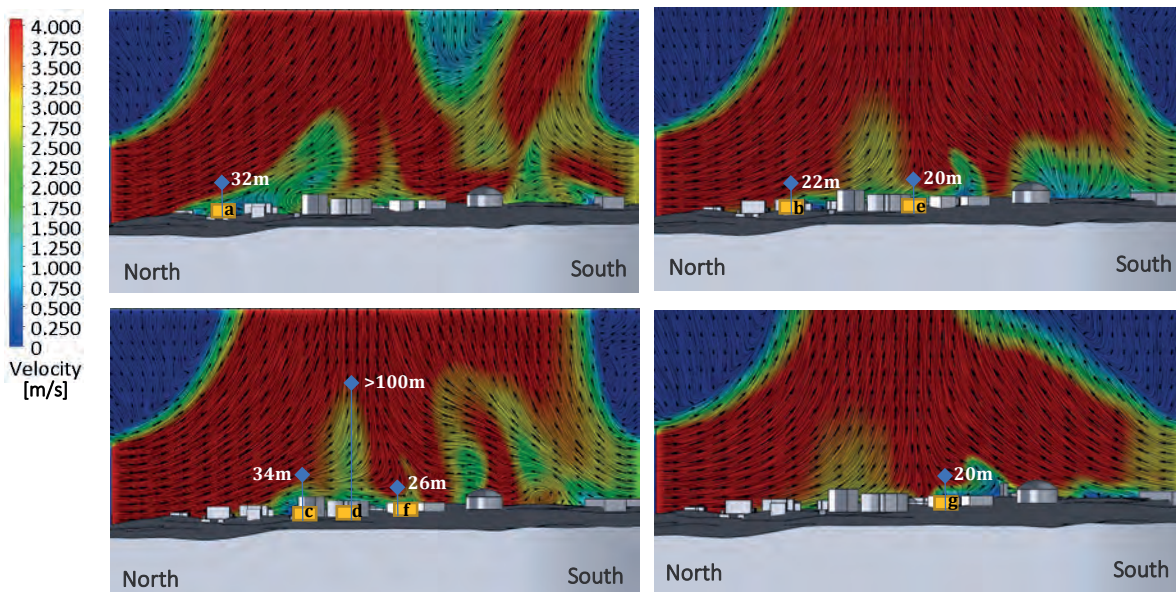


Figure 4.19 CFD Streamlines cut plots scanning along the y-axis (North to South).

These CFD simulations indicate that buildings “e” and “g” reach the maximum wind potential at 20 m, meanwhile the building “b” at 22 m and “f” at 26 m. This makes them the most viable options for the installation of the BUWTs’ configuration. In addition, buildings “a” and “c” are suitable for the proper SWTs installation but in this case, at a higher height of 32 m and 33 m, respectively. On the other hand, building “d” is not feasible for installing SWTs because the exploitable wind is located over a 100 m height.

For completeness in this study, the CFD simulations of the streamlines cut plot along the *x*-axis (East to West) were performed. The results are depicted in Figure 4.20, which shows the same heights for each building for reaching the maximum wind potential as the *y*-axis analysis. In both cases, an area of laminar wind speeds can be observed, surrounding the top of the buildings, with a prevailing wind direction from the East towards the Westside with average wind speeds of 4.0 m/s.

With these sets of simulations, the optimal height of the SWT tower can be determined, reducing the cost and time of feasibility studies for deploying projects for wind energy engineering in the present case study and others.

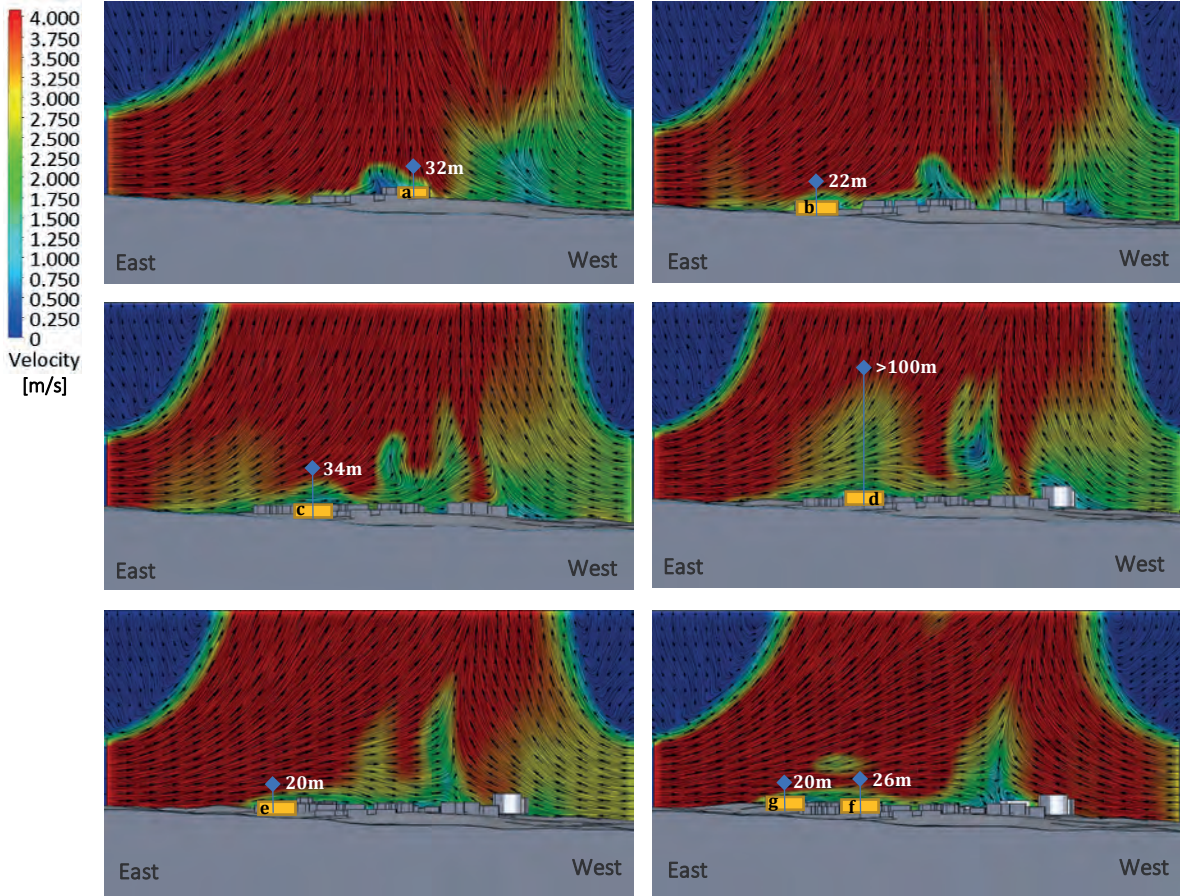


Figure 4.20 CFD Streamlines cut plots scanning along the *x*-axis (East to West).

Based on the buildings selected, a 3D representation is modeled with CAD tools for performing the new CFD simulations of the Building or Structure Domain. The 3D model will be useful in determining the behavior of the wind resource on the building itself and in deciding the optimal height and locations for the SWTs’ installation under the BUWTs’ configuration.

Figure 4.21 shows the three-dimensional model, which is 65 m long, 38 m wide, and 10.5 m high.

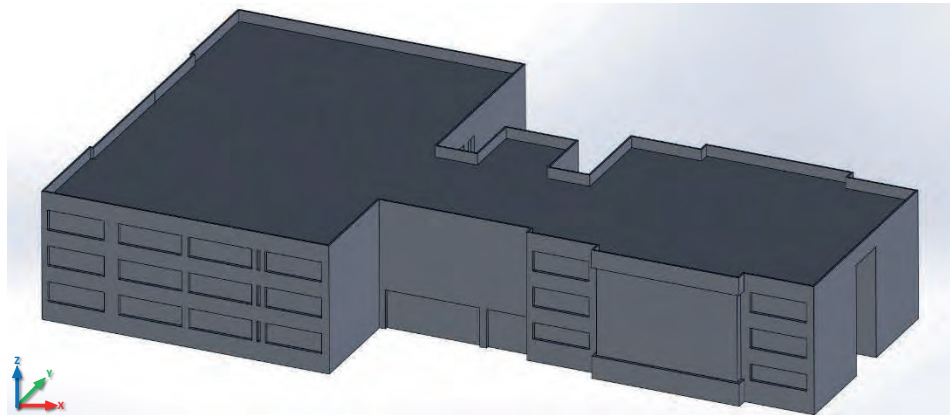


Figure 4.21 3D model of the UAZ building in the isometric view.

From the previous CFD simulations of the VCD 16 and 36 segments, the wind speed at which the building is subjected corresponds to an average of 3.81 m/s. It is important to notice that in this case, the wind speed does not present a decrease in the CFD simulation because of the interaction of the buildings or structures. In order to perform the CFD analysis, the initial and boundary conditions are presented in Table 4.8.

Table 4.8 Initial and boundary conditions for the CFD simulations ( $\mu S$ ) of the UAZ case study.

Analysis Type	Fluid Type	Boundary Conditions	Initial and Environment Conditions	Mesh Configuration
Type of flow: external	Air with all its physical properties	Roughness length: 400,000 $\mu m$	<i>a) Thermodynamic parameters:</i> -Temperature environment: 293.52 °K. -Atmospheric pressure of 78,010 Pa	-Automatic mesh with 2,609,200 control volume cells -Fluid cells contacting solids 32,778
Gravitational force: -9.81 m/s <sup>2</sup>	Turbulent flow		<i>b) Velocity parameters:</i> Average wind speed of 3.81 m/s at 153°. It comprises 3.38 m/s in the "x" component and speed of 1.72 m/s for the "y" component.	
			<i>c) Turbulence parameters:</i> -Length of turbulence of 38 m -Turbulence intensity of 0.0377%.	
			<i>d) Humidity parameters:</i> -Average relative humidity of 50.16%.	

Figure 4.22 shows the result of the CFD simulations of the Structure or Building Domain, in which the contour graphs of the velocity parameter are shown at different heights of the selected building, with the prevailing wind coming from the East-southeast (ESE) cardinal direction equivalent to 153° with the northern cardinal point as reference.

At ground level, in Figure 4.22 a), the velocity contour plot of the building shows a low presence of turbulence zone; at this 0 m height around the building, some SWTs in a side-mounted wind turbine configuration could be installed. In Figure 4.22 b), the turbulence parameter begins to increase in the rear part of the building at a height of 3.5m.

Figure 4.22 c) and d) show an increment of the turbulence zones, especially at the rear. This is a good indicator that this zone is not feasible for SWTs installation at these heights of 7 m and 10.5 m, respectively. In general, these simulations determine that the presence of turbulence both in the north and in the left part of the building sides are not suitable locations for the implementation of small wind projects. Furthermore, this turbulence is incremental concerning the height of the building.

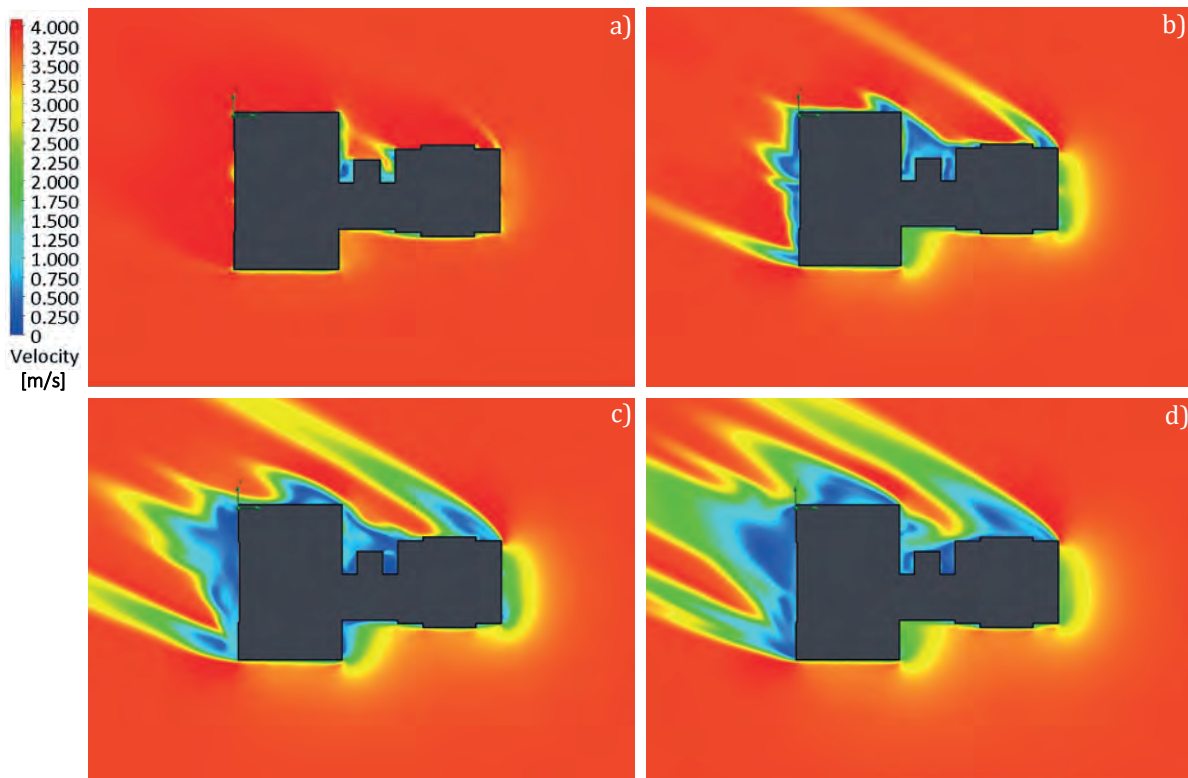


Figure 4.22 CFD Simulation of the top view of the interest building, contour plot at 4.0 m/s.

In addition, other CFD simulations were also performed in order to corroborate the heights illustrated in Figure 4.19 and Figure 4.20. Similarly, the cross-sections of the three-dimensional model can be developed, resulting in the CFD simulations, which can be analyzed in Figure 4.23.

In Figure 4.23 a), it is possible to observe the turbulence zone with a decrease of the wind speed in the left part of the building, extending to the left side to about 55 m. This CFD analysis shows that it can be determined that there is no problem with the turbulence parameter when placing the small wind turbines at a height of 30 m.

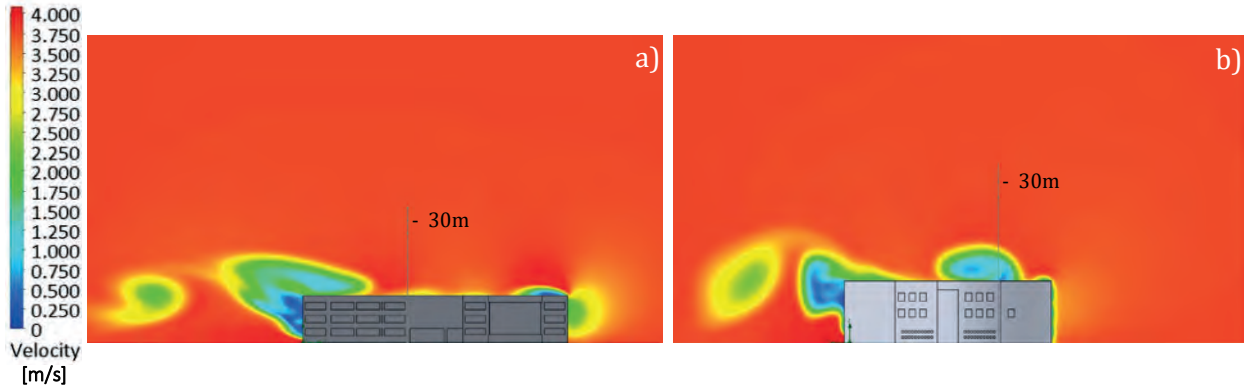


Figure 4.23 CFD Simulation side view of the interest building, contour plot of the a) transversal, and b) longitudinal view at 4.0 m/s.

In addition, Figure 4.24 shows the isometric views of the three-dimensional model in a) longitudinal and b) transversal cuts plots. These results show that a hub height higher than 30 m would be an optimum location. In addition, this confirms the findings in Figure 4.19 and Figure 4.20, which yield an average hub height of 33 m for the SWTs' installation.

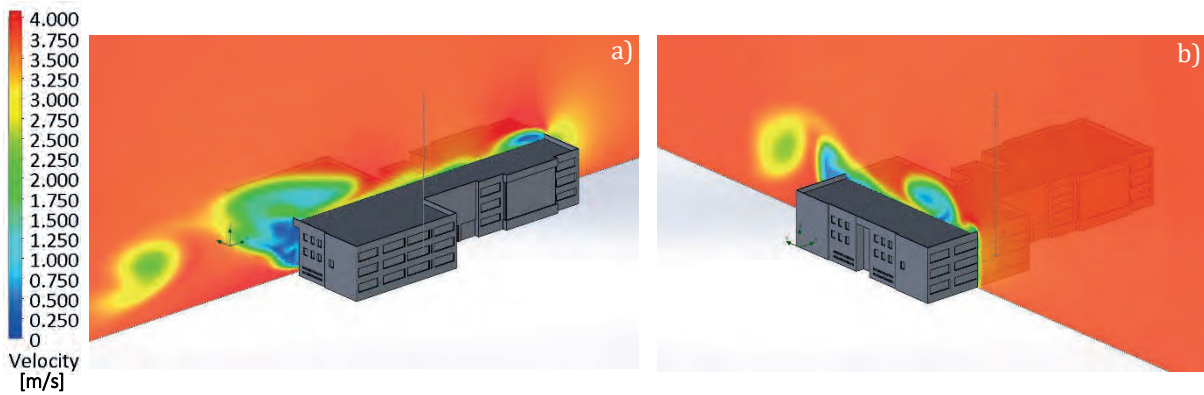


Figure 4.24 CFD Simulation isometric view of the interest building, contour plot of the a) longitudinal, and b) transversal view at 4.0 m/s.

With the results, it is possible to determine the optimal SWT tower height of 21.5 m, allowing to state an average hub height of 32 m for the selected buildings, which corresponds to 3.04 times the height of the building. This cannot be a statement common rule since; every case study has different initial and boundary conditions.

This determines the use of CFD techniques that assist in the design processes for feasibility studies of wind emplacement, reducing the time and cost in the development of wind energy engineering projects for rural and urban environments.

### 4.4 Selection of the small wind turbines SWTs based on a three-dimensional frequency histogram

As mentioned earlier in this chapter, for applying the VCD analysis on the UAZ campus, a measurement system was installed, including a WindMaster ultrasonic anemometer equipment.

Through this measurement equipment, the wind resource assessment in three components of spatial dimension has been developed; this is in the “*u*”, “*v*” and “*w*” vectors. Based on this advantage, the section of the SWTs’ selection in Stage 5 of the proposed methodology is performed in a three-dimensional frequency histogram.

This analysis of the wind resource in three spatial components will permit determining how is the behavior of the wind in the z-axis and, as a result, will determine if it corresponds to a VAWT or HAWT configuration.

A code in MATLAB® software was developed to implement the selection of the SWTs’ model and evaluate the wind resource. Figure 4.25 shows the average time series per day of the three vector components of the wind speed for one year from September 2017 to September 2018 with a minute time-stamp record.

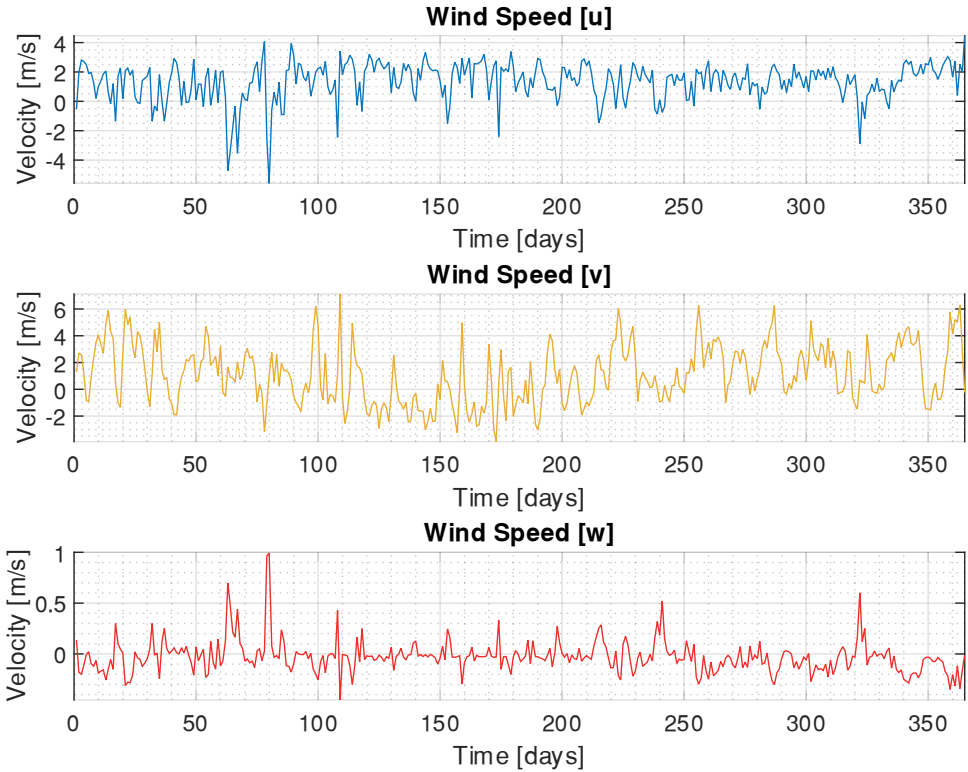


Figure 4.25 Components of the wind speed of the WindMaster ultrasonic anemometer.

Once the analysis and refinement of the wind resource data are carried out, the wind speed and direction are calculated using these vectors. Figure 4.26 corresponds to the same sampling period of one year and reveals a wind speed average of 3.8 m/s.



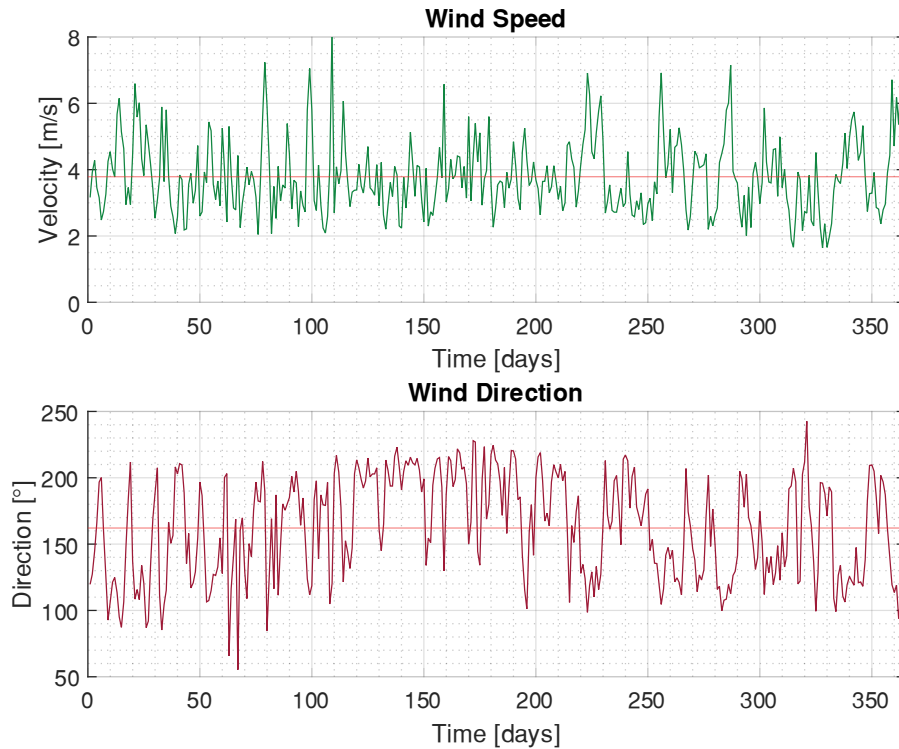


Figure 4.26 Wind speed and wind direction of the wind resource data of the WindMaster station.

Figure 4.27 shows a comparison between a) the wind rose diagram with 36 segments and b) the scatter plot wind resource assessment with the wind speeds and directions, resulting in the vector average of the velocity that is constructed for each measurement.

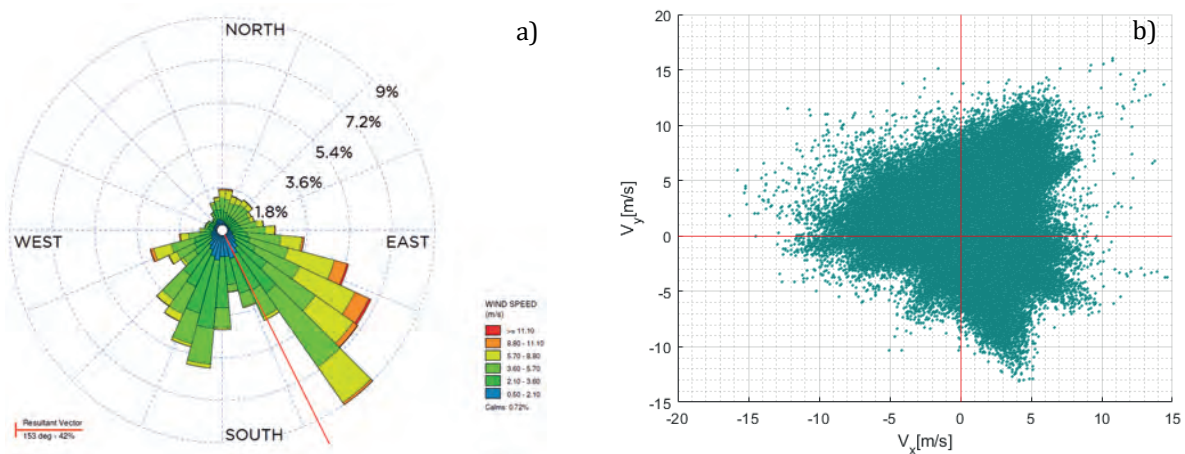


Figure 4.27 Wind rose diagram and scatter plot for the one-year wind speed data in the UAZ case study.

The scatter plot in Figure 4.27 b) shows that the points accumulate around the four regions in the quadrants along the velocity plane  $V_x$ - $y$ . These regions can be defined as “states,” as mentioned in [117]. Equilibrated points accumulated along the first and second quadrants of the figure can be appreciated, which correspond to the higher wind speeds and direction represented in the wind rose diagram.

In order to perform a more in-depth analysis of the wind data, a three-dimensional frequency histogram is developed, as shown in Figure 4.28 a), in which the number of velocity vectors found in a specific quadrant is presented. In this case, the second quadrant coincides with the highest frequency presented in the wind rose of Figure 4.27 a). In the same way in Figure 4.28 b), a greater density is observed in the same quadrant. It is possible to say that at least four states, one for each quadrant can be found.

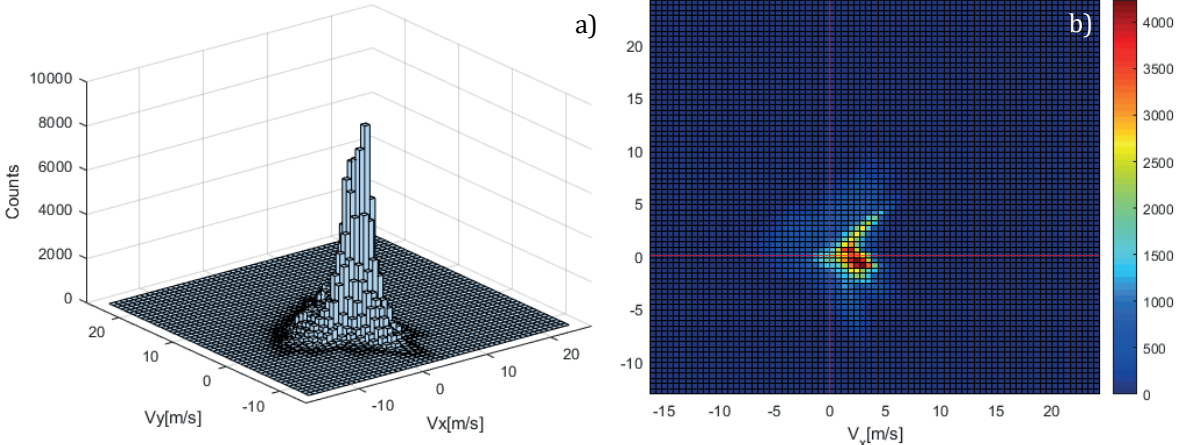


Figure 4.28 Three-dimensional frequency histogram a) and density graph b) for the velocity vectors.

To determine or develop the number of possible states, one of the most used clustering methods is the *k*-means algorithm. This method is used to section a data set of *n*-points in *k*-groups or clusters, which are classified employing proximity criteria [117].

For the application of the *k*-means algorithm, it is necessary to propose the optimal number of groups that are in the data set (*k*). In this case, five main clusters are proposed. In Figure 4.29 a), the graphic representation of the states in the *V<sub>x</sub>* and *V<sub>y</sub>* components are shown. Figure 4.29 b), though, details the three-dimensional clustering in five groups or clusters with their respective centroids. It is possible to observe a centered and flat grouping with almost zero changes in the vertical component of the wind *V<sub>z</sub>*. This indicates a uniform wind resource with prevailing southeasterly winds with a frequency of 42% to 153° relative to the northern cardinal point.

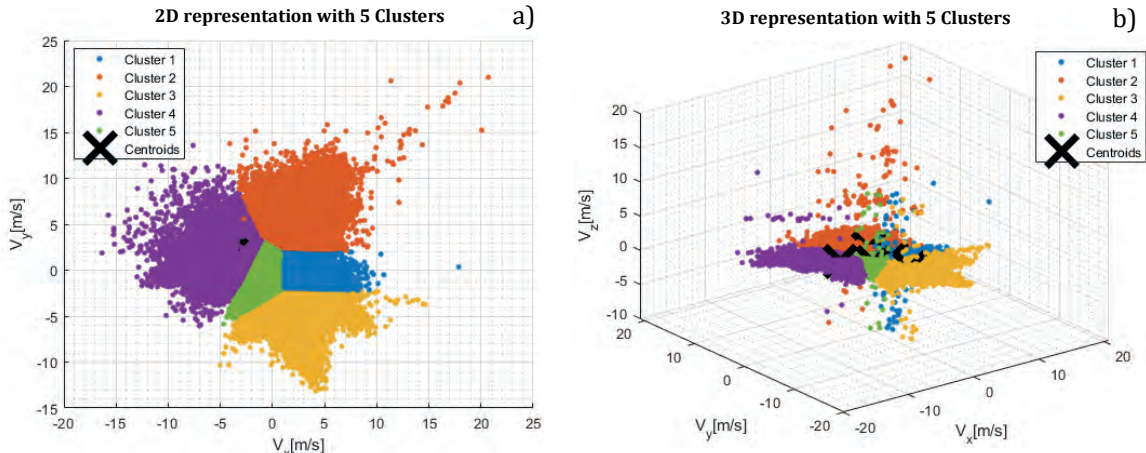


Figure 4.29 *K*-means clustering applied to the UAZ case study data with five clusters in a) 2D representation and b) 3D representation.

This same wind resource analysis was developed in  $k$ -means clustering techniques, which is shown proposing two main states  $k = 2$ , detailing in a two-dimensional study in Figure 4.30 a), and a three-dimensional analysis in Figure 4.30 b).

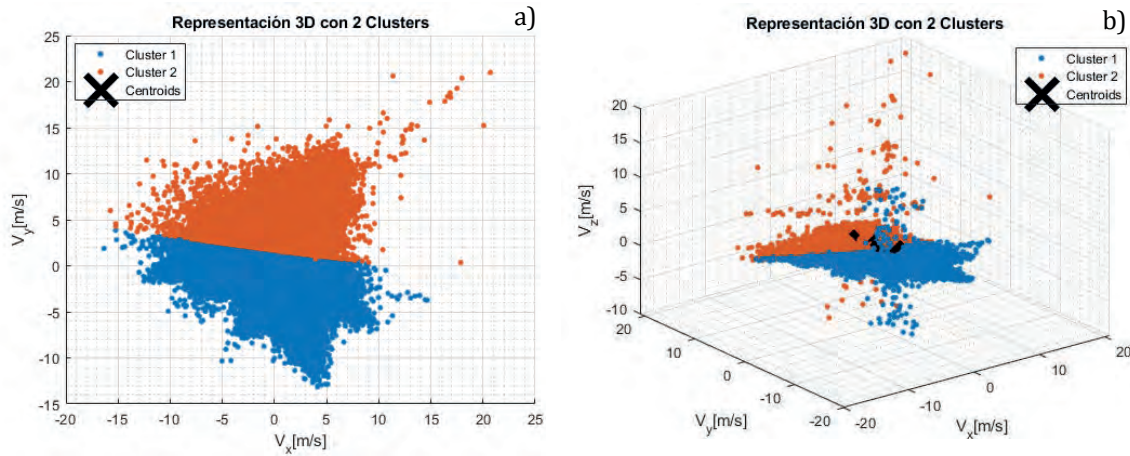


Figure 4.30  $K$ -means clustering applied to the UAZ case study data with two clusters in a) 2D representation and b) 3D representation.

All the partitions or clusters of the three-dimensional histogram are associated with the possible wind conditions. This allows the selection of the small wind turbine, with either vertical or horizontal axes.

This is based on the  $k$ -means analysis both in five clustering and two clustering in the three-dimensional representation, in which the grouped data formed a flat sheet along with the origin of the  $xy$ -axes and do not present a relevant change in the  $z$ -component.

The analyzed results indicate that a wind potential in the vertical component of the wind exists. With these wind conditions, a vertical axis wind turbine model will be indicated for exploiting the vertical winds like the Aeolos V-10 and Aeolos V-5 wind turbines modeled in Chapter 3.

## 4.5 CFD Analysis of the integration of building and SWTs domain

The next stage of the methodology in the present case study corresponds to the Domain of the arrangement of the structure or building - SWTs. The configuration of the small wind emplacement will be determined by the data of Table 3.10 in Chapter 3.

The possible matrix array for the four small wind turbines models is stated in Table 4.9, which represents the exact number of small wind turbines that can be located on the selected buildings corresponding to the maximum installed capacity that the wind emplacement can have, including the available area dimension of 1,706 m<sup>2</sup>.

Table 4.9 Configuration of the matrix arrangement dimension of the UAZ case study.

SWT Model	1 <sup>st</sup> SWT	2 <sup>nd</sup> STW	3 <sup>rd</sup> SWT	4 <sup>th</sup> SWT	5 <sup>th</sup> SWT	6 <sup>th</sup> SWT	7 <sup>th</sup> STW	8 <sup>th</sup> SWT	9 <sup>th</sup> SWT	Total capacity
Bergey 10 kW	0m	22 m	44 m	-	-	-	-	-	-	30 kW
XZERES 2.6 kW	0m	8 m	16 m	24 m	32 m	40 m	48 m	56 m	64 m	23.4 kW
A-V <sub>10</sub> 10 kW	0m	14 m	28 m	42 m	56 m	-	-	-	-	50 kW
A-V <sub>5</sub> 5 kW	0m	8 m	16 m	24 m	32 m	40 m	48 m	56 m	64 m	45 kW

The proposed layout for the wind emplacement corresponds to a matrix arrangement dimension with one row and five columns (1x5), with a 14 m distance between them, by selecting the Aeolos V-10 wind turbine model. As a result of the previous CFD simulations, the hub height considered is 32 m.

The proposed layout can be observed in Figure 4.31 a), which details the location on the roof of the building in a BUWTs configuration. Figure 4.31 b) shows the three-dimensional model of the Domain of the building -SWTs arrangement used for performing the CFD simulations of Stage 6 of the proposed methodology. Table 4.10 shows the initial and boundary conditions for defining the wind variables that set up the CFD study.

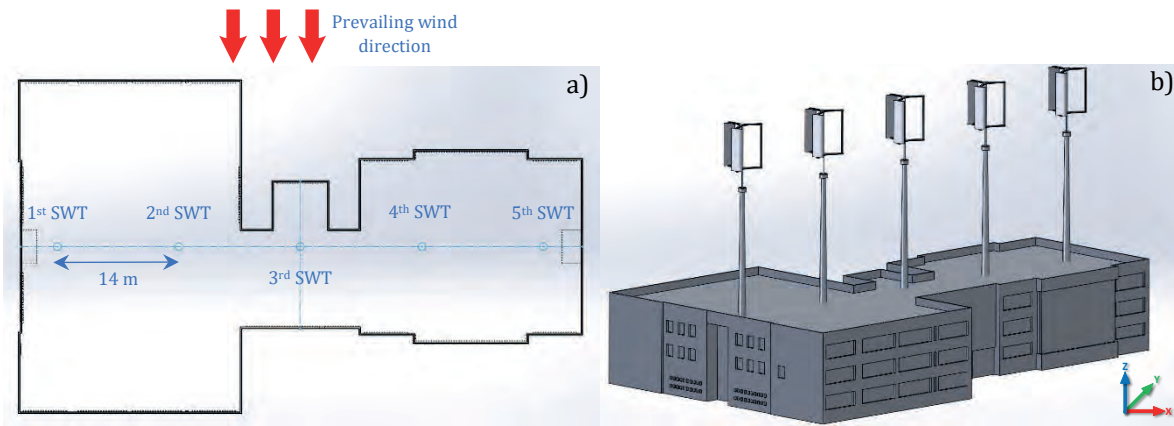


Figure 4.31 a) Layout of the matrix arrangement of the SWTs and b) 3D model design of the arrangement building - SWTs.

The CFD simulations with the conditions mentioned above consider the rotational state of the Aeolos V-10 wind turbine in order to confirm that the proposed distance between turbines is the affordable location for harnessing the maximum wind potential. These CFD simulations contemplate a resolution scale of 4.0 m/s.

Table 4.10 Initial and boundary conditions for the development of CFD simulations of SWTs.

Analysis Type	Fluid Type	Boundary Conditions	Initial and Environment Conditions	Mesh Configuration
Type of flow: internal	Air with all its physical properties	Roughness length: 400,000 $\mu\text{m}$	a) <i>Thermodynamic parameters:</i> -Temperature environment: 293.52 $^{\circ}\text{K}$ -Atmospheric pressure of 78,010 Pa	-Automatic mesh with 3,156,305 control volume cells -Fluid cells contacting solids 135,829
Gravitational force: -9.81 $\text{m/s}^2$	Turbulent flow		b) <i>Velocity parameters:</i> Operational wind speed of the small wind turbine: <b>-VAWT</b> Aeolos V-10kW – 3.81 m/s @ 13.23 rpm -Average wind speed of 3.81 m/s at 153°. It comprises 3.39 m/s in the "x" component and speed of 1.72 m/s for the "y" component.	

- 
- c) *Turbulence parameters:*
  - Length of turbulence of 38 m
  - Turbulence intensity of 0.0377%.
- 
- d) *Humidity parameters:*
  - Average relative humidity of 50.16%.
- 

## 4.6 CFD Post-processing

The CFD simulations results of the Domain of the arrangement of the structure or building - SWTs are depicted in Figure 4.32, which characterizes the a) isometric view, b) side view, c) front view and d) top view of the wind streamlines that interact with the Aeolos V-10 wind turbine model and the interest building of the UAZ campus.

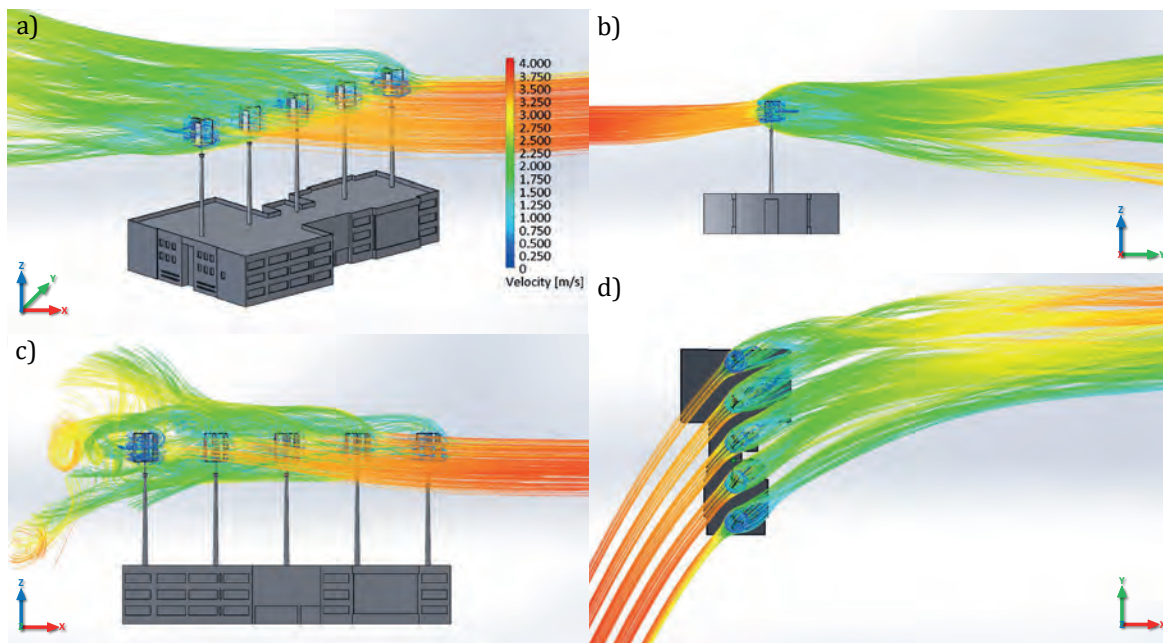


Figure 4.32 Rotational-state CFD simulation of the matrix array for the Domain of the arrangement of the building - SWTs – Streamlines a) Isometric, b) Side, c) Front, and d) Top views at 4.0 m/s.

In Figure 4.32 a), the wind streamlines can be observed that interact with the SWTs present in the inlet conditions of the velocity magnitude vector of 3.81 m/s. This wind speed remains constant until the interaction with the airfoils of the Aeolos wind turbine model.

From this point of interaction, as is expected, a considerable reduction of the wind speed is shown because of the kinetic potential extracted by the wind turbines, and a speed reduction from 3.81 m/s to 1.25 m/s is registered in the wind direction of 153°. In addition, a turbulence intensity in the back part of the SWTs around 42% is presented.

Figure 4.32 b) presents a similar result to the standalone CFD simulation of the rotational state of the Aeolos V-10 wind turbine. In this case, a flow bifurcation along the z-axis is depicted but with a higher reduction of the inlet wind speed.

In Figure 4.32 c) and d), where the side and top view of CFD simulation are presented, respectively, a light interference of the wind speed can be observed after the interaction of the wind with the SWTs; however, this does not interfere with the operation of the small wind turbines. Although there is a high turbulence intensity, it is achieved that the SWTs receive the full available wind resource.

The CFD simulations determine that the distance between turbines is correct, and in this case, the flow that passes through each SWTs, and a full available wind resource is usable. In addition, the proposed tower height of 21.5 m is also validated.

In order to give a first approximation of the wind speed behavior at the hub height of 32 m, on the five buildings selected, a three-dimensional model that integrates the building and the SWTs' array have been implemented in the VCD of 36 segments together with the Site Domain model and the Complex Domain models. Figure 4.33 shows the implementation of the VCD of 36 segments depicting the cut plot of the wind speed parameter at the specified height.

For the buildings “a” and “b”, the prevailing wind direction comes from the North and Northeast cardinal direction, respectively, whereas for buildings “e”, “f” and “g”, the prevailing wind direction comes from the East direction, which derives in a parallel wind direction according to the position of the building, keeping off the wind incidence on the SWTs with the proposed matrix layout in Figure 4.31. In this sense, a new layout is determined and analyzed for these last buildings.

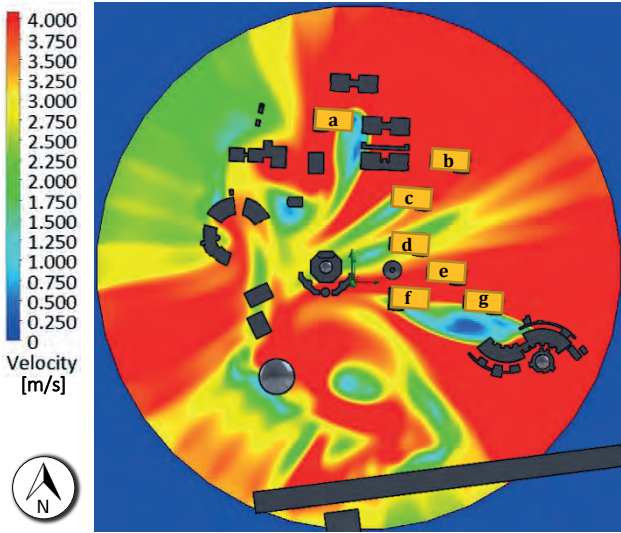


Figure 4.33 CFD Simulation with the VCD 36 segments implementation at a total hub height of 32 m.

This second layout will permit the interaction of the SWTs with the wind stream that comes from the East side of the UAZ Siglo XXI campus. The new proposed matrix array for the interest buildings “e”, “f” and “g” is stated in Table 4.11, which represents the exact number of SWTs that can be located on the interest building corresponding to the maximum installed capacity that the wind emplacement can have and also based on the dimensions of the selected building. The wind turbine selection also corresponds to the Aeolos V-10 wind turbine model, based on the maximum total installed capacity of 30 kW per building.

Table 4.11 Configuration of the matrix arrangement dimension of the UAZ case study.

SWT Model	1 <sup>st</sup> SWT	2 <sup>nd</sup> STW	3 <sup>rd</sup> SWT	4 <sup>th</sup> SWT	5 <sup>th</sup> SWT	Total capacity
Bergey 10 kW	0 m	22 m	-	-	-	20 kW
XZERES 2.6 kW	0 m	8 m	16 m	24 m	32 m	13 kW
A-V <sub>10</sub> 10 kW	0 m	14 m	28 m	-	-	30 kW
A-V <sub>5</sub> 5 kW	0 m	8 m	16 m	24 m	32 m	25 kW

Based on the above, the proposed layout for the wind emplacement corresponds to a matrix arrangement dimension with one row and three columns (1x3), with a 14 m distance between turbines. The proposed layout can be observed in Figure 4.34 a), which details the roof location of the interest building in a BUWTs configuration. On the other hand, the three-dimensional model of the small wind turbine is integrated into the model of the building, which is shown in Figure 4.34 b).

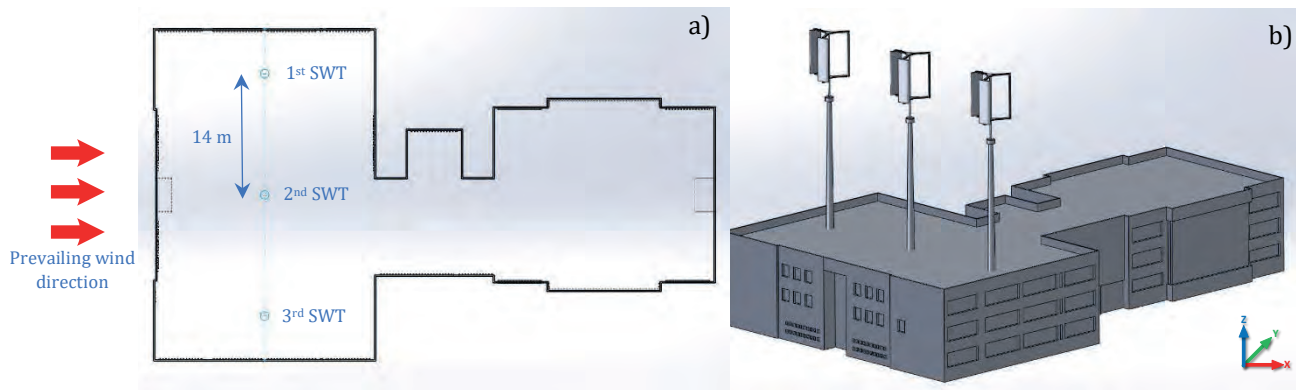


Figure 4.34 a) Layout II of the matrix arrangement of the SWTs and b) the 3D model design of the arrangement building - SWTs.

This CFD simulation is shown in Figure 4.35, which depicts the behavior of the wind speed mentioned earlier. The interest buildings from “a”, “b” and “e” to “g” are marked in order to focus on the behavior of the wind streamlines that reach these buildings.

Based on these CFD simulations, interest buildings “a” and “b” are considered the most suitable locations for the SWTs’ installation. This is due to these buildings receiving an affordable wind resource above 4.0 m/s, and despite is considered as turbulent simulation, these results consist of a laminar flow that reaches the SWTs with optimum cut-in wind speed. In addition, building “a” has only four suitable SWTs, i.e., 40 kW, while interest building “b” has a maximum total installed capacity of 50 kW.

On the other hand, buildings “e”, “f” and “g” have good wind resource potential but with a (1x3) layout, i.e., 30 kW per building. Note, that interest buildings “c” and “d” have a reduced wind resource potential from the North cardinal direction and the Eastside because it is below from the cut-in speed of 2.5 m/s, and therefore is not an affordable location for the proper installation of the BUWTs configuration.

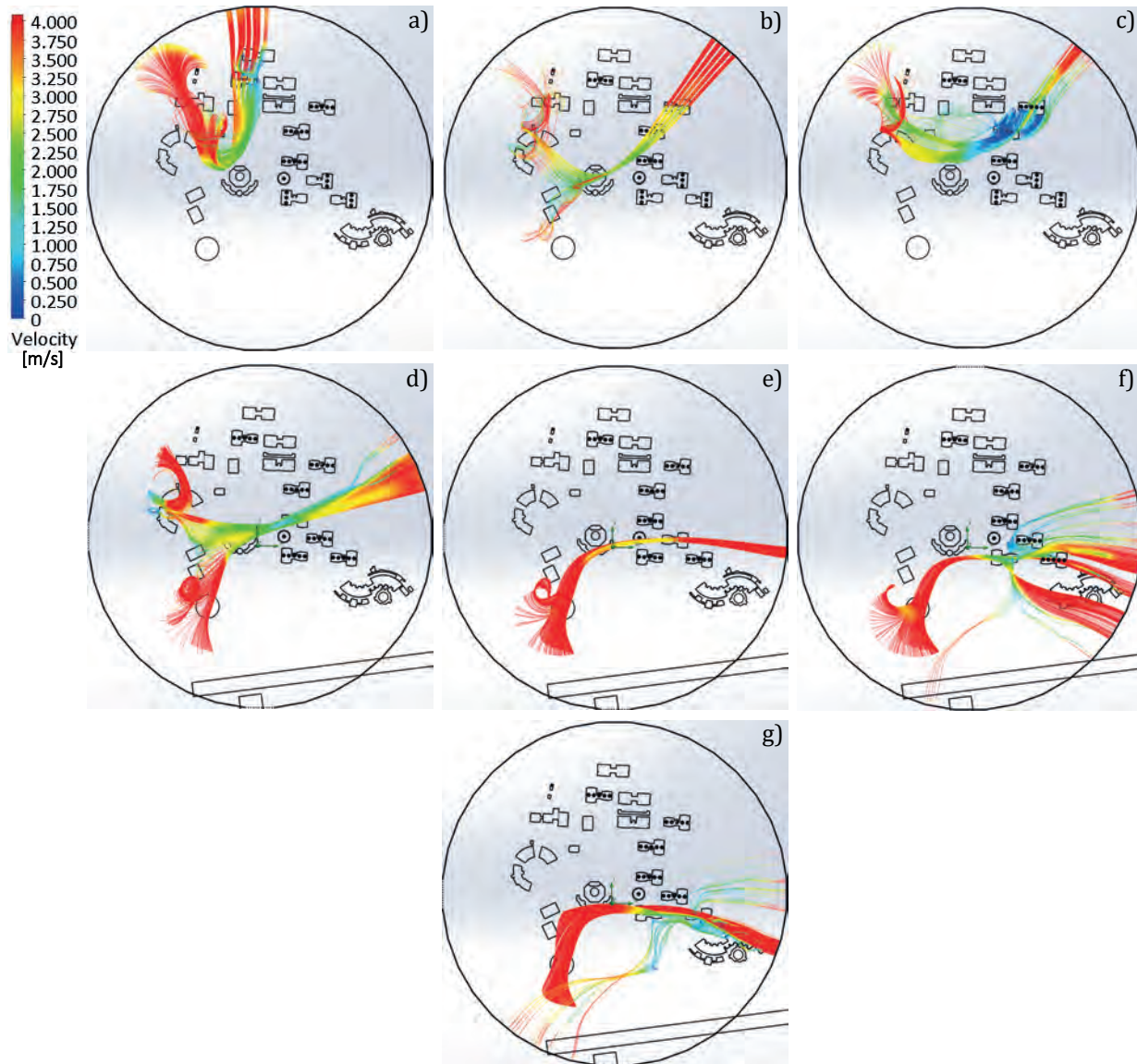


Figure 4.35 CFD Streamlines of the Aeolos V-10 SWTs layout I and the VCD integration of the seven buildings from a) to g).

This new layout is considered in order to have the proposed SWTs perpendicularly, reaching the wind stream that flows from the East side of the campus, according to the position of buildings “e”, “f” and “g”. The CFD simulations with this new layout are shown the Figure 4.36, which depicts only interest buildings “e”, “f”, and “g” since interest buildings “a” to “d” present the same CFD results.



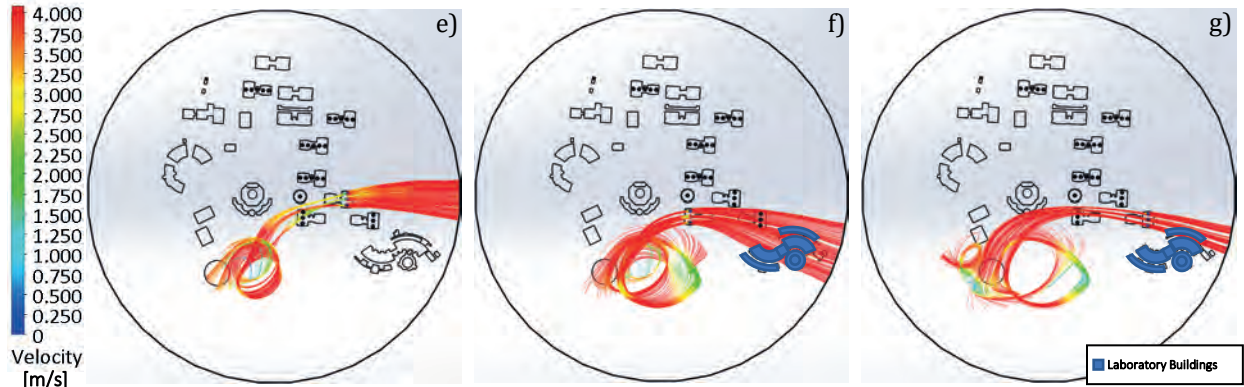


Figure 4.36 CFD Streamlines of the Aeolos V-10 SWTs layout II and the VCD integration of the interest buildings from e) to g).

These new CFD results with the layout II configuration that proposed a total installed capacity of 30 kW per building shows that building “e” presents a considerable improvement. The wind speed of 4.0 m/s presented in the CFD simulation is received in building “e” by the three SWTs, which determines a good location for the wind emplacement.

On the other hand, buildings “f” and “g” also have a good wind resource potential. The interaction of the wind speed with other structures, specifically the Laboratory Buildings, does not interfere with the wind direction from the 110° and 120° degrees from the VCD wind rose implementation. In this sense, building “f” receives a wind resource around 3.8 m/s, determining that this building is feasible for SWTs installation. Moreover, in building “g”, the SWTs located on the northern part of the building has a good wind resource potential of around 4.0 m/s, receiving the proper wind resource, because the wind flow that comes from the 110° direction is predominant and the tower height proposed is correct.

These previous results allow stating and reconfiguring the proposed wind emplacement for the UAZ Siglo XXI campus in a rural environment. Buildings “a” and “b” comprise a total of nine SWTs. Furthermore, buildings “e” to “g” are configured with three SWTs in each interest building, obtaining a total installed capacity of 180 kW with 18 Aeolos V-10 wind turbines.

This type of CFD post-processing allows validating the proposed methodology with the implementation of the VCD of 16 and 36 segments, for determining the zones with high wind energy incidence, allowing to describe the behavior of the velocity parameter with other structures that are in contact with the fluid.

## 4.7 Discussion and conclusions

Virtual Computational Domains VCD of 16 and 36 segments were proposed in the present chapter. These new CFD domains are naturally implemented in the proposed methodology in Chapter 4 to assess the installation of small-scale wind turbines. Results show that the VCD in both cases has higher quality and fidelity in the wind resource maps generated comparing with the unidirectional method. First, analyses of both domains, the VCD of 16 and 36, were performed. For better results, a steady case with a good wind resource potential is used for demonstrating the effectiveness of the new VCD.

The methodology developed and applied in this case study allows stating that this site is affordable for developing the wind emplacement with higher installed capacity for three important aspects caused by good wind conditions, the available space on the UAZ campus, and the rural location of the case study.

It can be noted that when performing the unidirectional CFD simulation, only six buildings can be considered suitable for the SWTs' installation in a BUWTs configuration. On the other hand, the implementation of the VCD of 16 and 36 segments the number of potential building augment considerably, representing a total of 16 and 17 buildings, respectively, obtaining more hot wind spots around the buildings. Table 4.12 shows a comparison between the case studies developed in this research showing the percentage of the potential buildings performing BUWTs' configuration, comparing the CFD simulations with and without the VCD implementation.

Table 4.12 Comparison between the VCD implementation and unidirectional CFD simulations.

Evaluated concept	TESE Case Study	IIUNAM Case Study		UAZ Case Study			
	Unidirectional	Unidirectional	16 VCD	36 VCD	Unidirectional	16 VCD	36 VCD
Potential buildings	8 / 36	6 / 28	14 / 28	15 / 28	6 / 23	16 / 23	17 / 23
Wind hot spots	4	2	6	7	5	7	7
Buildings penetration percentage	22.2 %	21.4 %	50.0 %	53.6 %	26.0 %	69.6 %	73.9 %
Hub height	30 m - 4.16 times the height of the building	58 m - 1.56 times the height of the building		32 m - 3.04 times the height of the building			
Tower height	23 m	27 m		21.5 m			
Building height	7.2 m	37 m		10.5 m			
VCD height	-	62 m		80 m			

In conclusion, the implementation of the proposed VCD is a useful tool that permits the identification of more wind hot spots in both BUWT and BEWT configurations, increasing the possibilities of developing small wind projects to harness the wind resource where the unidirectional CFD simulations do not present potential wind areas.

The methodology employed in all the analyzed case studies does not present any concern for being implemented in any other different topographic conditions or different initial conditions, as presented in the urban and rural cases. In this sense, the UAZ case study is feasible for developing a wind emplacement by the wind conditions and the location selected.

# CHAPTER 5

---

## CONCLUSIONS AND FUTURE RESEARCH

---

### 5.1 Conclusions

The goal of the present research has been the development of a practical methodology regarding micro-siting ( $\mu$ S) of small wind turbines, in both rural and urban areas and in agreement with the IEA Task 27. The research work is divided into two main parts: a novel methodology based on CFD analysis and the implementation of a new virtual computational domain (VCD) based on a wind rose diagram, which represents the main concerns in this dissertation.

The CFD methodology presented was proposed based on seven stages, which comprises from the site selection and wind resource assessment to the CFD analysis of the topography, structure, or complex and SWTs - building integration. These stages aim to be a tool that will allow the pre-feasibility studies of small wind projects for exploiting the wind resource with small wind turbines in complex terrains.

The methodology has been used in several projects from scarce to optimal wind resource, and results show the value of this implementation in comparison with traditional methods such as wind tunnel analysis. In this thesis, only two case studies are presented, which are implemented and validated following the methodology: one in the urban environment and other in a rural area. The methodology has proven to be easy to replicate in any site conditions, including different wind resource, topography, and roughness length.

On the other hand, the innovative implementation of a VCD and its application in the methodology allows a more accurate evaluation for the use of the wind resource by using the wind rose diagram, which is a very well-known and widely accepted tool for the evaluation of the wind resource. The VCD of 16 segments allows using more than one wind direction in the CFD analysis and results in a detailed wind resource map representation with higher resolution.

Results show that implementing the VCD 16 and 36 segments, the number of potential buildings augment considerably, obtaining more wind hot spots around the buildings in a BUWTs configuration. This can be compared with many cases that use only the unidirectional CFD simulation, in which only a few potential buildings can be considered for SWTs installation.

In addition, the implementation of the CFD analysis of the SWTs in the methodology, including the VCD, helped to propose the matrices arrangements for each wind turbine model selected. These arrays have been proposed in order to obtain the maximum installed capacity based on the SWTs analyzed and the dimension of the building or structure selected.

Based on the previous premise, different layouts configuration to each case study were proposed for obtaining the maximum benefit of these types of projects using a BUWTs configuration.

Last but not least, this novel methodology maximizes the cost-benefit and improves the quality of the wind resource maps at the micro-siting scale, supporting the implementation of the CFD analysis applied to the small wind energy industry.

It can be concluded that the implementation of both the methodology and the VCD wind rose are useful tools that permit the identification of new wind hot spots in both BUWTs and BEWTs configurations, increasing the possibilities of developing small wind projects to harness the wind resource.

## **5.2 Future research**

The present work has made progress in harnessing the wind resource in urban and rural zones through SWT technologies. It is clear, however, that a lot of more work needs to be done.

The structure of this developed methodology can be implemented in any CFD software or numerical solution. This is an advantage since both the methodology itself and the Virtual Computational Domain can be easily migrated to open-source software like OpenFOAM® in a Linux distribution that would allow accessing this methodology for finding optimal zones for the installation of small wind projects in an affordable way.

An interface for adding new small wind turbines models that are available on the market needs further work, including their respective CFD simulations, in order to propose more than one option and several new matrices layouts. An extensive catalog of SWTs will bring more options for the installation of these devices, both in the urban and rural environments.

New CAD modeling software will be researched to allow a greater area of study of the topographic model by increasing the topographic area, which will assist the generation of wind resource maps in large-scale wind technologies.

In the context of the VCD implementation, as future development, the idea of implementing the VCD at different heights arises in order to have a representation of the wind resource according to the urban boundary layer. Taking into consideration the roughness length and the estimation of the wind speed at different heights with the Hellmann exponential law or logarithmic wind profile law can be studied.

Another important aspect of being considered for future research is the application of this methodology to other urban and rural case studies with wind potential, where financing can be obtained for developing the physical installation of the SWT based on the CFD results and for evaluating the power generation of the turbines.

Based on the results established in the methodology allows identifying the potential wind hot spots in order to install a small wind project in a BUWTs configuration. One of the future works will be the implementation of the methodology not only using the BUWT configuration but also BEWTs configuration in order to take advantage of the detected wind streams derived from the CFD simulations, to install SWTs out of the buildings of the case studies selected.

Future research also includes the application of the current methodology to other terrain areas like coastal zones, helping to develop feasibility studies and the implementation of electrical microgrids, by using hybrid renewable energies like wind and solar energy. This can be helpful in relation to the social impact that the installation of these types of technologies brings to rural areas that are outside of the electrical distribution networks.

As future work, it is considered that as a great opportunity area is the application of the proposed CFD methodological tool developed in ocean energies, with particular emphasis on harnessing and locating potential submarine currents submarines currents, and their interaction with the emerging marine turbine technology.

### 5.3 References

- [1] A. Ricci, M. Burlando, A. Freda, and M. P. Repetto, "Wind tunnel measurements of the urban boundary layer development over a historical district in Italy," *Build. Environ.*, vol. 111, pp. 192–206, 2017.
- [2] K. Ahmad, M. Khare, and K. K. Chaudhry, "Wind tunnel simulation studies on dispersion at urban street canyons and intersections—a review," *J. Wind Eng. Ind. Aerodyn.*, vol. 93, no. 9, pp. 697–717, Sep. 2005.
- [3] A. G. Dutton, J. A. Halliday, and M. J. Blanch, "The Feasibility of Building-Mounted/Integrated Wind Turbines (BUWTs): Achieving their potential for carbon emission reductions. Final Report," 2005.
- [4] B. Blocken and T. Stathopoulos, "CFD Simulation of Pedestrian-level Wind Conditions Around Buildings: Past Achievements and Prospects," *J. Wind Eng. Ind. Aerodyn.*, vol. 121, no. c, pp. 138–145, 2013.
- [5] T. Stathopoulos and B. A. Baskaran, "Computer Simulation of Wind Environmental Conditions Around Buildings," *Eng. Struct.*, vol. 18, no. 11, pp. 876–885, 1996.
- [6] Y. Tominaga and T. Stathopoulos, "Numerical Simulation of Dispersion Around an Isolated Cubic Building: Model Evaluation of RANS and LES," *Build. Environ.*, vol. 45, no. 10, pp. 2231–2239, 2010.
- [7] S. Reiter, "Validation Process for CFD Simulations of Wind Around Buildings," *Eur. Built Environ. CAE Conf.*, pp. 1–18, 2008.
- [8] B. Blocken and J. Carmeliet, "Validation of CFD Simulations of Wind-driven Rain on a Low-rise Building Facade," *Build. Environ.*, vol. 42, no. 7, pp. 2530–2548, 2007.
- [9] B. Blocken, W. D. Janssen, and T. van Hooff, "CFD Simulation for pedestrian wind comfort and wind safety in urban areas: General decision framework and case study for the Eindhoven University campus," *Environ. Model. Softw.*, vol. 30, pp. 15–34, 2012.
- [10] D. Anitha, G. K. Shamili, P. Ravi Kumar, and R. Sabari Vihar, "Airfoil shape optimization using CFD and parametrization methods," *Mater. Today Proc.*, vol. 5, no. 2, pp. 5364–5373, Jan. 2018.
- [11] Q. Qu, X. Jia, W. Wang, P. Liu, and R. K. Agarwal, "Numerical study of the aerodynamics of a NACA 4412 airfoil in dynamic ground effect," *Aerosp. Sci. Technol.*, vol. 38, pp. 56–63, Oct. 2014.
- [12] B. S. Anil Kumar, Ramalingaiah, S. Manjunath, and R. Ganganna, "Computational investigation of flow separation over NACA 23024 airfoil at 6 million free stream Reynolds number using k-epsilon turbulence model," *Mater. Today Proc.*, vol. 5, no. 5, pp. 12632–12640, Jan. 2018.
- [13] S. A. Abdulqadir, H. Iacovides, and A. Nasser, "The physical modelling and aerodynamics of turbulent flows around horizontal axis wind turbines," *Energy*, vol. 119, pp. 767–799, Jan. 2017.
- [14] Y. Li, K.-J. Paik, T. Xing, and P. M. Carrica, "Dynamic overset CFD simulations of wind turbine aerodynamics," *Renew. Energy*, vol. 37, no. 1, pp. 285–298, Jan. 2012.

- [15] M. S. Siddiqui, A. Rasheed, M. Tabib, and T. Kvamsdal, "Numerical investigation of modeling frameworks and geometric approximations on NREL 5 MW wind turbine," *Renew. Energy*, vol. 132, pp. 1058–1075, Mar. 2019.
- [16] N. N. Sørensen, J. Johansen, and S. Conway, "CFD Computations of Wind Turbine Blade Loads During Standstill Operation TASK 3 . 1 Report," vol. 1465, no. June, 2004.
- [17] E. P. N. Duque, W. Johnson, C. P. Vandam, R. Cortes, and K. Yee, "Numerical Predictions of Wind Turbine Power and Aerodynamic Loads for the NREL Phase II Combined Experiment Rotor The NREL phase II combined experiment rotor."
- [18] J. Varela and D. Bercebal, "CFD Calculations of the Flow Around a Wind Turbine Nacelle," 1999.
- [19] M. Ayala, J. Maldonado, E. Paccha, and C. Riba, "Wind Power Resource Assessment in Complex Terrain: Villonaco Case-study Using Computational Fluid Dynamics Analysis," *Energy Procedia*, vol. 107, no. September 2016, pp. 41–48, 2017.
- [20] M. Make and G. Vaz, "Analyzing Scaling Effects on Off-shore Wind Turbines Using CFD," *Renew. Energy*, vol. 83, pp. 1326–1340, 2015.
- [21] R. Cattin, B. Schaffner, and S. Kunz, "Validation of CFD Wind Resource Modeling in Highly Complex Terrain.," *Accessed online.*, 2006.
- [22] L. Lu and K. Y. Ip, "Investigation on the Feasibility and Enhancement Methods of Wind Power Utilization in High-rise Buildings of Hong Kong," *Renew. Sustain. Energy Rev.*, vol. 13, no. 2, pp. 450–461, Feb. 2009.
- [23] H. Nasarullah Chaudhry, J. Kaiser Calautit, and B. Richard Hughes, "The Influence of Structural Morphology on the Efficiency of Building Integrated Wind Turbines (BIWT)," *AIMS Energy*, vol. 2, no. 3, pp. 219–236, 2014.
- [24] H. N. Chaudhry, J. K. Calautit, and B. R. Hughes, "Numerical Analysis of the Integration of Wind Turbines into the Design of the Built Environment," *Am. J. Eng. Appl. Sci.*, vol. 7, no. 4, pp. 355–365, 2014.
- [25] Y. G. Heo, N. J. Choi, K. H. Choi, H. S. Ji, and K. C. Kim, "CFD Study on Aerodynamic Power Output of a 110 kW Building Augmented Wind Turbine," *Energy Build.*, vol. 129, pp. 162–173, 2016.
- [26] S. L. Walker, "Building Mounted Wind Turbines and Their Suitability for the Urban Scale-A Review of Methods of Estimating Urban Wind Resource," *Energy Build.*, vol. 43, no. 8, pp. 1852–1862, 2011.
- [27] D. Ayhan and A. Sağlam, "A Technical Review of Building-mounted Wind Power Systems and a Sample Simulation Model," *Renew. Sustain. Energy Rev.*, vol. 16, no. 1, pp. 1040–1049, 2012.
- [28] L. Ledo, P. B. Kosasih, and P. Cooper, "Roof Mounting Site Analysis for Micro-wind Turbines," *Renew. Energy*, vol. 36, no. 5, pp. 1379–1391, 2011.
- [29] I. Abohela, N. Hamza, and S. Dudek, "Effect of Roof Shape, Wind Direction, Building Height and Urban Configuration on the Energy Yield and Positioning of Roof Mounted Wind Turbines," *Renew. Energy*, vol. 50, pp. 1106–1118, 2013.

- [30] H. Montazeri, B. Blocken, W. D. Janssen, and T. van Hooff, "CFD Evaluation of New Second-skin Facade Concept for Wind Comfort on Building Balconies: Case Study for the Park Tower in Antwerp," *Build. Environ.*, vol. 68, pp. 179–192, 2013.
- [31] D. P. Sari and W. B. Kusumaningrum, "A Technical Review of Building Integrated Wind Turbine System and a Sample Simulation Model in Central Java, Indonesia," *Energy Procedia*, vol. 47, pp. 29–36, 2014.
- [32] S. Zanforlin and S. Letizia, "Improving the performance of wind turbines in urban environment by integrating the action of a diffuser with the aerodynamics of the rooftops," *Energy Procedia*, vol. 82, pp. 774–781, 2015.
- [33] F. Toja-Silva, O. Lopez-Garcia, C. Peralta, J. Navarro, and I. Cruz, "An Empirical-heuristic Optimization of the Building-roof Geometry for Urban Wind Energy Exploitation on High-rise Buildings," *Appl. Energy*, vol. 164, pp. 769–794, 2016.
- [34] P. Johnson, D. Ryan, and J. Roeth, "Case Study of the Performance of the Erastus Corning Tower Small Wind Turbine and Building-Mounted Wind Recommendations NYSERDA's Promise to New Yorkers: New Yorkers can count on NYSERDA for objective, reliable, energy-related solutions," Albany NY, 2011.
- [35] A. Gagliano, F. Patania, A. Capizzi, F. Nocera, and A. Galesi, "A Proposed Methodology for Estimating the Performance of Small Wind Turbines in Urban Areas," in *Sustainability in Energy and Buildings*, 2012, pp. 539–540.
- [36] D. R. Drew, J. F. Barlow, and T. T. Cockerill, "Estimating the Potential Yield of Small Wind Turbines in Urban Areas: A Case Study for Greater London, UK," *J. Wind Eng. Ind. Aerodyn.*, vol. 115, pp. 104–111, 2013.
- [37] L. V. White and S. J. Wakes, "Permitting Best use of Wind Resource for Small Wind-Turbines in Rural New Zealand: A Micro-scale CFD Examination," *Energy Sustain. Dev.*, vol. 21, no. 1, pp. 1–6, 2014.
- [38] A. B. Tabrizi, J. Whale, T. Lyons, and T. Urmee, "Performance and safety of rooftop wind turbines: Use of CFD to gain insight into inflow conditions," *Renew. Energy*, vol. 67, pp. 242–251, 2014.
- [39] T. Simões and A. Estanqueiro, "A New Methodology for Urban Wind Resource Assessment," *Renew. Energy*, vol. 89, pp. 598–605, 2016.
- [40] A. S. Yang, Y. M. Su, C. Y. Wen, Y. H. Juan, W. S. Wang, and C. H. Cheng, "Estimation of Wind Power Generation in Dense Urban Area," *Appl. Energy*, vol. 171, pp. 213–230, 2016.
- [41] B. W. Yan and Q. S. Li, "Coupled On-site Measurement/CFD Based Approach for High-resolution Wind Resource Assessment Over Complex Terrains," *Energy Convers. Manag.*, vol. 117, pp. 351–356, 2016.
- [42] Q. Wang, J. Wang, Y. Hou, R. Yuan, K. Luo, and J. Fan, "Micrositing of roof mounting wind turbine in urban environment: CFD simulations and lidar measurements," *Renew. Energy*, vol. 115, pp. 1118–1133, Jan. 2018.



- [43] IEA, "IEA Wind Task 27: Einsatz von Kleinwindkraftanlagen in Gebieten mit turbulenten Strömungsbedingungen (Arbeitsperiode 2016-2018) - IEA Forschungskoooperation," *IEA Wind Task 27*, 2017. [Online]. Available: <https://nachhaltigwirtschaften.at/de/iea/technologieprogramme/wind/iea-wind-task-27-arbeitsperiode-2016-2018.php>. [Accessed: 25-Nov-2017].
- [44] M. Abbett and G. Moretti, "A time-dependent computational method for blunt body flows.," *AIAA J.*, vol. 4, no. 12, pp. 2136–2141, Dec. 1966.
- [45] J. F. Wendt, J. D. Anderson, and Von Karman Institute for Fluid Dynamics., *Computational Fluid Dynamics : An Introduction*, Third Edit. Springer, 2009.
- [46] G. I. Taylor and J. W. Maccoll, "The Air Pressure on a Cone Moving at High Speeds. II," *Proc. R. Soc. A Math. Phys. Eng. Sci.*, vol. 139, no. 838, pp. 298–311, Feb. 1933.
- [47] J. D. Anderson, *Computational Fluid Dynamics : The Basics with Applications*. McGraw-Hill, 1995.
- [48] J. A. Fay and F. R. Riddell, "Theory of Stagnation Point Heat Transfer in Dissociated Air," *J. Aerosp. Sci.*, vol. 25, no. 2, pp. 73–85, Feb. 1958.
- [49] F. G. Blottner, "Nonequilibrium laminar boundary-layer flow of ionized air," *AIAA J.*, vol. 2, no. 11, pp. 1921–1927, Nov. 1964.
- [50] J. G. Hall, A. Q. Eschenroeder, and P. V. Marrone, "Blunt-Nose Inviscid Airflows With Coupled Nonequilibrium Processes," *J. Aerosp. Sci.*, vol. 29, no. 9, pp. 1038–1051, Sep. 1962.
- [51] N. Sayma, *Computational Fluid Dynamics*. BookBoon, 2009.
- [52] O. Zikanov, *Essential Computational Fluid Dynamics*, 1ra ed. New Jersey: John Wiley & Sons, Inc., 2010.
- [53] A. Cogotti, "Evolution of performance of an automotive wind tunnel," *J. Wind Eng. Ind. Aerodyn.*, vol. 96, no. 6–7, pp. 667–700, Jun. 2008.
- [54] J. D. Mcalpine, "Computational Fluid Dynamics or Wind Tunnel Modeling?," pp. 1–5, 2004.
- [55] I. R. Cowan, "A comparison of wind–tunnel experiments and computational simulations of dispersion in the environs of buildings," *Int. J. Environ. Pollut.*, vol. 8, no. 3–6, pp. 699–707, 1997.
- [56] J. Tu, G.-H. Yeoh, and C. Liu, *Computational Fluid Dynamics: A Practical Approach*, 2nda ed. Reino Unido: Elsevier: Butterworth-Heinemann, 2012.
- [57] J. Blazek, *Computational Fluid Dynamics: Principles and Applications*, 1ra ed. Baden-Daetteil Suiza: Elsevier Butterworth-Heinemann, 2001.
- [58] Dassault Systemes, "Technical reference Solidworks Flow Simulation 2017," 2017.
- [59] Z. Sun and L. Xu, "Computational fluid dynamics in coronary artery disease," *Comput. Med. Imaging Graph.*, vol. 38, no. 8, pp. 651–663, Dec. 2014.

- [60] A. Javadzadegan, A. Moshfegh, H. H. Afrouzi, and M. Omidi, "Magnetohydrodynamic blood flow in patients with coronary artery disease," *Comput. Methods Programs Biomed.*, vol. 163, pp. 111–122, Sep. 2018.
- [61] A. K. W. Buck *et al.*, "Original article submission: Platelet stress accumulation analysis to predict thrombogenicity of an artificial kidney," *J. Biomech.*, vol. 69, pp. 26–33, Mar. 2018.
- [62] H. Montazeri and B. Blocken, "CFD simulation of wind-induced pressure coefficients on buildings with and without balconies: Validation and sensitivity analysis," *Build. Environ.*, vol. 60, pp. 137–149, 2013.
- [63] A. K. Mittal, D. Ghosh, S. Behera, I. A. Siddiqui, and D. S. Dharmshaktu, "Wind flow simulation in the vicinity of tall building through CFD," in *The Eighth Asia-Pacific Conference on Wind Engineering*, 2013.
- [64] J. Sumner, C. S. Watters, and C. Masson, "CFD in Wind Energy: The Virtual, Multiscale Wind Tunnel," *Energies*, vol. 3, no. 5, pp. 989–1013, May 2010.
- [65] J. S. Rodrigo, D. C. Martínez, I. M. Pérez, P. Patilla, and J. Van Beeck, "Numerical CFD Modelling of Non-neutral Atmospheric Boundary Layers for Offshore Wind Resource Assessment Based on Monin-Obukhov Theory," *Eur. Wind Energy Conf. Exhib. (EWEC 2008)*, p. 0, 2008.
- [66] R. Pereira, R. Guedes, and C. S. Santos, "Comparing WAsP and CFD Wind Resource Estimates for the 'Regular' User," *Eur. Wind Energy Conf. Exhib. 2010*, pp. 1–10, 2010.
- [67] S. Rajper and I. J. Amin, "Wind Turbine Micrositing: Comparison of Finite Difference Method and Computational Fluid Dynamics," vol. 9, no. 1, pp. 247–252, 2012.
- [68] P. Larin, M. Paraschivoiu, and C. Aygun, "CFD based synergistic analysis of wind turbines for roof mounted integration," *J. Wind Eng. Ind. Aerodyn.*, vol. 156, pp. 1–13, 2016.
- [69] B. Blocken, A. van der Hout, J. Dekker, and O. Weiler, "CFD Simulation of Wind Flow Over Natural Complex Terrain: Case Study with Validation by Field Measurements for Ria de Ferrol, Galicia, Spain," *J. Wind Eng. Ind. Aerodyn.*, vol. 147, pp. 43–57, 2015.
- [70] W. Tong, *Wind Power Generation and Wind Turbine Design*. Southampton, United Kingdom: WIT Press, 2010.
- [71] J.-D. Pitteloud and S. Gsanger, "Small Wind World Report Summary 2016," Bonn, Germany, 2016.
- [72] J.-D. Pitteloud and S. Gsänger, "Small Wind World Report Summary 2017," Bonn, Germany, 2017.
- [73] International Electrotechnical Commission, *International Standard: IEC 61400-12-1 Wind turbine generator systems*. 2017, p. 860.
- [74] International Electrotechnical Commission, *International Standard IEC 61400-2*, vol. 3. London: British Standards Institution BSI, 2006.
- [75] American Wind Energy Association AWEA, "Small & Community Wind," *Small & Community Wind*, 2017. [Online]. Available: <https://www.awea.org/small-and-community-wind>. [Accessed: 25-Nov-2017].

- [76] T. Willcock and S. Appleby, "UK Small-Scale Wind Survey Installed Capacity, Annual Generation & Market Growth," Oxfordshire, 2012.
- [77] S. Stankovic, N. Campbell, and A. Harries, *Urban Wind Energy*, no. April. Sterling VA: BDSP Partnership Ltd, 2009.
- [78] S. Hassanli, G. Hu, K. C. S. Kwok, and D. F. Fletcher, "Utilizing cavity flow within double skin façade for wind energy harvesting in buildings," *J. Wind Eng. Ind. Aerodyn.*, vol. 167, no. February, pp. 114–127, 2017.
- [79] A. Orrell, N. F Foster, S. L Morris, and J. S Homer, "2016 Distributed Wind Market Report," 2017.
- [80] C. Miles, "Survey of Urban Wind Energy Technology," *Sustain. Built Environ.*, no. October, 2006.
- [81] J. H. Ferziger and M. Peric, *Computational Methods for Fluid Dynamics*, 3rd Editio. Germany: Springer, 2002.
- [82] P. R. Spalart, "Detached-Eddy Simulation," *Annu. Rev. Fluid Mech.*, vol. 41, no. 1, pp. 181–202, Jan. 2009.
- [83] Bergey Windpower Co., "Excel 10 - Specification Data Sheet." [Online]. Available: [bergey.com/wp-content/uploads/excel-10-spec-sheet\\_2013.pdf](http://bergey.com/wp-content/uploads/excel-10-spec-sheet_2013.pdf). [Accessed: 18-Oct-2019].
- [84] XZERES Corporation, "Skystream 3.7 - Specification Data Sheet." [Online]. Available: <https://www.xzeres.com/wp-content/uploads/2019/01/7246-Spec-Sheet-Domestic-Skystream-3.7.pdf>. [Accessed: 18-Oct-2019].
- [85] F. Bañuelos Ruedas, "Impacto de la Generacion Electrica Usando Fuentes de Energia Eolica en la Red Electrica Nacional," Universidad Nacional Autónoma de México, 2011.
- [86] National Renewable Energy Laboratory (NREL), "Sistemas Eólicos Pequeños para Generación de Electricidad," Golden CO, 2007.
- [87] A. D. Peacock, D. Jenkins, M. Ahadzi, A. Berry, and S. Turan, "Micro Wind Turbines in the UK Domestic Sector," *Energy Build.*, vol. 40, no. 7, pp. 1324–1333, Jan. 2008.
- [88] Sistema de Monitoreo Atmosferico SIMAT, "Dirección de Monitoreo Atmosférico," *Monitoreo de la Calidad del Aire*, 2017. [Online]. Available: <http://www.aire.cdmx.gob.mx/default.php?opc=%27ZaBhnmI=%27>. [Accessed: 24-Nov-2017].
- [89] MEASNET, "MEASNET Procedure: Evaluation of Site Specific Wind Conditions, Version 1, November 2009.," 2009.
- [90] MEASNET, "MEASNET Procedure: Evaluation of Site Specific Wind Conditions, Version 2, April 2012.," 2016.
- [91] Blue Marble Geographics, "Global Mapper 19.1 - All-in-one GIS Software," 2018. [Online]. Available: <http://www.bluemarblegeo.com/products/global-mapper.php>. [Accessed: 21-Mar-2018].
- [92] J. Roeth, "Wind Resource Assessment Handbook," New York, 2010.

- [93] G. M. Masters, *Renewable and Efficient Electric Power Systems*, 2nd Editio. USA: John Wiley & Sons, Inc., 2004.
- [94] J. F. Manwell, J. G. McGowan, and A. L. Rogers, *Wind Energy Explained: Theory, Design and Application*, 2nd Editio. United Kingdom: John Wiley & Sons, Inc., 2009.
- [95] F. Bañuelos-Ruedas, C. Angeles-Camacho, and S. Rios-Marcuello, "Analysis and Validation of the Methodology Used in the Extrapolation of Wind Speed Data at Different Heights," *Renew. Sustain. Energy Rev.*, vol. 14, no. 8, pp. 2383–2391, Oct. 2010.
- [96] CFD-Online, "Turbulence length scale -- CFD-, the free CFD reference." [Online]. Available: [https://www.cfd-online.com/Wiki/Turbulence\\_length\\_scale](https://www.cfd-online.com/Wiki/Turbulence_length_scale). [Accessed: 06-Dec-2018].
- [97] CFD-Online, "Hydraulic diameter -- CFD-, the free CFD reference." [Online]. Available: [https://www.cfd-online.com/Wiki/Hydraulic\\_diameter](https://www.cfd-online.com/Wiki/Hydraulic_diameter). [Accessed: 06-Dec-2018].
- [98] N. T. Basse, "Turbulence intensity and the friction factor for smooth- and rough-wall pipe flow," Dec. 2016.
- [99] N. T. Basse, "Turbulence Intensity Scaling: A Fugue," Jan. 2018.
- [100] J. Thé and H. Yu, "A Critical Review on the Simulations of Wind Turbine Aerodynamics Focusing on Hybrid RANS-LES Methods," *Energy*, vol. 138, pp. 257–289, Nov. 2017.
- [101] B. Dose, H. Rahimi, I. Herráez, B. Stoevesandt, and J. Peinke, "Fluid-structure coupled computations of the NREL 5 MW wind turbine by means of CFD," *Renew. Energy*, vol. 129, pp. 591–605, Dec. 2018.
- [102] A. Farhan, A. Hassanpour, A. Burns, and Y. G. Motlagh, "Numerical study of effect of winglet planform and airfoil on a horizontal axis wind turbine performance," *Renew. Energy*, Aug. 2018.
- [103] C. Yan and C. L. Archer, "Assessing compressibility effects on the performance of large horizontal-axis wind turbines," *Appl. Energy*, vol. 212, pp. 33–45, Feb. 2018.
- [104] X. Cai, R. Gu, P. Pan, and J. Zhu, "Unsteady aerodynamics simulation of a full-scale horizontal axis wind turbine using CFD methodology," *Energy Convers. Manag.*, vol. 112, pp. 146–156, Mar. 2016.
- [105] H. F. Lam and H. Y. Peng, "Study of wake characteristics of a vertical axis wind turbine by two- and three-dimensional computational fluid dynamics simulations," *Renew. Energy*, vol. 90, pp. 386–398, May 2016.
- [106] M. Yi and Q. Jianjun, "Numerical Study of Flow Field and Aerodynamic Performance of Straight Bladed VAWT at Variable Tip Speed Ratios," *Open Mech. Eng. J.*, vol. 9, no. 1, pp. 1017–1024, Oct. 2015.
- [107] A. Rezaeiha, I. Kalkman, and B. Blocken, "CFD simulation of a vertical axis wind turbine operating at a moderate tip speed ratio: Guidelines for minimum domain size and azimuthal increment," *Renew. Energy*, vol. 107, pp. 373–385, Jul. 2017.
- [108] K. McLaren, S. Tullis, and S. Ziada, "Computational fluid dynamics simulation of the aerodynamics of a high solidity, small-scale vertical axis wind turbine," *Wind Energy*, vol. 15, no. 3, pp. 349–361, Apr. 2012.

- [109] K. H. Wong, W. T. Chong, S. C. Poh, Y.-C. Shiah, N. L. Sukiman, and C.-T. Wang, "3D CFD simulation and parametric study of a flat plate deflector for vertical axis wind turbine," *Renew. Energy*, vol. 129, pp. 32–55, Dec. 2018.
- [110] E. Acha, "Wind generation and its impact on the network," Glasgow, Scotland UK, 2011.
- [111] R. Shakoor, M. Y. Hassan, A. Raheem, and Y.-K. Wu, "Wake effect modeling: A review of wind farm layout optimization using Jensen's model," *Renew. Sustain. Energy Rev.*, vol. 58, pp. 1048–1059, May 2016.
- [112] M. F. Polster, "Comprehensive comparison of analytical wind turbine wake models with wind tunnel measurements and wake model application on performance modelling of a downstream turbine," 2017.
- [113] E. Hau, "Wind turbines Fundamentals, Technologies, Application, Economics," *Spectrum*, p. 791, 2006.
- [114] R. McKay, "Gill Instruments Ltd., WindMaster & Windmaster Pro Manual Issue 12." Lymington, Hampshire UK, p. 69, 2017.
- [115] J. F. Barlow, "Progress in observing and modelling the urban boundary layer," *Urban Clim.*, vol. 10, pp. 216–240, Dec. 2014.
- [116] R. Gasch, J. Twele, and C. Heilmann, *Wind Power Plants: Fundamentals, Design, Construction and Operation*, 2nd Editio. Berlin: Springer, Berlin, Heidelberg, 2012.
- [117] P. A. Sánchez-Pérez, M. Robles, and O. A. Jaramillo, "Real time Markov chains: Wind states in anemometric data," *J. Renew. Sustain. Energy*, vol. 8, no. 2, p. 023304, Mar. 2016.

# APPENDIX A



## FUNDAMENTAL EQUATIONS OF FLUID DYNAMICS

### A.1 Introduction

The CFD analysis takes aspects that describe physics; this is because three fundamental principles govern any fluid: The Conservation of the Mass (Equation of Continuity), The Second Law of Newton  $F = ma$  (Conservation of the Momentum or Momentum) and Conservation of Energy [1]. These can be represented in mathematical equations, which are usually partial differential equations or make use of integral equations. Furthermore, the CFD replace the partial differential equations of the flow of fluids with discrete algebraic forms, which are solved to obtain discrete numbers in space and time to obtain a numerical description of the field of the flow of interest. It even can be used as integral equations instead of partial differential equations [1], [2].

To understand this in a better way, Figure A.1 is shown, which describes the overview in a roadmap of the fundamental equations that describe the dynamics of fluids and how they can be used these equations to carry out a good CFD analysis. The fundamental principles of physics are applied to the flow model, resulting in equations that are mathematical expressions named equations of continuity, momentum, and energy, respectively. Each model of the flow produces a mathematical proposition of the fundamental equations that describe the fluids, some conservatively, and others in their non-conservative form [3].

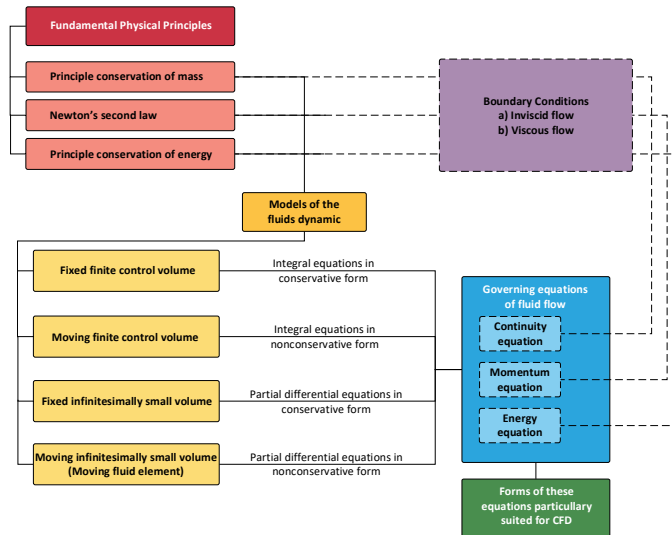


Figure A.1 Computational Fluid Dynamics analysis roadmap CFD [3].

After obtaining the fundamental equations of the flow of the fluids (continuity, momentum, and energy), these equations will have to be adapted for their use and to be able to propose solutions in the CFD analysis. Finally, boundary conditions contour conditions arise to have an approximate description of the fluid; to be able to solve the fundamental equations of fluid dynamics.

## A.2 Modeling of the flow

In order to develop correct modeling of the flow and to obtain the fundamental equations of the fluid in motion, it is required: First to choose the appropriate physical foundations of the laws of physics, previously mentioned as they are, the conservation of the mass, Newton's second law and conservation of energy. Second, apply these principles to the flow model and third extract the mathematical equations that make up these physical principles.

This aspect is fundamental in CFD analysis because it is not a trivial consideration. For example, a solid body is fairly easy to observe and define, but on the other hand, a fluid is a substance that is difficult to sustain and describe. If the solid body is in a translating motion, the velocity of each part of the body is the same; on the contrary, if a fluid is in motion, the speed is different at each point of the fluid. Therefore, it should visualize the fluid in motion and build one of the following four available models applying the fundamental principles of fluid dynamics.

The above, in relation to the laws of conservation, allow dividing the field of flow in a number of volumes and to concentrate the modeling in the behavior of the fluid in a finite region. From this comes the definition of Finite Control Volume [1].

### A.2.1 Finite control volume

Within the CFD analysis, the control volume  $V$  is defined as a finite region within a body of the closed volume, which is a part of the finite region of the fluid to be studied, and on the other hand the control surface  $S$ , it is defined as a closed surface surrounding the volume.

The fundamental principles of physics are applied to the fluid in question within the volume of control, therefore instead of observing the complete fluid as a whole, with the model of the control volume is limited to observe the fluid in a region finite volume, as shown in Figure A.2.

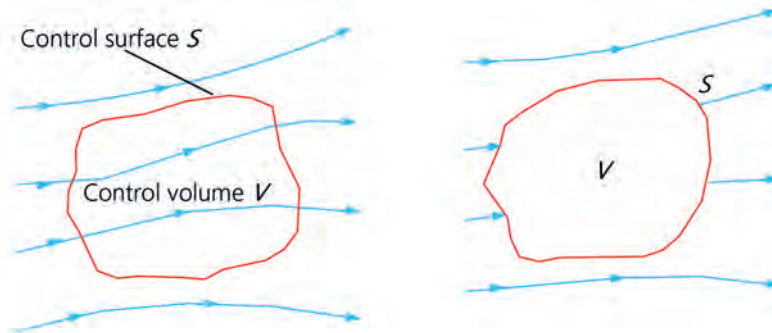


Figure A.2 Flow models of fluid through the finite control volume.

The fluid flow equations obtained by applying the fundamental principles of physics to a volume of finite control are integral. These integral forms of the fundamental equations can be manipulated indirectly to obtain partial differential equations.

These equations obtained from the volume of finite control fixed in space, both in an integral form and in partial derivatives, are called “*fundamental equations of the conservative form*,” as shown on the left side of Figure A.2. The equations obtained from the finite control volume moving with the fluid (right side of Figure A.2), either in integral or partial differential form, are called “*fundamental equations of the non-conservative form*” [2], [3].

### A.2.2 Infinitesimal fluid element

On the other hand, the CFD analysis can also consider a part of the fluid to be studied, this being an infinitesimal element of the fluid, with a differential volume  $dV$ . The fluid element is infinitesimal in the same way as the differential calculus. The fluid element can be fixed in space with the fluid moving through it, as seen on the left side of Figure A.3. In this sense and at the same time, it is moving in the current line with a speed vector  $\mathbf{v}$  equal to the velocity flow in each point. So again, instead of observing the entire flow as a whole, the fundamental principles of physics are applied only to a small infinitesimal element of the fluid.

This allows applying the fundamental principles of physics only to the element of the fluid, permitting to obtain the fundamental equations directly in the form of partial differential equations. In addition, these partial differential equations obtained from the element of the fixed fluid in space are again equations of the conservative form. The partial differential equations obtained from the fluid element in motion are classified as equations of the non-conservative form on the right side of Figure A.3.

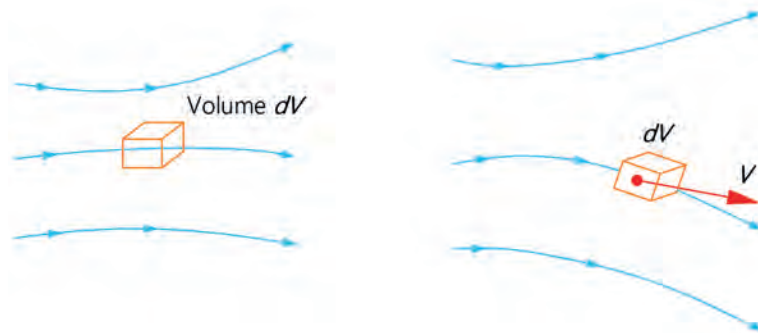


Figure A.3 Flow models of fluid through the infinitesimal fluid element.

It can be said that within the theory of aerodynamics, the form of the equations is irrelevant; they can be of the conservative or non-conservative form. However, there are cases in the CFD analysis where selecting the form of the equations is important, allowing to distinguish the conservative form against the non-conservative form according to the nomenclature used.

Additionally, a third model of fluid dynamics emerge and maybe a microscopic approach where the fundamental laws of matter are applied to the atoms and molecules of the fluids in question. This approach has a scope in the kinetic theory, which is a more elegant method with some long-term advantages.



Some CFD methods are presented with the solution of the fluid motion equations as well as the interaction of the fluid with solid bodies; in this case, the fluid used for the wind energy will be the masses of air. The equations of motion of a non-viscous fluid respond to the Euler equations, while the viscous fluids respond to the Navier-Stokes equations. Both types of fluids will be described later.

Qualitatively different types of viscous fluids can be described, which can be laminar or turbulent. The use of the Navier-Stokes equations for the laminar flows does not present difficulties in finding the solutions to this type of fluids. While for simulations of turbulent flows, it has drawbacks, and for this, the Reynolds Averaged Navier-Stokes (RANS) equations are used. On the other hand, the Large Eddy Simulation (LES) allows better precision in the prediction of turbulent flows.

The fundamental equations for Newtonian fluid dynamics named the Navier-Stokes (N-S) equations, the development of ways to reduce these equations, is an active area of research, in particular, the problem of turbulent flows using the Reynolds Average Navier-Stokes.

### A.3 The fundamental derivative (time rate change of a moving fluid element)

An important and standard notation in aerodynamics that is used in the CFD analysis is the fundamental derivative; which has an important physical meaning; this is that to give an example the derivative of the acceleration results in the velocity, and the derivative of the velocity gives us; as a result of the distance, these can be represented physically. This section explains the fundamental derivative and how it is represented in fluid dynamics.

Taking into consideration the Figure A.3, within the analysis of the infinitesimal fluid element in motion with the flow can be analyzed in a more profound way to determine the fundamental equations of fluid dynamics. This can be seen in Figure A.4, where is shown the fluid element moving through the Cartesian space [3].

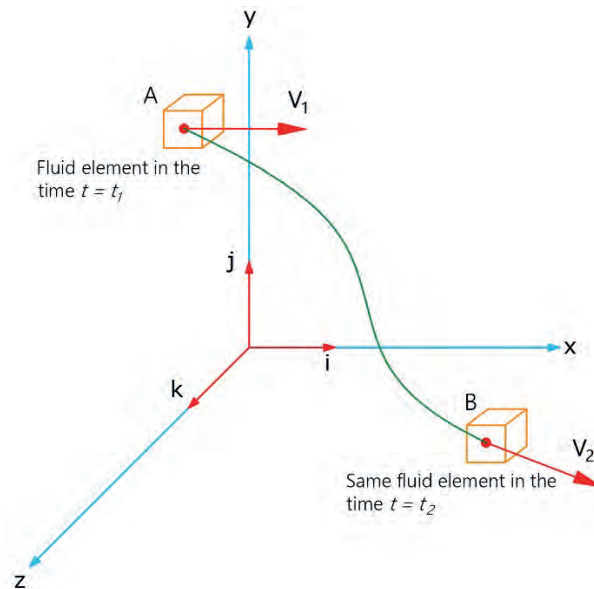


Figure A.4 Fluid element moving in the fluid flow.

Thus, the unit vectors along the axes “ $x$ ”, “ $y$ ” and “ $z$ ” are described by  $\vec{i}$ ,  $\vec{j}$ , and  $\vec{k}$  respectively. On the other hand, the velocity vector in the Cartesian plane is defined by:

$$\vec{V} = u \vec{i} + v \vec{j} + w \vec{k} \quad (\text{A.1})$$

where this vector, the components of the speed are given respectively by:

$$\begin{aligned} u &= u(x, y, z, t) \\ v &= v(x, y, z, t) \\ w &= w(x, y, z, t) \end{aligned} \quad (\text{A.2})$$

For these vectors, an unstable flow, or turbulent flow, is generally considered, where “ $u$ ”, “ $v$ ” and “ $w$ ” are functions of either space or location and time  $t$ . Likewise, it has a scalar density and is defined by:

$$\rho = \rho(x, y, z, t) \quad (\text{A.3})$$

At the time instant  $t_1$ , the fluid element is located at point A in

Figure A.4, so in that space and time, the density of the fluid element is:

$$\rho_1 = \rho(x_1, y_1, z_1, t_1) \quad (\text{A.4})$$

Subsequently for the time instant  $t_2$ , at point B, the density of the element of the same fluid is described as:

$$\rho_2 = \rho(x_2, y_2, z_2, t_2) \quad (\text{A.5})$$

Given that the density at point “A” is:  $\rho = \rho(x, y, z, t)$ , this function can be expanded based on the Taylor series, as shown below:

$$\begin{aligned} \rho_2 = \rho_1 + \left(\frac{\partial \rho}{\partial x}\right)_1 (x_2 - x_1) + \left(\frac{\partial \rho}{\partial y}\right)_1 (y_2 - y_1) + \left(\frac{\partial \rho}{\partial z}\right)_1 (z_2 - z_1) \\ + \left(\frac{\partial \rho}{\partial t}\right)_1 (t_2 - t_1) + (\text{higher order terms}) \end{aligned} \quad (\text{A.6})$$

Dividing the above for  $t_2 - t_1$ , and ignoring the higher-order terms, it is obtained as:

$$\frac{\rho_2 - \rho_1}{t_2 - t_1} = \left(\frac{\partial \rho}{\partial x}\right)_1 \left(\frac{x_2 - x_1}{t_2 - t_1}\right) + \left(\frac{\partial \rho}{\partial y}\right)_1 \left(\frac{y_2 - y_1}{t_2 - t_1}\right) + \left(\frac{\partial \rho}{\partial z}\right)_1 \left(\frac{z_2 - z_1}{t_2 - t_1}\right) + \left(\frac{\partial \rho}{\partial t}\right)_1 \quad (\text{A.7})$$

Observing at the left part of the Eq. (A.7), it is possible to say that this element is physically the average change speed in the density of the fluid element when moving from point A to point B. In the limit, as  $t_2$  approaches  $t_1$  this term will be:

$$\lim_{t_2 \rightarrow t_1} \frac{\rho_2 - \rho_1}{t_2 - t_1} \equiv \frac{D\rho}{Dt} \quad (\text{A.8})$$

$D\rho/Dt$  is the symbol for the speed of change of the density of the fluid element moving through the space vector. It is important to mention that the  $D/Dt$  symbol is called "Fundamental Derivative". On the other hand, the symbol of  $(\partial\rho/\partial t)_1$ , physically denotes that it is the rate of change of the density at the fixed-point A, and the change in density due to fluctuations is observed transients in the flow field. So  $D/Dt$  and  $(\partial\rho/\partial t)_1$  are physically different quantities.

Therefore, in Eq. (A.7), it can be observed that:

$$\begin{aligned} \lim_{t_2 \rightarrow t_1} \frac{x_2 - x_1}{t_2 - t_1} &\equiv u \\ \lim_{t_2 \rightarrow t_1} \frac{y_2 - y_1}{t_2 - t_1} &\equiv v \\ \lim_{t_2 \rightarrow t_1} \frac{z_2 - z_1}{t_2 - t_1} &\equiv w \end{aligned} \quad (\text{A.9})$$

In addition, taking into consideration the limit of Eq. (A.7) as  $t_2 \rightarrow t_1$ , it is obtained as:

$$\boxed{\frac{D\rho}{Dt} = u \frac{\partial\rho}{\partial x} + v \frac{\partial\rho}{\partial y} + w \frac{\partial\rho}{\partial z} + \frac{\partial\rho}{\partial t}} \quad (\text{A.10})$$

By examining Eq. (A.10) the fundamental derivative can be obtained in Cartesian coordinates:

$$\frac{D}{Dt} \equiv u \frac{\partial}{\partial x} + v \frac{\partial}{\partial y} + w \frac{\partial}{\partial z} + \frac{\partial}{\partial t} \quad (\text{A.11})$$

On the other hand, in Cartesian coordinates, the gradient operator vector  $\nabla$  is defined as:

$$\nabla \equiv \mathbf{i} \frac{\partial}{\partial x} + \mathbf{j} \frac{\partial}{\partial y} + \mathbf{k} \frac{\partial}{\partial z} \quad (\text{A.12})$$

Therefore, Eq. (A.11) can be written as:

$$\frac{D}{Dt} \equiv \frac{\partial}{\partial t} + (\vec{\mathbf{V}} \cdot \nabla) \quad (\text{A.13})$$

The Eq. (A.13) represents the definition of the operator of the fundamental derivative in vector notation; so that it is valid for any coordinate system.

It can be said that Ec. (A.13), the term  $D/Dt$  is the fundamental derivative, which has a physical representation of velocity of change following an element of the fluid in motion;  $\partial/\partial t$  is called *local derivative*, which is physically the velocity rate of change at a fixed point;  $\vec{V} \cdot \nabla$  is named as *convective derivative*, which physically represents the rate of change due to the movement of the fluid element from point A to point B in the flow field where the properties of the flow are especially different. This fundamental derivative applies to any variable in the flow field, such as static pressure, temperature, distance, being these:  $D\rho/Dt$ ,  $DT/Dt$ ,  $Du/Dt$ , etc. For example:

$$\frac{DT}{Dt} \equiv \underbrace{\frac{\partial T}{\partial t}}_{\text{Local derivative}} + (\vec{V} \cdot \nabla) \equiv \frac{\partial T}{\partial t} + u \frac{\partial T}{\partial x} + v \frac{\partial T}{\partial y} + w \frac{\partial T}{\partial z} \quad (\text{A.14})$$

The objective of deriving the previous equations is in order to interpret the fundamental derivative, which is essential as well as the total derivative of the calculation. This is, if:

$$\rho = \rho(x, y, z, t) \quad (\text{A.15})$$

Representing the above in a differential way, it is obtained as:

$$\frac{dp}{dt} = \frac{\partial \rho}{\partial t} + \frac{\partial \rho}{\partial x} \frac{dx}{dt} + \frac{\partial \rho}{\partial y} \frac{dy}{dt} + \frac{\partial \rho}{\partial z} \frac{dz}{dt} \quad (\text{A.16})$$

If,  $dx/dt = u$ ,  $dy/dt = v$  and  $dz/dt = w$ , the Eq. (A.16) is as follows:

$$\boxed{\frac{dp}{dt} = u \frac{\partial \rho}{\partial x} + v \frac{\partial \rho}{\partial y} + w \frac{\partial \rho}{\partial z} + \frac{\partial \rho}{\partial t}} \quad (\text{A.17})$$

By comparing Eq. (A.11) and Eq. (A.17) it can be seen that  $dp/dt$  and  $D\rho/Dt$  are the same. Therefore, the fundamental derivative is not more than the total derivative with respect to time. Furthermore, it can be said that Eq. (A.11), represents a fiscal meaning of the fundamental derivatives, while the deduction of Ec. (A.17) represents a mathematical form. Therefore, it can be used the symbol of  $(\partial/\partial t)_{\text{fluid element}}$  to say that the rate of change of “pressure, temperature, density, etc.,” following an element of the moving fluid [2], [3].

## A.4 Divergent velocity vector

In the previous section, it was determined the definition and its physical meaning of the fundamental derivative; this is because the fundamental equations governing fluids are commonly expressed in terms of the fundamental derivative [3]. Another important aspect to take into consideration in the equations of fluid dynamics is the divergence of velocity,  $\vec{V} \cdot \nabla$ .

It is considered again Figure A.2, which represents a volume of control moving with the fluid, which this volume is composed of particles of the fluid and in turn, moves with the flow; consequently, its mass is fixed and invariant with time.

However, its Volume  $V$  and the Control Surface  $S$  are changing over time and in turn moving in different regions of the flow, where different values of density  $\rho$  exist; that is, the Volume of Control of fixed mass, is in constant increase and decrease of its volume and at the same time changing its form, depending on the characteristics of the flow.

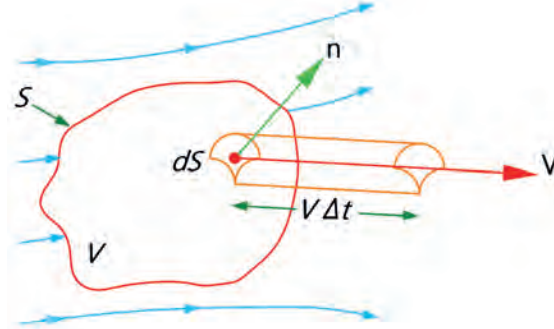


Figure A.5 Moving control volume for the representation of the divergence of velocity.

Considering an infinitesimal element of surface  $dS$  shown in Figure A.5 moving at a local velocity  $\vec{V}$ . There is a change in the volume of the control volume;  $\Delta V$ , due to the movement of the surface differential;  $dS$ , on the increase in time;  $\Delta t$ , is equal to the length of the volume, this being the base of the cylinder of the area  $dS$  and an altitude of  $(\vec{V} \Delta t) \cdot \vec{n}$ , where  $\vec{n}$  is a unit vector perpendicular to the control surface  $dS$  resulting in:

$$\Delta V = [(\vec{V} \Delta t) \cdot \vec{n}] dS = (\vec{V} \Delta t) \cdot d\vec{S} \quad (\text{A.18})$$

Where the vector  $d\vec{S}$  is defined as  $d\vec{S} \equiv \vec{n} dS$ . On the time increment  $\Delta t$ , the total change in volume of the entire control volume is equal to the sum of the Eq. (A.18) on the total control surface. In the limit as  $dS \rightarrow 0$ , the sum is then the surface integral:

$$\oiint_S (\vec{V} \Delta t) \cdot d\vec{S} \quad (\text{A.19})$$

Now, if this surface integral is divided by  $\Delta t$ , the result is physically the rate of change of the control volume, denoted by  $DV/Dt$ ; this is:

$$\frac{DV}{Dt} = \frac{1}{\Delta t} \oiint_S (\vec{V} \Delta t) \cdot d\vec{S} = \oiint_S \vec{v} \cdot d\vec{S} \quad (\text{A.20})$$

The Eq. (A.20)(A.21) is written in such a way that it represents the rate of change of the control volume as the volume moves with the fluid, and this physically represents the fundamental derivative. In this sense, by applying the divergence theorem of the vector calculation to the right side of the equation, it is obtained as:

$$\frac{DV}{Dt} = \iiint_V (\nabla \cdot \vec{V}) \delta V \quad (\text{A.21})$$

If the moving control volume is reduced to a small volume differential  $\delta V$ , it results in an infinitesimal moving element in motion, as shown in Figure A.2, then the Eq. (A.21) can be written as:

$$\frac{D(dV)}{Dt} = \iiint_{\delta V} (\nabla \cdot \vec{V}) \delta V \quad (\text{A.22})$$

It is assumed that  $\delta V$  is small enough that  $\nabla \cdot \vec{V}$  is the same value. Then the integral in Eq. (A.22), in the limit, as  $\delta V$  is reduced to zero, is given by  $(\nabla \cdot \vec{V}) \delta V$ . Therefore, it is obtained as:

$$\boxed{\nabla \cdot \vec{V} = \frac{1}{\delta V} \frac{D(\delta V)}{Dt}} \quad (\text{A.23})$$

If it is observed, the Eq. (A.23), on the left side, it has the divergence of the speed; while on the right side, it has its physical meaning. Which  $\nabla \cdot \vec{V}$  is the physical representation of the time rate of change of the volume of a moving fluid per unit volume [3].

As a conclusion to the above; it is important to take into consideration that when it is talked about fluid dynamics, and it is observed the velocity divergence symbol  $\nabla \cdot \vec{V}$ , the first thing that must be taken into account is its physical meaning as the time rate of change of the volume of a moving fluid element per unit volume.

## A.5 The continuity equation

The fundamental equations that govern the flows and fluids that result from the application of the principle of conservation of mass, applied to finite control volume models or infinitesimal fluid element, are called continuity equations.

### A.5.1 Principle of conservation of mass

The law of conservation of mass expresses the fact that the mass cannot be created in a fluid system, nor can it disappear from it.

#### Model of an infinite fluid element in motion with flow

Selecting the model of the Infinitesimal Fluid Element and represented by Figure A.3, where an element moving with the fluid is illustrated. The mass of this element is fixed and is given by the differential of mass  $\delta m$  and the volume of this element is denoted by  $\delta V$ , therefore:

$$\delta m = \rho \delta V \quad (\text{A.24})$$

According to the principle of conservation of the mass, it can be defined that the rate of change of the mass of the fluid element is zero, at the same time that the element moves along with the fluid. Taking into consideration the concept of the fundamental derivative, it is deduced as:

$$\frac{D(\delta m)}{Dt} = 0 \quad (\text{A.25})$$

Deriving and combining the Eq. (A.24) and Eq. (A.25) , it is derived as:

$$\frac{D(\rho\delta V)}{Dt} = \rho \frac{D(\delta V)}{Dt} + \delta V \frac{D\rho}{Dt} = 0 \quad (\text{A.26})$$

Furthermore, making one the volume differential in the previous expression; it is obtained as:

$$\begin{aligned} \rho \left[ \frac{1}{\delta V} \frac{D(\rho\delta V)}{Dt} \right] + \left[ \frac{\delta V}{\delta V} \right] \frac{D\rho}{Dt} &= 0 \\ \frac{D\rho}{Dt} + \rho \left[ \frac{1}{\delta V} \frac{D(\rho\delta V)}{Dt} \right] &= 0 \end{aligned} \quad (\text{A.27})$$

Inside the bracket in the Eq. (A.27) it can be observed the divergence vector of the velocity  $\nabla \cdot \vec{V}$ . Therefore, combining the Eq.(A.23) and Eq. (A.27) it is derived as:

$$\boxed{\frac{D\rho}{Dt} + \rho \nabla \cdot \vec{V} = 0} \quad (\text{A.28})$$

The Eq. (A.28) represents a partial differential equation and is the *Continuity Equation* in its non-conservative form [2].

### Model of volume fluid element fixed in space

Considering the model of finite volume fixed in space, illustrated in Figure A.6, in the control surface  $S$ , the flow velocity is represented by  $\vec{V}$ , and the area vector is  $d\vec{S}$

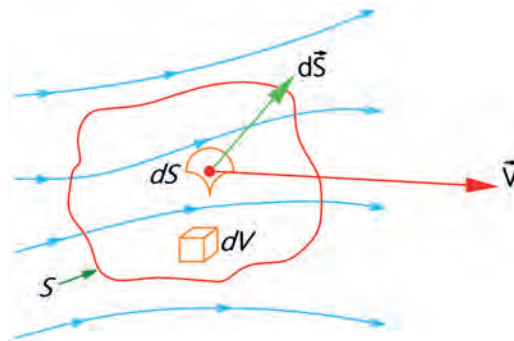


Figure A.6 Finite control volume fixed in space.

$dV$  is also defined as an elementary volume within the finite control volume. Now, applying the principle of conservation of the mass to this volume of control, it is obtained as:

$$\left\{ \begin{array}{l} \text{Mass flow leaves} \\ \text{the control volume} \\ \text{through the surface } \mathcal{S} \end{array} \right\} = \left\{ \begin{array}{l} \text{Time rate of} \\ \text{decrease inside} \\ \text{control volume} \end{array} \right\} \text{ or,} \quad (\text{A.29})$$

$$B = C$$

Defining the left side of the Eq. (A.28) in terms of the values shown in Figure A.6, it has: The mass or mass flow of a moving fluid of any fixed surface is equal to the product of density per area per velocity component perpendicular to the surface. Therefore, the mass flow through the area  $dS$  is:

$$\rho V_n dS = \rho \vec{V} \cdot d\vec{S} \quad (\text{A.30})$$

Therefore, it is denoted that  $d\vec{S}$  points to an address outside the control volume. Consequently, when  $\vec{V}$  also points outside the control volume, the product  $\rho \vec{V} \cdot d\vec{S}$  it is positive. Also, when the velocity vector  $\vec{V}$  points outside the control volume, the mass flow is leaving the control volume, and it can be said to be a leak or exit point. In contrast when the vector  $\vec{V}$  points inside the control volume, the mass flow  $\rho \vec{V} \cdot d\vec{S}$  is negative and therefore enters the control volume and is considered an input stream or drain [2]. The net mass flow outside the control volume through the control surface  $\mathcal{S}$ , is the summation of the mass flow elements shown in Eq. (A.29) so it can be represented in a surface integral, which is physically the left side of the equation being represented by:

$$B = \oiint_{\mathcal{S}} \rho \vec{V} \cdot d\vec{S} \quad (\text{A.31})$$

On the other hand, considering the right part of the equation, which describes the rate of change of the mass within the control volume, the mass contained in the elementary volume  $dV$  is  $\rho dV$ . The total mass within the control volume is then:

$$\iiint_V \rho dV \quad (\text{A.32})$$

The rate of change of the mass increase within the  $V$  is:

$$\frac{\partial}{\partial t} \iiint_V \rho dV \quad (\text{A.33})$$



In turn, the rate of change of the decrease of the mass within  $V$  is the negative of the previous expression, being as follows:

$$-\frac{\partial}{\partial t} \iiint_V \rho dV = C \quad (\text{A.34})$$

Carrying out the substitution of the Eq. (A.31) and Eq. (A.34) in the Eq. (A.29), it is obtained as:

$$\oiint_S \rho \vec{v} \cdot d\vec{S} = -\frac{\partial}{\partial t} \iiint_V \rho dV \quad (\text{A.35})$$

Alternatively, it may well be expressed in the form, which is the Continuity Equation in integral form; and of form conservative.

$$\boxed{\frac{\partial}{\partial t} \iiint_V \rho dV + \oiint_S \rho \vec{v} \cdot d\vec{S} = 0} \quad (\text{A.36})$$

Expressing this same equation in differential form and assuming that the control volume is fixed in space, the integration limits for the integrals of Eq. (A.36) are constant, and therefore the derivative of time  $\partial/\partial t$  can be placed inside the integral of volume.

$$\iiint_V \frac{\partial \rho}{\partial t} dV + \oiint_S \rho \vec{v} \cdot d\vec{S} = 0 \quad (\text{A.37})$$

The divergence theorem of the vector calculation is applied; in this sense, the surface integral in the above equation can be expressed as a volume integral:

$$\oiint_S (\rho \vec{v}) \cdot d\vec{S} = \iiint_V \nabla \cdot (\rho \vec{v}) dV \quad (\text{A.38})$$

Substituting the Eq. (A.38) in the Eq. (A.37), it is obtained as:

$$\iiint_V \frac{\partial \rho}{\partial t} dV + \iiint_V \nabla \cdot (\rho \vec{v}) dV = 0 \quad (\text{A.39})$$

Otherwise, factoring the triple integral of the surface can be expressed in the following way:

$$\iiint_V \left[ \frac{\partial \rho}{\partial t} + \nabla \cdot (\rho \vec{v}) \right] dV = 0 \quad (\text{A.40})$$

Since the Finite Control Volume is drawn arbitrarily in space, the only way for the integral in Eq. (A.40) to be equal to zero is that the integrand will be zero at all points within the volume of control; resulting in:

$$\boxed{\frac{\partial \rho}{\partial t} + \nabla \cdot (\rho \vec{V}) = 0} \quad (\text{A.41})$$

The Eq. (A.41) is also part of the *Continuity Equation* in its *conservative* form, and it can be noticed that when applying the finite control volume model, the Eq. (A.36) is obtained in its partial derivative equation form.

## A.6 The momentum equation

Another fundamental principle that governs fluid dynamics is the physical principle of Newton's Second Law:

$$F = ma \quad (\text{A.42})$$

The resulting equation of this physical principle is the Momentum Equation. In this section, the model of the moving fluid element represented on the right side of Figure A.3 will be selected. In Figure A.7, the same model is presented in a detail view.

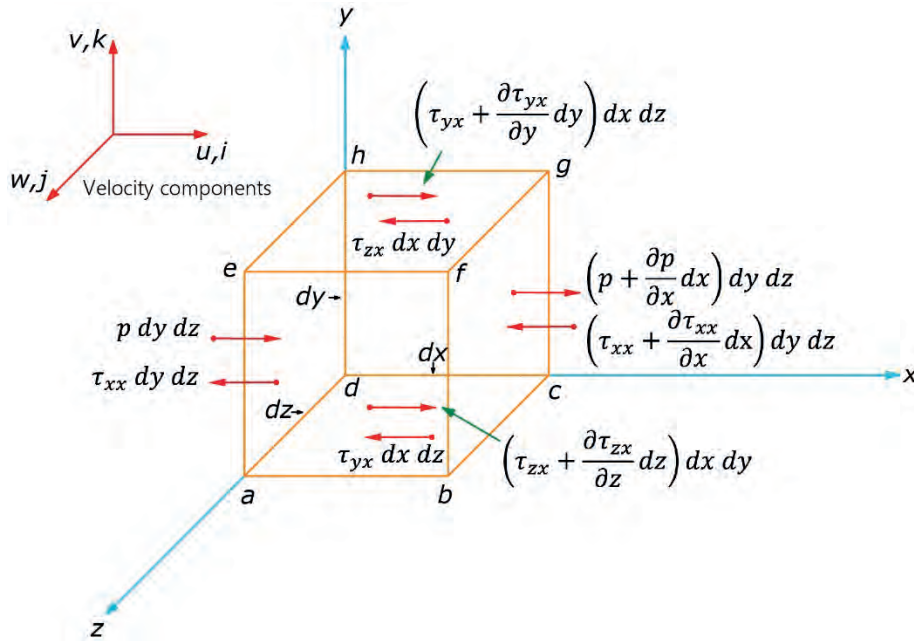


Figure A.7 Detailed view of the moving fluid element infinitesimal.

Newton's Second Law expressed above, when applied to the model in Figure A.7, expresses that the net force on the element of the fluid is equal to its mass multiplied by the acceleration of the element. The model presented will be used for the deduction of the x component of the Moment Equation.

As it is a vector relation, and therefore it can be represented in its three scalar relations along the axes  $x$ ,  $y$  and  $z$ . Deducing only the “ $x$ ” component of Newton's Second Law, it is obtained:

$$\sum F_x = ma_x \quad (\text{A.43})$$

Where  $F_x$  and  $a_x$  are the scalar components of “ $x$ ” of the force and acceleration, respectively. Considering the force in the direction  $x$ , two forces are presented:

- *Body Forces:* Are those forces that act directly on the volumetric mass of the fluid element. These types of forces act at a distance; examples of these are the gravitational, electrical, and magnetic forces.
- *Surface Forces:* Are those forces that act directly on the surface of the fluid element. And they can be generated by two sources: a) The distribution of the pressure acting on the surface imposed by the external fluid surrounding the fluid element, and b) the shear or shear forces and normal stress distributions acting on the surface, also imposed by the external fluid "pull" or "push" on the surface by means of friction.

For this deduction, the body forces will be denoted by the unit of mass acting on the element of the fluid by  $\vec{f}$  with its component in  $x$  being  $f_x$ . On the other hand, the volume of the fluid element is  $(dx dy dz)$ ; hence:

$$\left\{ \begin{array}{l} \text{Body forces on} \\ \text{fluid element acting} \\ \text{in } x \text{ direction} \end{array} \right\} = \rho f_x (dx dy dz) \quad (\text{A.44})$$

In turn, the shear and normal forces in a fluid are related to the speed of change of the deformation of the fluid element, as shown in Figure A.8 for the plane  $xy$ .

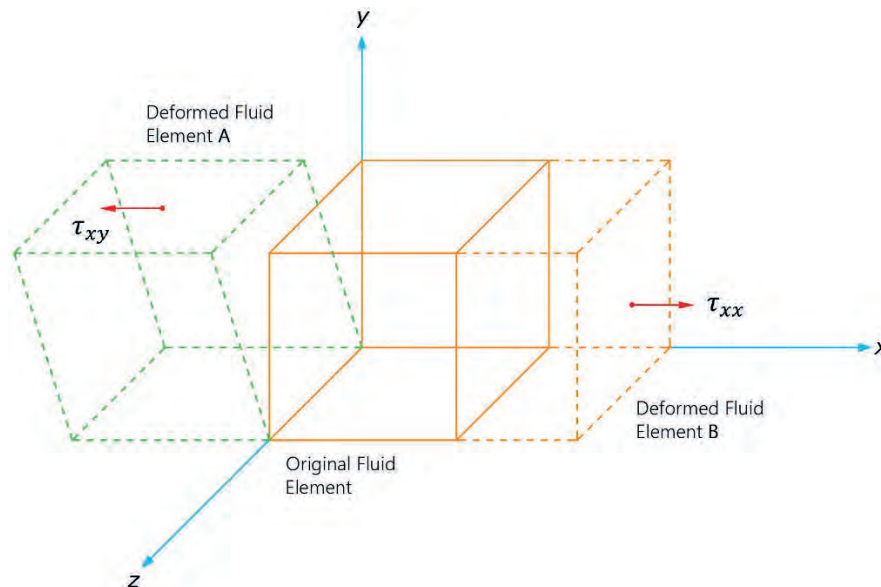


Figure A.8 Element of the deformed fluid due to the surface forces.

The shearing stress  $\tau_{xy}$  is directly related to the rate of change to the shear deformation of the fluid element represented by the deformed cube at the position A of Figure A.8. On the other hand, the velocity of change of the volume of the fluid element represents the normal stress, denoted by  $\tau_{xx}$  represented by the cube at the position B [2].

Both shear stress and normal stress depend on the gradient velocity vector. In most viscous flows, the normal stresses  $\tau_{xx}$  are of small magnitude with respect to shear stresses, and are usually not taken into consideration. It can be said that normal stresses are considered important when the gradient of the normal velocity  $\partial u/\partial x$  is very large, like those that exist within the shock wave of a flow or fluid.

The surface forces shown in Figure A.8 in the  $x$ -direction exerted on the fluid element and by convention will be denoted as  $\tau_{ij}$  as an effort in the  $j$ -direction exerted on the plane perpendicular to the  $i$ -axis. Showing the mentioned convention, the following considerations should be noted for purposes of deducing the moment equation that governs fluids.

Taking into account the face  $abcd$  the force in the  $x$ -direction due to the shear stress,  $\tau_{yx} dx dy$ . The face  $efgh$  is a face parallel to the face  $abcd$ , in a different  $z$  position; therefore, the shear stress in the  $x$ -direction on the face  $efgh$  is:  $[\tau_{yx} + (\partial\tau_{yx}/\partial y)dy] dx dz$ .

It should be noted that the directions of the shear forces of the faces  $abcd$  and  $efgh$ ;  $\tau_{yx} dx dy$ , the force is on the negative side of the  $x$ -direction, while the upper face,  $[\tau_{yx} + (\partial\tau_{yx}/\partial y)dy] dx dz$  is in the positive  $x$ -direction.

This convention allows saying that the directions are consistent with the positive increments in the three components of the velocity;  $u$ ,  $v$  and  $w$  occur in positive directions of the axes. For example, in Figure A.8, the  $u$  component is incremented in the  $y$ -direction; therefore, on the face  $efgh$ ,  $u$  is higher just above the face than on the same face, causing a stretch, which tries to pull the fluid element in the positive  $x$ -direction, towards the right. On the other hand, observing the face  $abcd$ ,  $u$  is much less under the face than on the same face, causing a retardation or drag action on the fluid element, which acts in the negative  $x$ -direction [3].

In addition, on the face  $dcgh$  the force  $\tau_{zx}$  acts in the negative direction of the  $x$ -axis, while on the face  $abfe$ , the force  $[\tau_{zx} + (\partial\tau_{zx}/\partial z)dz] dx dy$  acts on the positive  $x$ -direction. Whereas in the face perpendicular to the  $x$ -axis;  $adhe$ , the only forces acting are the pressure  $p dy dz$ , which acts in the direction of the fluid element, and  $\tau_{xx} dy dz$ , which is negative in the  $x$ -direction [3].

Last but not least, the reason why the normal effort  $\tau_{xx} dy dz$ , on the face  $adhe$ , is to the left at the  $x$ -direction; it is because it has a much lower value than the value of  $u$ , than on the face itself; on the contrary, there is an increase in  $u$  in the positive  $x$ -direction. Resulting in a viscous action of normal tension, which acts as suction on the face  $adhe$ ; that is, there is a dragging action to the left that wants to slow down the movement of the fluid element.

And on the face  $bcgf$ , the pressure force  $[p + (\partial p/\partial x)dx] dy dx$ , presses on the fluid element (in the negative  $x$ -direction), and because the value of  $u$  just to the right of the face  $bcgf$  is greater than the value of  $u$  on the face, there is a suction due to the normal viscosity tension that tries to take the element to the right (in the positive  $x$ -direction) with a force equal to  $[\tau_{xx} + (\partial\tau_{xx}/\partial x)dx] dy dz$  [2].

With the above, can be represented the net surface force in the  $x$ -direction of the element of infinitesimal fluid in motion:

$$\begin{aligned}
 \left\{ \begin{array}{l} \text{Net surface force} \\ \text{in the } x \text{ - direction} \end{array} \right\} &= \left[ p - \left( p + \frac{\partial p}{\partial x} dx \right) \right] dy dz \\
 &+ \left[ \left( \tau_{xx} + \frac{\partial \tau_{xx}}{\partial x} dx \right) - \tau_{xx} \right] dy dz \\
 &+ \left[ \left( \tau_{yx} + \frac{\partial \tau_{yx}}{\partial y} dy \right) - \tau_{yx} \right] dx dz \\
 &+ \left[ \left( \tau_{zx} + \frac{\partial \tau_{zx}}{\partial z} dz \right) - \tau_{zx} \right] dx dy
 \end{aligned} \tag{A.45}$$

The total sum of forces in the  $x$ -direction;  $F_x$ , is given by the sum of the Eq.(A.44) and Eq. (A.45), there the following expression is obtained by performing the cancellation of terms:

$$F_x = \left[ -\frac{\partial p}{\partial x} + \frac{\partial \tau_{xx}}{\partial x} + \frac{\partial \tau_{yx}}{\partial y} + \frac{\partial \tau_{zx}}{\partial z} \right] dx dy dz + \rho f_x(dx dy dz) \tag{A.46}$$

The Eq. (A.46) refers to the force in the  $x$ -direction, and is part of one of the components of Newton's 2nd Law. Now considering the part of the right side of Eq. (A.43), the mass of the fluid element, in the  $x$ -direction, which is represented by the following expression:

$$m = \rho dx dy dz \tag{A.47}$$

Likewise, the acceleration of the fluid element is also taken into account, in the  $x$ -direction, and it represents the rate of change of its velocity, and it is denoted by  $a_x$ , and it is the rate of change of the vector  $u$  and is denoted by the fundamental derivative being this:

$$a_x = \frac{Du}{Dt} \tag{A.48}$$

Grouping the Eq. (A.43) and Eq. (A.46) in the Eq. (A.48), it is obtained the following expression for the  $x$ -component.

$$\boxed{\rho \frac{Du}{Dt} = -\frac{\partial p}{\partial x} + \frac{\partial \tau_{xx}}{\partial x} + \frac{\partial \tau_{yx}}{\partial y} + \frac{\partial \tau_{zx}}{\partial z} + \rho f_x} \tag{A.49}$$

Likewise, the group of moment equations for a viscous flow is also shown for the  $y$ -component and  $z$ -component.

$$\boxed{\rho \frac{Dv}{Dt} = -\frac{\partial p}{\partial y} + \frac{\partial \tau_{xy}}{\partial x} + \frac{\partial \tau_{yy}}{\partial y} + \frac{\partial \tau_{zy}}{\partial z} + \rho f_y} \tag{A.50}$$

$$\boxed{\rho \frac{Dw}{Dt} = -\frac{\partial p}{\partial z} + \frac{\partial \tau_{xz}}{\partial x} + \frac{\partial \tau_{yz}}{\partial y} + \frac{\partial \tau_{zz}}{\partial z} + \rho f_z} \quad (\text{A.51})$$

It can be said then that the Eq. (A.49) to Eq. (A.51) are the components of  $x$ ,  $y$ , and  $z$  of the moment equation. These are partial differential equations obtained from the fundamental physical principle of the infinitesimal fluid element. They are also of the *non-conservative* form because the element of the fluid moves with the flow.

These equations are of scalar type, and are called *Navier-Stokes equations* which govern the behavior of the fluids; in honor of the French engineer Claude-Louis Navier, who in 1823 deduced the fluid mechanics equations for viscous flows of molecular form, and the Irish mathematical physicist George Stokes, who in 1845 also deduced the equations for viscous fluids in a little different way to those of Navier but in essence similar [4].

The Navier-Stokes equations can be presented in the *conservative* form, taking into consideration the Eq. (A.49) and rewriting the equation of the form of the fundamental derivative, it is obtained as:

$$\rho \frac{Du}{Dt} = \rho \frac{\partial u}{\partial t} + \rho \vec{V} \cdot \nabla u \quad (\text{A.52})$$

Performing the expansion of the derivative of Eq. (A.52), it is derived as:

$$\rho \frac{\partial u}{\partial t} = \frac{\partial(\rho u)}{\partial t} - u \frac{\partial \rho}{\partial t} \quad (\text{A.53})$$

Recalling the identity of the divergence vector of the product of scalar times a vector, we have:

$$\rho \vec{V} \cdot \nabla u = \nabla \cdot (\rho u \vec{V}) - u \nabla \cdot (\rho \vec{V}) \quad (\text{A.54})$$

Substituting the Eq. (A.53) and Eq. (A.54) in Eq. (A.52):

$$\rho \frac{Du}{Dt} = \frac{\partial(\rho u)}{\partial t} - u \left[ \frac{\partial \rho}{\partial t} + \nabla \cdot (\rho \vec{V}) \right] + \nabla \cdot (\rho u \vec{V}) \quad (\text{A.55})$$

The terms that appear inside the bracket represents the continuity equation presented in Eq.(A.49) of the finite control volume, which is equal to zero. Therefore the Eq. (A.55) is reduced to:

$$\rho \frac{Du}{Dt} = \frac{\partial(\rho u)}{\partial t} + \nabla \cdot (\rho u \vec{V}) \quad (\text{A.56})$$

Substituting the above in Eq. (A.49) it can be observed the following for the  $x$ -component, and also, it is presented for the  $y$ -component and  $z$ -component. These new set of equations from Eq. (A.57) to Eq. (A.59) the Navier-Stokes equations of the *conservative* form.

$$\frac{\partial(\rho u)}{\partial t} + \nabla \cdot (\rho u \vec{V}) = -\frac{\partial \rho}{\partial x} + \frac{\partial \tau_{xx}}{\partial x} + \frac{\partial \tau_{yx}}{\partial y} + \frac{\partial \tau_{zx}}{\partial z} + \rho f_x \quad (\text{A.57})$$

$$\frac{\partial(\rho v)}{\partial t} + \nabla \cdot (\rho v \vec{V}) = -\frac{\partial \rho}{\partial y} + \frac{\partial \tau_{xy}}{\partial x} + \frac{\partial \tau_{yy}}{\partial y} + \frac{\partial \tau_{zy}}{\partial z} + \rho f_y \quad (\text{A.58})$$

$$\frac{\partial(\rho w)}{\partial t} + \nabla \cdot (\rho w \vec{V}) = -\frac{\partial \rho}{\partial z} + \frac{\partial \tau_{xz}}{\partial x} + \frac{\partial \tau_{yz}}{\partial y} + \frac{\partial \tau_{zz}}{\partial z} + \rho f_z \quad (\text{A.59})$$

## A.7 The energy equation

Previously in the preceding sections, the equations of both Continuity and Momentum were deduced, taking into consideration the model of a moving infinitesimal fluid element; for the Energy Equation, the same model will be used, but now taking into consideration the principle of the *conservation of energy*.

### A.7.1 Principle of energy conservation

One element that needs to be addressed is the Principle of Energy Conservation, which is based on the 1st Law of Thermodynamics<sup>3</sup>. Which takes into consideration the internal energy, the kinetic energy, and the potential energy required to perform a job and produce heat.

For the case of fluid dynamics, when the model of the infinitesimal fluid element in motion, as shown in Figure A.7 is taken into consideration (*non-conservative model*), it can be obtained:

$$\left\{ \begin{array}{l} \text{Rate of change of} \\ \text{energy inside the} \\ \text{fluid element} \end{array} \right\} = \left\{ \begin{array}{l} \text{Net flux of} \\ \text{heat into} \\ \text{the element} \end{array} \right\} + \left\{ \begin{array}{l} \text{Rate of working done on} \\ \text{the element due to body} \\ \text{and surface forces} \end{array} \right\} \quad (\text{A.60})$$

or,

$$A = B + C$$

The terms mentioned above will be denoted by the letters A, B, and C respectively to begin with the deduction of the principle of conservation of energy. It is worth mentioning that these equations of the principle of conservation of energy will be used when it is required to perform models in which there is heat transfer between fluids or boundary conditions of the model to be studied.

---

<sup>3</sup> The first law of thermodynamics relates work and heat transferred exchanged in a system through of a new thermodynamic variable, the internal energy. This energy is not created or destroyed, it is only transformed

Evaluating  $C$ , which corresponds to the rate of work performed on the element of infinitesimal fluid in motion due to the forces of volume and surface. Therefore, the work done by the force exerted on the body in motion is equal to the product of the force by the component of the velocity in the direction of the force. Therefore, the work is done by force acting on the element of the fluid vector velocity  $\vec{V}$  is:

$$\rho \vec{f} \cdot \vec{V} (dx dy dz) \quad (\text{A.61})$$

Considering again only the forces in the  $x$ -direction, the work done by the pressure and the shear forces on the fluid element in motion are calculated simply by multiplying the  $x$ -component of the velocity  $u$ , by the forces on faces. Being the work done by the face  $abcd$ , and having a shear stress  $\tau_{yx}$  multiplied by the velocity component remaining as  $u\tau_{yx}$ , similar expressions are also shown in the other faces of the fluid element [2].

In order to describe the energy of the fluid element, the model with these practical considerations is presented in Figure A.9. It can be seen that the forces in the positive  $x$ -direction perform positive work, while the negative forces in the  $x$ -direction do negative work.

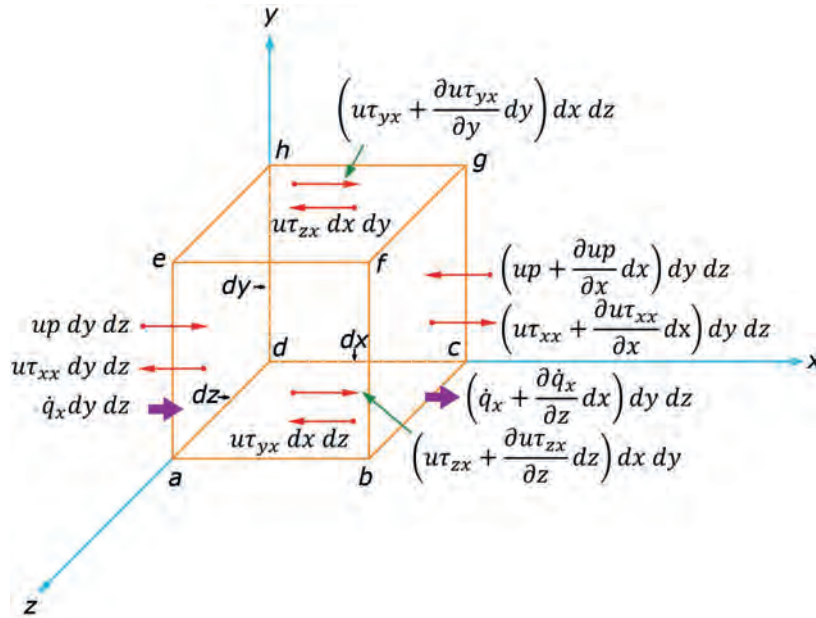


Figure A.9 Energy flows of the  $x$ -component of the infinitesimal fluid element.

Observing the forces due to the pressure of the faces  $abcd$  and  $bcgh$  in Figure A.9, it can be stated that the net rate of work in the  $x$ -direction is:

$$\left[ up - \left( up + \frac{\partial(up)}{\partial x} dx \right) \right] dy dz = - \frac{\partial(up)}{\partial x} dx dy dz \quad (\text{A.62})$$



Likewise, the net rate of work realized by the shear forces on the faces  $abcd$  and  $efgh$  is:

$$\left[ \left( u\tau_{yx} - \frac{\partial(u\tau_{yx})}{\partial y} dy \right) - u\tau_{yx} \right] dx dz = -\frac{\partial(u\tau_{yx})}{\partial y} dx dy dz \quad (\text{A.63})$$

This same procedure is performed for the missing work forces and considering the surface forces of Figure A.9, the net work done on the moving fluid element due to these forces in the  $x$ -component is simplified in:

$$\left[ -\frac{\partial(up)}{\partial x} + \frac{\partial(u\tau_{xx})}{\partial x} + \frac{\partial(u\tau_{yx})}{\partial y} + \frac{\partial(u\tau_{zx})}{\partial z} \right] dx dy dz \quad (\text{A.64})$$

Taking into consideration the previous expression, it is possible that the total work on the fluid element in motion is the sum of the contributions of the surface forces in the  $x$ ,  $y$ , and  $z$  directions, together with the contribution of the forces of the body. In this sense, the element C of the Eq. (A.60) is given by:

$$\begin{aligned} C = & \left[ -\left( \frac{\partial(up)}{\partial x} + \frac{\partial(vp)}{\partial y} + \frac{\partial(wp)}{\partial z} \right) + \frac{\partial(u\tau_{xx})}{\partial x} + \frac{\partial(u\tau_{yx})}{\partial y} + \frac{\partial(u\tau_{zx})}{\partial z} \right. \\ & + \frac{\partial(v\tau_{xy})}{\partial x} + \frac{\partial(v\tau_{yy})}{\partial y} + \frac{\partial(v\tau_{zy})}{\partial z} + \frac{\partial(w\tau_{xz})}{\partial x} + \frac{\partial(w\tau_{yz})}{\partial y} \\ & \left. + \frac{\partial(w\tau_{zz})}{\partial z} \right] dx dy dz + \rho \vec{f} \cdot \vec{V} dx dy dz \end{aligned} \quad (\text{A.65})$$

Now considering the B element of the Eq. (A.60) which corresponds to the net flow of heat in the element of infinitesimal fluid in motion, it is due to two main reasons:

- Volumetric heat as the absorption or emission of radiation.
- The heat of transfer along the surface due to temperature gradients, such as thermal.

Therefore,  $\dot{q}$  is defined as the velocity addition rate of volumetric heat per unit mass. Taking into consideration that the mass of the fluid element in motion in Figure A.4 is  $\rho dx dy dz$ , there is a volumetric heat of:

$$\left\{ \begin{array}{l} \text{Volumetric heating} \\ \text{of the element} \end{array} \right\} = \rho \dot{q} dx dy dz \quad (\text{A.66})$$

It can be seen in Figure A.9 that, the heat transferred by thermal conductivity, towards the fluid element along the face  $adhe$  is  $\dot{q}_x dy dz$ ; where  $\dot{q}_x$ , is the heat transferred in the  $x$ -direction, per unit time per unit area by thermal conductivity. On the other hand, the heat transferred outside the fluid element on the face  $bcbf$  is:  $[\dot{q}_x + (\partial\dot{q}_x/\partial x) dx] dy dz$ . Therefore, the net heat transferred in the  $x$ -direction in the fluid element through the thermal conductivity is:

$$\left[ \dot{q}_x - \left( \dot{q}_x + \frac{\partial \dot{q}_x}{\partial x} dx \right) \right] dy dz = -\frac{\partial \dot{q}_x}{\partial x} dx dy dz \quad (\text{A.67})$$

Adding the corresponding terms to the  $y$ -direction and  $z$ -direction along with the missing faces of Figure A.9 we have:

$$\left\{ \begin{array}{l} \text{Heating of the} \\ \text{fluid element by} \\ \text{thermal conduction} \end{array} \right\} = -\left( \frac{\partial \dot{q}_x}{\partial x} + \frac{\partial \dot{q}_y}{\partial y} + \frac{\partial \dot{q}_z}{\partial z} \right) dx dy dz \quad (\text{A.68})$$

The B term of the Eq. (A.60) corresponds to the sum of the Eq. (A.67) and Eq. (A.68):

$$B = \left[ \rho \dot{q} - \left( \frac{\partial \dot{q}_x}{\partial x} + \frac{\partial \dot{q}_y}{\partial y} + \frac{\partial \dot{q}_z}{\partial z} \right) \right] dx dy dz \quad (\text{A.69})$$

Since the heat flux produced by the thermal conductivity is proportional to the gradient of the local temperature, on the fluid element in the  $x$ ,  $y$  and  $z$ -directions it can be expressed as:

$$\dot{q}_x = -k \frac{\partial T}{\partial x}; \quad \dot{q}_y = -k \frac{\partial T}{\partial y}; \quad \dot{q}_z = -k \frac{\partial T}{\partial z} \quad (\text{A.70})$$

Where  $k$ , is the thermal conductivity. Therefore, Eq. (A.69) can be rewritten as follows:

$$B = \left[ \rho \dot{q} + \frac{\partial}{\partial x} \left( k \frac{\partial T}{\partial x} \right) + \frac{\partial}{\partial y} \left( k \frac{\partial T}{\partial y} \right) + \frac{\partial}{\partial z} \left( k \frac{\partial T}{\partial z} \right) \right] dx dy dz \quad (\text{A.71})$$

Finally, we have the A term of the Eq. (A.60) which is associated with the rate of change of the internal energy of the fluid element. This internal energy of the element is simply the microscopical energy; that is, the energy due to the rotational, translational, vibratory, and electric energy that molecules and atoms can have. Considering, in this case, a gas (air) that is in motion; therefore, the fluid element has two energy contributions, which are:

- The Internal Energy due to the random molecular movement, which will be denoted by  $e$  (per unit mass).
- The Kinetic Energy due to the translational motion of the fluid element, where  $V^2/2$  is this kinetic energy per unit mass.

Therefore, it can be said that the infinitesimal fluid element has two sources of energy, both internal energy, and kinetic energy. The sum of these two energies is the total energy of the system. The total energy is  $e + V^2/2$

As it is an element of the fluid in motion, the rate of change of the total energy per unit mass is given by the fundamental derivative and as the mass of the fluid element is:  $\rho dx dy dz$ , we have:

$$\boxed{A = \rho \frac{D}{Dt} \left( e + \frac{V^2}{2} \right) dx dy dz} \quad (\text{A.72})$$

Therefore, the final energy equation is obtained by substituting Eqs. (A.65), (A.71) and (A.72) in Eq. (A.60), obtaining:

$$\begin{aligned} \rho \frac{D}{Dt} \left( e + \frac{V^2}{2} \right) = & p\dot{q} + \frac{\partial}{\partial x} \left( k \frac{\partial T}{\partial x} \right) + \frac{\partial}{\partial y} \left( k \frac{\partial T}{\partial y} \right) + \frac{\partial}{\partial z} \left( k \frac{\partial T}{\partial z} \right) \\ & - \frac{\partial(up)}{\partial x} - \frac{\partial(vp)}{\partial y} - \frac{\partial(wp)}{\partial z} + \frac{\partial(u\tau_{xx})}{\partial x} + \frac{\partial(u\tau_{yx})}{\partial y} \\ & + \frac{\partial(u\tau_{zx})}{\partial z} + \frac{\partial(v\tau_{xy})}{\partial x} + \frac{\partial(v\tau_{yy})}{\partial y} + \frac{\partial(v\tau_{zy})}{\partial z} \\ & + \frac{\partial(w\tau_{xz})}{\partial x} + \frac{\partial(w\tau_{yz})}{\partial y} + \frac{\partial(w\tau_{zz})}{\partial z} + \rho \vec{f} \cdot \vec{V} \end{aligned} \quad (\text{A.73})$$

The Eq. (A.73) is the energy equation of the *non-conservative* form in terms of the total energy  $e + V^2/2$ . And it can be said that this particular section, the whole theory of the equations that govern fluids like the equations of continuity, momentum, and energy, constitute the Navier-Stokes equations, and are the fundamental basis for fluid dynamics.

## A.8 Equations for non-viscous fluids (Euler equations)

A non-viscous fluid is where the phenomena of transport of viscosity, mass diffusion, and thermal conductivity are neglected, and therefore, not considered. The fundamental equations that govern fluids for an unstable, three-dimensional, compressible, non-viscous flow are [2], [3] described in the following section.

### A.8.1 Euler Energy equations

#### Non-conservative form

$$\frac{D\rho}{Dt} + \rho \nabla \cdot \vec{V} = 0 \quad (\text{A.74})$$

#### Conservative form

$$\frac{\partial \rho}{\partial t} + \nabla \cdot (\rho \vec{V}) = 0 \quad (\text{A.75})$$

## A.8.2 Euler Momentum equations

### Non-conservative form

For the  $x$ ,  $y$ , and  $z$  components:

$$\begin{aligned}\rho \frac{Du}{Dt} &= -\frac{\partial p}{\partial x} + \rho f_x \\ \rho \frac{Dv}{Dt} &= -\frac{\partial p}{\partial y} + \rho f_y \\ \rho \frac{Dw}{Dt} &= -\frac{\partial p}{\partial z} + \rho f_z\end{aligned}\tag{A.76}$$

### Conservative form

For the  $x$ ,  $y$ , and  $z$  components:

$$\begin{aligned}\frac{\partial(\rho u)}{\partial t} + \nabla \cdot (\rho u \vec{V}) &= -\frac{\partial \rho}{\partial x} + \rho f_x \\ \frac{\partial(\rho v)}{\partial t} + \nabla \cdot (\rho v \vec{V}) &= -\frac{\partial \rho}{\partial y} + \rho f_y \\ \frac{\partial(\rho w)}{\partial t} + \nabla \cdot (\rho w \vec{V}) &= -\frac{\partial \rho}{\partial z} + \rho f_z\end{aligned}\tag{A.77}$$

## A.8.3 Euler Energy equations

### Non-conservative form

$$\rho \frac{D}{Dt} \left( e + \frac{V^2}{2} \right) = p \dot{q} - \frac{\partial(Up)}{\partial x} - \frac{\partial(vp)}{\partial y} - \frac{\partial(wp)}{\partial z} + \rho \vec{f} \cdot \vec{V}\tag{A.78}$$

### Conservative form

$$\begin{aligned}\frac{\partial}{\partial t} \left[ \rho \left( e + \frac{V^2}{2} \right) \right] + \nabla \cdot \left[ \rho \left( e + \frac{V^2}{2} \right) \vec{V} \right] \\ = p \dot{q} - \frac{\partial(Up)}{\partial x} - \frac{\partial(vp)}{\partial y} - \frac{\partial(wp)}{\partial z} + \rho \vec{f} \cdot \vec{V}\end{aligned}\tag{A.79}$$

# APPENDIX B



---

## SOLUTION FOR COMPUTATIONAL FLUID DYNAMICS

---

### B.1 Solution methods for Computational Fluid Dynamics

Most of the important physical processes of nature are governed by the Partial Differential Equations. In the previous chapter, the equations that govern fluids were described in the study of fluid dynamics. These equations, from the mathematical point of view, are Partial Differential Equations (PDE), which knowing the mathematical properties of the PDE, will allow analyzing the behavior of the same, as well as the selection of the numerical method for the solution of the system of equations.

The fundamental equations that govern fluids are complex. In this context, an exact analytical solution can only be found in simplified situations. Furthermore, if not, the mathematical analysis and the initial development of numerical methods will take part in the solution of the equations of the model. The equations of the model will allow presenting the elements of a problem of PDE well modeled and will allow discussing the mathematical classification of the PDE, its consequences for the properties of the solution, and the importance of fluid dynamics and heat transfer.

#### B.1.1 Classification of the PDE processes

The study of fluid flows and heat transfer are processes that evolve, for this from the practical point of view; it is desirable to classify these processes into two main groups:

- Processes in equilibrium (independent of time): This type of problems that are in equilibrium, appear when the interest is in a stable state, and when the properties of the system do not change over time.
- Processes in the transient state (evolution in time or change over time): On the other hand, processes in a transient state, the physical properties of the system change over time.

Computational fluid dynamics analysis can be applied for both types of processes, but different numerical approaches are required. For problems in equilibrium, the equation must be solved numerically only once in order to determine an approximation to the time-independent  $u(x)$  solution in the space domain  $\Omega$ . And for the transitory processes, or also called marching problems, they should be resumed with initial conditions that give a state at a time  $t = t_0$  the solution advances in time to determine the approximations for  $u(x, t)$  at a time  $t > t_0$  [5].

## B.2 Introduction to numerical solution for ordinary and PDE's

The equations that describe fluid flows are ordinary equations or partial differential equations, which combine properties and variables of fluids, such as the components of speed, pressure, density, etc., and its derivatives. Nevertheless, for most of these equations, there are no analytical methods to find their solutions. Therefore, different *numerical methods* should be used, which allow producing approximate solutions thanks to the computational tools [6].

The main characteristics of a solution are the accuracy of the numerical method and its approximation to the solution of the problem and on the other hand, the stability of the method, which must not accumulate errors of the previous calculations in the iterations of the solution. The first step to the numerical solution of a certain problem is its *Numerical Discretization*, which means that each component of the differential or the partial differential equation is transformed into a numerical analog, and can be represented in the computer and subsequently processed by a computer program, built on an algorithm [6].

### B.2.1 Discretization approaches

The discretization refers to the process of replacing partial (or integral) derivatives in the fundamental equations of fluids with discrete numbers. In other words, it is the process in which differential or integral functions or equations include functions, which have infinite continuous values in the domain and are approximated by analogous expressions that prescribe values only in a finite number of discrete points or volumes in the domain.

PDE's analytical solutions involve expressions of closed-form that give the variation of the dependent variables continuously through the domain.

On the other hand, numerical solutions can only respond at discrete points in the domain, called mesh points. The discretization of partial differential equations is called finite differentiation, and the discretization of the integral form of the fundamental equations is called finite volumes [3].

To be able to develop the above, first, it is necessary to have space, which is where the flow is going to be calculated or also called *physical space*; this is divided into a number of geometric elements called cells of the mesh. This process, which was described in Section 3.3, is known as *mesh generation*. Connecting thus the points of the mesh or grid (called nodes or vertices) in the physical space and connecting them by straight lines or lines of the mesh [1].

This mesh usually consists of a two-dimensional system, can be formed by triangles or quadrilaterals, and in three dimensions formed by tetrahedrons, hexahedra, prisms, or pyramids. The most important requirement of the mesh is that there should be no gaps between the cells of the mesh, and there should not be superpositioning of the cells; at the same time, it has to be a smooth mesh on its surface [1].

It can be said that there are two ways in which the mesh can be generated, the first of them:

1) Mesh Coupled to the Solid, Figure B.1 a).- This type of meshing is generated, following the contour of the physical space. The main advantage of this approach is that the flow can be resolved precisely in the contours, which are essential in the case of the cutting layers along with the solid bodies. The disadvantage that arises is the high degree of complexity in the generation of the mesh, especially in very elaborate geometries [1].

2) Cartesian mesh, Figure B.1 b).- This type of meshing occurs when the edges of the grid cells are oriented parallel to the Cartesian coordinates. Its main advantage is that the calculation of flows is much simpler than meshing coupled to the body. In this context, it is more difficult to have a more accurate result [1].

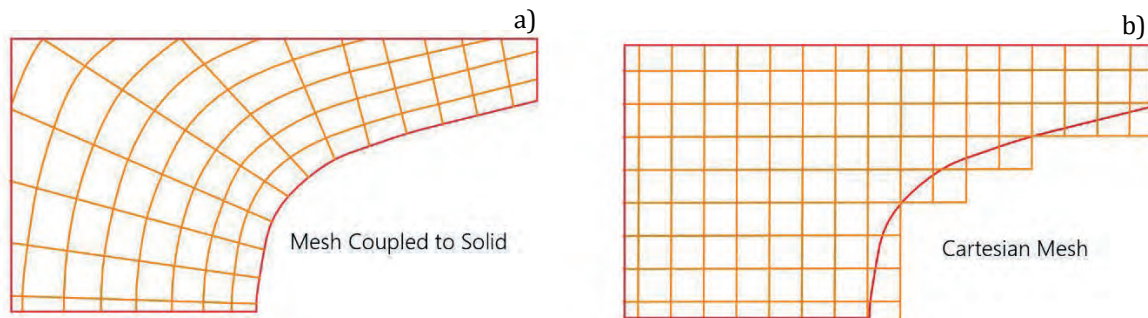


Figure B.1 Types of mesh generation a) Meshing coupled to the solid, b) Cartesian meshing.

Currently and generally in the industry, meshing coupled to the body is used, due to the configuration of the geometric complexity of the solids or bodies to be studied.

### B.3 Spatial discretization

The Spatial Discretization of the Navier-Stokes equations is based on three main methods: *Finite Differentiation*, *Finite Volume*, and *Finite Element*. These three methods are based on different mesh types to be able to discretize the fundamental equations of the fluids, which can be stated two types of meshing:

- Structured Mesh, Figure B.2 a).- In this mesh, each point of the mesh, call vertex or node) are identified by the indexes  $i, j, k$  and the corresponding Cartesian coordinates  $x_{i,j,k}$ ,  $y_{i,j,k}$  and  $z_{i,j,k}$ . The cells of the mesh are quadrilaterals in 2D and hexahedrons in 3D. This type of mesh is used by SolidWorks software and implemented in the models of the case studies proposed in this project.
- Unstructured Mesh, Figure B.2 b).- The points of the mesh do not have a particular order so that the cells can have a different adjacent cell. Previously this type of mesh used cells in the form of triangles in 2D and 3D tetrahedrons; at present, the unstructured meshes consists of a combination of quadrilaterals and triangles in 2D, while in 3D it uses hexahedrons, tetrahedra, pyramids, and prisms.

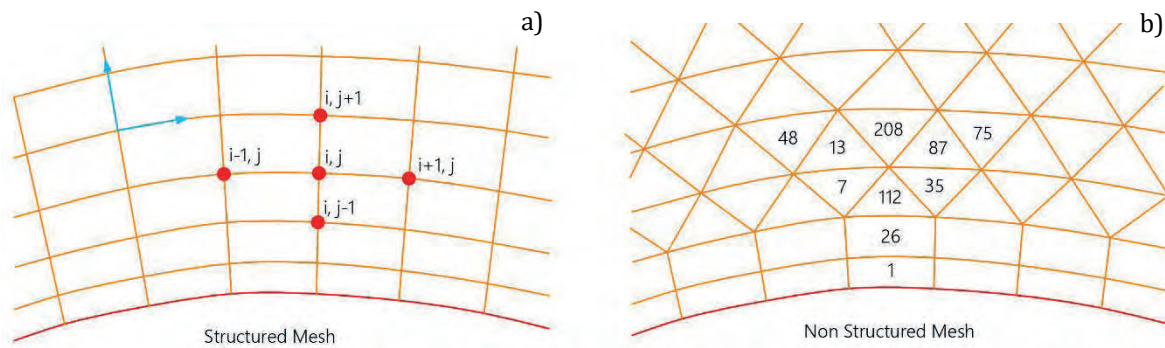


Figure B.2 Types of meshing a) Structured meshing - solid tracking, b) Unstructured meshing - mixed mesh.

Once the mesh is generated, the next step is to determine how the fundamental equations of the fluids are discretized. The three main methods of discretization are described below.

### B.3.1 Finite Difference Method (FDM)

This method was the first and easiest method, which was developed to give numerical solutions to the PDEs, and it was introduced by Euler in the year 1768 [1]. In this method, its fundamental base is the conservation of the form of the differential equations, and the domain of the solution is represented by a mesh or grid. Where each point of the mesh, the differential equations are approximate being replaced by partial derivatives by approximations in terms of nodal values of the functions.

The Finite Differentiation Method is a method that can be applied to any mesh; however, it is applied to a uniform or structured mesh, which works in a simple and effective way. The mesh needs to be structured where the points of the mesh should be located at the points of intersection of the families of the rectilinear curves [4], [6].

The series expansion of Taylor or the polynomial adjustment, are used to obtain approximations to first and second derivatives of the variables with respect to the coordinates. The disadvantage of the FDM is that conservation does not comply unless special care is taken. In addition, the restriction to simple geometries is a significant disadvantage in complex flows [6].

An important advantage of the Finite Differentiation Method is its simplicity, as well as the possibility of obtaining high order approximations easily and therefore achieving a high order of accuracy in spatial discretization [1].

### B.3.2 Finite Volume Method (FVM)

The Finite Volume Method directly uses conservation laws; that is, using the integral form of the Navier-Stokes and Euler equations. This method was first used by McDonald in 1971 and Mac-Cormack and Paullay in 1972, for 2D simulations of non-viscous fluids. And for flows in three dimensions by Rizzi and Inouye in 1973. The FVM discretizes the fundamental equations, first dividing the physical space into an arbitrary number of control volumes called polyhedral [1].



This method, which is used by SolidWorks Flow Simulation, uses the integral form of the fundamental equations of fluids. In this method, the domain of the solution is divided into a finite number of control volumes, and the conservation equations are applied to each volume. At the center of each control volume, there is a computational node in which the values of the variable are calculated.

The FVM can be used in any mesh type so that it can be used in complex geometries. The grid defines only the control volume borders and does not need to be related to a coordinate system. The FVM approach is one of the simplest methods to understand and to program since the terms used that need to be approximated have a physical meaning, so it is the most popular method in engineering.

There is more than one way to define the form and position of the control volumes within the computational domain with respect to meshing. Two of the basic approaches are mentioned below [1]:

- *Centered Cell Scheme.* The quantities of the flow are stored in the centroids of the mesh cells. Thus, the control volumes are identical to the cells of the mesh Figure B.3 a).
- *Vertex Cell Scheme.* The variables of the flow are stored in the points of the mesh. The control volume can be either the union of all the cells that share the point of the mesh or some volumes centered around the point of the mesh Figure B.3 b).

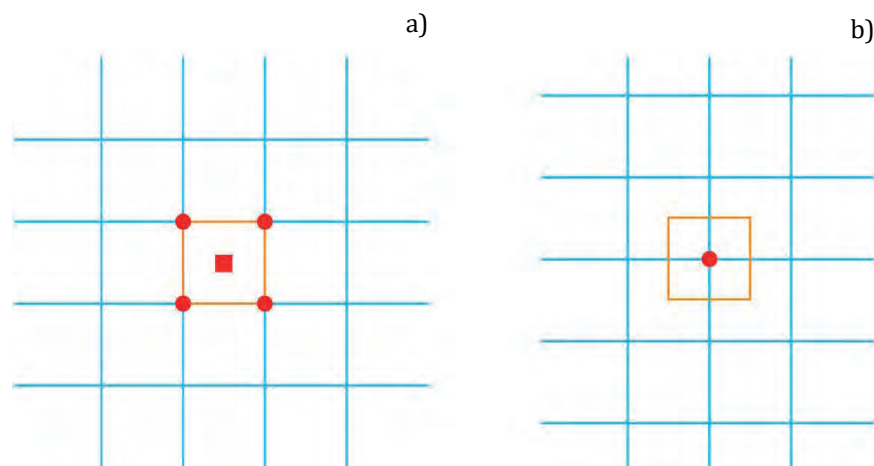


Figure B.3 Basic approaches FVM meshing a) Cell-centered control volume, b) Vertex cell control volume.

One of the disadvantages that the FVM presents before the FDM is that older systems of the second order are more difficult to develop in 3D. This is because the FVM requires three levels of approximation, which are interpolation, differentiation, and integration.

### B.3.3 Finite Element Method (FEM)

The Finite Element Method (FEM) is based on the *Method of Weighted Residuals*. This method is practical to solve partial differential equations was developed between 1940 and 1960, mainly for dynamic structural problems, which was later extended to the use in the dynamics of fluids. The FEM was introduced by Turner in 1956, and it was not until the 1990s that the FEM gained popularity for the solutions of the Euler and Navier-Stokes equations [1], [4].

The FEM is similar to the FVM, this because the domain is divided into a series of discrete volumes or finite elements that usually do not have a structure; in 2D, they use triangles or quadrilaterals, while in 3D they are usually composed of tetrahedra or hexahedra. These, in turn, form a mesh without structure [7].

An important advantage of the FEM is that it can handle different geometries. This is because the construction of meshes is much easier for finite elements. These meshes can be refined, simply by dividing each element. This method is usually applied to non-Newtonian fluids [7].

## B.4 Turbulence in the CFD analysis

Turbulence can be defined as the state of a flow that is characterized by its fluctuating and random nature, which is the result of the loss of stability of a laminar flow. Laminar flows are characterized because the fluid particles move in layers or sheets.

As mentioned in Section 3.3, where depending on the characteristics of the fluid, having a Reynolds number greater than 4,000, this being a critical value, the flow will have a turbulent behavior. In this sense, the particles are characterized by being agitated, disorderly, and randomly.

Most of the fluids in nature, the atmospheric climate, the flow through a cylinder of a combustion engine, the mixing of a cup of coffee, are fluids of turbulent behavior, and in the same way, the wind resource is part of this type of fluid behavior. On the contrary of the turbulent flows, they are the laminar flows.

These turbulent fluids are different in size from mixing a rate of coffee to sizes of storms or tornadoes on the earth's surface, but one thing in common is the Reynolds Number  $Re$ . These turbulent flows have a higher degree of friction as well as heat transfer compared to laminar flows. This non-dimensional Reynolds number is derived from Eq. (B.1) representing the flow in a pipe.

$$Re = \frac{\rho UD}{\mu} \quad (B.1)$$

In 1883 the Irish scientist Osborne Reynolds, who studied the conditions in which a fluid is moving inside a pipeline, went from laminar flow to turbulent flow when the fluid moved chaotically when reaching a certain speed. With these studies, the Reynolds number was proposed, which indicates that the generation of turbulence depends on the relationship between the inertial forces and the viscosity forces [4], [8].

To understand how the boundary layer is formed, it is said that when studying the turbulent flows around an obstacle, it can be considered that the movement is non-viscous, in all the fluid, except in an area close to the body where the viscous effects are predominant. This area near the body, usually thin, is known as a boundary layer.

This boundary layer is formed from the flow of a free current with a velocity  $U_\infty$ , approaching towards a flat surface as can be depicted in Figure B.4. The flow will have no-slip or zero speed due to friction. As the flow approaches the wall, the boundary layer is formed where the flow varies from zero on the wall to the velocity  $U_\infty$  in the flow current [4].

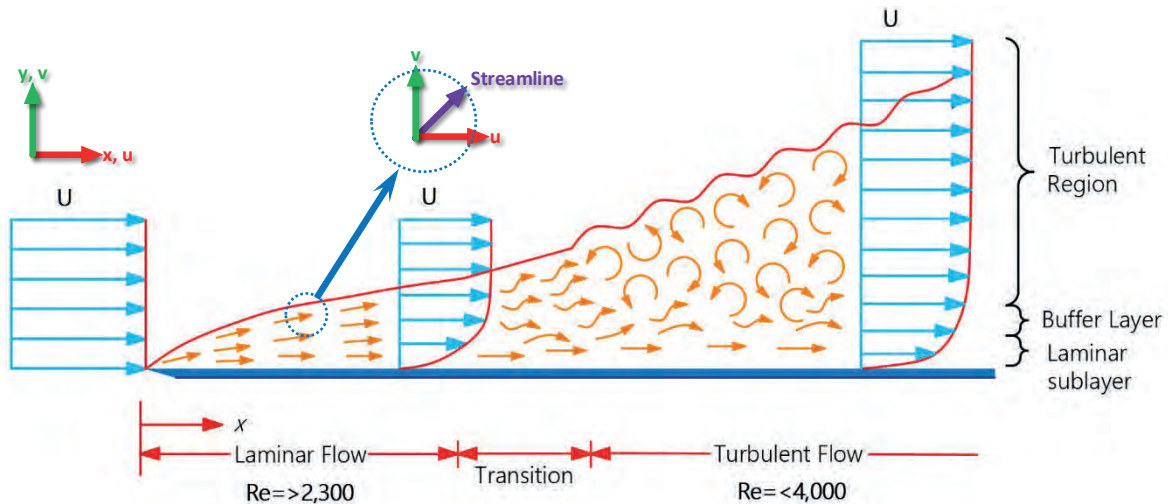


Figure B.4 Boundary layer over a flat surface.

When the Reynolds number is small, it means that the forces of inertia are small compared to viscous forces. As the distance  $x$  increases along the surface, the Reynolds number increases, and for this reason, the inertial forces begin to predominate, causing instability to the boundary layer [4]. In addition, exist a transition zone until the flow develops in turbulent flow with disorganized eddies.

Below the turbulent boundary layer, a region near the wall or surface remains in a laminar form, which is called a laminar sublayer. The following shows the schematic classification of the approaches for the prediction of turbulent flows, which according to Bardina [9], there are six categories which can be divided into sub-categories, at the current date exists an infinity of models for turbulent flow modeling [7].

- The first approach is about the use of *correlations*, such as those that give the friction factor as the functions that express the Reynolds Number or the Prandtl Number. This method is very useful, but it is limited to simple flows and can only be characterized by a few parameters. It does not require the use of the computer.
- The second uses *integral equations*, which can be deduced from the equations of motion, integrating one or more coordinates. Usually, this reduces the problem to one or more PDEs that can later be solved.

- The third method is based on the obtained equations, which are averaged equations of movement over time, on a coordinate, which means that the flow does not change. This approach is called *one-point closure* and leads to a set of PDEs called Reynolds Averaged Navier-Stokes (RANS), proposed by O. Reynolds.
- The fourth type of method is called *two-point closure*. This uses equations for the correlation of velocity components at two spatial points or, commonly, the Fourier transform of these equations. This method is rarely used except for homogeneous turbulence.
- The fifth is the Large Eddy Simulation (LES), which helps to solve large-scale flow movements, by means of approximations or modeling of small-scale flow movements.
- The sixth and final approach method is the Direct Numerical Simulation (DNS), where the Navier-Stokes equations are solved for all movements in a turbulent flow.

These methods require the solution of mass, momentum, and energy conservation equations. Figure B.5 illustrates the approaches of the methods described above, classified according to their level of complexity.

The main difficulty that the turbulent flows have is that the variations of their physical parameters are the greater range of scales of length and time than laminar flows. Although the equations that govern laminar and turbulent fluids are similar, the equations that describe turbulent fluids are usually much more difficult and costly to solve.

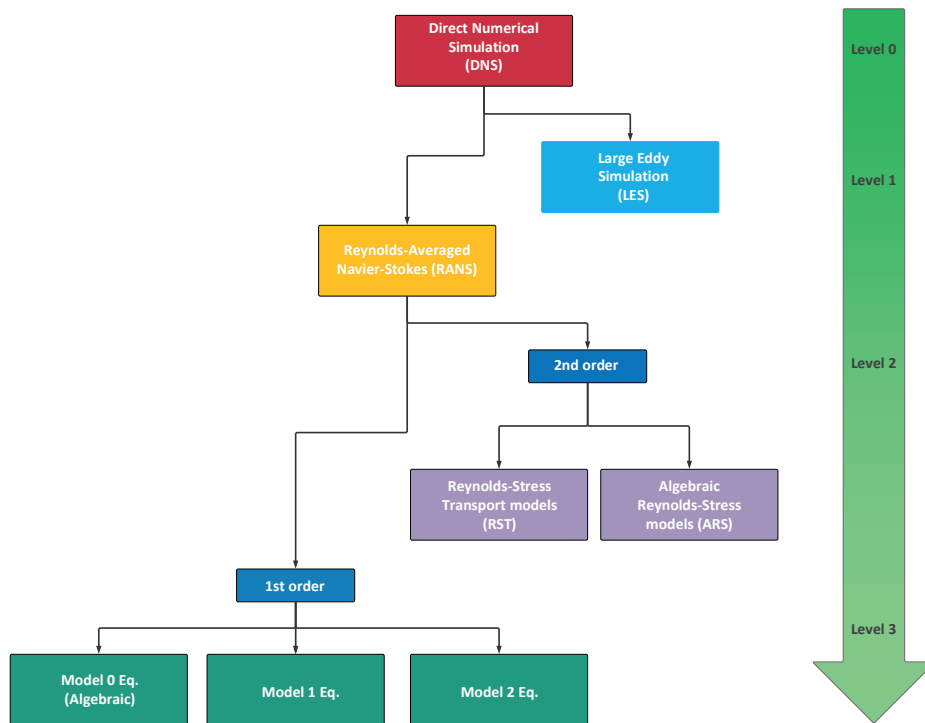


Figure B.5 Hierarchy of turbulence models [1].

# APPENDIX C



## 3D TOPOGRAPHIC TERRAIN MODELING PROCEDURE

### C.1 Modeling procedure for 3D modeling of topographic terrains.

The present Appendix C shows the modeling procedure to characterize any topographic terrain in Solidworks®, which is the CAD tool used in the present research project. This evaluation of the topographical terrains uses three different software in order to develop the 3D model of the terrain that is a fundamental part of the roughness length in the CFD simulations.

The first step includes the use of Google Earth® software; this software will serve as the geo-localization of the interest site with the possibilities to develop a small wind project. The next derived steps permit to set up the location of the proposed site, which are described below:

- Based on the wind potential is determined the location of the project in the navigation map of Google Earth® software.
- A circumference layout is traced with a 500 m radius with the center in the interest site. This step uses the ruler tool by selecting the circle option to draw the figure on the map.
- 

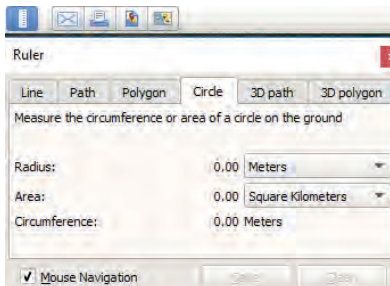


Figure C.1 Circle menu in Google Earth software.

- A polygon is traced, following the circumference of the circle traced previously. This tool of the polygon is also founded in the ruler tool.

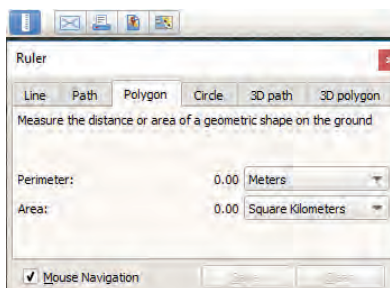


Figure C.2 Polygon menu in Google Earth software.

- Both, the circle and polygon created of the multiple interest sites are saved as places in with any name provided by the user, with file extension .kmz

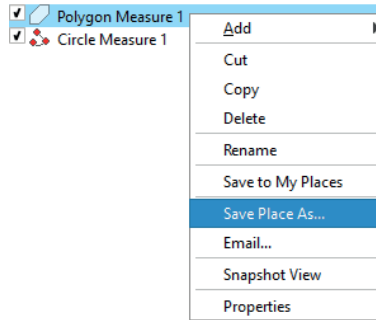


Figure C.3 Right-click menu list in Google Earth software.

- Taking into consideration the figures created in Google Earth®, the layout of the circle is recommended to take a screenshot of the interest site, which will later serve as a sketching model for the evaluation of the wind project.

Step two takes place to the Global Mapper® software, this software operates as a database of the topographic conditions, in this software will be imported the .kmz files created in the previous step in order to locate the region of the interest site. The following derived steps mention this process:

- First of all, it has to be configured the georeferenced system based on the location of the interest site. In this case, considering that the case studies selected are located in Mexico, which corresponds to the 14 Zone derived from the projection of the Universal Transverse Mercator (UTM) coordinates system. In the 14 Zone is considered the following Cartesian coordinates: 102° W - 96° W North Hemisphere, with a latitude 19° 19' 46.10" N and longitude of 99° 10' 55.87" W.

This UTM configuration is located in the bar Tools → Configure...→Projection.

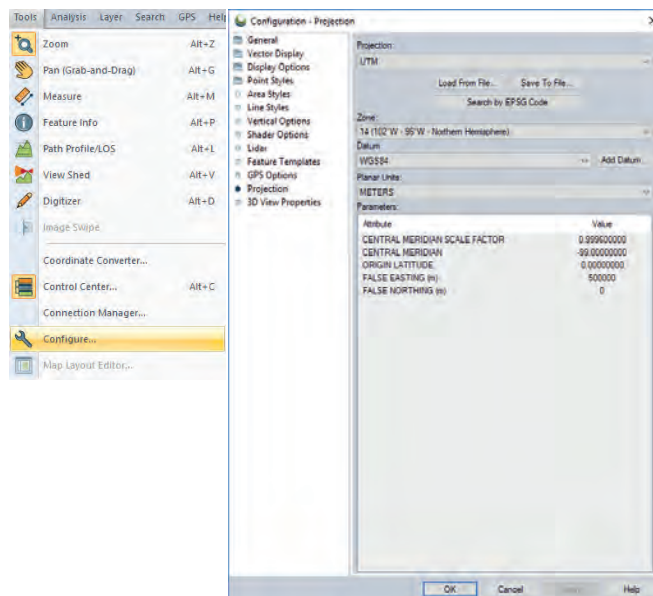


Figure C.4 Configuration projection menu in Global Mapper software.

- Is proceeded to open the .kmz files that previously were saved in the Google Earth® software.
- Download the topographic and terrain data from the AESTER GDEM database and click Connect.

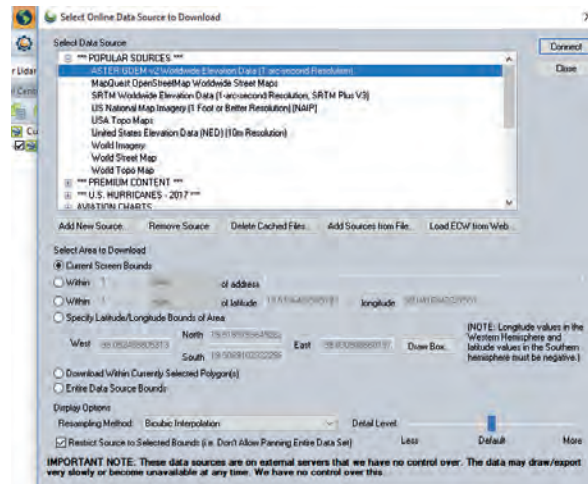


Figure C.5 Source maps menu in Global Mapper software.

- Localize the study area in the map of Global Mapper® represented by the polygon and circle created in Google Earth®.

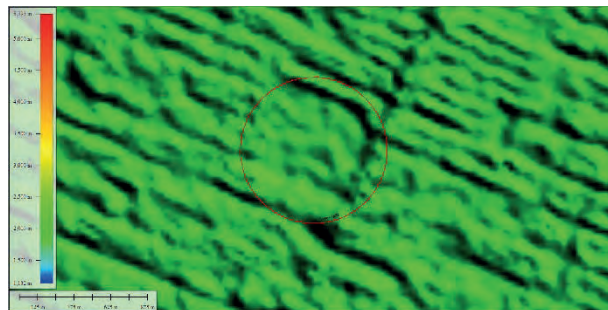


Figure C.6 Localization of the circle figure file in Global Mapper software.

- Export a new file with a dot cloud elevation format - XYZ Grid (Elevation grid format).

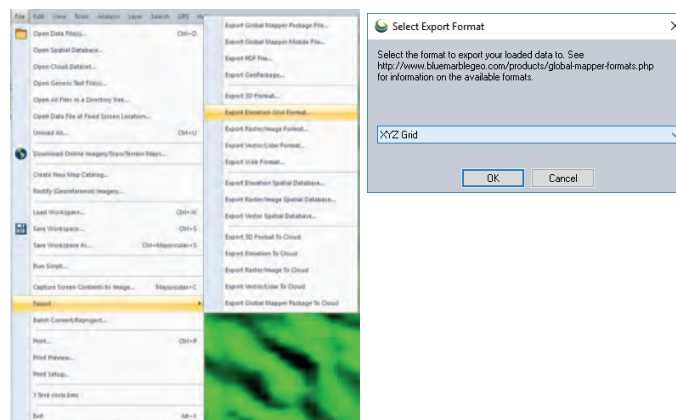


Figure C.7 Export menu options in Global Mapper software.

- Select the region according to the export limits of Solidworks® and traced by the edge of the circle of radius of 500 m, with the option of XYZ Grid Export Options in the tab Export Bounds → Draw a Box...

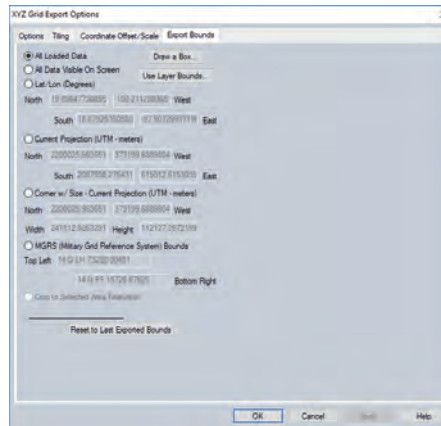


Figure C.8 Export menu options in Global Mapper software.

- In the scale and displacement configuration option, configure it with a suitable scale so that Solidworks® can configure the file correctly and not leave the limits of the model.
- Save the new file of the cloud elevation topography with extension .xyz grid file. This file will serve as the base of the roughness length and topography of the selected site of study.

The last and third step takes place in the use of Solidworks® software, in this step is developed the 3D model of the topography data acquired by the AESTER GDEM database of the Global Mapper® software.

- First, it is recommended to enable the Scanto3D complement, which helps to read the cloud point .xyz file.
- Open the file created with Global Mapper® software (point cloud .xyz file).
- Take into consideration that the image shown corresponds to the level curves to be able to model the 3D solid that will later serve us to evaluate the wind potential of the wind site.
- Once the cloud points are loaded, it has to be developed a 3D sketch selecting these points generated by the file.
- Within the sketch in 3D, develop curves with the spline command, following the point cloud in one direction, either horizontally or vertically, until completing the entire cloud of points.

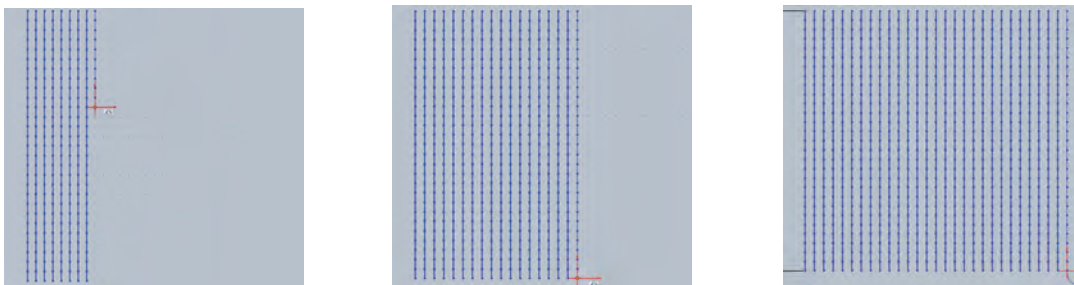


Figure C.9 Development of the grid points with spline command in SolidWorks.



- After the cloud points are covered in its totality, the next step is with the command insert → surface it must be created a solid surface through the splines created previously marked as an open-loop with all the lines created based on the cloud points.



Figure C.10 Creation of the solid surface through splines.

- In the end, it is obtained a result like the following in both 2D and 3D modeling.

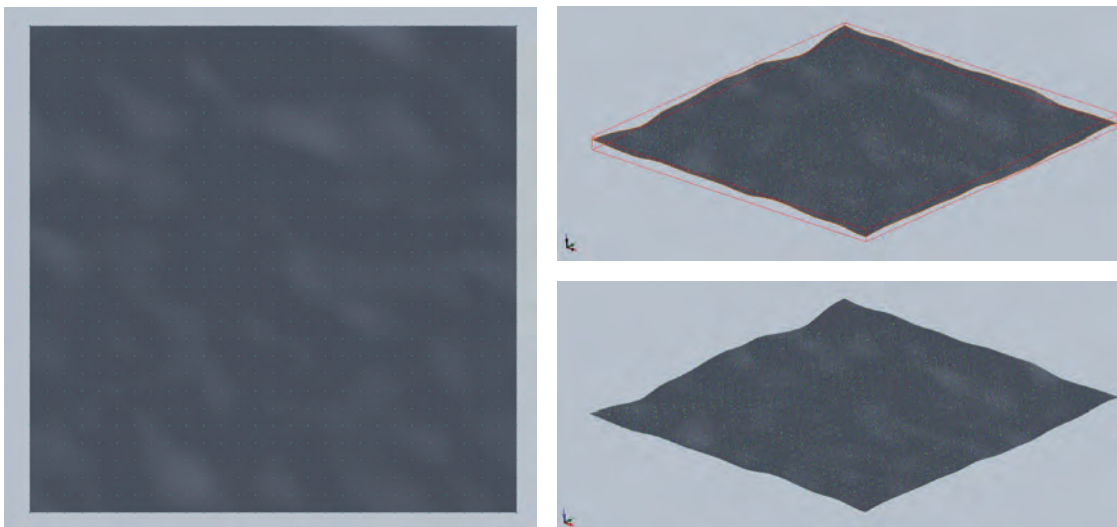


Figure C.11 Results of the 3D topography surface in SolidWorks.

- On the previous 3D surface modeled, it is proceeded with the development of a square figure, size limited by the extreme sides of the cloud points to model a rectangular parallelepiped on the elevation plane.
- Create the rectangular model in 3D with a considerable height in order to subsequently perform an intersection operation with the topographic surface of the area of interest.
- Move the parallelepiped at a distance above the previously created surface.

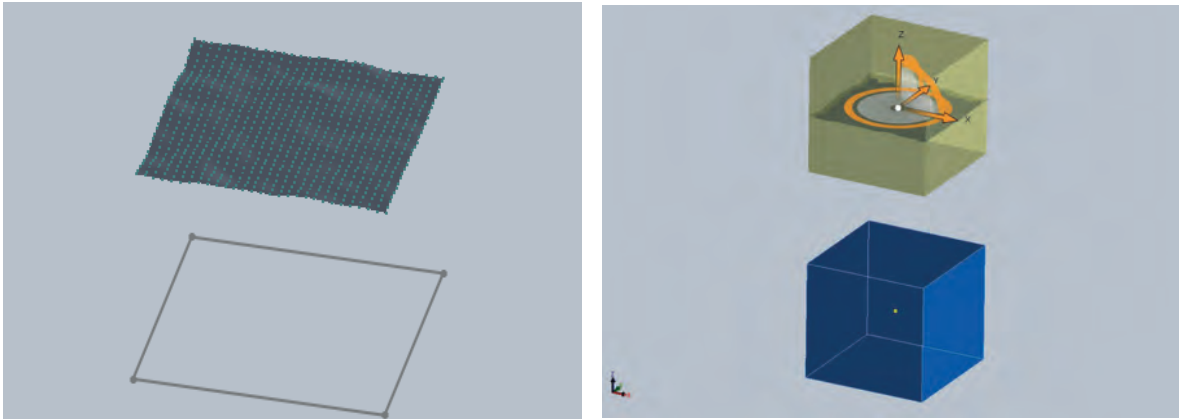


Figure C.12 Creation process of the 3D solid of the topography.

- Now is considered to perform the intersection operation between both models, the rectangular parallelepiped and the topographic surface of the interest site.

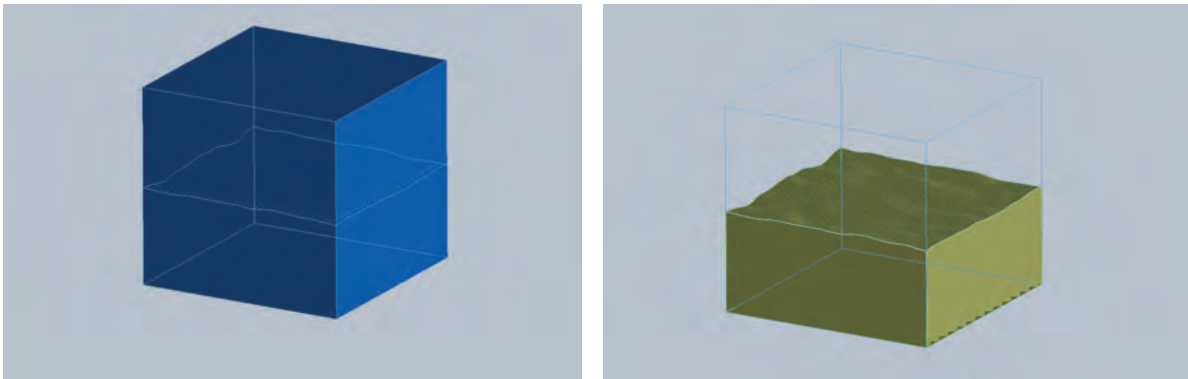


Figure C.13 Intersection operation of the 3D solid of the topography.

At the end of this process, it is obtained the 3D model of the topography terrain, which will characterize the roughness length of any interest site. This model will operate as the base of the 3D complex model that describes the building or structures that will be studied in the CFD simulations.

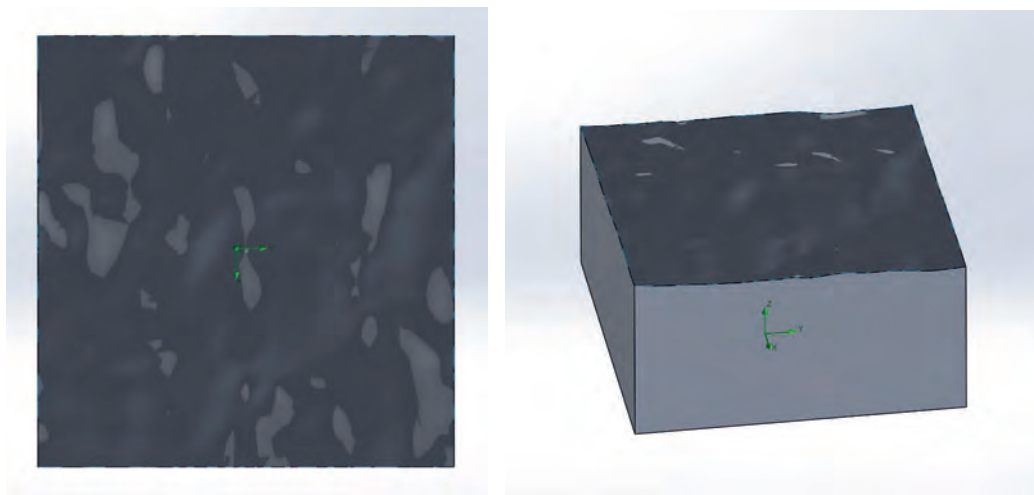


Figure C.14 Final results of the 3D modeled topography.

# APPENDIX D



## OPERATION PRINCIPLE OF THE ULTRASONIC ANEMOMETER WINDMASTER 3-AXIS

### D.1 Ultrasonic anemometer WindMaster 3-Axis

The ultrasonic anemometer works with three pairs of transducers; each pair measures the time in which an ultrasonic pulse travels from one transducer to another; that is, from a transducer on the upper side to its opposite transducer. Comparing the time in which a pulse travels from the lower transducer to the upper transducer.

As it is shown in Figure D.1, the air velocity along the axis between each pair of transducers can be calculated from the flight times on each axis.

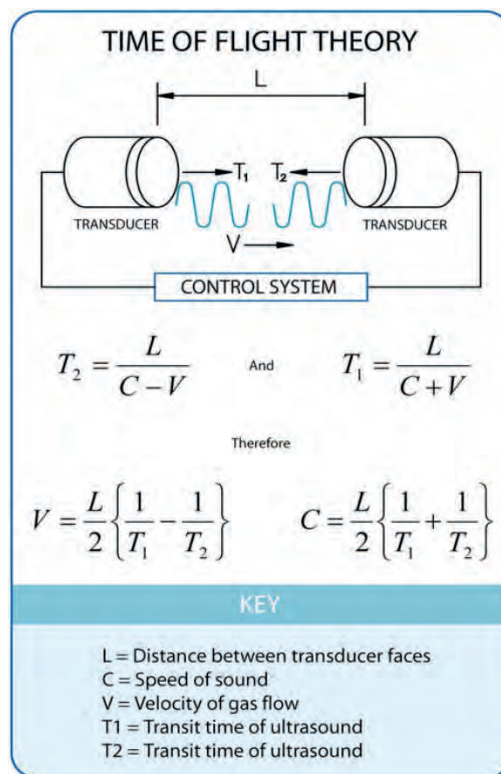


Figure D.1 Operation principle of the ultrasonic anemometer [10].

The above calculation is independent of factors such as temperature. Also, from the speeds of the three axes, the wind speed is calculated, either as speed vectors U, V, and W or as Polar and a speed vector W.

It can be seen in Figure D.1 that the speed of sound in the air can be calculated from the times of flight. From this, the sonic temperature can be derived from the formula:  $T_{SI} = C_1^2/403$

Where  $T_{SI}$  is the sonic temperature, which differs from the absolute temperature by a quantity to the water vapor contained in the air. This difference is around  $\pm 1\text{ }^\circ\text{C}$  to  $2\text{ }^\circ\text{C}$  and decreases as the temperature decreases. Whereas  $C_1^2$  is the speed of sound, this without considering effects such as relative humidity.

Based on the operating manual of the manufacturer Gill Instruments, it is required to select a position in which the device is free of any obstacle or structure, which impedes the flow of air or induces turbulence flows. It is also required that the device is installed outside the reach of radars or radio transmitters. Under these parameters, in addition to considering the alignment of the anemometer with the mark on the base of the device, the mast was built in which said the device was installed, for its location in the measurement campaign in case study C.

Figure D.2 shows the schematic diagram of the WindMaster anemometer in its isometric view, as well as the top view and the polarity alignment of the vectors  $U+$ ,  $V+$ , and  $W+$ . Being that the vector  $U+$  is defined towards the direction in line with the North cardinal point as indicated in the diagram. The vector  $V+$  is defined in the direction of  $90^\circ$  counterclockwise in relation to the North cardinal direction. Furthermore, the vector  $W+$  is defined vertically by the mounting axis [10].

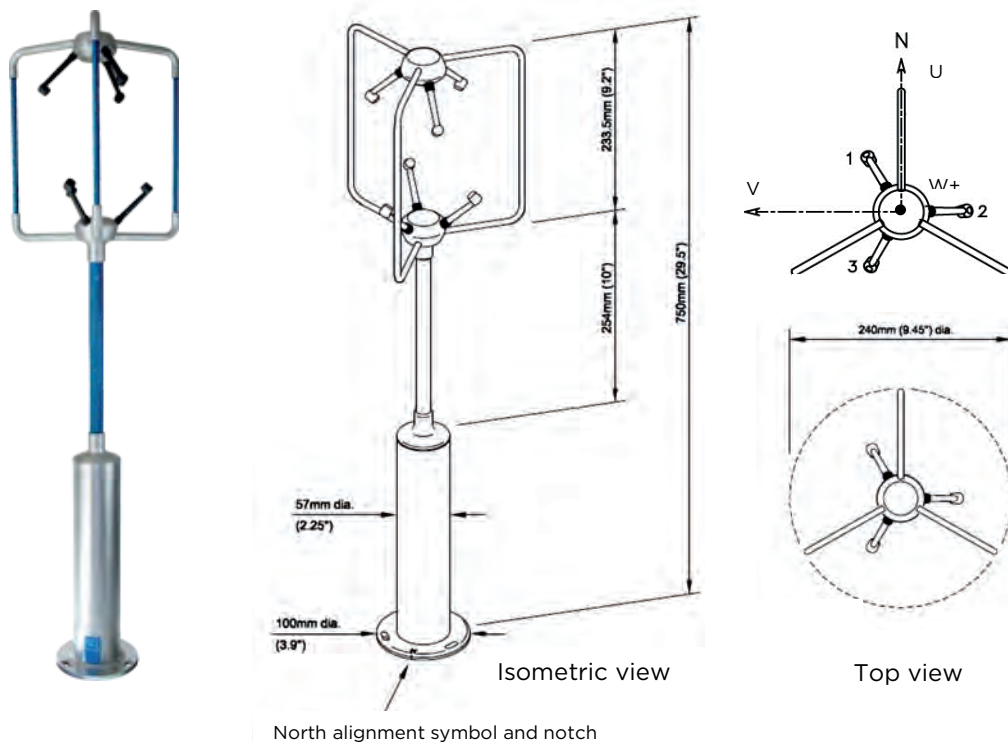


Figure D.2 Schematic diagram of WindMaster ultrasonic anemometer from Gill Instruments [10].

Among some of the main considerations to take into account in order to install the ultrasonic anemometer include:

- Ensure that the power supply operates at a voltage range of 9 to 30VDC at all times.

- Avoid turbulence caused by surrounding structures that will affect the WindMaster's accuracy, such as trees, other masts, and buildings.
- The standard exposure of wind instruments on the level of open ground is 10 m above ground level. Open ground is defined as an area where the distance between the sensor and any obstruction is at least ten times the height of the obstruction.
- If the sensor is to be mounted on a mast arm, a tower or mast, then the arm must be at least twice as large as the minimum diameter or diagonal of the tower. The arm should be placed on the prevailing wind side of the tower.
- If mounted on a mast, then the distance of an adjacent mast must be ten times the other diameter of the mast.
- If mounted in a building, the sensor must be mounted at a height of 1.5 times the height of the building.

The WindMaster ultrasonic anemometer can be detailed with Table A.1 in relation to the technical specifications for its optimal handling within the measurement campaigns [10].

Table A.1 Operational, technical specifications of the WindMaster ultrasonic anemometer.

Parameter	Ultrasónic WindMaster
<b>Outputs</b>	
Sample rate	20 or 32 Hz
Units of measure	m/s, mph, KPH, knots, ft/min
Format	Vector UVW or Polar coordinates
Averaging	0 - 3600s
<b>Wind speed</b>	
Range	0 - 50 m/s
Resolution	0.01 or 0.001 m/s
Accuracy [12 m/s]	<1.5% RMS
<b>Wind direction</b>	
Range	0 - 359.9°
Resolution	1° or 0.1°
Accuracy [12 m/s]	2°
<b>Speed of sound</b>	
Range	300 - 370 m/s
Resolution	0.01 m/s
Accuracy	< ±0.5% @ 20°C
<b>Power supply</b>	
<b>Digital Output</b>	
Protocol (ASCII and Binary)	RS232, RS422, RS485
<b>Sonic temperature</b>	
Range	-40°C to +70°C
<b>General data</b>	
Weight	1.0 kg
Size	750mm x 240mm
Environmental protection	IP65
Operating temperature	-40°C to +70°C
Humidity	<5% to 100%
Precipitation	Operation up to 300 mm/hour

Regarding the operation mode of WindMaster ultrasonic anemometer, it has the ability to operate in eight operating modes or message formats, according to the specific needs and parameters to be evaluated in the measurement campaigns, which are mentioned below depending on the type of wind measurements to use [10].

- Mode 1 – ASCII, UVW, Continuous
- Mode 2 – ASCII, Polar, Continuous
- Mode 3 – ASCII, UVW, Polled
- Mode 4 – ASCII, Polar, Polled
- Mode 5 – Binary, Polar Short
- Mode 6 – Binary, UVW Short
- Mode 7 – Binary, Polar Long
- Mode 8 – Binary, UVW Long

From the eight operating modes or format in which the data is displayed, the two most representative operating modes are in the ASCII code of the WindMaster 3D Axis anemometer, the first of them is presented in vector form and provides the wind speed along its three components on the "U", "V" and "W" axes, which is shown in the Figure D.3.

**a) Mode 1 - ASCII, UVW**

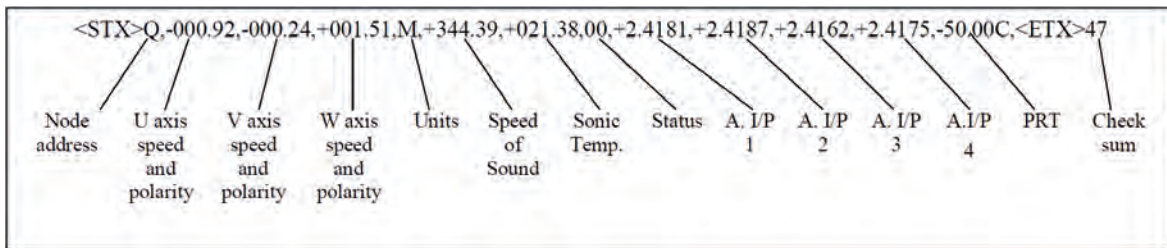


Figure D.3 Registration string in Mode 1 - ASCII, UVW (Continuous) ultrasonic anemometer.

The format with the previous configuration is represented with the following character string: <STX><ID>, ±UUU.UU,±VVV.VV,±WWW.WW,U,±CCC.CC,±TTT.TT,SS,[±1.1111, ±2.2222, ±3.3333, ±4.4444], ±PP.PPC,<ETX>CC<CR><LF>. Each of the variables of the previous character string represents the values shown in Table A.2

Table A.2 Characters string in ASCII format - Continuous recording of the ultrasonic anemometer.

String	Interpretation
<STX>	- Start of string character (ASCII value 2)
<ID>	- Anemometer identification (A-Z)
±UUU.UU	- Velocity in 'U' axis 0.01ms <sup>-1</sup> units
±VVV.VV	- Velocity in 'V' axis 0.01ms <sup>-1</sup> units
±WWW.WW	- Velocity in 'W' axis 0.01ms <sup>-1</sup> units
U	- Units (M=m/s, N=knot, P=mph, K=kph and F=fpm)
±CCC.CC	- Speed of sound in 0.01ms <sup>-1</sup> units
±TTT.TT	- Sonic temperature in degrees C.
SS	- Status data (Codes 00 to 0B)
±1.1111	- Analog input 1 in volts
±2.2222	- Analog input 2 in volts
±3.3333	- Analog input 3 in volts
±4.4444	- Analog input 4 in volts
±PP.PPC	- PRT temperature in degrees C.
<EXT>	- End of string character (ASCII value 3)
CC	- Checksum for all characters
<CR><LF>	- Carriage Return and Line Feed

The operation mode 1 - ASCII, UVW Continuous, or message format is the best one that adapts to the needs and which will be selected for the development of the wind resource measurement campaign in the present case study. This mode has a normal or high-resolution sampling resolution which can be selected in the RS232 serial port configuration.

For sampling and capturing WindMaster ultrasonic anemometer records, as well as evaluating the wind resource. Only the third to the ninth variable corresponding to the magnitude of the wind in the vector U, V, and W, as well as the unit type (meters), the speed of sound, the temperature, and the state of the anemometer, will be taken into account respectively. The eighth variable of the character string corresponds to the ambient temperature in degrees Celsius.

To determine the parameters of wind speed and direction that will be used in the analysis of computational fluid dynamics, derived from the variables shown in the vectors, it was necessary to perform the calculations of the velocity components in "U" and "V", with the following fundamental trigonometry equations.

For the variable of the resulting wind speed, we have the expression:

$$V_R = \sqrt{U^2 + V^2} \tag{D.1}$$

On the other hand, for the direction variable, the mathematical function of the tangent arc atan2 is used, which through the signs of the vectors U and V, the direction angle can be calculated in the correct quadrant of the plane. The result is shown in radians, so it is necessary to convert to degrees by multiplying the result by the constant  $180/\pi$  and adding  $180^\circ$  for the correction of the angle to the north cardinal to the results with a negative sign.

$$D_v = -atan2\left(\frac{V}{U}\right) 180/\pi \quad \text{If } D_v < 0 \Rightarrow D_v + 180 \tag{D.2}$$

For finalizing the previous explanation, the configurable mode 2 of the WindMaster ultrasonic anemometer is described below.

**b) Mode 2 - ASCII, Polar**

This second format of the sampling record allows carrying out a measurement campaign without making any calculation, obtaining directly the values of the direction and magnitude of the wind. This sampling, which for each record throws a string of characters with the following structure, shown in Figure D.4.

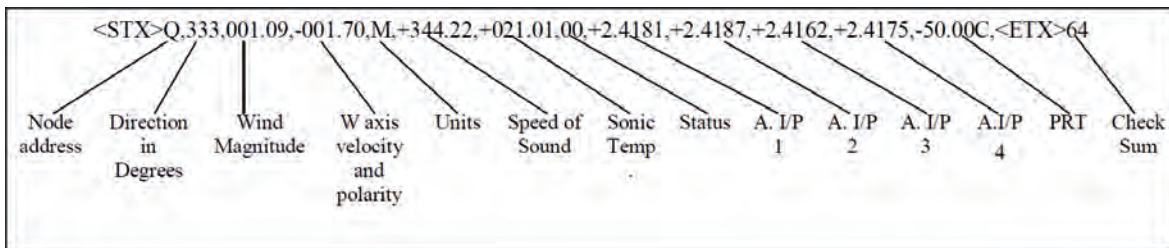


Figure D.4 Registration string in Mode 2 - ASCII, (Polar) ultrasonic anemometer.

The previous string characters shows the configuration of the registers that are generated when the ultrasonic anemometer is in operation, in such a way that it is represented in the following form:

<STX><ID>,DDD,MMM.MM,±WWW.WW,U,±CCC.CC,±TTT.TT,SS,[±1.1111,±2.2222,±3.3333,±4.4444],± PP.PPC,<ETX>CC<CR><LF>. Where each of the values is identified with its interpretation shown in Table A.3.

Table A.3 Characters string in ASCII- Polar format recording of the ultrasonic anemometer.

<b>String</b>	<b>Interpretation</b>
<STX>	- Start of string character (ASCII value 2)
<ID>	- Anemometer identification (A-Z)
DDD	- Direction in degrees
MMM.MM	- Wind magnitude
±WWW.WW	- Velocity in 'W' axis $0.01\text{ms}^{-1}$ units
U	- Units (M=m/s, N=knot, P=mph, K=kph and F=fpm)
±CCC.CC	- Speed of sound in $0.01\text{ms}^{-1}$ units
±TTT.TT	- Sonic temperature in degrees C.
SS	- Status data (Codes 00 to 0B)
±1.1111	- Analog input 1 in volts
±2.2222	- Analog input 2 in volts
±3.3333	- Analog input 3 in volts
±4.4444	- Analog input 4 in volts
±PP.PPC	- PRT temperature in degrees C.
<EXT>	- End of string character (ASCII value 3)
CC	- Checksum for all characters
<CR><LF>	- Carriage Return and Line Feed

The previous operation modes are the two more representatives for the functioning of the WindMaster ultrasonic anemometer. The message format mode configuration one was used for the present doctoral project and installed in the Case Study C corresponding to the wind measurement campaign in situ at the academic campus Siglo XXI of Universidad Autónoma de Zacatecas. All the specifications presented in the user manual [10] were used for the proper pre-installation, installation, and configuration in the wind resource measurement campaign.



# APPENDIX E



---

## DEVELOPMENT OF THE DATALOGGER FOR THE ULTRASONIC ANEMOMETER WINDMASTER 3-AXIS

---

### E.1 Datalogger for anemometer WindMaster 3-Axis

Among the main parameters for the wind resource assessment in the measurement campaigns, are the wind speed and direction. These parameters must be measured by specialized equipment to obtain the wind resource, called anemometers; in this case, an ultrasonic type anemometer was used. Among other devices to be used in the same purpose to concentrate the wind data in the measurement campaigns are the dataloggers or data acquirer, which allow the sampling, capture, and storage of the variables of the wind resource, to later perform its processing and evaluation.

This document shows the development and innovation of a datalogger, using a low-cost computational resource such as the Raspberry Pi-3. The use of WindMaster Datalogger, as already mentioned, allows the acquisition, processing, and collection of data obtained through a WindMaster 3-Axis Ultrasonic anemometer.

The WindMaster 3-Axis Ultrasonic anemometer directly measures different types of variables such as wind speed, wind direction, temperature, etc. These are received over an electronic system through the interface RS232 for processing and storage the wind variables through different processes of the system.

The WindMaster Datalogger selects the variables of wind direction, wind speed, sound velocity, ambient temperature, and system state, which are obtained directly from the data sent by the WindMaster 3-Axis anemometer. Some of the variables will be used to obtain the extractable wind power. The device has a backup power system around 20,000 mAh that allows that despite the failure of the main power, the system continues to operate normally through the battery.

WindMaster Datalogger works in such a way that the anemometer when measuring the aforementioned variables sends the data of the variables through a DB9 connector adapter with RS232-USB interface, which is connected to a Raspberry Pi-3, which is responsible for processing the wind data. Within the Raspberry, Pi-3 are the codes developed in Python programming language, which make the relevant calculations of the averages wind variables and power calculations. In addition, in order to save the data of the different variables, a database was created in MySQL.

The system was added the possibility of generating files with extension .csv (values separated by commas), which contain the values of the database and which are generated by the user through a line of code when required; the generated files contain the wind data obtained per day. In order to acquire the wind data from the Raspberry Pi-3, this is communicated through a PLC (Power Line Carrier) device.

At the transmission endpoint, it is connected to the ethernet port of the Raspberry Pi-3 and at the receiving endpoint it is connected to a router which through, via FTP (File Transfer Protocol) communication can be entered into the Raspberry Pi-3 system through a personal computer to be able to save or consult the generated files.

The backup power system is carried out due to a 5 VDC lithium-ion battery, with a nominal current of 2 A, at a load capacity of 20,000 mAh. This backup system, when generating a cut in the power supply of the 127 VAC line, activates a relay that makes the change of the power supply, allowing the system to continue operating. The device developed WindMaster Datalogger has a self-executing program, which allows the system can be restored automatically whenever there is a power failure or system restart.

### **E.1.1 Software development of the WindMaster Datalogger**

The data processing software was developed in Python programming language, both for sampling and obtaining the variables for wind resource data processing. The software processes the signals obtained through the WindMaster 3D-Axis anemometer and uses the equation of the wind potential that makes it possible to obtain the estimated wind power calculation through the obtained data using the standard equation of wind power.

$$P_{wind} = \frac{1}{2} \rho v^3; \quad [W/m^2] \quad (B.1)$$

Where  $\rho$  is the density, with an altitude of 0 m a.s.l. which corresponds to an ambient temperature of 15 °C, taking the value of 1,225 [Kg/m<sup>3</sup>]. The wind speed  $v$  takes the value of the average speed of the sampling period.

In this context, the software that makes up the WindMaster Datalogger system is described, which allows the operation and capture of the variables of the wind resource. Within these software or subroutines that compose the WindMaster Datalogger are:

#### **1.- wind\_master.py**

This code routine is located in the operating system of the Raspberry Pi-3: /home/pi/WindMaster/wind\_master.py. This code is responsible for initializing the communication between the WindMaster 3D-Axis anemometer and the Raspberry Pi-3. In addition, this code is in charge of obtaining the anemometer wind data through the RS232-USB adapter, as well as selecting the values of interest for the case study and processing them for the generation of the database.

## 2.- AutoReset\_windmaster.py

This code routine is located in the path of the Raspberry Pi-3: /home/pi/WindMaster/AutoReset\_windmaster.py. This code allows that the memory of the Raspberry Pi-3, permit that the code wind\_master.py be self-executed either from an initial process, after an error, or after a restart or power failure of the Raspberry Pi-3.

## 3.- Generator\_csv.py

This other developed Python code is located at the path: /home/pi/Windmaster/generator\_csv.py, and is responsible for accessing the MySQL database and generating the .csv file from these data. This .csv file contains the variables of interest for the evaluation of the wind resource.

## 4.- Flag

This is a file used by AutoReset\_windmaster.py located and is located at the path: /home/pi/Desktop/Flag. This subroutine of the program allows the reading of the error flag and thus ensures that the main code is functioning correctly. It checks that the state of the power is on, allowing the reset to be carried out in case of failure or that the anemometer is not working correctly.

## 5.- Database

The primary component of WindMaster Datalogger is the development and storage of the database, where the values of the different variables obtained and calculated using MySQL, which is a relational database management system and is considered the most common open-source database in the world, for web development environments.

The database was created to store the obtained and calculated data, which is assigned the name of bd\_windmaster. The MySQL manager database supports a number of SQL data types in several categories: numeric types, date and time types, string (character and byte) types, spatial types. This database is structured with the type of data shown in Table E.1; this data is assigned to the wind variables required for the wind resource assessment.

Table E.1 Variables that make up the MySQL database for the WindMaster datalogger.

Field	Type	Null	Key	Default	Extra
t	int (10) unsigned	YES		NULL	
Direction	smallint (5) unsigned	YES		NULL	
Magnitude	float	YES		NULL	
Speed	float	YES		NULL	
Temp	float	YES		NULL	
Status	tinyint (3) unsigned	YES		NULL	

The following section will be discussed the electrical diagram, which describes the control operation and communication of WindMaster ultrasonic anemometer with the WindMaster datalogger.

### E.1.2 Electrical diagram of the WindMaster Datalogger

The WindMaster Datalogger operates at a nominal voltage of 12 VDC and has a total consumption of approximately 2 A. The electronic block diagram is shown in Figure E.1, in which all the components comprising the system are specified. This device, as previously mentioned, has an energy backup system, which feeds only the electronic system and, on the other hand, for the communication between the PLCs, the 127 VAC power connection is needed.

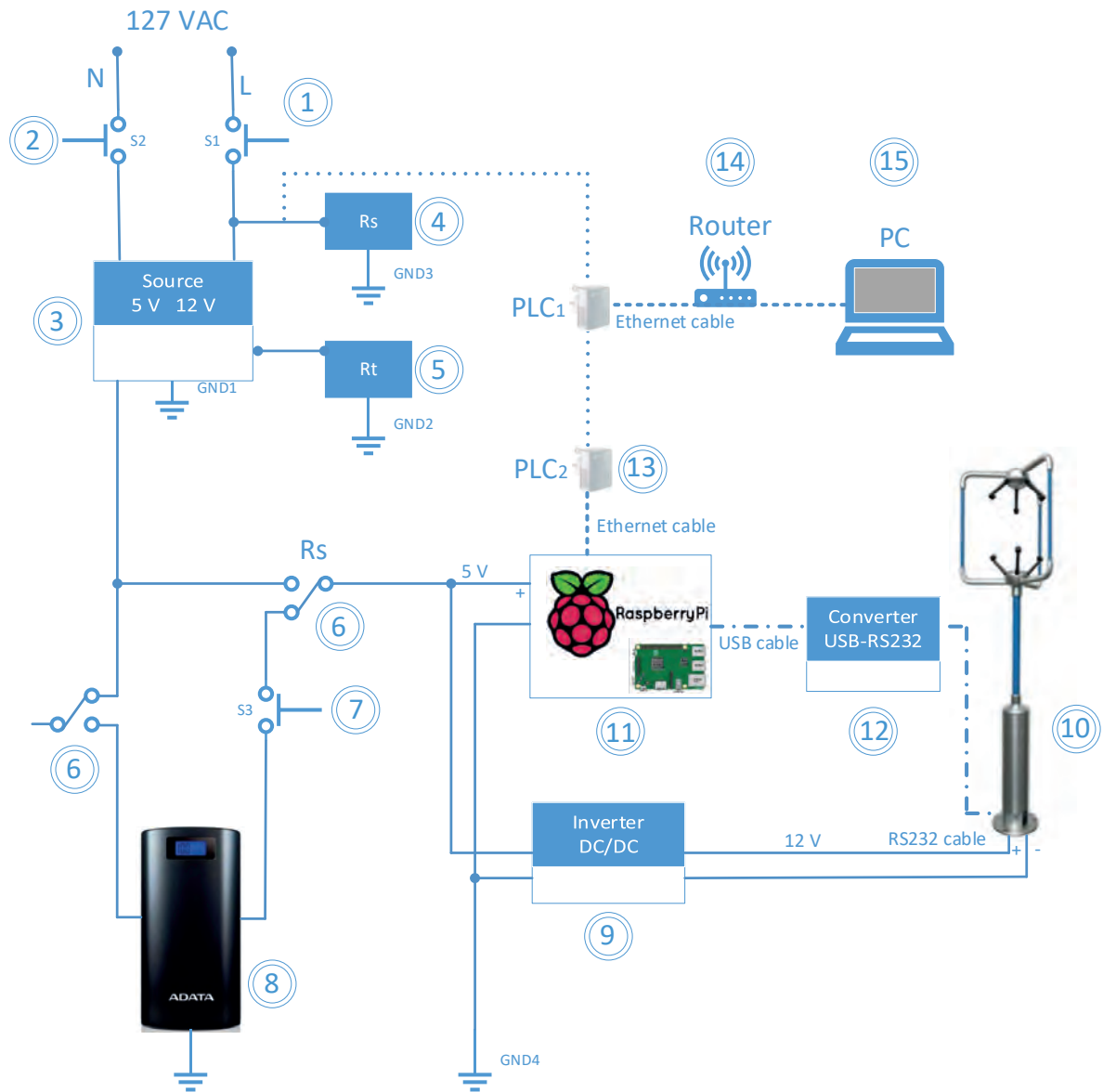


Figure E.1 Block diagram of the WindMaster datalogger.

Table E.2 shown the lists of the components that composite the complete system of the datalogger, showing the general interconnection of the components for the solution of the WindMaster ultrasonic anemometer.

Table E.2 Main components of the WindMaster datalogger block diagram.

Component No.	Description
1	Line connection switch of 127 VAC.
2	Neutral connection switch.
3	Power supply 127 VCA to 5 and 12 VCD.
4	Switch bypass relay. Controls the power source that supplies power to the system. While the 127 VAC line is in operation, it activates the charge mode to the backup battery, and the power source (3) is the one that supplies the system with power. Otherwise, the battery changes from charging mode to output mode and thus feeds the system.
5	Timmer off delay relay. This element allows that the system does not have a short circuit while the backup battery comes into operation.
6	Relay switch. Change the power between the backup battery and the power source.
7	Battery backup connection switch.
8	Backup battery, 5 VDC, 2A, 20,000 mAh. Supplies electrical power to the system while there is no power supply of 127 VAC
9	Boost converter DC/DC. It raises the voltage from 5 V to 12 VDC since the sensor needs a 12 VDC power supply for its operation.
10	Sensor (Wind Master 3-Axis). Ultrasonic anemometer that obtains the parameters of the wind resource and other variables.
11	Raspberry Pi-3 is the microcomputer responsible for the execution and control of the software developed. This device is responsible for receiving, processing, and storing the data generated by the sensor.
12	RS232-USB adapter allows serial communication between the ultrasonic anemometer and the Raspberry Pi-3.
13	PLC adapter (Power Line Carrier). The PLC's are used for sending and receiving the data through the electrical line and the external computer device to acquire the wind resource data processed by the microcomputer.
14	Router / SWITCH LAN. Connection for the computer through WIFI.
15	Personal computer

### E.1.3 Database and file generator of the WindMaster datalogger

The database acquires the data through the wind\_master.py program, which sends the data to the MySQL database manager in which the wind data is generated. In Figure E.2, the database contained in MySQL with the variable values is shown.

```

| Date | u.uuu | v.vvv | w.www | speed of s | temp. | status | wind speed | wind direction | wind power
| 1544516247 | -0.175 | -0.883 | -0.098 | 341.976 | 17.188 | 0 | 0.948 | 281.217 | 0.615
| 1544516308 | 0.046 | 0.109 | -0.159 | 342.045 | 17.305 | 0 | 0.527 | 113.217 | 0.213
| 1544516368 | 0.755 | 0.575 | -0.005 | 342.024 | 17.268 | 0 | 1.087 | 142.677 | 1.042
| 1544516428 | 0.666 | 0.251 | 0.116 | 342.477 | 18.039 | 0 | 0.799 | 159.344 | 0.969
| 1544516488 | 1.831 | -0.379 | -0.036 | 342.024 | 17.269 | 0 | 1.894 | 191.717 | 4.365
| 1544516548 | 1.198 | -0.176 | 0.007 | 342.438 | 17.973 | 0 | 1.34 | 188.362 | 2.091
| 1544516609 | 1.03 | 0.528 | -0.141 | 342.249 | 17.652 | 0 | 1.244 | 152.847 | 1.496
+-----+-----+-----+-----+-----+-----+-----+-----+-----+
641987 rows in set (20.98 sec)

```

Figure E.2 Components of the wind resource data in the MySQL database.

To access the Raspberry system is used the FTP (File Transfer Protocol). This protocol allows the user to access the system through the FileZilla Client software that was previously installed on the PC. The software makes use of the IP assigned to the Raspberry by the router, which permits the communication to download the generated .csv files.

This allows generating daily files of type .csv (values separated by commas) that contain the values obtained from the database. Figure E.3 shows an example of a file generated by the generator\_csv.py program.

	A	B	C	D	E	F	G	H	I	J
1	Hora	u	v	w	c	Temp	s	mag	dir	P
2	07:09:49	-6.022	0.935	1.146	345.437	23.091	0	6.208	8.832	158.513
3	07:10:49	-6.497	0.954	1.305	345.129	22.563	0	6.669	8.352	199.861
4	07:11:50	-5.882	1.686	1.007	345.643	23.445	0	6.277	15.993	172.718
5	07:12:50	-6.037	-0.14	1.496	345.716	23.57	0	6.142	358.669	152.374
6	07:13:50	-6.475	-0.654	1.564	345.73	23.594	0	6.58	354.231	188.456
7	07:14:50	-6.865	-1.317	1.466	345.854	23.806	0	7.056	349.133	227.566
8	07:15:50	-6.122	-0.762	1.157	345.761	23.647	0	6.328	352.902	195.001
9	07:16:51	-6.912	-0.764	1.594	344.849	22.085	0	7.012	353.686	237.837
10	07:17:51	-6.149	-0.44	1.403	344.463	21.425	0	6.229	355.898	159.155
11	07:18:51	-5.638	-0.398	1.175	344.824	22.042	0	5.729	355.961	127.74
12	07:19:51	-6.777	0.016	1.434	345.105	22.523	0	6.824	0.137	200.52
13	07:20:52	-6.264	-0.369	1.536	345.102	22.517	0	6.356	356.622	167.856
14	07:21:52	-6.458	-0.819	1.484	345.048	22.424	0	6.569	352.77	183.402
15	07:22:52	-5.391	-0.702	1.101	345.025	22.387	0	5.488	352.577	108.054
16	07:23:52	-4.857	-0.308	1.041	344.983	22.315	0	4.961	356.369	82.652
17	07:24:52	-4.404	-0.519	0.922	344.918	22.203	0	4.465	353.269	57.017
18	07:25:53	-3.341	-0.799	0.726	344.854	22.093	0	3.467	346.537	29.068

Figure E.3 Example .csv file generated with the WindMaster datalogger.

As was mentioned before, the generator software code permits developing the .csv files. The following line code must be entered from the Raspberry Pi-3 Terminal in order to call all the wind data from the database and generate the .csv files per day:

**sudo python /home/pi/WindMaster/generator\_csv.py**

The installation of the WindMaster datalogger was carried out in the facilities of the Academic Unit of Electrical Engineering of the Autonomous University of Zacatecas, the measurement campaign had a duration of more than one year, which correspond to the guidelines to a proper wind resource assessment [11], [12]. Figure E.4 shows the installation of the WindMaster ultrasonic anemometer.



Figure E.4 Final installation of the WindMaster datalogger.

## E.2 Installation of the ultrasonic anemometer WindMaster

The Software and Computing Building (S&C) is located north of the academic campus, specifically at the coordinates of  $22^{\circ} 46' 23''$  north latitude and  $102^{\circ} 38' 39.17''$  west longitude is where was installed the anemometer ultrasonic. This building has a height of 10.5 m and dimensions of 65 m long by 38 m wide. It is oriented towards the North cardinal point, located at the height of 2,311 m a.s.l.

Figure E.5 shows the aerial view of the location of the S&C Building within the campus and the location of the installation of the WindMaster ultrasonic anemometer. The equipment used for the measurement campaign is a 3-axis measuring device, with no moving parts like the traditional cup anemometers. This device, made of aluminum and carbon fiber, has a measurement range of wind speeds of up to 45 m/s.



Figure E.5 Location of the S&C Building and the anemometer within the UAZ campus.

Commonly when acquiring the equipment of anemometric measurement, the manufacturer recommends possible solutions for the data logger, which requires an extra investment to part of the measuring equipment. The WindMaster ultrasonic anemometer uses the serial port RS232, RS422, and RS485; in this sense, the manufacturer recommends using the CR7 datalogger model to perform this connection.

The anemometer was installed in the Building of Software and Computing Engineering, taking into consideration the principle that the sensor must be mounted 1.5 times the height of the building [10]. In addition, it was considered that the selected building has a height of 10.5 m, the mast of the anemometer will be 6 m high from the last floor of the building, leaving the anemometer installed at a total height of 16.5 m.

The manufacturing process of the mast was designed and carried out where the WindMaster ultrasonic anemometer was mounted, based on the recommendations of the manufacturer. Figure E.6 shows the fabrication and assembly process of the 4" diameter mast on the Software and Computing Engineering Building.



Figure E.6 Process of manufacturing, assembling, and installing the WindMaster anemometer.

The tubular mast is supported and tensioned with three tensioners, from the top tip of the mast to its base. The height of the datalogger is located at 1.7 m from the base of the mast, making it easily accessible for maintenance maneuvers inside the cabinet. Figure E.7 shows the final installation of the WindMaster ultrasonic anemometer, allowing the operation of recording and storage of the wind resource data of the on-site measurement campaign.



Figure E.7 Final installation of the WindMaster ultrasonic anemometer.



# APPENDIX F



---

## CFD COMPUTATIONAL RESOURCE

---

### F.1 Computational resource

In the development of the present doctoral research, related to the derived CFD simulations, these were developed with a workstation with the following specifications:

- Operating System: Microsoft Windows 10 Enterprise
- Processor: AMD Ryzen Threadripper™ 1950X 16-Core Processor, 3400 MHz, 16 principal processors, 32 logical processors
- Graphics Processor Unit (GPU) adapter: NVIDIA Quadro P4000  
GPU Memory 8 GB - GDDR5  
Max Power Consumption: 105 W
- Physical memory installed (RAM): 32.0 GB

### F.2 Computational time

The simulations presented in this doctoral research sum more than 150 CFD simulations, equivalent to an averaged time of 2.3 hours per each CFD simulation. This averaged time is strictly dependent on the mesh resolution of the models used in the case studies. The total time stated previously of the CFD simulations not considers the time of the computational CAD design process of the geometries used in this doctoral research. It can be confirmed that the higher the number of cells in the meshing process, the higher the consumption of computational time of the CFD simulations.

### F.3 Appendix References

- [1] J. Blazek, *Computational Fluid Dynamics: Principles and Applications*, 1ra ed. Baden-Daetteil Suiza: Elsevier Butterworth-Heinemann, 2001.
- [2] J. F. Wendt, J. D. Anderson, and Von Karman Institute for Fluid Dynamics., *Computational Fluid Dynamics : An Introduction*, Third Edit. Springer, 2009.
- [3] J. D. Anderson, *Computational Fluid Dynamics : The Basics with Applications*. McGraw-Hill, 1995.
- [4] N. Sayma, *Computational Fluid Dynamics*. BookBoon, 2009.
- [5] O. Zikanov, *Essential Computational Fluid Dynamics*, 1ra ed. New Jersey: John Wiley & Sons, Inc., 2010.
- [6] T. Petrila and D. Trif, *Basics of fluid mechanics and introduction to Computational Fluid Dynamics*, vol. 500. Boston: Springer Science, Business Media, Inc., 2005.
- [7] J. H. Ferziger and M. Peric, *Computational Methods for Fluid Dynamics*, 3rd Editio. Germany: Springer, 2002.
- [8] J. Tu, G.-H. Yeoh, and C. Liu, *Computational Fluid Dynamics: A Practical Approach*, 2nda ed. Reino Unido: Elsevier: Butterworth-Heinemann, 2012.
- [9] J. Bardina, J. Ferziger, and W. Reynolds, "Improved subgrid-scale models for large-eddy simulation," in *13th Fluid and PlasmaDynamics Conference*, 1980.
- [10] R. McKay, "Gill Instruments Ltd., WindMaster & Windmaster Pro Manual Issue 12." Lymington, Hampshire UK, p. 69, 2017.
- [11] MEASNET, "MEASNET Procedure: Evaluation of Site Specific Wind Conditions, Version 2, April 2012.," 2016.
- [12] J. Roeth, "Wind Resource Assessment Handbook," New York, 2010.